Experimental investigations for development of an innovative SiC sensor for spectrometry of neutrons under harsh environmental conditions

Zur Erlangung des akademischen Grades

Doktor der Ingenieurwissenschaften (Dr.-Ing.)

von der KIT-Fakultät für Maschinenbau
des Karlsruher Instituts für Technologie (KIT)

genehmigte

Dissertation

von

Dóra Szalkai

Tag der mündlichen Prüfung: 24. September 2018

Hauptreferent: Prof. Dr.-Ing. Robert Stieglitz

Karlsruher Institut für Technologie (KIT)

Korreferent: Prof. Dr. Kai Zuber, Ph.D.

Technische Universität Dresden (TUD)

Szüleimnek.

ACKNOWLEDGEMENT

I would like to express my deep gratitude to Professor Dr. Robert Stieglitz and Dr. Axel Klix, my research supervisors, for the opportunity to participate in the research work of the Karlsruhe Institute of Technology (KIT). Furthermore I would like to thank their useful critiques of my experimental work and presentations. I wish to thank Dr. Axel Klix with the help and guidance in nuclear measurement technics.

I wish to thank Professor Dr. Kai Zuber, from the Technical University Dresden (TUD), who accepted to be one of my thesis supervisor.

I am very grateful to the Institute of Neutron Physics and Reactor Techniques (INR) at the KIT, for providing me the necessary facilities, materials and equipment to complete my work.

I thank my colleagues, Daniel Gehre and Toralf Döring for their help and technical support on the experiments and set-up solutions. Without their invaluable help this Ph.D. work would have been never accomplished.

I wish to acknowledge the help provided by the participants of the I-SMART project, particularly Fatima Issa, Ludo Vermeeren, Raffaello Ferrone, Abdallah Lyoussi and Laurent Ottaviani. I would thank the opportunity to work together with them, the high quality sensors and the technical support during the measurements and the helpful comments on the prepared manuscripts and reports.

I would express my special thanks to Péter Tüttő, for his zestful help during my work. I am very grateful to him, for the knowledge and advices which he imparted to me about semiconductor physics and devices, mathematical methods and material science.

I would like to show my gratitude to the members of Helmholtz Zentrum Dresden Rossendorf (HZDR), Thomas Süssmilch, Armin Winter and Annett Nitzsche for participation in the design work and the preparation of the sample holders for the different measurements; without their help the tests at high temperatures and in magnetic field could not be carried out. I thank Isabel Kösterke, Dr. Elizabeth Laurent Green and Dr. Yurii Skourski for their unconditional help in my work.

I thank Dr. Anne Stunault and Felix Kandzia from the Institute Laue-Langevin for their help, attendance and contribution to the measurements at high magnetic fields.

I am indebted to many of my colleagues at the KIT-INR and TUD, particularly Dr. Arkady Serikov, Dr. Alexander Konobeev, Prasoon Raj, Ingeborg Schwartz, Dr. Keitaro Kondo, Tom Rücker and Dr. Alexander Domula for their help, suggestions and friendship.

I wish to thank all the participants of our tests at SCK-CEN, HZDR, CEA-Cadarache, Schlumberger Limited for their support.

I thank Dr. Csaba Major for his help during the three years and for his support in everything.

Last but not least, I want to thank and dedicate this Ph.D. work to my parents, who have supported me during all my life.

ABSTRACT

This dissertation work contributes to the development and validation of an innovative neutron detector for fusion diagnostics measurements in the tritium breeding Test Blanket Module (TBM) of the ITER fusion reactor. The boundary conditions in a fusion reactor system range from extreme temporal temperature fluctuations to challenging static and dynamic electrodynamic and electromagnetic fields impacting the sensor signals.

This work presents new results from experimental testing of novel 4H-SiC diode structures. Tests are carried out with several geometries of 4H-SiC diode detectors under different environmental and irradiation conditions.

Fast neutron detection with 4H-SiC sensors are conducted from room temperature up to 500 degrees Celsius. Maintaining a stable reverse current of the diode by bias voltage control a structured energy histogram form has been found even at 500 °C. This enables the use of that sensor type for neutron spectroscopy at elevated temperatures. For high temperature tests, an appropriate small volume set-up has been developed, including the heating system and sample holders.

Thermal neutron measurements are carried out at room temperature with several new types of diode detectors supplied with one or two ^{10}B neutron converter layers outside the sensitive volume of the diodes. Well-defined histogram structure has been found for three diode geometries at room temperature. Due to the high diffusion ability of boron at high temperatures, diodes for thermal neutron measurements are feasible to apply properly only outside the ITER's TBM system.

Under the same physical conditions high signal stability with a low count number deviation has been established for both fast and thermal neutron tests. Many diodes with the same geometrical structure have been irradiated with thermal neutrons, these tests have resulted the same signal structure with slight differences in the signal count rates. Repeatability tests with fast neutron irradiated SiC diodes at different temperatures up to 500 °C have shown also negligible count rate deviations.

For the first time measurements are performed with semiconductor neutron detectors in an external magnetic field. The influence of high magnetic fluxes has been studied in magnetic field intensities between ~ 0.5 and ~ 1 Tesla during 14 MeV fast neutron irradiation and in addition in an 8 Tesla field during epithermal neutron irradiation and there has not been found any effect on the sensor signal. The results suggest a magnetic field independent SiC detector operation even in fusion facilities up to 8 Tesla.

Two methods to estimate the diffusion length and minority charge carrier lifetime of neutron irradiated SiC have been developed applying the measured count rate values at different bias voltage levels.

The two calculations result in nearly the same diffusion length values. Based on the resulting values of the diffusion length, the influence of temperature on the minority carrier movement and the detector signal has been investigated. It was observed, that the diffusion length increases with higher temperatures, which agrees with today's knowledge.

A collection of Monte Carlo simulation models has been developed including each of the tested SiC sensor design in order to have a better understanding of the output signal. The simulation software used is Geant4, which is a proper code to reproduce the different signal features on the recorded pulse height spectra, thus their origin can be reconstructed for fast and thermal neutron sources. These models have been successfully applied to explain the measured data.

The investigations carried out with 4H-SiC detectors in harsh environment are limited to neutron irradiation. Further experiments are needed to get to know the detector behavior for charged particles as electrons and ions under similar conditions. Testing the combined effect of magnetic field and high temperature could actually create the same environment as the real measurement conditions inside the ITER-TBM system. The present work can be ideal base for these later measurements.

KURZFASSUNG

Diese Dissertation trägt zur Entwicklung und Bewertung eines neuartigen Neutronendetektors bei, der zur Neutronenflussmessung zu Diagnosemessungen in den zur Untersuchung der Tritiumbrutraten vorgesehenenTest Blanket Modulen (TBM) des ITER Fusionsreaktors eingesetzt werden soll. Während des Betriebes des Reaktors herrschen in den TBM extreme Umgebungsbedingungen, wie hohe Temperaturen und starke elektromagnetische Felder, welche die physikalischen Eigenschaften des Detektors erheblich beeinflussen.

Die vorliegende Arbeit stellt Ergebnisse von Messungen mit neuartigen 4H-SiC Diodendetektoren vor. Die Testszenarien beinhalte verschiedene Detektorgeometrien und Umgebungs- und Bestrahlungsbedingungen.

Die Untersuchung von schnellen Neutronen mit 4H-SiC-Detektoren wurde im Bereich zwischen Raumtemperatur und 500 °C durchgeführt. Die Ausgangssignale wiesen eine hohe Stabilität in einem großen Temperaturbereich auf. Für die Tests unter diesen hohen Temperaturen wurde ein Versuchsaufbau entwickelt, der die Heizung und die Halterung für den Detektor umfasst.

Funktionaletests mit thermischen Neutronen fanden unter Raumtemperatur statt. Es kamen hierbei verschiedene neue Detektorgeometrien zum Einsatz, welche mit ein oder zwei 10B dotierten Schichten versehen wurden um thermische Neutronen zu absorbieren. Für drei Detektorgeometrien wurden bei Raumtemperatur Messungen durchgeführt, die eine hohe Stabilität aufwiesen. Es wurde festgestellt, dass die Dioden für Messungen bei hohen Temperaturen innerhalb der TBM-Umgebung ungeeignet sind, da von Boratomen verursachte Kristallfehler zu einem erhöhten elektrischen Rauschen führen.

In dieser Arbeit wurden erstmals Messungen mit SiC-Neutronendetektoren in starken magnetischen Feldern durchgeführt. Der Einfluss des Magnetfeldes auf das Detektorsignal wurde bei Feldstärken zwischen 0,5 und 1 Tesla während der Bestrahlung mit 14 MeV-Neutronen untersucht. Zusätzlich wurde bei der Bestrahlung mit epithermischen Neutronen ein magnetisches Feld von 0 bis 8 Tesla genutzt. Es konnten bei diesen Feldstärken keine Einflüsse des Magnetfeldes auf den Messergebniss beobachtet werden. Die Ergebnisse deuten darauf hin, dass der Detektor auch in Fusionssystemen bei magnetischen Feldstärken von bis zu mehr als 1 Tesla eingesetzt werden kann.

Neben den experimentellen Untersuchungen wurde auch theoretische Arbeiten im Bereich der SiC-Teilchendetektoren durchgeführt. Es wurden zwei Methoden entwickelt um die Diffusionslänge und die Ladungsträgerlebensdauer von SiC-Halbleitern zu ermitteln, indem die Zählrate bei unterschiedlicher Vorspannung gemessen wurde. Die Ergebnisse der beiden Messungen der Diffusionslänge lieferten nahezu dasselbe Ergebnis. Auf Basis der Ergebnisse konnte der Einfluss der Temperatur auf die

Minoritätsladungsträger und das Detektorsignal untersucht werden. Es wurde hierbei festgestellt, dass sich die Diffusionslänge mit steigender Temperatur verringert, was auch dem aktuellen Stand der Wissenschaft entspricht für SiC.

Mehrere Monte Carlo Simulationen wurden durchgeführt, die zum besseren Verständnis der von den unterschiedlichen Detektoren aufgenommenen Signale beitragen. Die verwendete Software Geant4 erlaubt es, die Ausgangssignale des Detektors zu simulieren, sodaß die einzelnen Komponenten, die zum Signal beitragen, genauer analysiert werden können.

Die weitreichenden Untersuchungen von 4H-SiC- Detektoren unter schwierigen Umgebungsbedingungen beschränken sich auf die Bestrahlung mit Neutronen. Es sind weitere Experimente von Nöten, die das Verhalten des Detektors bei Bestrahlung mit geladenen Teilchen wie Elektronen oder Ionen bei ähnlichen Bedingungen untersuchen. Basierend auf den Versuchen in starken Magnetfeldern, können weitere Experimente unter hohen Temperaturen zum besseren Verständnis von Messinstrumentierung in Fusionsanlagen beitragen.

TABLE OF CONTENT

1. INTRODUCTION

1.1 Neutron flux measurements under physical conditions of a fusion reactor

For several years, big efforts are made for new developments in fusion technology with the aim to establish an alternative energy source despite using fission nuclear power or fossil fuels, which are producing non negligible amounts of nuclear waste or air pollutants and also present safety risks. With the application of fusion power these harmful factors could be mitigated or completely avoided.

In the framework of the international development project, ITER (The Way), a new experimental fusion facility based on the tokamak principle will be constructed. In November of 1985, the project was born and in 1988 the conceptual design work for the project began. The final design for ITER was approved in 2001 by the member states, the European Union (via EURATOM), Russian Federation, USA, Japan, China, Korea and India. ITER is an experimental forerunner of the DEMO and of future fusion reactors. The scientific goal of the ITER project is to achieve at least ten times higher fusion power (FP) harnessing than the heating power (HP) to maintain the plasma, which is expressed by the quality factor weighting FP to HP. [1]

The ITER with the supporting buildings will be located in Cadarache, in France. The experimental facility enables to model a fusion power reactor, to test technical solutions, to investigate the fusion scenarios and the impact on the surrounding materials, etc. The fusion processes will take place in the tokamak's vacuum vessel thus the design and the application of proper materials are crucial factors in case of the tokamak's facilities due to the extreme physical conditions during the reactor operation, such as high temperature, strong electrical and magnetic fields.

The fuel of future fusion power reactors is served by two isotopes of hydrogen, deuterium and tritium. The estimated necessary amount of tritium per day is 500 grams to power a fusion reactor to 1 GW electrical output and around 2.5 MW thermal power assuming a 37% efficiency of the thermodynamic conversion cycle. In order to maintain this reactor power the estimated yearly tritium consumption is between 100 and 200 kg [2]. The deuterium supply from sea water is practically unlimited (33 mg deuterium/l), but tritium can be found only in trace amounts on the Earth estimated around 12 kg. Most of the tritium has been generated in atmospheric nuclear tests and now is dissolved in the oceans [3]. Consequently, the amount of tritium required for power reactor operation must be produced artificially. The tritium production is planned to be solved by lithium containing a tritium breeding system surrounding the fusion plasma [1]. Test Blanket Modules (TBM) are foreseen for ITER, which allow testing several breeding blanket concepts in a real fusion reactor environment.

To maintain the stable and safe function of a fusion reactor, concurrently the full online supervision of the plasma density, pressure and temperature distribution, a continuous validation and measurement of the flux of neutrons generated by plasma reactions are necessary. The neutrons are responsible for the production

of the heat, thereby convert the fusion power into usable form, they drive the tritium production in the tritium breeding blanket and these neutrons are also damaging the surrounding structural material. The expected neutron spectrum along radial direction inside HCPB TBM system of the ITER varies from the plasma facing side wall to its back side. The neutron energy occurs from thermal up to fast neutron (up to ~ 15 MeV) energies.

Reliable measurement methods of neutrons in fusion environment became increasingly important due to the development status and the forthcoming commissioning of ITER. The applied sensors have to be able to detect neutrons from thermal energy up to ~14.1 MeV. They have to withstand several hundreds of degrees Celsius and strong electromagnetic field depending on the location inside the tokamak and the building. The neutron flux density in the breeding blanket plays an important role for tritium production and thereby its accountancy. Thus, neutron flux measurements are necessary in the TBMs of the reactor, which also allow for checking and validating nuclear data simulation codes.

Neutron detection is based on conversion to charged particles by means of scattering with light nuclei or nuclear reactions emitting charged particles. Some materials have high cross-section for thermal neutron reactions as ^{10}B, ^{6}Li and ^{157}Gd, thus resulting reaction products (ions, photons) serve information about the incoming neutrons. Fast neutrons are detected by measuring the energy deposition of charged particles after nuclear reactions or collisions. Another detection method is their thermalization by collisions in materials with high hydrogen content followed by any thermal neutron detection method. Merely some detector types may be considered due to the extreme environmental conditions and limited space in the TBM system. Currently, there are specific neutron detection solutions under investigation, such as neutron foil activation method, self-powered neutron detectors, micro fission chambers and wide band-gap semiconductor detectors [4].

The present thesis discusses silicon-carbide (SiC) semiconductor sensors. This wide band-gap material has been chosen because of its' beneficial physical properties (high temperature resistance, high breakdown voltage, low thermal expansion, etc.) and ability to perform on-line neutron flux monitoring. In the last decades, 4H-SiC crystal production has undergone substantial progress and several types of SiC sensors were investigated under different environmental conditions in research laboratories. The earlier examinations have also covered short term high temperature tests with charged particle irradiation, but no extensive long term measurements with neutrons at elevated temperatures were carried out. Besides the detection ability and resulted signal with SiC detectors at such high temperature, the proper conditions of detector operation need to be established. Because of the increasing electrical noise and high probability of damaging effects at high temperatures, it is important to find the most appropriate electrical set-up, as the applied bias voltage value on the hot diode or its proper encapsulation, for the long term operation and lifetime of the sensor.

Numerous different nuclear reactions may occur between fast or thermal neutrons and the nuclei of the SiC crystal. For the present work, in order to fully understand the electric signal generation of the investigated SiC sensors, several measurements in different neutron fields, at elevated temperatures or in magnetic fields

followed by proper analysis and simulation of the signal have been carried out. Monte Carlo simulations of the sensors in the neutron field were built. The resulting signal has also been considered as a consequence of solid state physical processes besides nuclear, thereby the change of some physical properties of neutron irradiated SiC crystal are investigated.

The main objective of the work presented here is the examination of the behavior of 4H-SiC pn-diode detectors at elevated temperatures during neutron irradiation with the aim to ascertain the suitability of SiC detectors for application inside the ITER TBM system. The tests are focused on the realization of long term and repeated irradiations in order to examine the signal stability, the degradation of the sensor and to find the proper measurement settings for 4H-SiC sensors at high temperatures.

Additionally, comprehensive experimental work has been carried out with 4H-SiC diode sensors supplied with boron converter layer to detect thermal neutrons. The aim is to establish the proper geometry construction for thermal neutron irradiation tests in fusion environment; bearing in mind the effect of crystal degrading secondary generated particles. Furthermore, the sources of the different recorded signal with several different geometrized sensors are discussed.

Like in fusion reactor environment, the applied sensors will exposed to strong magnetic field, as well, 4H-SiC detectors have to be investigated at this condition. The next objective is the realization of the first neutron irradiation test measurements with 4H-SiC diode detector in permanent magnetic field. The maximum magnetic field applied in these tests was 8 Tesla.

An appropriate computer model of SiC detectors was created to support the analysis of the experimental tests and as a tool for calibration in future measurements. Thoroughly modelled detector geometries and sophistically described physical processes are necessary to simulate the signal of small size diode detectors. These calculations provide the basis of the interpretation of the resulting signal and show the contribution of the events from the different sensor parts. These models can be used to further optimize the detectors.

One of the important properties of semiconductor devices is the diffusion length of minority charge carriers because it provides information about the crystal quality. Previous research works with SiC based on the examination of signal generated by light and heavy charge particle bombardment. Other consideration has to be applied in case of diodes irradiated exclusively with neutrons. For this purpose, the present thesis discusses new evaluation methods to establish the saturation count rate at a given neutron flux and the diffusion length of minority charge carriers in a certain SiC diode type.

1.2 Working methodology

The present doctoral thesis bases on experimental work performed in the framework of the international I-SMART (Innovative Sensor for Material Ageing and Radiation Testing) project [5]. It focuses on experimental tests under ITER-relevant conditions and their analysis.

To help the understanding of the detector behavior, two types of Monte Carlo simulations have been applied during the work. The Geant4 simulation package has been used to investigate the signal generation of the certain detectors. The distribution and location of the thermal neutron sensitive ^{10}B-ions in the ion-implanted SiC-crystal has been modeled with the SRIM/TRIM software. The ionization and energy loss processes originating from ions with different masses are examined, as well, with the latter program.

Following the first tests, improved detector geometries with the most beneficial electrical and geometrical properties (low noise, well-defined signal structure, etc.) and electronic set-ups (low electrical noise, compatible units to signal process, regulated measurement set-up by software, etc.) are sorted out for thermal neutron tests in nuclear reactor environment and fast neutron measurements at elevated temperatures. The detector signals are carefully analyzed and the results are compared from the different irradiation sessions with different SiC detector geometries, neutron sources and electronics. The identification of the distinct contributors to the output signal is supported by Geant4 Monte Carlo simulations. Additionally to the nuclear physics considerations, the influence of the semiconductor physical properties, such as the temperature dependence of the band-gap energy and electron-hole pair creation energy are also taken into account and applied to the signal analysis.

Neutron irradiation tests at high temperatures up to 500 °C have been carried out. These measurements have been conducted using low noise SiC sensors which are specially designed for high temperature application. Further experiments have been performed under fast neutron irradiation (with the same sensor type as by high temperature tests) in a permanent magnetic field up to 1 Tesla and in epithermal neutron field (with the sensor type applied for thermal neutron measurements) up to 8 Tesla.

2. PHYSICAL CONDITIONS IN THE ITER TOKAMAK AND TEST BLANKET MODULES

A cross-sectional view of the tokamak is shown in Fig.1 with the cryostat, which covers the vacuum vessel and superconducting magnets. 18 toroidally arranged segmented solenoid magnets, 6 poloidal field coils, 18 correction coils and a central solenoid coil build the magnetic field inside the reactor. These coils form the plasma into a curved toroidal shape. The maximum magnetic field could reach up to 13 Tesla at the windings and up to 4.5-5 Tesla at the center of the plasma [1]. The inner part of the tokamak, faced directly to the plasma is referred to as blanket. The blanket module provides shielding and requires cooling. To maintain the fusion plasma several physical circumstances must be granted at the same time.

Fusion reaction between the fuel deuterium and tritium ions can occur at high temperature, where the ions are separated from their electrons; with other words the plasma status is evolved. At the average temperature 10 keV fusion reaction between deuterium and tritium ions takes place through $^{2}H + {}^{3}H \rightarrow \alpha +$ neutron + 17.6 MeV reaction and for an amount of ions. With energy less but near to 0.1 MeV energy this reaction can come about by quantum tunneling effect. Plasma temperature up to 150 million degrees Celsius and therefore ions and electrons with energy above 0.1 MeV is planned to be developed by introduction of high energy deuterium ions into the reactor vessel - therefore particle collisions produce heat-, by high frequency electromagnetic field and by external microwave heating [1]. The fusion process between the induced deuterium and tritium results in neutrons with 14.12 MeV mean energy and helium nuclei with 3.49 MeV. The helium ash will be extracted by the divertor part of the reactor and the neutrons will deposit their energy in the plasma facing walls. In the tritium breeding blanket, fast and thermal neutrons will drive the tritium production process due to the endotherm $^{7}Li(n, \alpha+n)^{3}H$ - 2.5 MeV and exotherm $^{6}Li(n, \alpha)^{3}H$ + 4.8 MeV reactions, respectively.

The sufficient tritium production rate is crucial for future fusion power reactors to maintain the fusion plasma. Thereby, 6 tritium breeding test blanket modules (TBM) based on different breeding blanket concepts for validation tests in ITER are under design in different countries. Two of the TBM's are developed by the European Union, called the Helium Cooled Pebble Bed – HCPB TBM- and Helium Cooled Lithium Lead – HCLL TBM - see in Fig.2-a and Fig.2-b. Four additional TBM's are under construction in other countries, that are not discussed in the present work, but it is worth listing them: the Dual Coolant Lithium Lead – DCLL - is foreseen by the USA, the Water Cooled Ceramic Breeder – WCCB - from Japan, the Helium Cooled Ceramic Breeder – HCCB TBM from China and the Lithium Lead Ceramic Breeder – LLCB - developed by India and the Russian Federation. Test operation with the two European TBM's are planned to be performed in the equatorial port #16 of the ITER's tokamak [6,7].

The anticipated temperature is between 250 °C and 650 °C inside the TBM, in some areas even more. The average magnetic field at the TBM's location is up to 4 Tesla. The cooling in both cases is served by helium channels located inside the module's volume. As a structural material of the modules, ferromagnetic EUROFER was chosen. Additionally, neutron multiplier materials such as beryllium and LiPb

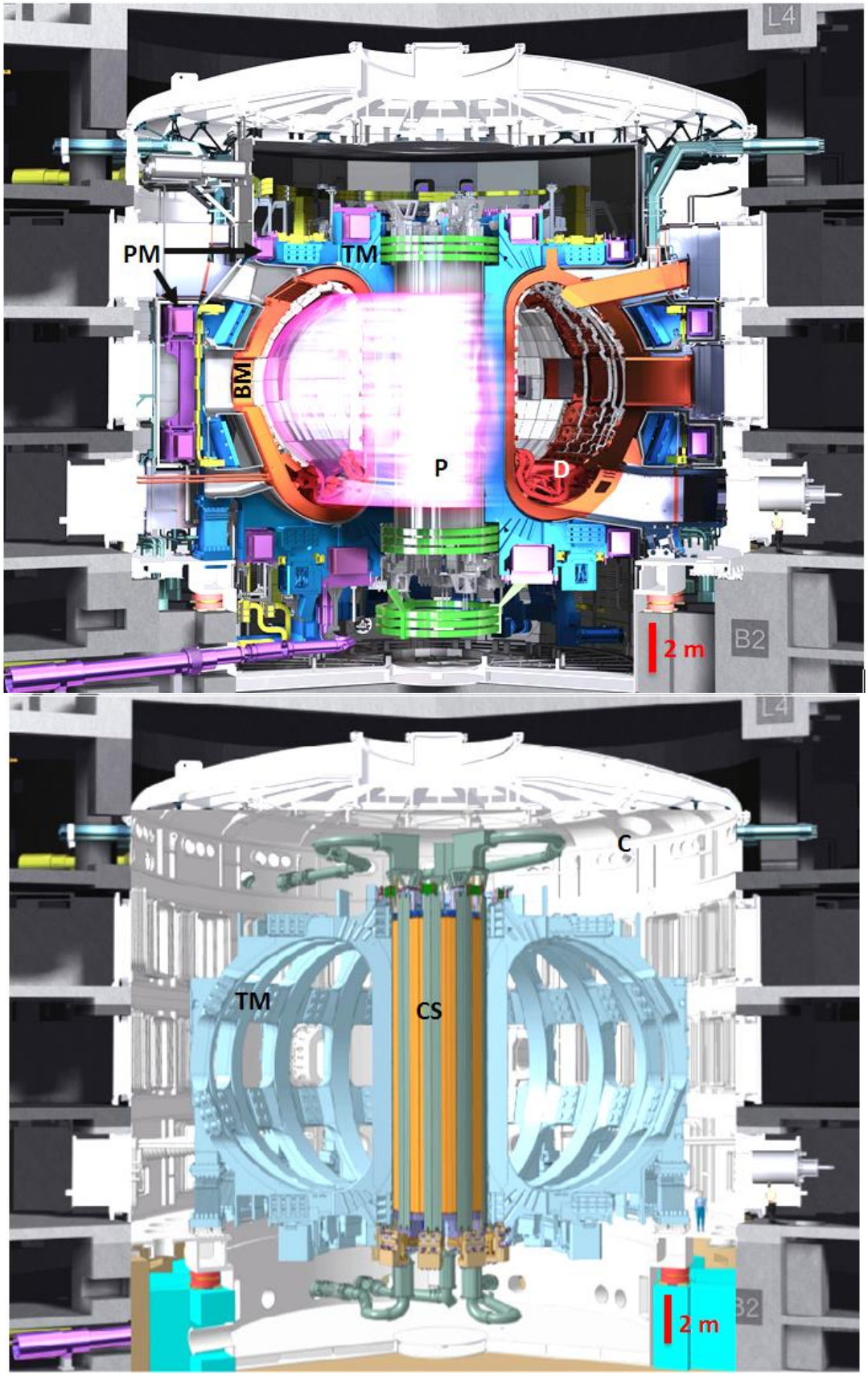

Fig.1 – Schematic 3D vertical cut through the ITER Tokamak The upper picture interprets the reactor volume with the plasma P, poloidal magnets PM, toroidal magnets TM, divertor D, cryostat C, central solenoid CS and the blanket module BM. The lower picture shows the central solenoid and the toroidal magnets without the surrounding facilities. Source: [1]

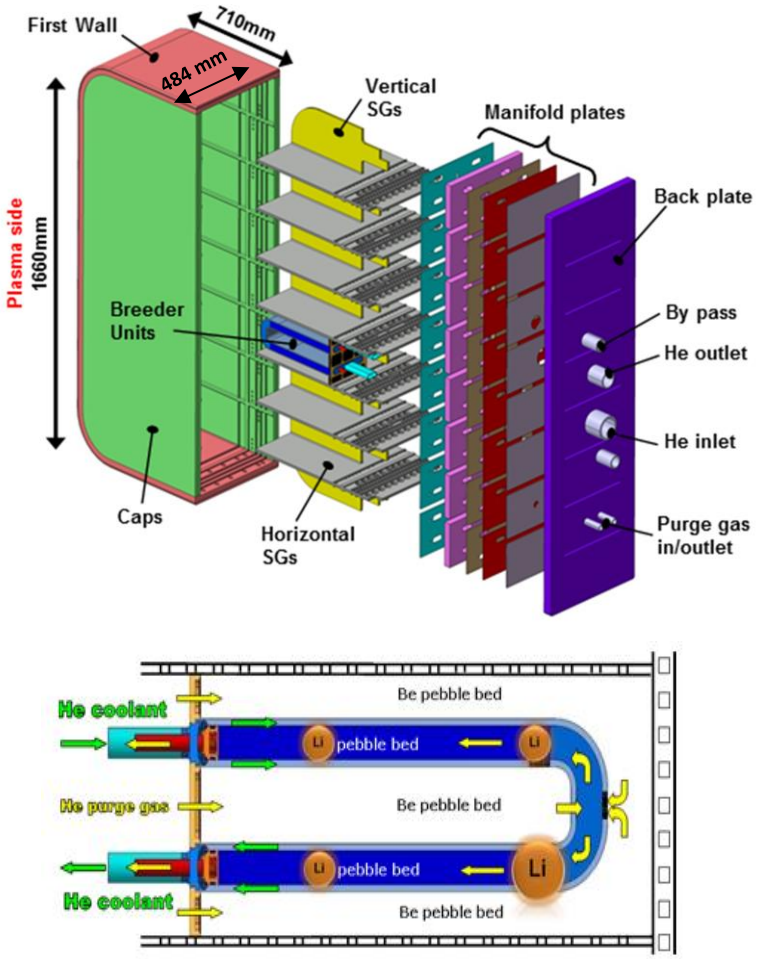

Fig.2-a - Exploded view of the Helium Cooled Pebble Bed – HCPB test blanket module, the purge gas and the coolant flow inside the breeder unit, SG – stiffening grids (Source: [7])

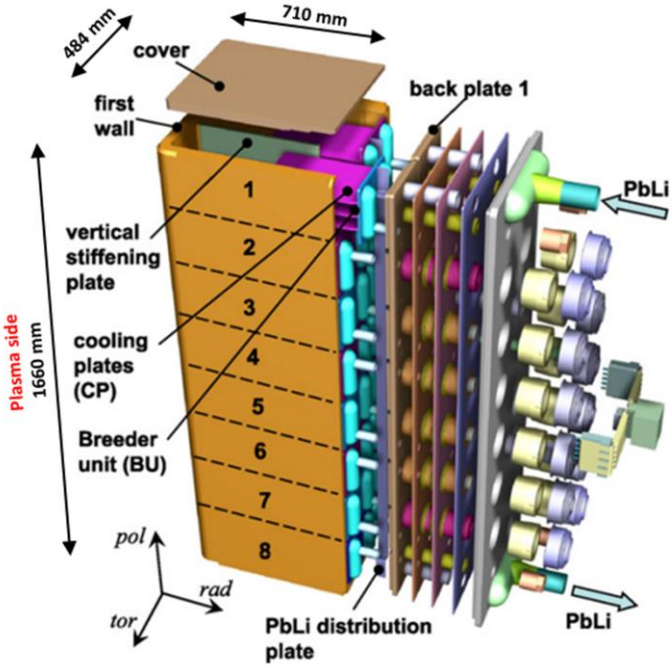

Fig.2-b – Exploded view of the Helium Cooled Lithium Lead – HCLL test blanket module design proposed by CEA (Source: [8])

support extra neutron production, which further increases the tritium production efficiency [6,7].

The expected neutron group fluxes along radial direction inside HCPB TBM system of the ITER is shown in Fig.3. It is obvious that the neutron energy varies from thermal up to < 15 MeV. Furthermore, the plasma side wall is the most exposed to the neutron irradiation. Behind the first wall this energy region is less dominant compared to the higher ones.

The neutron flux in the TBM is around 10^{14} $cm^{-2}s^{-1}$ in the front from which the expected fast neutron flux is maximum 10^{14} $cm^{-2}s^{-1}$ and the thermal neutron flux is maximum 10^{9}-10^{13} $cm^{-2}s^{-1}$.

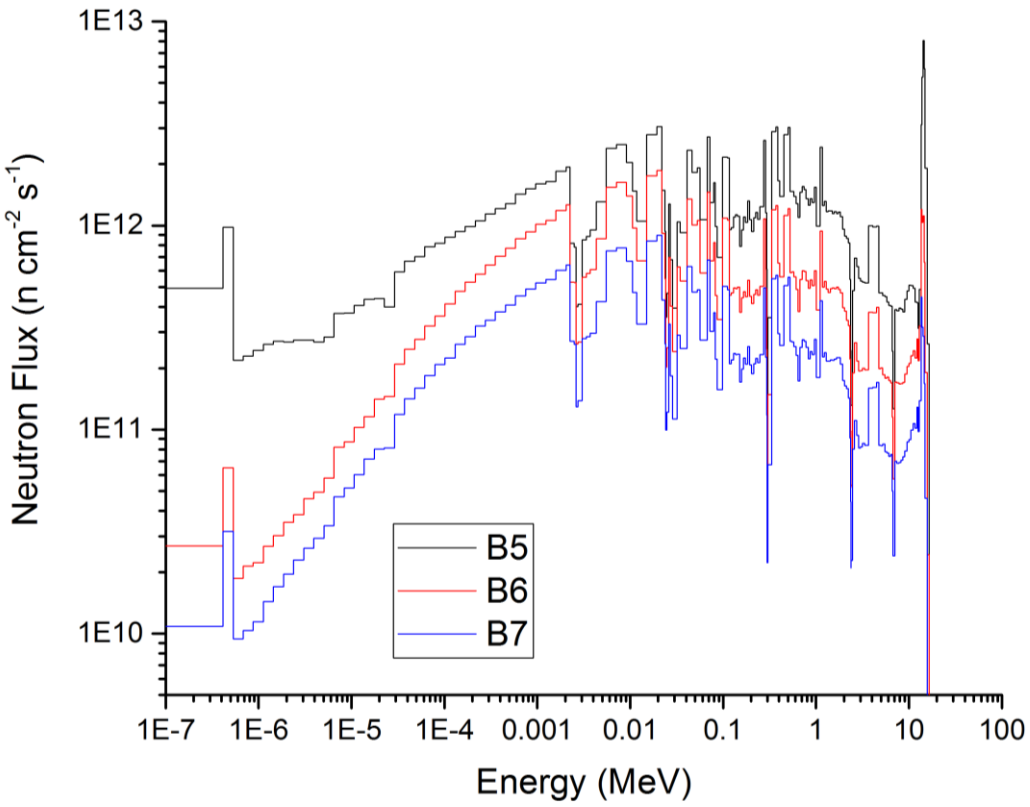

Fig.3 - Variation of the expected neutron spectra along the radial direction in the ITER HCPB TBM at three position relative to the plasma: B5 – plasma side front wall, B6 – mid plane, B7 – back wall. Source: [9]

Due to the extreme environmental conditions in the fusion environment, the validation and direct measurement of the performance of the ITER pose challenges. A planned test position of the neutron flux measurement is inside the TBM, where the average magnetic field will be ~4 Tesla or even more and the temperature is estimated between 350-500 °C, in some places up to 950 °C. Significant electromagnetic noise needs to be considered in the measurement positions inside the TBM due to the external heating system for example. To measure the neutron field the applied detector system should withstand all the above-mentioned harsh environmental conditions. For this purpose, several types of nuclear detectors are under investigation;

their capabilities must be checked to decide which of them are, with adaptations, appropriate as a measurement device in the TBM during the operation of the reactor.

A possible candidate for neutron flux measurement is neutron activation analysis (NAA) because of its robustness; among others the electronics can be kept away from high dose rate areas. Main problems of NAA technique are the fairly limited access into the TBM, its invasiveness, and that the measurement is ex situ, thereby the monitoring of the TBM could not be real-time. With the application of self-powered neutron detectors (SPND) [10], the measurement would become in situ inside the TBM. The commercially available SPND detectors have a high sensitivity to thermal neutrons, but up to now, there is no proper solution to detect fast neutrons [4]. Additional radiation detectors, which are developed and investigated for harsh environmental condition measurements, are wide band-gap semiconductors, as diamond and silicon-carbide, as diode detectors. Semiconductor sensors could be made sensitive from thermal up to fast neutron energies simultaneously, applying thermal neutron converter materials, such as lithium-6 or boron-10 nuclei. A benefit of these detectors is their small size and the structured device geometry due to the technological developments evolved up today. Disadvantage of semiconductor sensors is their limited lifetime under ionizing radiation. They may not be suitable for high duty DT cycles later in the ITER research program but may serve as neutron monitors during DD cycles and early low duty DT cycles. The detection of neutrons in semiconductor detectors happens via secondary charged particles. Fig.4 illustrates some basic reactions between fast and thermal neutrons and SiC.

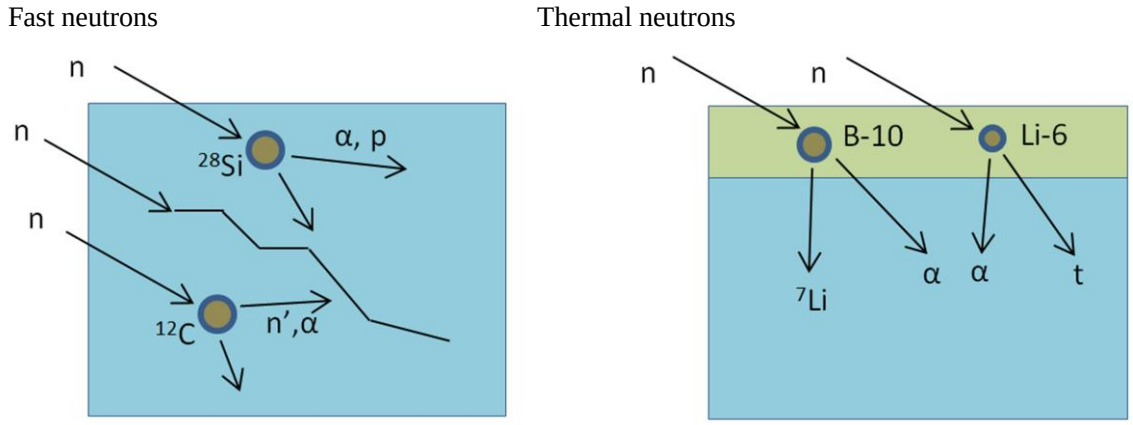

Fig.4 – Basic reactions between SiC and fast and thermal neutrons

3. SILICON CARBIDE SEMICONDUCTOR SENSOR FOR NEUTRON DETECTION

3.1 State of the art of SiC nuclear detectors

Due to their beneficial physical properties, SiC and diamond semiconductor detectors are potential candidates for operation under extreme environmental conditions. Radiation detection techniques using semiconductor materials already have a strong experimental and theoretical background.

Investigation of detection with diamond crystals are carried out since the 1920's. The first available documented tests with natural diamond were published in 1923 [11], in which the electrical response of the crystal for UV light was observed. From the 1940's the direct examination of ionizing radiation with diamond detectors came to the prominence, and up today several developments in the crystal manufacturing process have led to improved detectors [12, 13]. The main types of diamond detectors are CVD (chemical vapor deposition) detectors and single crystal detectors. With the evolution of the material and detector quality, the role of diamond detectors in reactor and plasma monitoring have increased during the last few years and they appear to be a possible sensor for measurements at high particle flux and in high temperature environment.

Later, silicon carbide came to the fore as a competitor of diamond detectors. The hexagonal structured 4H-SiC crystal is one of the most proper candidate materials for measurements under extreme conditions. Its excellent properties, such as detector signal stability under high temperature, were observed already in the early experiments. To examine the operation of 4H-SiC as nuclear detector at elevated temperatures, Babcock and Chang conducted the first test measurements with SiC semiconductor sensor already in 1962 [14]. They prepared SiC pn-diode detectors to measure 5 MeV alpha particles at detector temperatures up to 700 °C. A broadening in the measured alpha peak and a shift towards higher energy channels were seen at higher temperatures. In tests conducted at 700-800 °C, the level of the electronic noise reached the level of the signal, thereby the temperature limit was defined for the use of 4H-SiC detectors prepared with the technology at that time. Between 2009 and 2011 extensive tests with SiC Schottky detectors were carried out in the framework of the NEUP 09-842 project [15]; beside several results, this work contributes to the establishment of electron-hole pair generation energy as a function of the temperature in 4H-SiC-based alpha detectors. In the same work further detailed examinations of the effect of the temperature, leakage current on peak broadening and energy shift in the recorded energy spectrum were also performed. In 2011, further extended experiments at high temperature were carried out by Kalinina et al. [16]. They applied Al-implanted 4H-SiC pn-diodes to detect 3-8 MeV alpha particles up to 375 °C ambient temperature. The effect of the temperature on the signal of the diodes was carefully examined and the different noises and current contributions which have occurred by rising temperature were investigated.

In 1999, Seshadri et al. [17] published their work about high flux neutron irradiation test results with 4H-SiC Schottky detectors. The achieved fast neutron fluence in the measurement position was 10^{17} cm^{-2}. No significant change in the energy resolution, noise characteristics or detector efficiency were observed. Due to

the neutron induced radiation damage of the crystal, decreased charge collection efficiency was found after higher applied neutron fluences. Additional test of 4H-SiC MESFET's and Ni, Ti/Schottky barrier diodes (SBD) at 1 MeV neutron irradiation were performed by Zhang Lin et al. in [18] in 2010. The current characteristic of the two types of devices was recorded. The forward characteristics of SBD detectors did not change significantly, the electrical behavior of the SBD remains stable under higher neutron fluence (~10^{14}-10^{15} cm^{-2}). In case of MESFET devices, the drain current decreased and the threshold voltage increased at elevated neutron fluences. It was established that the higher doping concentration of the active region of the device ensures better tolerance to neutron irradiation. Extensive examination and analytical work in the topic of 4H-SiC radiation detectors was carried out by Ruddy et al. in several works. In 2006, they published their remarkable research [19] about the fast neutron response of a 4H-SiC pin-diode detector. Three different neutron sources, americium-beryllium and californium-252 isotopes and 14 MeV neutrons supplied by a deuterium-tritium neutron generator were applied to the measurements. After additional analysis in [20] it was found that SiC diode detectors are proper devices to perform fast neutron spectrometry measurements due to their high energy resolution ability.

To detect neutrons in the thermal energy region, additional solutions have to be applied to form the proper crystal detector, for this purpose a variety of thermal neutron converter materials were introduced which are based on ^{6}Li or ^{10}B. It is worth noting the work of McGregor et al. [21,22,23] due to their comprehensive examinations in thin film coated thermal neutron detector development and characterization for GaAs. By describing the different applied sensors and specific computer simulations created these researches help the further developments with other semiconductor materials. Further examination of SiC detector irradiated with thermal neutrons was carried out by Dulloo et al. [24] and by Kim et al. [25]. The thermal neutron converter layers contained ^{6}Li isotope and the secondary particles from the nuclear reaction $^{6}Li(n,\alpha)^{3}H$ were detected in the active volume of the diode detectors. Boron-10 containing converter material was applied by Ruddy [26] in the form of $Zr^{10}B_2$ and the signal of the secondary ions from $^{10}B(n,\alpha)^{7}Li$ reactions was investigated.

Several tests were performed by different research groups with SiC crystal detectors using X-ray, gamma photon and heavy charged particle sources. The present work is based upon the literature of thermal and fast neutron detection and on the research supporting the evaluations applied therein. Particular attention is paid to the possibility of adapting the specific sensors investigated here to the environmental conditions in the ITER TBM. The sensors should withstand high neutron flux, strong electro-magnetic field and elevated temperature at the same time, this is challenging to achieve. To obtain the proper SiC detector for these physical circumstances new diode structures and measurement proceedings have to be developed and applied.

3.2 Physics of SiC semiconductor detectors

Semiconductor crystals can be divided into two main groups: mono-elemental semiconductors, as silicon and diamond are built up by one chemical element and compound semiconductors formed by two or

more different elements, as gallium arsenide, silicon carbide, cadmium zinc telluride, etc. In both types, the atoms are occupying well defined positions relative to each other and thereby, they form certain crystal structures. With the 14 types of Bravais lattices depicted in Fig.5 all the crystal structures can be described [27].

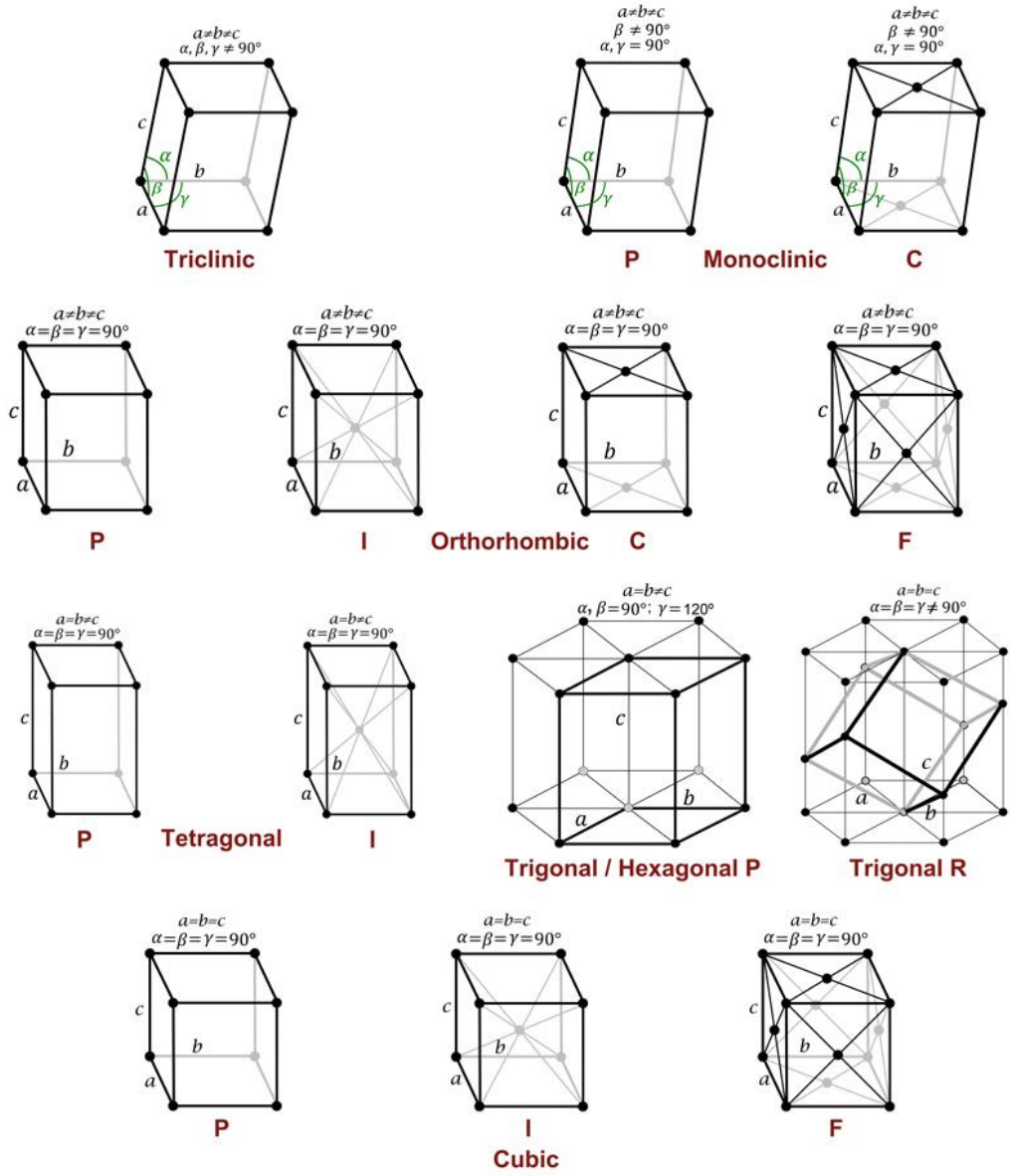

Fig.5 – Schematic spatial structure of semiconductor Bravais lattices. Source: [28]

Solid materials can be built up in different crystal structures; the group of the similar crystal structures for the same compound material is referred to as polytypes. Silicon-carbide has more than 200 polytypes, from what 3C(β)-, 4H- and 6H(α) crystal forms are known as power device materials. 4H- and 6H-SiC have hexagonal (H) structure with 2 different lattice constants, 3.07 Å and 10.05 Å for 4H-SiC, 3.08 Å and 15.12 Å for 6H-SiC crystals. The 3C-type SiC has cubic (C) lattice with a lattice constant of 4.36 Å [29,30].

Depending on the structure of the crystal, electrons with certain energies could interact with the lattice due to their diffraction on the periodic potential field formed by the crystal's atoms. There are energy levels that are forbidden in the periodic lattice applying the "nearly free electron model". These energy gaps could be established from the following, [31]:

$$\boldsymbol{k} = \pm \frac{\pi}{\alpha}, \tag{1}$$

where $\boldsymbol{k}$ is the wavenumber and a is the lattice constant. In a periodic lattice the wave function Ψ with the coordinate variable x of the electrons can be written in the form of:

$$\Psi_1 = \exp(i\boldsymbol{k}x) = \exp\left(\frac{ix\pi}{\alpha}\right), \tag{2}$$

$$\Psi_2 = \exp(-i\boldsymbol{k}x) = \exp\left(-\frac{ix\pi}{\alpha}\right),$$

The combinations of the two wave functions are:

$$\Psi^+ = \Psi_1 + \Psi_2 = 2\cos(\boldsymbol{k}x), \tag{3}$$

$$\Psi^- = \Psi_1 - \Psi_2 = 2isin(\boldsymbol{k}x).$$

The probability density function of the electrons in the lattice can be expressed by the square function of the absolute value of the combined functions, $|\Psi^+|^2$ and $|\Psi^-|^2$. The band-gap energy (E_g) can be determined by the following integral:

$$E_g = \int U(x)(|\Psi^+|^2 - |\Psi^-|^2)\, dx = U. \tag{4}$$

In the integral $U(x) = Ucos(2\pi x/a)$ is the potential energy of an electron at the crystal point x with a maximum magnitude U. Solving the integral it can be seen that the gap energy is equal to the Fourier component of the crystal potential [31]. $|\Psi^+|^2$ and $|\Psi^-|^2$ mark the positions of the electrons related to the atoms in a crystal's lattice, where they could be found with the highest probability. The first energy bands, built by these electrons are called as conduction band and valence band, their relating band edge energies are indicated by E_c and E_v. E_c and E_v indicate the energy values regarding the minimum energy level of the conduction band and the maximum energy level of the valence band. Therefore, the more common form of Eq.(4) can be written with these energy levels:

$$E_g = E_c - E_v \ . \tag{5}$$

If the band edges of the conduction and valence bands have the same $\boldsymbol{k}$ crystal momentum the band-gap is called direct bandgap. If the $\boldsymbol{k}$ vectors are different, the gap is indirect [31, 32], see in Fig.6. In case of indirect band-gap electrons have to change their momentum to jump from the valence band to the conduction band, while as for direct band-gap the transition happens directly, without a momentum change. During de-

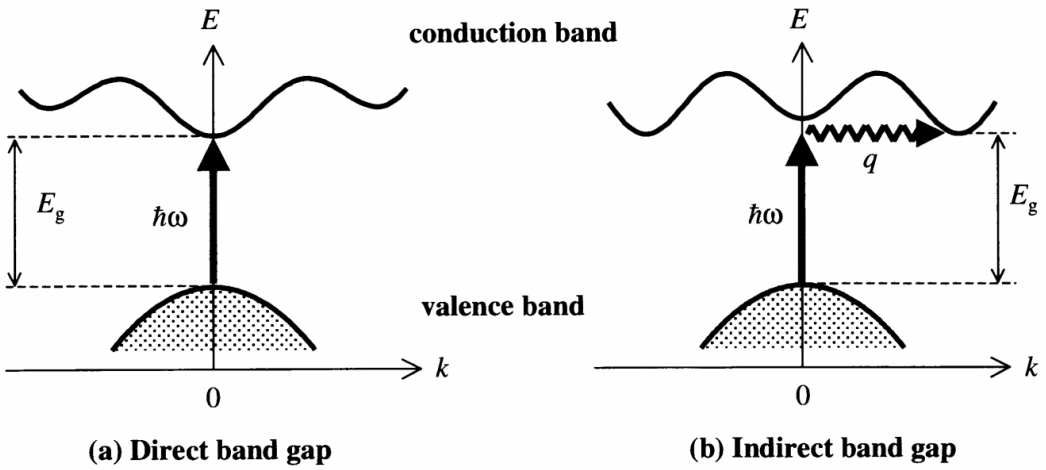

Fig.6 – The structure of direct (a) and indirect (b) band gaps. ***k*** – momentum vector, ***E*** – energy, ***ħω*** – photon energy, $\boldsymbol{E_g}$ – band gap energy. The vertical arrows represent the photon absorption, while the wavy arrow illustrates the momentum transfer by phonon absorption or emission. Source of picture:[33]

excitation process from the conduction band to the valence band a photon is emitted with the energy equal to the gap energy. Semiconductors with direct band-gap are proper materials to produce light emitting- and laser diodes because of the direct energy transfer in form of photons. Due to the momentum change in case of indirect gaps as 4H-SiC, the energy transition will be carried out by photon emission, in addition in form of phonon transfer to the crystal.

The vast majority of semiconductor devices are made from materials listed in Table I. [34-38]. For usual instruments, such as diodes, transistors, MOSFETs, silicon is still market leader material, but in some special cases, higher band-gap materials are required. 4H-SiC and diamond are two candidates for high temperature applications due their significant higher gap energies than in case of silicon or other common semiconductor materials. Additional advantage of 4H-SiC and diamond is their high breakdown voltage,

TABLE I.

PROPERTIES OF DIFFERENT SEMICONDUCTOR MATERIALS

Material	Band gap (eV)	Ionization energy (eV)	Dielectric constant	e^- mobility ($cm^2\ V^{-1}\ s^{-1}$)	h mobility ($cm^2\ V^{-1}\ s^{-1}$)	Breakdown field (Vcm^{-1})
Silicon	1.12	3.6	11.7	1350	450	0.3×10^6
SiC	3.26	8	9.7	1000	115	3×10^6
Diamond	5.5	13	5.7	1800	1200	$\sim 10^7$
GaAs	1.43	4.2	12.8	8000	400	0.4×10^6
Ge	0.67	2.96	16	3900	1900	$\sim10^5$
InP	1.35	4.2	12.4	4600	150	$\sim5\times10^5$
CdTe	1.44	4.43	10.9	1100	100	
$Cd_{0.9}Zn_{0.1}Te$	1.57	4.64	10	1000	120	

e^- - electron
h – hole

which provide high stability even at high electric field, what is important in high power device technology, as well [39-41].

The band gap energy and thereby the necessary energy to create an electron hole pair depends on the temperature. Materials with higher gap energy have lower thermal noise than materials with lower gap energy. In case of 4H-SiC the band-gap energy dependence on the temperature can be described by the following equation:

$$E_g = E_g(0) - 6.5 \times 10^{-4} \times \frac{T^2}{T+1300\,K} \quad , \tag{6}$$

where $E_g(0)$ is the band-gap energy at 0 °K temperature and T is the temperature [42].

The higher the gap energy, the higher the energy required to break the covalent bonds in the crystal. Incoming particles could ionize the crystal and rise electrons from the valence band to the conduction band, and at the same time, holes are generated as a lack of the electrons in the valence band. In presence of an electric field, the produced electron-hole pairs can be collected on electrodes with an opposite polarity [43]. For ionizing radiation it was observed, that the necessary energy in 4H-SiC to create an electron-hole pair exceed the band-gap energy. For example in case of a β- irradiation 5.05 eV is needed for pair creation [44]. The ionization energy at different temperatures for 4H-SiC for light and heavy ions was established by several research groups; the next relation was found by Garcia et al. [45]:

$$E_i = E_g(T) - 2.5 \times 10^{-4} \times T + 4.64\ eV\ , \tag{7}$$

where E_i is the average energy required to generate an electron-hole pair and E_g is the band-gap energy at a certain temperature T (K). Applying Eq.(7), the pair creation energy of 4H-SiC at 273 degree Kelvin (0 °C) results to 7.8 eV; similar values have been established by S. K. Chaudhuri (E_i = 7.28 eV) and by Giudice et al. (E_i = 7.78 eV) with α-spectroscopic measurements in [46] and [47] and by Bertuccio and Casiraghi (E_i = 7.8 eV) with γ-irradiation tests in [48]. According to these data E_i is larger than the gap energy by a factor of ~2.4. The ratio of E_i(T) and E_g(T) decreases up to ~200 K and increases at higher temperatures (see Fig.7).

The theoretical average number (N_{av}) of electron-hole pairs that can be generated is expressed by the division of the total deposited energy (E) of an ionizing particle in the material and E_i required producing a charge pair [34] at a certain temperature:

$$N_{av} = E/E_i \ . \tag{8}$$

For a given energy deposition in 4H-SiC the number of the generated electron-hole pairs at 773 K (500 °C) is 5.05 % higher than at absolute zero temperature and 3.61 % higher than at room temperature. For 1 MeV energy deposition the N_{av} values and their difference relative to the absolute zero temperature as a function of

the temperature are depicted in Fig.8. The calculation predicts a higher current value at higher temperatures for the same energy deposition in 4H-SiC crystal.

In case of semiconductor detectors, the probabilistic fluctuation in the number of the generated electron-hole pairs (N) is characterized by the variance of the squared difference of N and its variation $\overline{N}$ divided by $\overline{N}$, which is referred to as the Fano-factor (F):

$$\overline{(N-\overline{N})^2} = F\overline{N}\,. \tag{9}$$

The Fano-factor results in smaller fluctuation than the simple statistical, Poisson variance (σ) of the number of the generated charge carrier pairs ($\sigma = \sqrt{\overline{N}}$) [34,49-51].

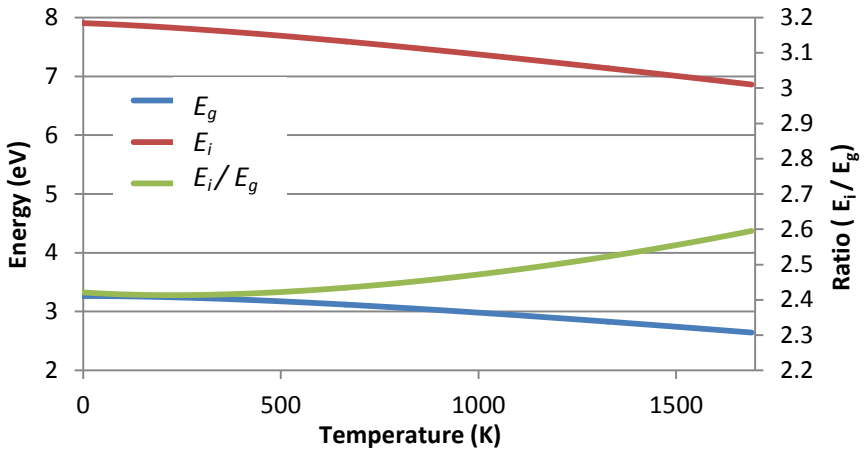

Fig.7 - Dependence of the band gap energy (E_g) and electron-hole pair generation energy (E_i) as well as their ratio (E_i / E_g) as a function of temperature for 4H-SiC

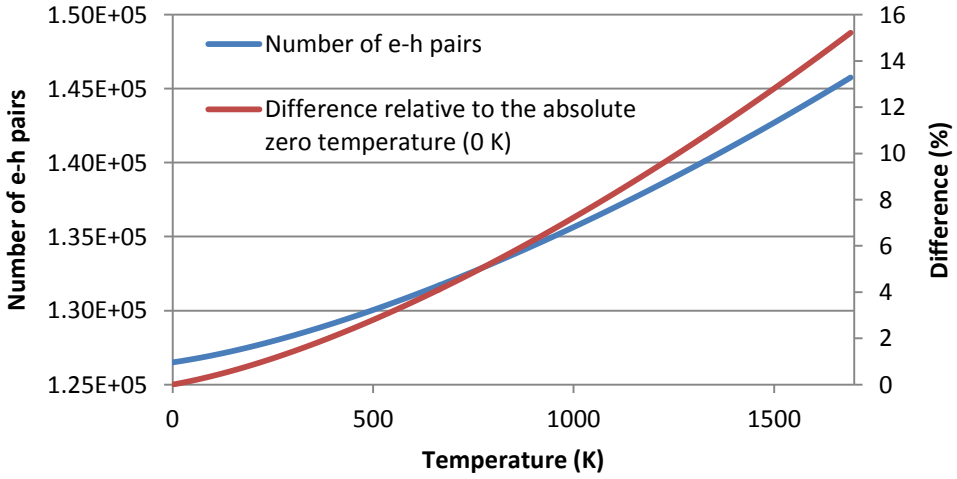

Fig.8 - Average number of the electron-hole pairs generated by 1 MeV energy deposition in 4H-SiC crystal at different temperatures (blue line). Difference of the number of electron-hole pairs at different temperatures compared to the value at 0 K (red line).

Pure semiconductor materials without intentional implanted atoms are referred as intrinsic crystals. Their physical properties are defined by the atoms building up the crystal. The intrinsic free carrier concentration (n_i) in a crystal is determined for certain materials and strongly depends on the temperature, thus the following equation is [32]:

$$n_i^2 = n \cdot p = N_c(\mathrm{T}) \cdot N_v(\mathrm{T}) \cdot \exp\left(\frac{-E_g(\mathrm{T})}{2k_B \mathrm{T}}\right), \tag{10}$$

where n and p are the densities of the electrons and holes (in the range of $10^{12} - 10^{18}$ cm^{-3}), in other words, the occupied conduction band levels and the regarding valence band levels, k_B is the Boltzmann constant and T is the temperature in degree Kelvin**.** The temperature dependence of the band gap energy is expressed in Eq.(**6).** N_c(T) and N_v(T) are the effective densities of states in the conduction and valence bands and they can be written as:

$$N_c = 2M_c\left(\frac{2\pi m_n k_B T_L}{h^2}\right)^{3/2}, \tag{11}$$

$$N_v = 2\left(\frac{2\pi m_p k_B T_L}{h^2}\right)^{3/2},$$

where M_c (constant) is the number of the equivalent energy minima in the conduction band, m_n and m_p represent the effective electron and hole masses in the unit and order of magnitude of ~10^{-31} kg, T_L is the lattice temperature in kelvin and h is the Planck constant (6.62×10^{-34} m^{2}kg s^{-1}) [32].

By means of implantation of different atoms the electrical properties of the semiconductor device are influenced. Depending on the electron configuration of the implanter the concentration of electrons or holes can be changed in a crystal but the n_i^2 value remains constant. Adding implanter atoms with less valence electrons compared with the valence electron number of the crystal atoms, the doping atoms are referred to as acceptors. In the opposite case if the dopant atoms have more valence electrons than the crystal atoms, the dopant atoms are called donors. Typically dopants are chosen from the neighboring group elements of the semiconductor material in the periodic table of elements [34]. Consequently, in case of silicon aluminum is an acceptor type and phosphorus is a donor type dopant. In silicon carbide, silicon and carbide are occupying the second and third periods in the 14th group with four valence electrons, thereby SiC could have donor atoms from the 15th group, as nitrogen and phosphorus, and acceptor atoms from the 13th group, as boron and aluminum.

On the boundary of two different type doped crystal layers, a junction layer is formed, which is called pn-junction, referring to the positive (p) and negative (n) sides of the junction. Due to the concentration difference of charge carries in the pn-junction a diffusion of the charge carriers will continue until an equilibrium state in energy in reached. Then a depletion layer is formed around the pn-junction without free charge carriers, see in Fig.9. On the two sides of the depletion layer or space charge region (SCR) a diffusion potential (U_d) or “built-in bias” is formed, which can be expressed by the following equation:

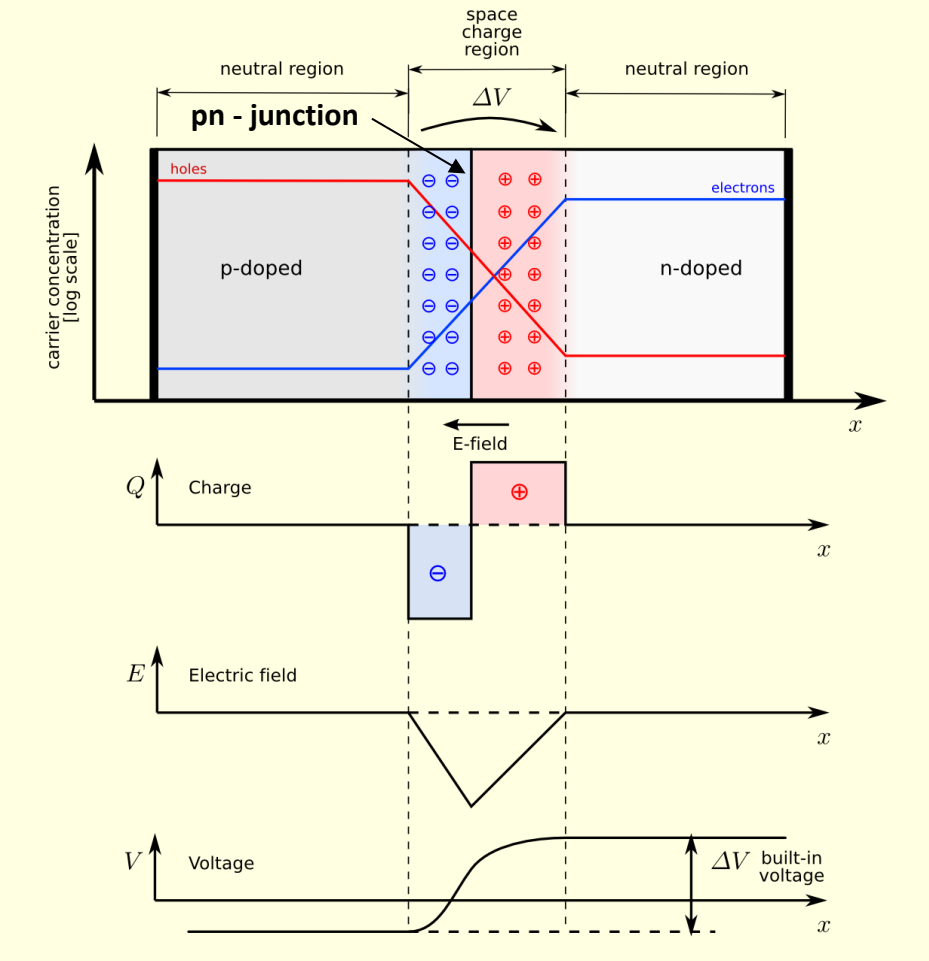

Fig.9 – Schematic of the layer structure of pn-diode and the evolved electric field inside it at zero bias voltage. Source: [56]

$$U_d = U_T \cdot \ln\left(\frac{N_d N_a}{{n_i}^2}\right), \tag{12}$$

where the thermal potential is $U_T = (k_B \cdot T)/q$ = 25 meV for room temperature (k_B : Boltzmann constant, q: elementary charge). N_d and N_a sign the volumetric concentration of donor and acceptor ions [34]. In case of 4H-SiC, the intrinsic carrier concentration, n_i, is established in the literature around 6.7×10^{-11}cm^{-3} [52-55]. The space charge region caused by this built-in potential protrudes into the p- and the n-type material sides of the diode and occupies different thicknesses inversely proportional to the doping concentration in the two layers. Accordingly, in case of a typical SiC heterojunction diode construction, a heavily doped p+ layer is formed on the weakly doped n-type layer, where the majority of the depletion takes place inside the n-type region. The width of the depletion layer (W) can be expressed from the second integral of the Poisson equation:

$$-\frac{d^2U(x)}{dx^2} = \frac{\rho}{\varepsilon_0 * \varepsilon_{r(SiC)}} = \frac{q}{\varepsilon_0 * \varepsilon_{r(SiC)}}(N_a - N_d), \tag{13}$$

$$W = \sqrt{\frac{2*\varepsilon_0*\varepsilon_{r(SiC)}}{q}\left(\frac{1}{N_a}+\frac{1}{N_d}\right)} \cdot \sqrt{U(x = x_n)}, \tag{14}$$

here $\sqrt{U(x = x_n)}$ is equal to the built-in potential, U_d, ε_0= 8.85 × 10^{-15} $AsV^{-1}m^{-1}$ and $\varepsilon_r(SiC)$= 9.7 are the permittivity of the free space and the SiC's relative dielectric permittivity [32,34].

Applying an external bias voltage on the two sides of a diode, the width of the depleted layer may be changed, as it is demonstrated in Fig.10. In case of forward biasing (the positive polarity is connected to the p-side of the diode and the negative to the n-side) the barrier voltage and the depletion decrease; at the voltage value, which exceeds the barrier voltage, a current flow of carriers is starting, the resistance of the junction decreases and the diode becomes conductive [30].

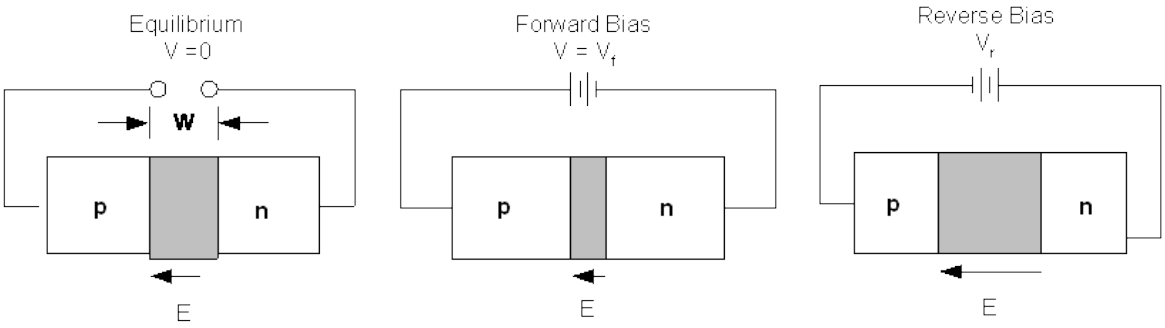

Fig.10 – Change of the depletion width (***W***) and electric field (***E***) in a pn-diode for zero bias, forward and reverse biasing. (Source: [57])

In case of semiconductor radiation detectors the detection of the different particles takes place in the depletion layer, in other words in the sensitive zone of the diode. Accordingly, the external electrical field should have a reverse direction relative to the diode's polarities [34]. Applying a reverse bias on the diode will increase the thickness of the depletion width hence, the sensitive volume and the resistance of the diode. Similar to Eq.(14) the depletion width changes with the square root of the voltage by:

$$W(U) = \sqrt{\frac{2*\varepsilon_0*\varepsilon_{r(SiC)}}{q}\left(\frac{1}{N_a}+\frac{1}{N_d}\right)} \cdot \sqrt{U_d - U_{bias}}\,, \tag{15}$$

where U_{bias} is the applied bias voltage [34]. The resulted depletion width as a function of bias voltage is depicted in Fig.11 for a specific diode considered in this work (D1, described in Sect. 4.1) as an example.

In accordance with this the above-mentioned temperature dependency of the physical parameters as well as the thickness of the depleted zone varies at different ambient temperatures. To illustrate the temperature dependency of *W*, after combining the above expressions, the Eq. (15) can be written as:

$$W(U,T) = \sqrt{\frac{2*\varepsilon_0*\varepsilon_{r(SiC)}}{q}\left(\frac{1}{N_a}+\frac{1}{N_d}\right)} \cdot \sqrt{\frac{kT}{q}\ln\left(\frac{N_a N_d}{N_C(T)N_V(T)\exp\left(\frac{-E_g(T)}{2kT}\right)}\right) - U_{bias}}. \tag{16}$$

Depiction of Eq. (16) in the temperature range of 0 - 600 °C and bias voltage range of 0 - 400 V shows slightly varying depletion thickness values. To illustrate the depletion thickness at different temperatures and

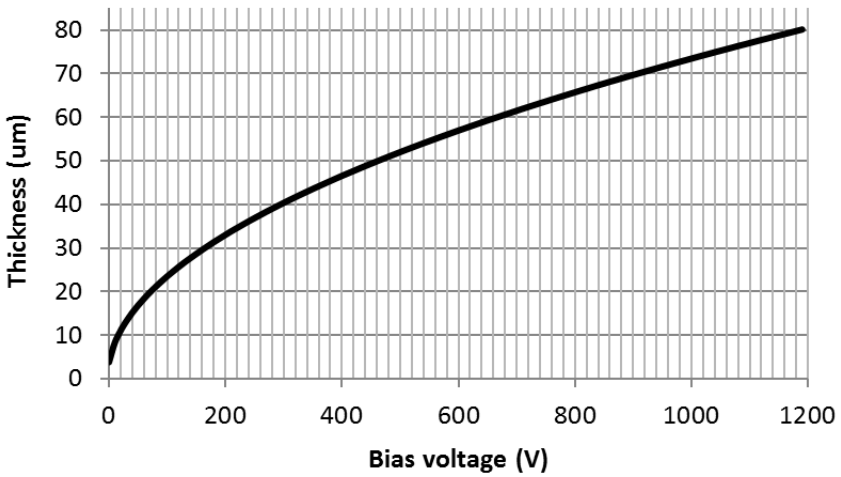

Fig.11 - Width of the depleted volume as the function of bias voltage (calculated for D1 diode geometry introduced in Section 4.1.)

bias voltages, a calculation with typical values of $N_d=5\times10^{14}$ cm^{-3} and $N_a=10^{19}$ cm^{-3} has been performed (data of D5 type diode in Chapter 4.). As it can be seen in Fig.12**,** the value of the resulting depletion thickness is stronger influenced by the temperature at lower bias voltages than at higher ones. Below 20 V reverse bias voltage, the thickness of the depletion decreases at higher temperatures. At 0 V it yields 2.42 µm at room temperature and 2.06 µm at 500 °C, which is a 0.36 µm difference. At 20 V biasing its thickness is 6.74 µm at room temperature and 6.62 µm at 500 °C, which is a 0.12 µm difference only. The highest theoretical operating temperature of 4H-SiC power devices can reach about 1000 ºC. In practice, this limit is determined by several factors, as the thermal tolerance of the various materials used to create the detector, the current flow through the junction [58], microplasma breakdowns in reverse bias mode due to impurities [15], etc.

In addition to the temperature dependent leakage current the diode current is increased by the charge carriers inside the sensitive zone generated by incident particles under irradiation. Current flow through the

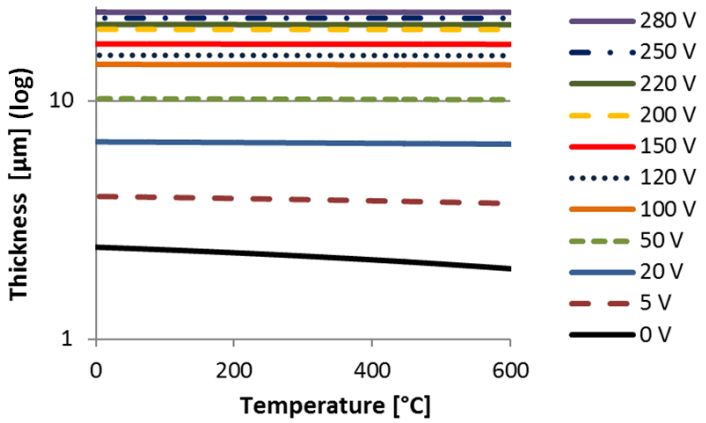

Fig.12 - Depletion width of the D5 type diode with a pn-junction in the bias voltage range of 0-280 V and at the ambient temperatures 0-600 °C

junction may elevate the junction temperature higher than the ambient temperature. This process, beyond a critical junction temperature, could lead to a thermal runaway effect [59,60]. The maximum junction temperature in case of SiC at a certain sensor temperature is [58]:

$$T_{junctionMax} = \frac{\alpha}{\alpha-1} \cdot T_{sensor}\ , \tag{17}$$

where T [°C] is the temperature and α is a constant of 2.4.

Finally, it is noteworthy to discuss the effect of external magnetic field on the free charge carriers in semiconductor material. The movement of charge carriers generated by ionization process in a semiconductor detector is oriented to the leading order by the present electrostatic force ($\boldsymbol{F}$) built by the applied bias voltage on the sensor's electrodes:

$$\boldsymbol{F} = q\boldsymbol{E} \tag{18}$$

where q is the elementary charge [As] and E is the electric field strength [V/m]. The drift velocity ($\boldsymbol{v}$) of the electrons and holes may be expressed by

$$\boldsymbol{v}_p = \mu_p \boldsymbol{E} \text{ (holes) and } \boldsymbol{v}_n = -\mu_n \boldsymbol{E} \text{ (electrons)}, \tag{19}$$

where μ_p and μ_n are the holes and electrons drift mobility values. Application of an external magnetic field ($\boldsymbol{B}$) on the detector influences this movement with different extents for electrons and holes due to their different Hall-mobility (μ^H) value [61]. The total force acting on charge carriers is the composed of the electrostatic part (eq. 18) and the Lorentz-Force ($\boldsymbol{v} \times \boldsymbol{B}$) and reads to:

$$\boldsymbol{F} = q(\boldsymbol{E} + \boldsymbol{v} \times \boldsymbol{B}). \tag{20}$$

The Lorentz force acts at an angle θ with respect to the electric field lines. θ designates the angle between the particle's velocity and the field vectors, *tangent* θ can be expressed as

$$tan\ \theta_p = \mu_p^H \boldsymbol{B} \text{ (holes) and } tan\ \theta_n = \mu_n^H \boldsymbol{B} \text{ (electrons).} \tag{21}$$

For extreme cases, when the magnetic field strength is much larger than the electric field ($|\boldsymbol{B}| >> |\boldsymbol{E}|$) the path of moving electrons and holes can have a deflection, which could lead to loss in collected charge carriers e.g. on the electrodes of a diode.

3.3 Signal formation in semiconductor detectors

Moving charged particles lose part of their energy through collisions with the surrounding electrons in material and thereby they will decelerate. This process is referred as ionization loss and results in electron-hole pair generation in the semiconductor material. The rate of transferred energy for non-relativistic particles is inversely proportional to the particle energy or velocity. The corrected Bethe-Bloch formula describes the

dependence of rate of the ionization loss on the properties of the absorber material and the moving particle [61]:

$$\frac{dE}{dx} = 2\pi N_0 r_e^2 m_e c^2 \rho \frac{Z}{A}\frac{z^2}{\beta^2}\left[ln\left(\frac{2m_e\gamma^2 v^2 W_{max}}{I^2}\right) - 2\beta^2 - \delta - 2\frac{C}{Z}\right] \quad (22)$$

where:

$2\pi N_0 r_e^2 m_e c^2$ = 0.1535 MeV $c^2 \times g^{-1}$;

x is the path length in the direction of the incident particle in the unit of $g \times cm^{-2}$;

$r_e = \frac{e^2}{4\pi m_e c^2}$ = 2.817 × 10^{-13}cm is the classical electron radius;

m_e = 9.109 × 10^{-31} kg is the electron mass;

N_0 = 6.022 × 10^{23} mol^{-1} is the Avogadro's number;

I is the effective ionization potential averaged over all electrons;

Z is the atomic number of medium;

A is the atomic weight of the medium;

ρ is the density of medium;

z is the charge of traversing particle;

v is the velocity of traversing particle;

$\beta = v/c$ the velocity of traversing particle in units of speed of light;

$\gamma = \frac{1}{\sqrt{1-\beta^2}}$;

δ is a density correction at high energies;

C is a shell correction for the non-stationary atomic electrons inside the material and W_{max} is the maximum energy transfer in a single collision.

Charged particles are producing even more electron-hole pairs per unit length with the obtained path length in the solid material and with a decrease of the velocity. The charge pair density has a maximum value at the stopping point of the particle. The plot of the ionization density as a function of the penetration depth in the material is referred as Bragg curve [61], see in Fig.13.

Moving heavy charged particles generate a cloud or plasma of electron-hole pairs. The electric field built-up by an external bias voltage on a bipolar semiconductor detector cannot penetrate into this charge cloud till these charge carriers are dissipated by bipolar diffusion. In the absence of the plasma state the electrons and holes start their drifting motion in the direction of the imposed electric field and thus they can be collected on the electrodes of the detector [73].

As stated above, generation and movement of charge carriers in a semiconductor can be influenced by temperature and magnetic field. The higher the temperature the more thermal noise contribution to a detector

signal appears. The high magnetic field will deflect the electrons and holes from their original path of drifting according to a static electric field.

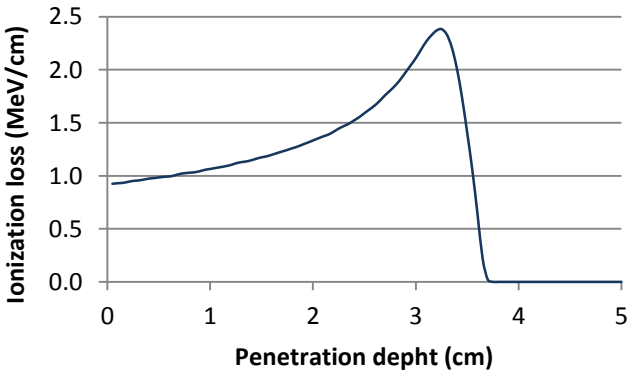

Fig.13 – The ionization loss as a function of the penetration depth of a 5 MeV helium nucleus in air. The curve is referred to as Bragg curve.

3.4 Signal processing

The collected electron-hole pairs generate electric charge on the electrodes proportionally to the deposited energy inside the sensor. To obtain a signal, which can be further processed, a preamplifier is used. This converts the collected charge into voltage signal. The height of the output voltage pulse depends on the amplification of the preamplifier. In case of a charge sensitive preamplifier the pulses are shaped with identical rise and decay time, thus the output signals can be distinguished by their amplitudes. The amplified signal can be processed by further electronic components as digitizer and multi-channel analyzer. The digitizer converts the analog signal to digital and the different pulse amplitude values to discrete steps each corresponding to a unique output bit pattern [34]. The multi-channel analyzer sorts the digitalized signal into energy bins corresponding to given voltage levels, thereby to the different levels of detector charge values. This arranged series of data can be depicted with computer programs as a pulse height spectrum (or energy histogram). The quality of the recorded signal depends almost on all parameters of the detector installation. Evolved signal structures on the spectrum are characteristic to the generating reactions.

3.5 Nuclear interactions with SiC

Reactions between neutrons and material are divided into two main groups. The first is the elastic scattering, where no change in the kinetic energy of the projectile neutron in the center of mass system occurs and there is no threshold energy for the reaction. In the second type of reactions, the kinetic energy of the projectile neutron is not conserved; the reactions could be inelastic scattering of neutrons and nuclear reactions, where new secondary ions are generated. Except for the ground state inelastic scattering events, all these reactions befall above a given threshold energy [62].

In nuclear interactions the energy, which may be deposited in the surrounding material, depends on the kinetic energy of both the projectile and the target particle as well as on the masses of the participating ions. Applying the conservation of momentum after a collision in the laboratory system in x and y directions (see in Fig.14) yields:

$$\sqrt{m_P T_P} - \sqrt{m_X T_X} cos\theta = \sqrt{m_R T_R} cos\varphi \tag{23}$$

and

$$\sqrt{m_X T_X} sin\theta = \sqrt{m_R T_R} sin\varphi \,, \tag{24}$$

where m_P, m_R and m_X are the masses of the projectile, residual and emitted particles and T_P, T_R and T_X denote the kinetic energy of them. The reaction energy Q expressed by the energy of the projectile, residual and the emitted particles reads to:

$$Q = T_x + T_P - T_R \tag{25}$$

From the prior relation the energy of the emitted particle can be computed to:

$$\sqrt{T_X} = \frac{\sqrt{m_P m_X T_P}\, cos\theta \pm \sqrt{m_P m_X T_P cos^2\theta + (m_R + m_X)(m_R Q + (m_R - m_P) T_P)}}{m_R + m_X} \,, \tag{26}$$

where θ and φ denote the angle of the emitted and residual particles with respect to the incident particle direction in laboratory frame [63]. Scattering reactions of 14.7 MeV neutrons on Si and C nuclei to the ground state energy level produce maximum energy edges on the pulse height spectrum at ~2 MeV and ~4.2 MeV. No threshold energy, thereby no reaction energy in Eq. (26) should be considered. Inelastic scattering reactions could generate excited states of the target nucleus at different energy levels and do not occuring nuclear transition (listed in Table II). Inelastic reactions of SiC crystal with 14 MeV neutrons could form well-defined detector signal, here the kinetic energy of the projectile neutrons is not conserved. Nuclear reactions producing new elements occur beyond a threshold energy and need a reaction energy value to tear out ions

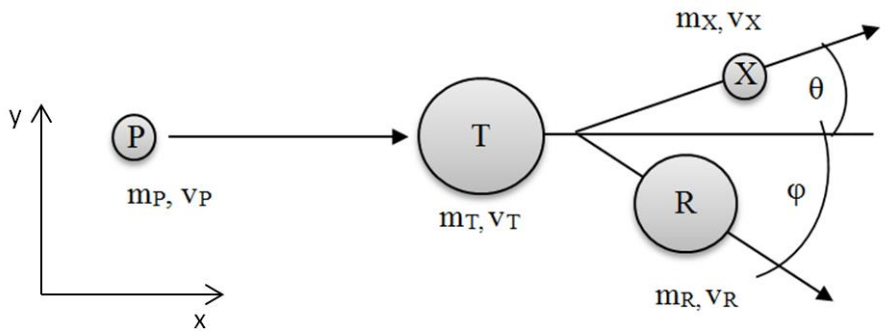

Fig.14 - Schematic diagram of a nuclear collision in a laboratory frame and corresponding coordinate system (based on the Fig.10.1 in [62]).

from the target nuclei. SiC provides several reaction channels with fast neutrons, which produce new secondary charged particles in the reactions output channels. An important reaction group is represented by the four-body reactions of $^{12}C(n,3\alpha+n')$, that include several processes occurring at different energies and through different ways involving intermediate ejectiles, such as ^{8}Be,^{9}Be, ^{5}He. Nevertheless, due to its high cross section (209 mbarn) compared to other deep inelastic processes between 14 MeV neutrons and SiC, a significant part of the recorded signal from ~2 MeV up to 7 MeV [64] may be attributed to these reactions. Here it is worth noting, that interactions between fast neutrons and carbon atoms produce α particles with a strong forward angular distribution; their completion mostly occurs through direct reactions [64],[65]. The measurement of the full kinetic energy released in these reactions can be performed in that case if all secondary particles could stop inside the sensitive volume of the detector, otherwise partial energy deposition can happen, which causes signal loss. $^{12}C(n,\alpha)^{9}Be$ ground state reaction produces one of the most prominent full energy peaks in the histogram, e.g. for 14.96 MeV projectile neutron energy at 9.2 MeV. This reaction peak has been used as a reference point on the energy histogram for energy calibration.

In addition to the scattering events, ^{28}Si nuclei exhibits several nuclear reaction paths with fast neutrons, which produces secondary ions, mostly in the reactions of $^{28}Si(n,\alpha)^{25}Mg$ and $^{28}Si(n,p)^{28}Al$. According to present knowledge, $^{28}Si(n,\alpha)^{25}Mg$ reaction have 15 and the $^{28}Si(n,p)^{28}Al$ reaction 13 different excitation energy levels in addition to the ground state energy level reactions [66]. Therefore, due the many excited states of these reactions, several full energy peaks at distinct energy levels may be observed in the energy histogram of the sensor reading. The higher the nuclear reaction cross section, the more significant the visible signal contribution of the reaction is, see in Table II. Prominent full energy peaks are caused by

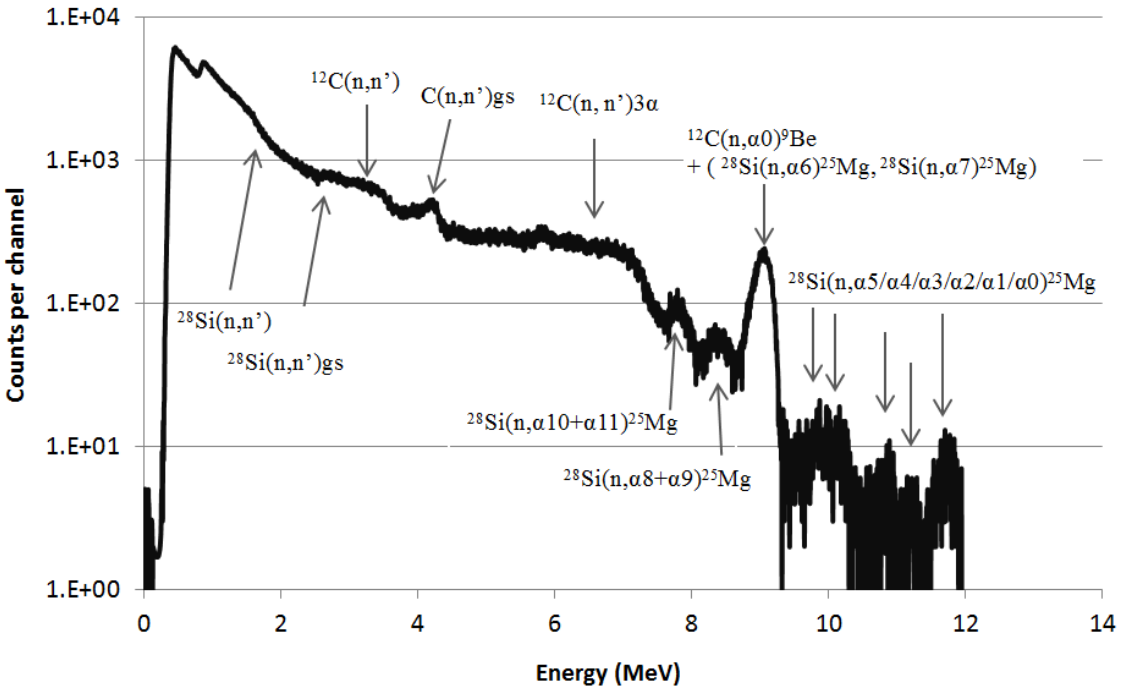

Fig.15 - Energy histogram recorded with a 4 mm × 5 mm surface 4H-SiC detector irradiated with 14 MeV fast neutrons as a function of the deposited energy

TABLE II.
MAIN NUCLEAR REACTIONS BETWEEN SiC AND 14 MeV FAST NEUTRONS

Reaction	Q – value (MeV)	Energy threshold (MeV)	σ at 14.57 MeV neutron energy (mbarn)	Dep. E with 14.96 MeV neutrons(MeV)	Dep. E with 14.13 MeV neutrons(MeV)
$^{28}Si(n,\alpha0)^{25}Mg$	-2.65	2.74	9.18	12	11.48
$^{28}Si(n,\alpha1)^{25}Mg$	-3.23	3.35	2.95	11.72	10.89
$^{28}Si(n,\alpha2)^{25}Mg$	-3.63	3.76	4.64	11.32	10.49
$^{28}Si(n,\alpha3)^{25}Mg$	-4.26	4.41	7.23	10.69	9.86
$^{28}Si(n,\alpha4)^{25}Mg$	-4.61	4.77	6.20	10.34	9.51
$^{28}Si(n,\alpha5)^{25}Mg$	-5.21	5.40	2.55	9.74	8.91
$^{28}Si(n,\alpha6)^{25}Mg$	-5.38	5.58	6.10	9.57	8.74
$^{28}Si(n,\alpha7)^{25}Mg$	-5.45	5.64	4.14	9.50	8.67
$^{28}Si(n,\alpha8)^{25}Mg$	-6.05	6.27	5.76	8.90	8.07
$^{28}Si(n,\alpha9)^{25}Mg$	-6.06	6.28	4.12	8.89	8.06
$^{28}Si(n,\alpha10)^{25}Mg$	-6.55	6.79	5.09	8.40	7.57
$^{28}Si(n,\alpha11)^{25}Mg$	-6.62	6.85	5.35	8.33	7.50
$^{12}C(n, n')gs$	-	0	420.6	-	-
$^{12}C(n, n')2+$	-4.43	4.80	210.6	10.52	9.69
$^{28}Si(n, n')gs$	-	0	522.37	-	-
$^{28}Si(n, n')^{28}Si+$	-1.77	1.84	124.45	13.18	12.35
$^{12}C(n, 3\alpha+n')$	-7.27	7.88	209 **	7.68	6.85
$^{12}C(n, \alpha0)^{9}Be$	-5.70	6.17	62.3	9.25	8.42
$^{28}Si(n,p0)^{28}Al$	-3.86	3.99	6.72	11.1	10.27
$^{28}Si(n,p1)^{28}Al$	-3.89	4.02	5.05	11.06	10.23
$^{28}Si(n,p2)^{28}Al$	-4.83	5.00	1.15	10.12	9.29
$^{28}Si(n,p3)^{28}Al$	-4.87	5.04	6.09	10.08	9.25
$^{28}Si(n,p4)^{28}Al$	-5.23	5.41	2.93	9.72	8.89
$^{28}Si(n,p5)^{28}Al$	-5.48	5.67	3.28	9.48	8.65
$^{28}Si(n,p6)^{28}Al$	-5.48	5.67	4.29	9.47	8.64
$^{28}Si(n,p7)^{28}Al$	-5.99	6.21	4.02	8.96	8.13
$^{28}Si(n,p8)^{28}Al$	-6.06	6.27	3.04	8.89	8.06
$^{28}Si(n,p9)^{28}Al$	-6.13	6.35	5.00	8.82	7.99
$^{28}Si(n,p10)^{28}Al$	-6.34	6.57	4.42	8.61	7.78
$^{28}Si(n,p11)^{28}Al$	-6.44	6.67	3.58	8.51	7.68
$^{28}Si(n,p12)^{28}Al$	-6.51	6.74	4.74	8.44	7.61
$^{28}Si(n,p13)^{28}Al$	-6.84	7.09	4.70	8.11	7.28

* Data from Kondo et. al. in [64], Q – reaction energy, σ – nuclear cross-section, Dep. E – deposited energy

$^{28}Si(n,\alpha)^{25}Mg$ ground state and excited state reactions as illustrated in Fig.15. The average cross section values for these interactions range from 1 mbarn to 12 mbarn cross section in the 14-15 MeV neutron energy domain. The above listed reactions with Si and C nuclei are depicted in the pulse height spectrum above, which shows the recorded count number as a function of the deposited energy with a 4H-SiC detector irradiated with D-T neutrons.

To detect thermal neutrons, the application of thermal neutron converter materials is necessary. Nuclei, such as gadolinium-157 (254.000 barn), cadmium-113 (20.000 barn), lithium-6 (940 barn) and boron-10 (3890 barn) isotopes [67-69] have high cross section values to thermal neutrons in different type of nuclear interactions. ^{157}Gd and ^{113}Cd have radiative capture with slow neutrons and these reactions result in γ-radiation in the output channels, which could be beneficial in case of large volume detectors, where γ-photons can stop. Usually ^{10}B and ^{6}Li are applied as neutron converters for most of the thermal neutron detector development. In case of solid state detectors, these materials have to be deposited or incorporated on- or inside the detector. Thermal neutron capture by ^{10}B and ^{6}Li generate light charged particles. Reaction between thermal neutrons and ^{10}B isotope could occur in two ways; in the first an α-particle, an excited state $^{7}Li^*$ ion and a γ-radiation are produced:

$$^{10}B + n \rightarrow {}^{4}He\ (1.47\ MeV) + {}^{7}Li^*\ (0.84\ MeV) + \gamma\ (0.48\ MeV), \quad (27)$$

and in the second case an α-particle and a ^{7}Li ion in ground state:

$$^{10}B + n \rightarrow {}^{4}He\ (1.77\ MeV) + {}^{7}Li\ (1.015\ MeV). \quad (28)$$

The branching ratio of the occurrence of the two reactions is 94 % for Eq.(27) and 6 % for Eq.(28). Thermal neutron measurements in the present work have been conducted by applying ^{10}B -implanted 4H-SiC diode detectors. Reaction between ^{6}Li ions and thermal neutrons results in α-particles and tritium ions in the output channel:

$$^{6}Li + n \rightarrow {}^{3}H\ (2.73\ MeV) + {}^{4}He\ (2.05\ MeV). \quad (29)$$

Further nuclear interactions could occur in the surrounding material around the detector. One of the most important reactions occurs between neutrons and ^{27}Al nuclei in the reaction series of $^{27}Al(n,\gamma)^{28}Al(\beta^-)^{28}Si$. This process exhibits a large thermal neutron cross-section of 12 barns [70]. Hence, the generated charged β-particles from an aluminum encapsulation of the detector could significantly contribute to the recorded signal of the sensor. The secondary β-particles have an average energy of ~1.25 MeV [71] with upper threshold energy of ~2.86 MeV [72]. But β-particles will deposit less energy in a thin sensitive detector volume than protons or α-particles due to their significant longer path range and lower ionization loss in solid materials.

4. SILICON-CARBIDE DETECTOR DESIGN INVESTIGATED IN THIS WORK

During the I-SMART project several 4H-SiC diodes have been developed and investigated in thermal and fast neutron irradiation environments. The sensors were prepared and provided by Aix-Marseille University and AMPER University INSA de Lyon in France. The subsequently described diode properties have been provided by these institutions. In the following, implantation profiles and geometry of the investigated diode types are discussed.

All diode detectors have been developed with one single pn-junction and with the deposition of a crystalline cover layer on the crystalline substrate, a so called epitaxial layer with low n-type dopant concentration. To create the sensitive zone reverse biasing on the two sides of the diode has been applied, as it is shown in Fig.16. As the bias voltage and electric field increase depletion inside the epitaxial layer occurs due to the collection of the free charge carriers on the two electrodes with opposite polarity. The depleted volume (or space charge region) is considered as the sensitive volume of a diode detector, because only particles, which produce electron-hole pairs in this volume, can be detected. Here, the drifting carrier movement due to the electric field is considered and the diffusion of less abundant- minority- charge carriers due to charge concentration difference inside the electrically neutral layers is not discussed. These charge pairs drift under the influence of the electric field and are collected on the two opposite polarity electrodes of the diode. Based on the known doping concentration values of the p+ an n- layers, the thickness of the space charge region for a given diode can be calculated using Eq.(15). The electric field trough of the depleted zone is defined as the applied bias voltage per thickness of the depleted volume. In a typical case, a 100 V bias voltage trough of 20 μm thickness results in 50 kV/cm. The thickness of the depleted volumes as a function of the applied bias voltage are given in the **Appendix A** for all the diodes considered in the present work.

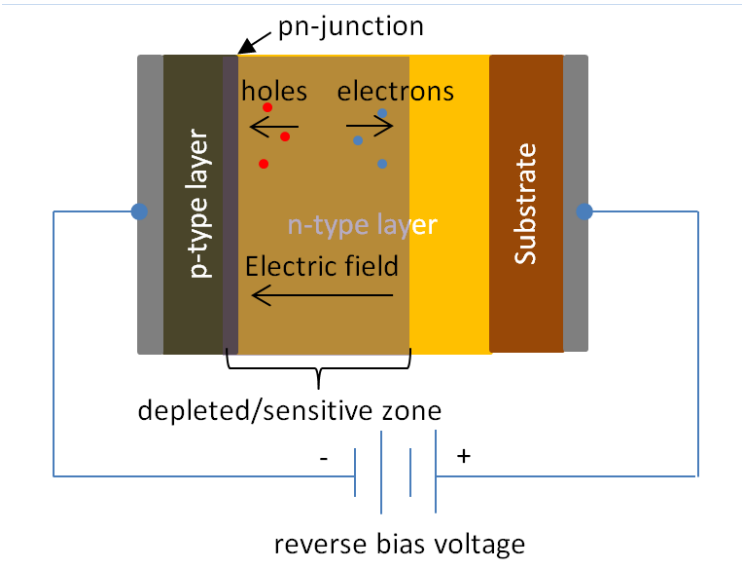

Fig.16 - Schematic of operation principle of pn-diode under reverse bias

Several diode constructions have been produced and investigated in this project. The most promising geometries are described in the following parts of the thesis. The geometry data form the basis of the models and complementary Monte Carlo simulations for the analysis of the measured data. For distinctions, the diode structures are designated as D1, D2, etc.

4.1 D1 structure detector

The first type of 4H-SiC sensor studied is a pn-diode. On n-type SiC substrate several additional layers are deposited by means of chemical vapor deposition (CVD). On the 4H-SiC substrate 80 μm thick n^--type SiC epitaxial layer with ~2×10^{14} cm^{-3} nitrogen concentration has been deposited; the n^--type layer serves as sensitive volume in case of all the other SiC detectors. To establish the pn-junction, a 1 μm thick p^+-epitaxial layer has been deposited on the n^--layer. This layer is covered with a 1 μm thick p^{++} - SiC epitaxial support layer. The p^+ and p^{++}-layers are implanted with aluminum atoms providing a ~2×10^{17} and 2×10^{19} cm^{-3} atomar density. To create the anode contact of the diode a 4 μm thick aluminum metal layer has been applied on the top of the p^{++}- layer. In case of diodes, which are aiming to detect thermal neutrons, ^{10}B-isotopes with ~5×10^{15} cm^{-2} fluence were implanted with 2 MeV energy inside the anode contact. A schematical vertical cut of the D1-type detector is depicted in Fig.17. The surface area of the D1 – type samples is either 2 × 2 and 5 × 5 mm^2, respectively [74].

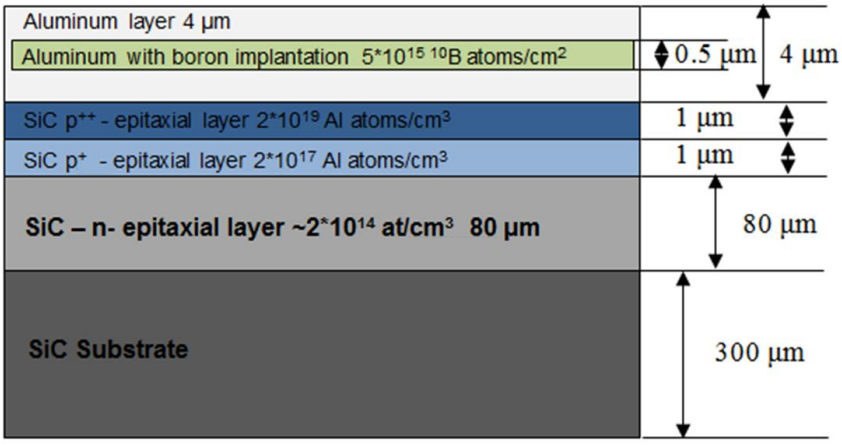

Fig.17 – Dimensions of the layering in the D1 structure diode geometry.

4.2 D2 structure detector

D2 structure detectors are the improved form of D1 – type detectors with a much smaller surface area, less than 1 mm^2. Thereby the leakage current, which can flow through the pn-junction even if no biasing on the diode is applied, is lowered. Additionally, a shorter distance between the ^{10}B-implanted layer and the pn-junction is applied to obtain a higher signal to detect thermal neutrons. On the n^--type epitaxial layer with 10^{14}

cm^{-3} nitrogen concentration a 1 μm thick aluminum doped SiC p^+-type epitaxial layer has been deposited with 10^{19} cm^{-3} concentration [74]. On the p^+ layer Ti/Ni/Al/Ni ohmic contact with a thickness of 200 nm is attached [75]. Overlying a 1 μm thick aluminum metallization layer is placed. Around the aluminum contact additional 1.5 μm thick SiO_2 ring surface is located, which has a 6-7 times larger surface than the aluminum metallization surface area. Both layers, the aluminum metallization and the SiO_2 layers are implanted with ^{10}B-isotopes to form the thermal neutron converter layer (NCL). The NCL layers have a distance of ~1.8 μm and ~2.2 μm from the pn-junction for the aluminum metal and SiO_2 layers, respectively. A vertical cut of the detector illustrates the structure of D2-type diode geometry in Fig.18.

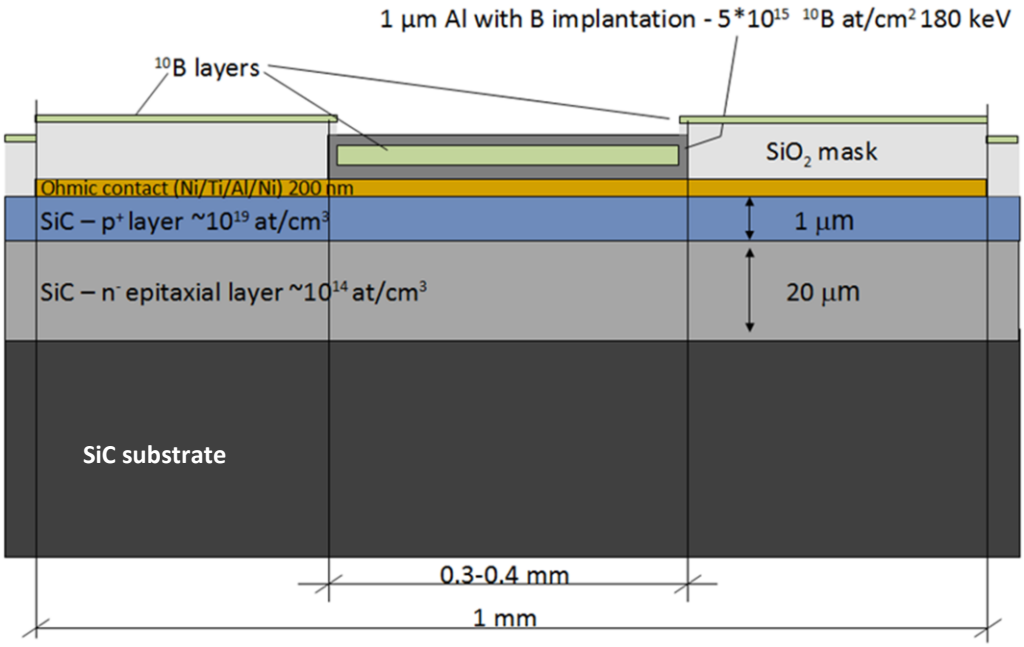

Fig.18 – Vertical cut and layer dimensioning of the D2 structure diode geometry

4.3 D3 structure detector

The sketch of D3 type geometry is depicted in Fig.19. On the 4H-SiC substrate a 15 μm thick n-type SiC epitaxial layer with 10^{14} cm^{-3} nitrogen concentration has been grown. On the top of this a 0.5 μm thick SiC p+ layer with 10^{19} cm^{-3} aluminum content is applied by means of ion implantation, to form the pn-junction. Inside the p+ layer ^{10}B atoms with a concentration of $5\times10^{15}cm^{-3}$ are implanted. The distance between the boron implanted converter layer and the pn-junction, in other words the edge of the sensitive region, is less than 0.4 μm. On the p-type layer a 100 nm thick Ti/Ni/Al/Ni anode ohmic contact and on the substrate side of the diode a Ni cathode ohmic contact is deposited. On the upper surface an Al-metallization is realized via evaporation to create a contact surface. [76,77].

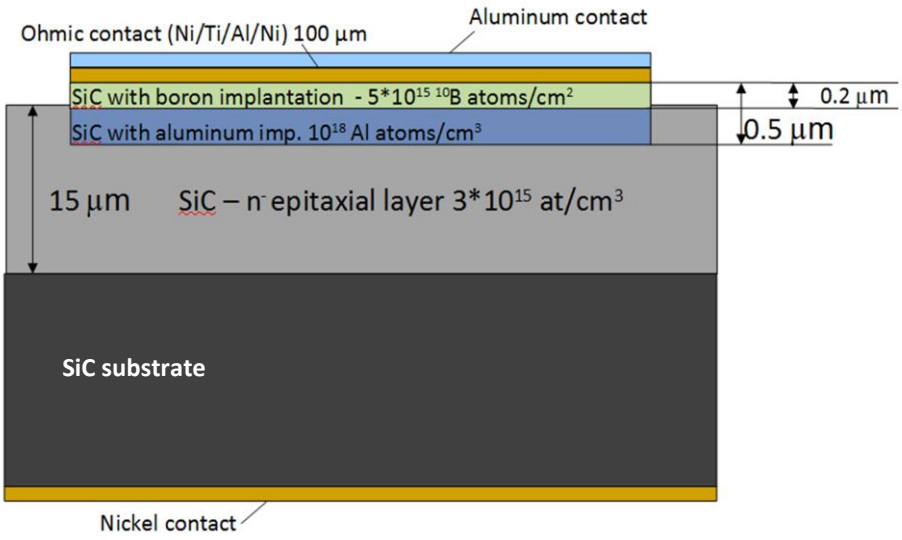

Fig.19 – Vertical cut and dimensioning of layers in the D3 structure diode geometry.

4.4 D4 structure detector

The D4 diode detector differs from the other concepts [78]. The pn-juntion of the diode is created by ion implantation of ^{10}B-isotopes in five implantation steps with different energies. The collective implantation concentration in the boronized layer results in a density of ~ 10^{20} atoms×cm^{-3}. This layer is inside the 10 µm n-type epitaxial layer. All structures are established on a 350 µm thick SiC substrate. To create the ohmic contact on the diode, a 200 nm thick Ni/Ti/Al/Ni metal layer is deposited. Except the metalized areas a 1.5 µm thick SiO_2 layer covers the top of the wafer. A vertical cut of the D4 diode structure is shown in Fig.20.

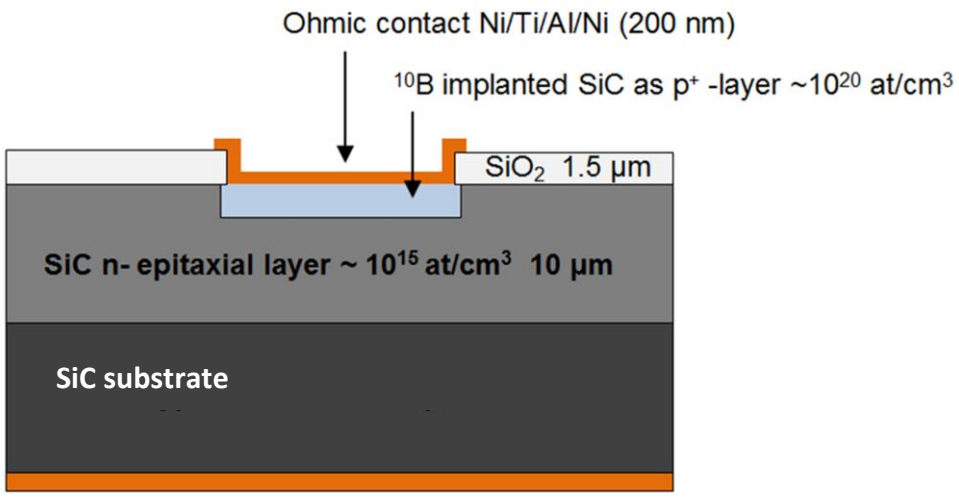

Fig.20 – Vertical cut and layer dimensioning of the D4 structure diode geometry.

4.5 D5 structure detector

The D5 detector structure has been developed to allow a signal acquisition at elevated temperatures up to 300-500 °C. On a 350 µm thick n+-type 4H-SiC substrate a 0.5 µm thick buffer n-epitaxial SiC layer with 10^{18} cm^{-3} nitrogen concentration was grown. On this layer another buffer layer consisting of a 20.9 µm thick n-type epitaxial layer with 5.42 x 10^{14} cm^{-3} nitrogen concentration was deposited. To create the pn-junction a 10^{19} cm^{-3} concentration aluminum-doped, 1µm thick p+ layer was further placed above. To create a high temperature resistant metallic contact 300 nm thick nickel and 250 nm thick gold layers were deposited on the p+ layer. In Fig.21 a vertical cut of the D5 detector geometry is shown.

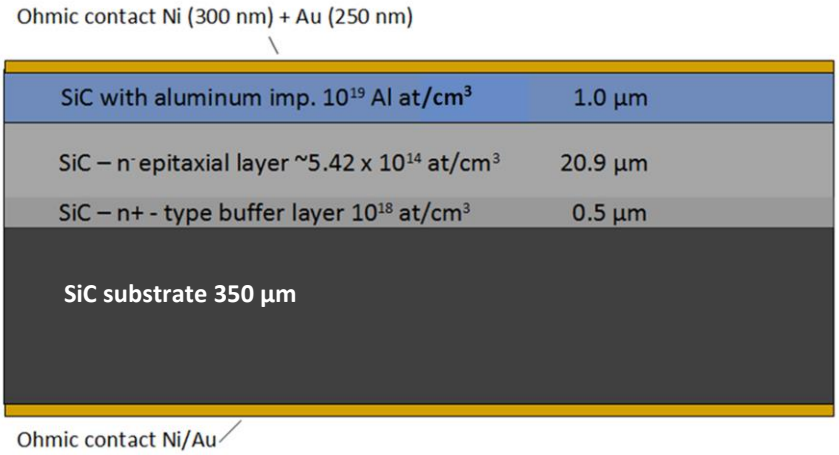

Fig.21 – Vertical cut and layer dimensions of the D5 diode geometry.

4.6 D6 structure detector

The D6 detector type has the same layer thickness structure as the D5 type. D5 and D6 deviate by the type of ohmic contact, which is provided in the D6-type by aluminum instead of Au/Ni. Additionally, the detector D6 has on top a ^{10}B-implated p^+- epitaxial layer and is illustrated in Fig.22.

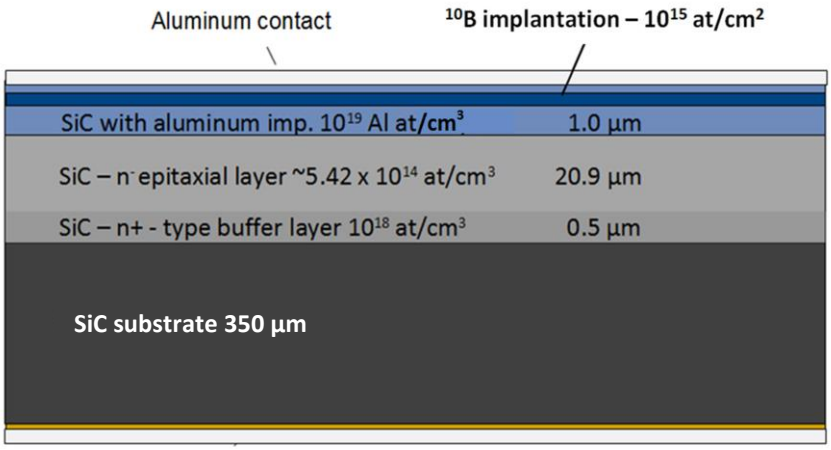

Fig.22 – Vertical cut and layer dimensions of the D6 diode geometry.

5. SIMULATION OF THE DETECTORS

In this section the Monte Carlo simulation tools-Geant4 [79, 80] and the SRIM/TRIM [81, 82] software – is used to evaluate the signal based on the geometry of the investigated SiC diode detectors are introduced.

5.1 Geant4 - GEometry ANd Tracking

"Geant4 is a toolkit for the simulation of the transport of particles within matter. Its areas of application include high energy, nuclear and accelerator physics, as well as studies in medical and space science." [79]. All aspects of the simulation process are included in Geant4. This scopes:

- the geometry of the system,
- the materials,
- the fundamental particles of interest,
- the generation of primary events,
- the particle tracking through materials and electromagnetic fields,
- the physics processes for particle interactions,
- the response of sensitive detector components,
- the generation of event data,
- the storage of events and tracks,
- the visualization of the detector and particle trajectories [80].

The code of Geant4 is written in C++ programming language and can be handled by different operating systems as Linux, Unix and Windows.

For the present work, the Geant versions 4.9.5 p01 and 4.10.00 p01 are used. The thermal neutron simulations for SiC diode detectors are conducted in Geant4.9.5 p01 code while the fast neutron calculations in the Geant4.10.00 version. To perform the simulations the development environments Visual Studio 2010 Express and 2013 Express C++ are applied [83]. The Geant4 applications are created using the CMake 2.8 cross-platform builder [84]. The visualization of the developed detector geometry is realized by VRML vector graphics files in the Geant4 application. The resulting VRML files are handled with Cortona3D software [85].

To attain high quality results convergence thresholds are set for the small volume SiC diode detectors introduced in Chapter 4. Stepping and energy loss length parameters are optimized to geometries in the size range from 100 nm to few millimeters. The minimum range of secondary particle production, in other words the production threshold for the defined detector volumes is 0.1 μm. For higher energetic charged particles the ionization energy-step/range ratio is equal to 0.001, where the final range corresponding to the minimum energy is 1 μm. A charged particle at the minimum energy finishes its tracking in one step [86].

To build appropriate sensor geometry, the Geant4 modeler Constructive Solid Geometry (CSG) serves several geometrical primitives, such as box, tube, parallelepiped, trapezoid, etc. The construction of SiC detector geometry is based on circular geometrical forms and rectangular shaped elements. For all primitives the solid- logical- and physical volumes are defined. These volumes describe the dimensions (solid volume), the material (logical volume), the position and the container volume of the unit (physical volume). The boundary of the outermost container is the wall of the so called World volume, which contains all the geometrical components in the simulation model. The sensitive detector volume from where the final event information is collected is designated by appointing the name of the corresponding logical volume.

The detector material is constructed by direct definition of the applied chemical elements (natural and artificial compositions, as well) and their abundance in the given material in the different layers of the simulated sample. This method is applied both for molecules and compound materials as ion implanted layers of a diode with low concentration of impurity atoms.

Although, several predefined physics list with standard threshold values are available in Geant4 code, due to the specific diode dimensions in this work a routine has been developed to create the physical processes. The applied physics models describe nuclear reactions for energies from thermal up to 20 MeV. The reactions between neutrons and the material are handled by the High Precision Neutron Physics class (hp_physicslist), which is specially developed for neutron-material reactions up to 20 MeV and uses ENDF B/VII nuclear database with JENDL extensions [66]. Although High Precision Neutron Physics is able to handle a wide range of nuclear reactions, some necessary calculations are still not included. Missing processes are the resonance four-body $^{12}C(n,3\alpha+n')$ reactions, which are important for calculations with SiC [87]. Additional nuclear reactions are determined by general models of the Geant4 physics, such as multiple scattering and ionization process during the energy deposition of charged particles (α, triton, deuterium and further ions), photon interactions (photo-electric effect, Compton scattering, gamma conversion) and electron/positron interactions (multiple scattering, ionization, Bremsstrahlung), etc. Depending on the modeled set-up the neutron source ejects neutrons isotropic in 4π ste-radian as for thermal neutron simulations or in a definite direction from a point, surface or a volume. The energy specrum of the source neutrons is defined by applying the General Particle Source (GPS) sub-routine of Geant4. GPS enables to describe thermal neutron source with a Maxwellian distribution, fast neutron source with a Gaussian distribution with a given σ standard deviation and neutrons with freely defined energy spectra to model natural isotopes sources, as AmBe or Cf-252.

How the different SiC diode sensors have been modeled in Geant4 is described in the following. The D1 detector is modelled with ~5×5 mm^2 rectangular surface. The geometry is described by box volumes placed on each other. On a 250 μm thick SiC substrate layer a 20 μm thick n-type epitaxial layer is placed. The maximum depletion thickness of D1-type detector is 80 μm, thinner value has been set with the aim to compare the signal of this sensor with the other diodes with similar thickness values. This epitaxial layer

represents the sensitive volume of the detector. The next element is a 2 μm thick SiC layer, the p^+ and p^{++} - epitaxial layers of the sensor with1 μm thickesses. Each of the units is localized in a space called World Volume. To create the 0.5 μm thick boronized layer inside the 4 μm aluminum metallization the containing volume of the boronized layer has to be the logical volume of the metal layer instead of the World Volume, and its position should be set relative to the midpoint of metal layer. The position of the different layers in edge view is visualized with VRML graphics in Fig.23.

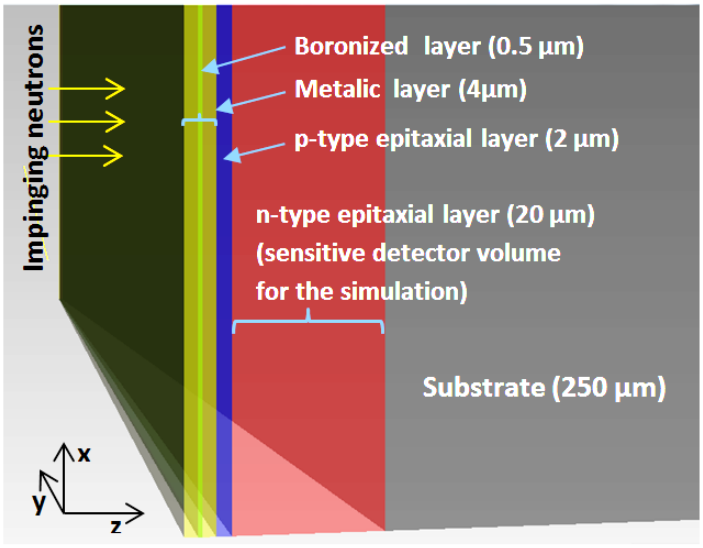

Fig.23 - VRML graphics of the position of the different layers of D1 diode modelled with the Geant4 toolkit

The D2 detector has a more complicated geometry. The surface of the D2-type sensor's ohmic contact is covered with a SiO_2 mask having a concentric bore hole above the aluminum metallization. Both the SiO_2 and the aluminum layer are implanted with boron-10 nuclei at two different distances from the sensitive volume of the detector, as illustrated in Fig.18. To depict this structure in the simulation a volume consistent calculation model with all dimensions is applied. The boron containing SiO_2 layer (1 mm outer diameter and 300 μm inner diameter) partially covered the edge of the circular shaped aluminum metallization with 350 μm diameter, indicated with (*) in Fig.24. The additional circular boron layer with 300 μm diameter was located inside the aluminum layer. The p-type epitaxial layer and the substrate have 1 mm diameter and circular form.

Only cylindrical volume units are applied to describe the geometry of D3 and D5 type detectors. The layering of the D3 sensor has been modelled according to the geometric set-up described in Chapter 4.3 and for the spatial extension a sensor diameter of 1mm is assumed. The material of the boronized layer is described as a mixture of 30 % boron-10 and 70 % SiC, the p-type epitaxial layer contains 2×10^{-4} % aluminum concentration. Most of the simulations for the fast neutron signal investigations are performed for the 2 mm area D5-type detector from Chapter 4.5, which does not contain boron implantation. A cylindrical shaped SiC substrate layer serves as the mother volume of the 1 μm thick p-type SiC layer and the sensitive layer. For the calculations, air and SiC are applied as the material of the substrate.

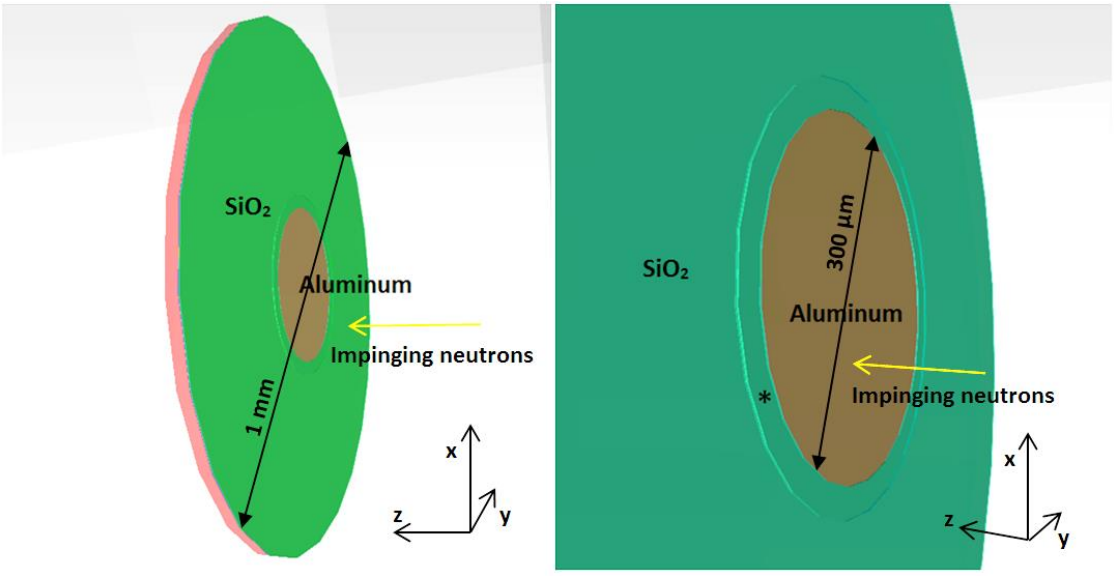

Fig.24 – Remote (left) and close (right) view of VRML graphics of developed Geant4 model of D2-type detector. The star in the right figure indicates the aluminum layer partially covered by SiO_2.

The simulations are used to identify and analyze the different contributions of the layers to the model sensor signal. By a comparison of the measured and computed signals the main sources for deviations can be investigated. Additionally, a careful modelling enables a sensor improvement.

5.2 SRIM – Stopping and Range of Ions in Matter

"SRIM is a collection of software packages, which calculate many features of the transport of ions (up to 2 GeV/amu) in matter." [81]. In the point of view of the present work the most important calculations include stopping range of ions with less than 10 MeV energy, their distribution inside the target after stopping and the energy loss method of moving ions in matter.

The stopping range of ^{10}B-nuclei during the implantation process of the SiC diode detectors are investigated to get information about the inner layer structure of the developed sensors. Furthermore, the range of ^{7}Li- and ^{4}He-nuclei generated by thermal neutron reactions with ^{10}B-ions is simulated. The results contribute to the explanation of the detector signal in neutron field and of the origin of the different signal parts on the energy histograms.

Additional calculations with SRIM/TRIM software are conducted to establish the energy loss of ions by ionization of the detector material, phonon, damage generation, etc. [82]. Thereby, this type of calculation allows to analyze the effect of pulse height defect on the resulting energy histogram after different reactions between fast neutrons and SiC [19,29]. For recoil and damage calculations the Kinchin-Pease formalism has been applied, which is a quick statistical estimation [89].

The SRIM/TRIM software has limitations; from that some important ones are listed in the following. The transport of impinging ions in the target is calculated in the package TRIM (Transport of Ions in Matter). The angle of the incident beam can be set. The default incident angle is 0° and then the beam encounters the target surface perpendicular and the maximum applicable angle is 89.9°. Nonetheless, wrong results can occur for too narrow angles (few degrees) closed with the target surface [88]. For compound materials containing common elements (H, C, N, etc.), SRIM uses the CAB (Core and Bond) approach as a correction for the Bragg's rule (more detail in [82]). For conducting compound targets with band-gap might be an error with the calculated stopping correction being too small. Other example for the limitations with CAB that three light target atoms, Li, Be and B, are considered by SRIM without bonding correction because of the lack of experimental data on their bond in compounds. It is noteworthy that during damage calculations the target is considered as perfect and the effect of previous ions is not taken into account. Finally, the target temperature is 0 °K thus the thermal effects do not contribute to damage events.

6. MEASUREMENTS COMPILATION FOR NEUTRON IRRADIATION TESTS

This chapter discusses the neutron facilities, where the experiments are conducted. Thereafter, the different measurement electronics applied to the tests are presented. To provide the basis of understanding and analysis of the following discussed results the processing of the detector output signal to energy spectra is outlined. Different measurement set-ups have been applied for thermal and fast neutron measurements; these are introduced in the next sub-chapters. The specific supplementary details for the tests at elevated temperature or at high magnetic field are separately discussed. In the last point the neutron sources are presented.

6.1 Measurement facilities

Most experiments have been conducted at the neutron generator of the Technical University of Dresden (TUD) and at the research reactor BR-1 of SCK-CEN Belgium. In the followings, the two research facilities will be introduced in more detail.

6.1.1 DT neutron generator in the TUD Neutron Laboratory at ELBE (HZDR)

The experiments with fast neutrons have been carried out in the Neutron Laboratory of the Technical University of Dresden (TUD) in Germany, with a deuterium-tritium neutron generator. The generator built in the early 2000's is mostly used for fusion neutronics experiments. Its main functional parts are a Cockcroft-Walton high voltage generator, a duoplasmatron ion source, an accelerator tube, quadrupole focusing magnets around the deuterium beam and a solid tritium target. The available maximum acceleration voltage is 300 kV and an additional extraction voltage of 45 kV is applied. The different sections of the neutron generator are shown in Fig.25.

For the present work, the measured sensor has been located typically 10-15 cm away from the generator's tritium target surface, perpendicularly faced to the direction of neutrons leaving the target, as in Fig. 26. The average neutron yield in the continuous operation mode of the generator is in the range of 10^9-10^{11} neutrons per second depending on the selected deuterium beam current and energy, as well as the tritium target age.

For the discussion of fast neutron measurements the world coordinate system is introduced as follows:

- **z** designates the rotation axis of the terminal tube of the neutron generator as well as the nominal deuterium beam direction (exactly positioned on the rotation axis)
- **x** and **y** appoint the vertical and the horizontal axes, respectively, see in Fig.26.

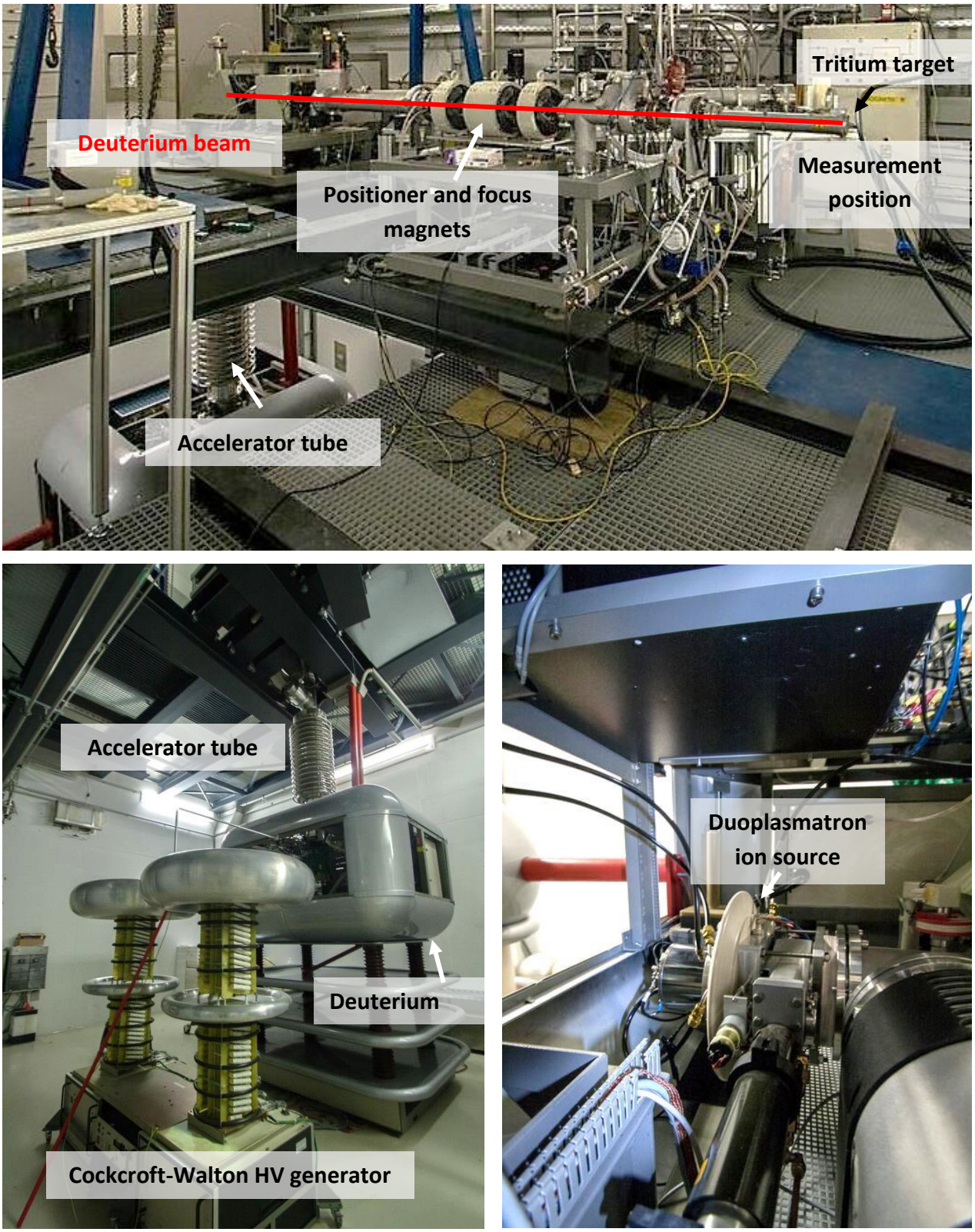

Fig.25 – The fast neutron generator of the Neutron Laboratory of the Technical University Dresden. (Upper: The terminal part of the neutron generator after the accelerator tube. Here the deuterium beam travels through the positioner and focusing magnets and meets the tritium target. Lower left: The accelerator tube and the Cockroft-Walton high-voltage generator. Lower right: The duoplasmatron ion source.)

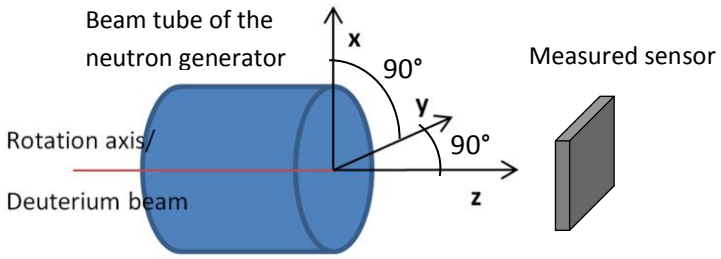

Fig.26 - Coordinate system fixed to the terminal tube of the neutron generator applied for explanation of fast neutron measurements

Neutrons are produced by DT fusion reaction in the tritium target. The neutron spectrum is a distribution with a mean energy and peak width depending on angle with respect to the deuterium beam. As an example, substituting in to the Eq.(26), for 125 keV deuterium beam the neutron energy varies between 14.89 MeV and 13.39 MeV from 0° to 180° relative to the direction of the deuterium beam. Furthermore, the deuterium ions are decelerated inside the target, thus the DT-reactions occur at different energies. The middle energy values of neutrons leaving the target in the function of the angle are illustrated in Fig.27.

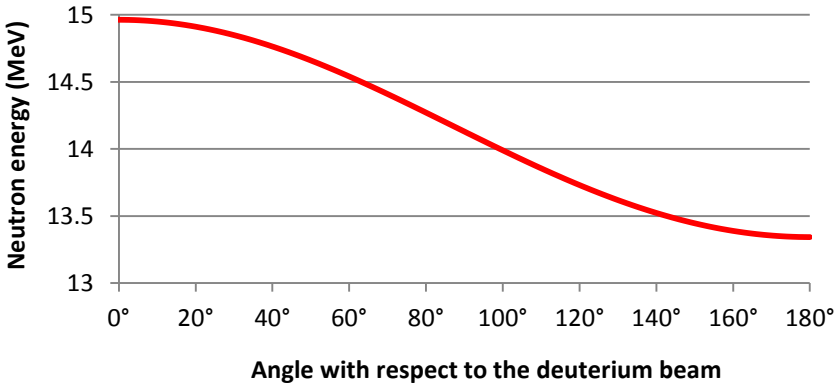

Fig.27 - Angular distribution of mean energy of the DT neutrons generated in the TUD Neutron facility the angle is with respect to the deuterium beam.

The deuterium beam creates an oval formed beam spot on the tritium target, of which position has an uncertainty of 1-1.5 cm around a constant position due to the manual focusing of the deuterium beam with quadrupole magnets. To determine the beam spot and its position photographic papers have been fixed in front of the target surface during some of the irradiation sessions with the neutron generator. Fig.28 a-c represent the oval distribution of the neutron beam. After converting the recorded photograph into an intensity map the spatial intensity distribution is obtained. In Fig.29-a and b the effect of stronger deflection of the deuterium beam relative to the midpoint of the tritium target (cross in the circle in the picture) is shown as a bare photograph and in a false color picture of it. These photographs illustrate that the deuterium beam line could differ from the direction of the theoretical z axis, thus in this case neutrons with the maximum energy are not moving into the direction outlined by the rotation axis of the beam tube.

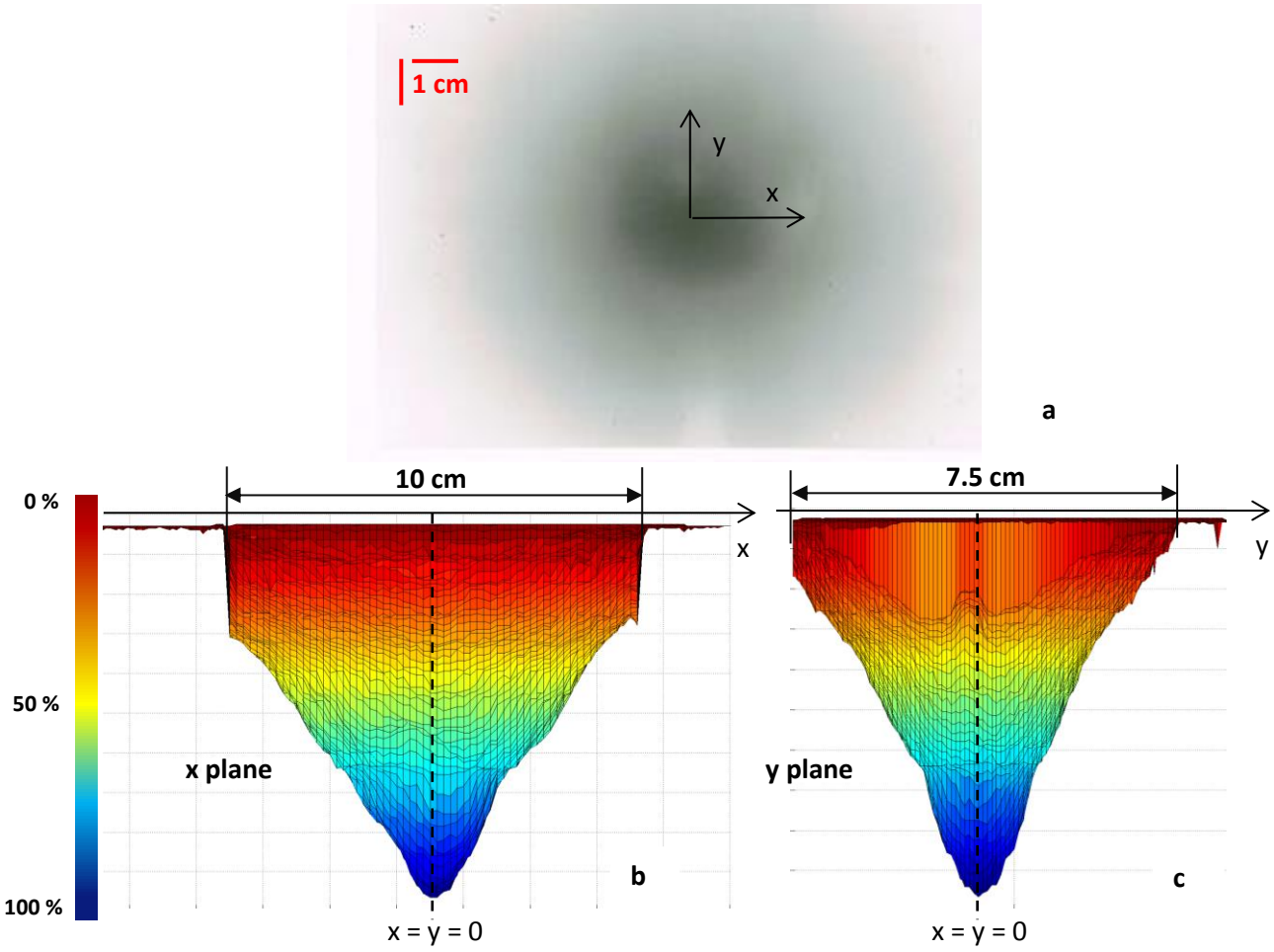

Fig.28-*a* - Beam spot generated by ionizing radiation on a photo paper directly fixed in front of the tritium target. The intensity of darkening is proportional to the neutron fluence through the paper. *b* and *c* – Intensity map of the photograph in two mutually perpendicular positions

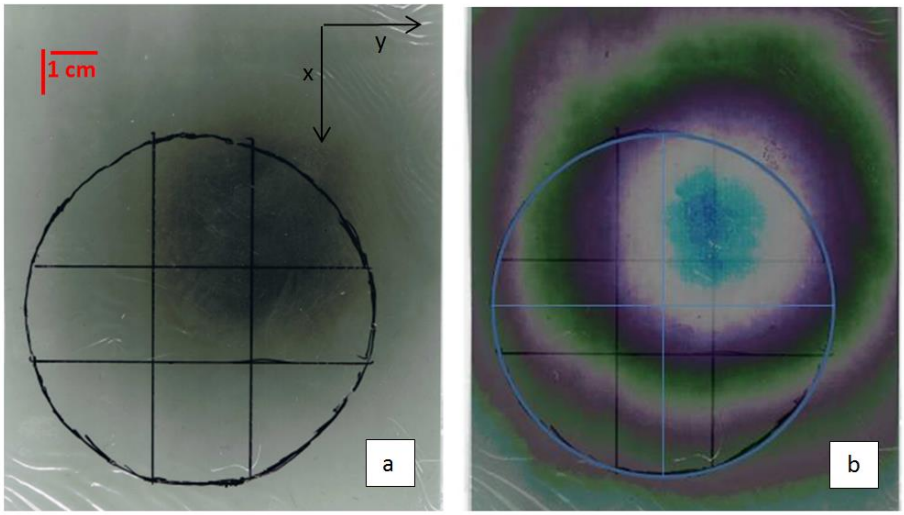

Fig.29 – Deviation of the neutron source position relative to the tritium target (drawn circle with cross) position recorded with a photo paper fixed to the tritium target; *a* – original photograph, *b* – false color photograph

6.1.2 Belgian Reactor 1

Thermal neutron irradiation sessions of SiC sensors are conducted in the central large cavity of the Belgian Reactor 1 (BR1) at SCK-CEN, in Mol in Belgium. The BR1 reactor is an air cooled, graphite moderated reactor using natural uranium fuel and is used for research work and radioisotope production [90, 91]. A photo of BR1 reactor from 1956 and a cross-sectional cut including the central large cavity are shown in Fig.30 a and b. At present the maximum power of the reactor amounts to 700 kW. Experiments with 4H-SiC neutron detectors are performed in a pure Maxwellian thermal neutron field with a mean neutron energy of 25 meV and 7×10^{8} $cm^{-2}s^{-1}$ neutron flux. The typical gamma dose rate is 1 Gyh^{-1}. No fast neutrons can be measured at the location of the test position.

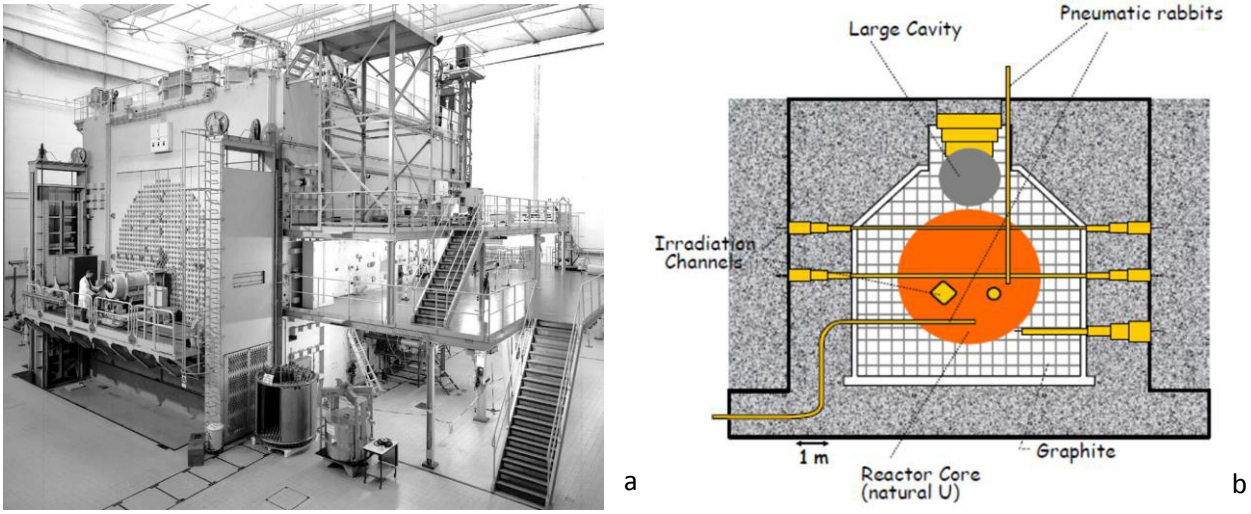

a b

Fig.30-a,b – The First Belgian Reactor in Mol, SCK-CEN (Source of the pictures : [89,90]).

6.2 Measurement read-out electronics

The examined diodes are mounted in aluminum boxes and for the high temperature measurements, in aluminum capsules. These boxes are connected to the measurement electronics, first to the preamplifier through a 50 Ohm coaxial cable. Four types of preamplifiers have been used during the experiments. For the first preliminary tests with the D1-type 4H-SiC detector irradiated with 14 MeV fast neutrons, a charge sensitive preamplifier from GSI Darmstadt and a Fast ComTec TA1000B Fast Pulse/Timing Preamplifier have been applied [92]. For the first thermal neutron measurement session in the BR1 reactor, a charge sensitive Canberra-2004 semiconductor detector preamplifier has been installed (noise contribution: < 2.8 keV full width at half maximum (FWHM) at 0 pF; charge rate capability up to 4.5×10^{6} MeV/sec for silicon; integral nonlinearity: <±0.02% for ±10 V output [93]).

For later and for most of the measurements, as fast neutron tests performed at elevated temperatures and for extended thermal neutron tests, electronics of CAEN S.p.A have been chosen as a standard [94]. The

amplification of the sensor signal is done by a four channel CAEN A1422 charge sensitive preamplifier with the parameters:

- 400 mV/MeV amplification,
- <200 pF input capacitance for silicon detectors,
- <3.6 keV FWHM noise contribution for silicon detectors,
- ± 3.5 V linear range of the output,
- <±0.05% integral non linearity,
- <110 ns rise time of the output signal,
- 14 μs decay time of the output signal,
- 3.41×10^6 MeV^2s^{-1} maximum energy squared count-rate product.

This preamplifier has led the bias voltage to the diode detectors supplied by a DT5780 type 2-channel CAEN digital multi-channel analyzer (MCA), which acquires the detector signal and transfers it to a personal computer. The MCA box also has a maximum ±500 V/3 mA high voltage output with a tolerance of 2%. The device also measures the reverse (DC) current on the preamplifier output. The maximum sampling rate of the MCA is 100 MS/s (mega samples per second). The signal recording and time parameters have been adjusted in the DPP-PHA firmware software supplied by CAEN S.p.A. The ± 12 V power supply to the preamplifier's operation is provided by a DT5423 power supply [94]. The arrangements of the above listed electronics for a certain measurement at different facilities are referred in the later text as Set-up 1, 2, 3 and 4.

6.2.1 Set-up 1

Preliminary experiments with D1 diodes have been performed at BR1 (SCK-CEN, Mol). These tests have been carried out with a Canberra-2004 semiconductor detector preamplifier and a Caen DT-5720 desktop digitizer, the bias voltage to the SiC detector has been supplied by an Ortec 660 dual high voltage NIM-module [95], the signal is processed by the DPP (Digital Pulse Processing)-Firmware of the digitizer. Three meters long coaxial cable between the charge sensitive preamplifier and the detector has been mounted due to the position of the central cavity of the BR1 reactor, where the detector was located. By these first tests the proof of principle is ensured for the later measurements. The sketch and block diagram of Set-up 1 for measurements with D1 type detector in the BR1reactor is shown in Fig.31

6.2.2 Set-up 2

Further thermal neutron measurements with D2, D3 and D4-type detectors have been conducted with a second set-up (referred as Set-up 2). This included a Caen 1422 four channel charge sensitive preamplifier, a DT-5780 multi-channel analyzer and high voltage supply; the measurement parameters have been adjusted by the DPP-PHA firmware software of the multi-channel analyzer. Three meters long coaxial cable between the charge sensitive preamplifier and the detector has to be mounted due to the position of the central cavity of the

BR1 reactor, where the tests have been executed. The preamplifier could not be inserted for geometrical reasons. The sketch and block diagram of the applied measurement set-up for measurements with D2, D3 and D4 type detectors in the BR1reactor is shown in Fig.32.

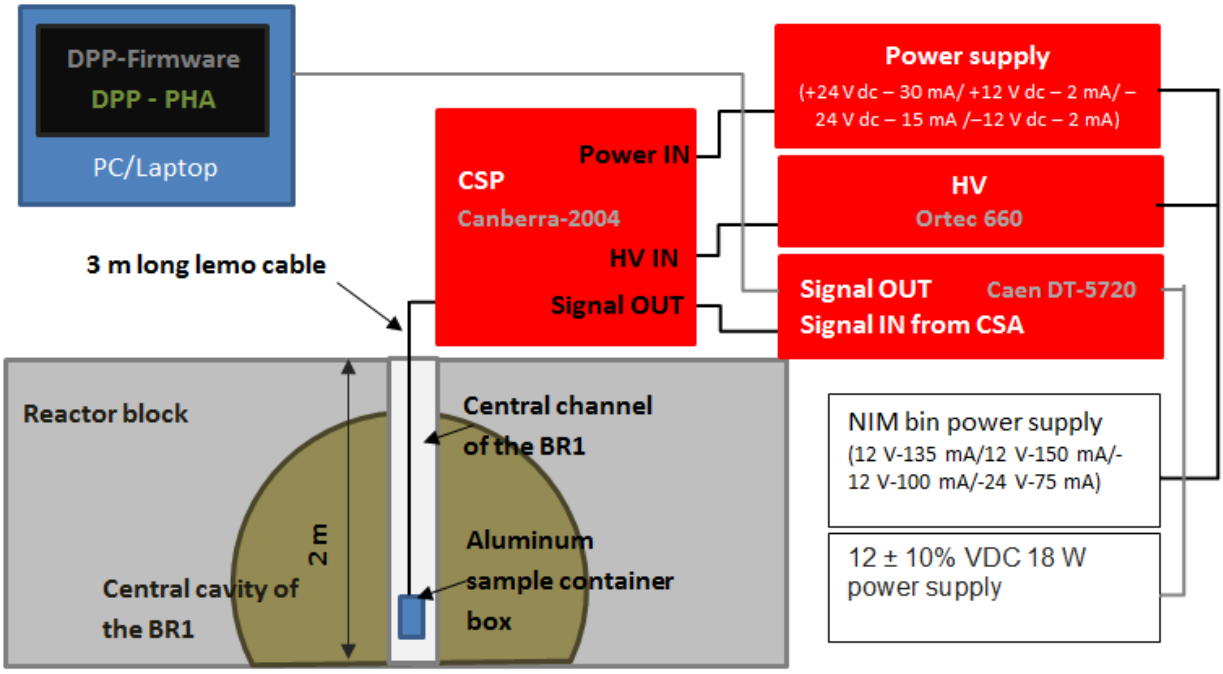

Fig.31 - Set-up 1: The sketch of the applied set-up for measurements with D1 type detector in the BR1reactor in thermal neutron spectrum with a digitizer

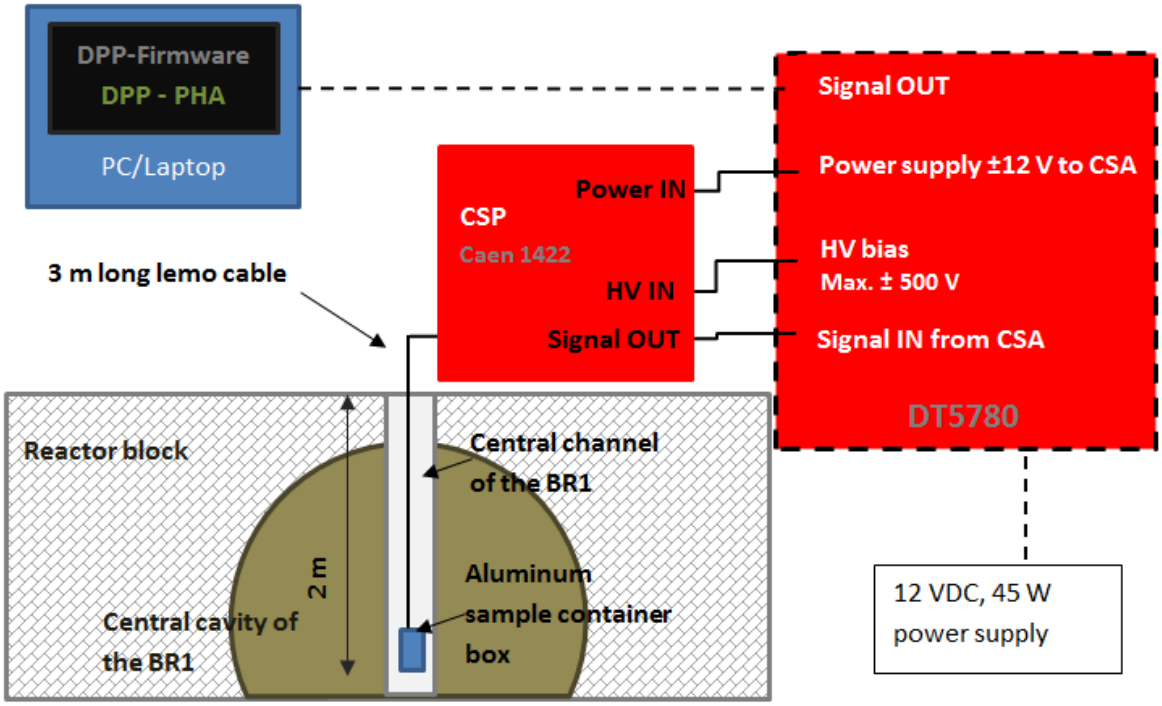

Fig.32 - Set-up 2: The sketch of the applied measurement set-up for measurements with D2, D3 and D4 type detectors in the BR1reactor in thermal neutron spectrum with a compact digitizer

6.2.3 Set-up 3

For the first measurements of DT neutrons with D1 type detectors a Fast ComTec TA1800 timing preamplifier and a GSI Darmstadt charge sensitive preamplifier were used; energy histograms were recorded with MPA-3 PC-board Multiparameter Analyzer System [96]. The SiC diodes were biased by an Ortec 660 power supply. The energy histograms were recorded and the measurements were controlled with a personal computer using the MPANT user interface of the MPA-3 system [96]. The Fast ComTec TA1800 timing preamplifier has its own power supply, while the charge sensitive GSI CSA is operated with a laboratory power supply. The sketch of the applied set-up (referred as Set-up 3) for measurements with D1 type detector in fast neutron spectrum is shown in Fig.33.

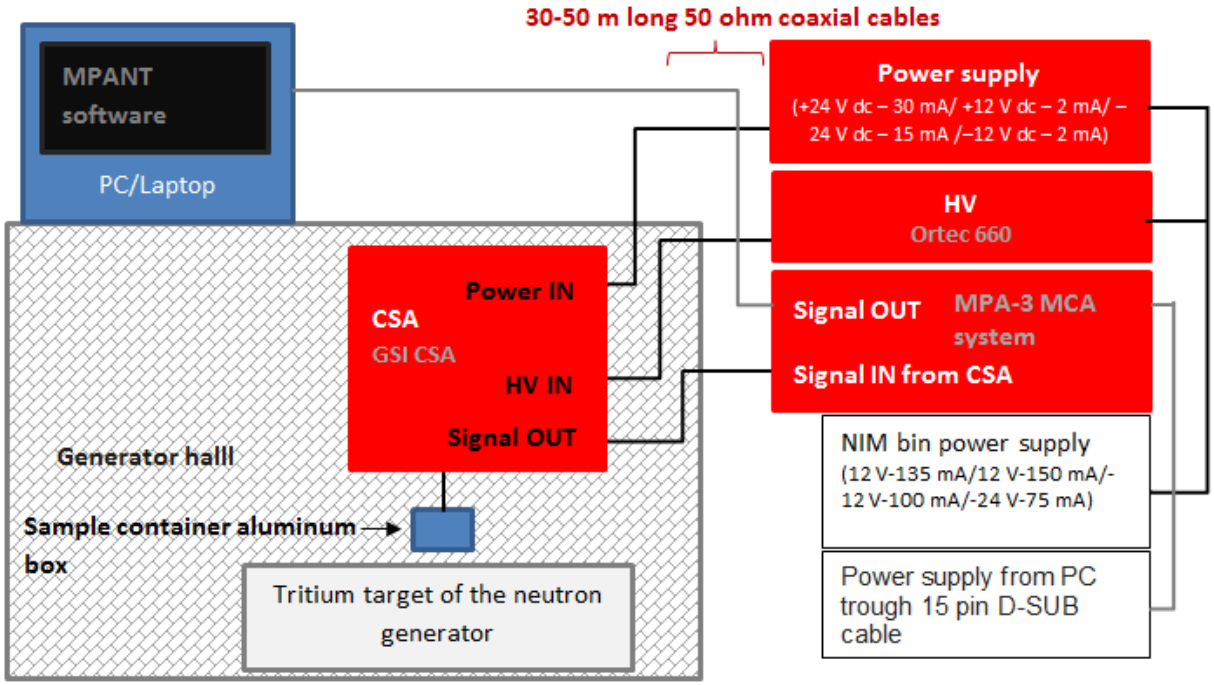

Fig.33 - Set-up 3: The sketch of the applied measurement set-up for measurements with D1 type detector in the in fast neutron spectrum with analog signal processing chain

6.2.4 Set-up 4

For later tests with fast neutrons with D2 and D5 diodes the following new measurement electronics from CAEN have been applied:

- a CAEN 1422 four channel charge sensitive preamplifier,
- a DT5780 Multichannel Analyzer (MCA) based on waveform digitization, which includes the high voltage supply for the detector biasing, the power supply of the preamplifier and the signal processing system and measures the reverse (DC) current from the tested diode.

The MCA has been connected through an USB cable to a personal computer and the measurements and set-up have been controlled by the DPP-PHA software from CAEN.

For all set-ups the diode containing aluminum box has been connected to the preamplifier in the front of the tritium target of the DT generator in the neutron generator hall; the preamplifier has been connected and the signal has been lead through 30-50 meters long coaxial cables to the measurement room. The sketch and block diagram of the applied set-up (referred as Set-up 4) for measurements with D2 and D5 type detectors in fast neutron spectrum is shown in Fig.34.

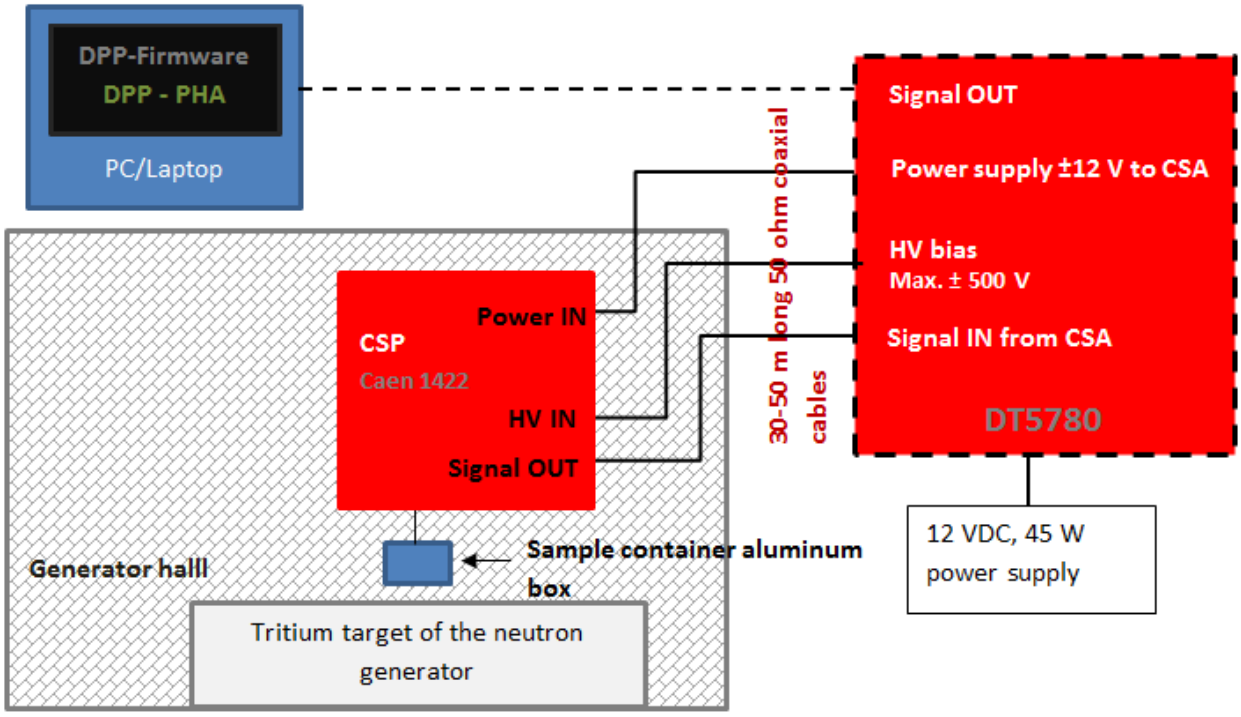

Fig.34 - Set-up 4: The sketch of the applied measurement set-up for measurements with D2, D3 and D4 type detectors in fast neutron spectrum

All the applied electronics are optimized for measurements with silicon detector. Due to the different quality of the tested SiC diodes the calibration of the recorded spectra are conducted after signal recording applying the method introduced later in Section 6.3.

6.2.5 Noise considerations of the electronics and the sensor

For most measurements the CAEN A1422 charge sensitive preamplifier with the DT5780 type CAEN MCA has been applied. Generally, in radiation detection systems the main noise source is at the beginning of the measurement chain, at the input FET (field-effect transistor) of the preamplifier. Noise parallel with the input (as fluctuation of the diode leakage current and the input gate-source current of the FET) and in series

with the source of the signal (Johnson noise and thermal noise of the input FET) are considered [10]. The noise is amplified in the same way as the low-level signal, thereby low-pass filtering in the preamplifier is applied to eliminate the high frequency noise. The noise of the further signal chain can be almost neglected due to its much lower level compared to the amplified detector signal. Following the procedure described in [10], the noise contribution of a preamplifier to the FWHM value of unit eV can be obtained by multiplying 2.35 with the root mean square (RMS) value of the noise, or with the noise equivalent charge. In the latter case one has to multiply with the ionization energy to create an electron-hole pair for semiconductor detectors. The CAEN A1422 has a noise contribution of less than 3.6 keV to the FWHM value for silicon detectors. From that it can be concluded that the RMS value of noise can reach up to 1.53 keV, which refers to as the signal level of ~423 electron-hole pairs in silicon detectors (after dividing with ionization energy of silicon, 3.62 eV). Due to the amplification of 400 mV/MeV of the CAEN A1422 this value corresponds to a 0.61 mV signal level. Because in 4H-SiC crystal electron-hole pairs are generated at ~7.78 eV energy, the predicted amplification of the preamplifier resulted as 186 mV/MeV due to the fewer charge pairs generated for the same energy deposition than in silicon. Thus, the estimated noise level caused by the preamplifier connected with SiC sensor is at least 0.28 mV (>1.51 keV, energy of ~193 electron hole pairs and 3.5 keV FWHM noise contribution).

For all set-ups coaxial cables are applied to conduct detector signal. Although short distance between the preamplifier and the detector has to be maintained, in case of Set-up 1 and 2 the length of the cable could reach up to 3 meters. This length cause ~15 ns (5.1 ns/m) delay of the signal and ~300 pF (~100 pF/m for 50 Ohm lemo cable for Set-up 1 and 2) capacitance [34], which is higher than the maximum 200 pF input capacitance of the CAEN 1422 preamplifier. The input voltage level sensed by the preamplifier is equal to the collected charge divided by the input capacitance [34]. Thus, depending on the detector capacitance the input voltage, thereby the amplified signal may decrease. For measurements with Set-up 3 and 4 cables with 15-30 cm length have been applied, of which capacitance do not exceed the maximum input capacitance of the preamplifier.

Digital signal processing has been carried out by the CAEN DT5780 MCA. Inside the DPP-PHA software the time parameters for the measurements can be adjusted. Up to 10 000 counts per second (cps) the MCA enables to achieve negligible dead-time [94]. During the irradiation tests with CAEN electronics the maximum recorded cps has not exceeded 10 000.

One important source of noise is the temperature dependent leakage current, which can cause a voltage drop across the diode according to $V_{Diode} = V_{bias} - I_{leakage} \times R_{Bias}$, For common silicon diodes the leakage current doubles for 8 °C increase of temperature [97]. Tests at high temperature at optimized bias voltage levels have been carried out to avoid an elevated reverse current flow according to the diode equation $I = I_{leakage}\left(e^{\frac{qV}{kT}} - 1\right)$, where I is the current flowing through the diode, $I_{leakage}$ is the leakage

current, q an V are the elementary charge and bias voltage, finally k and T are the Boltzmann constant and the temperature [34].

6.3 Calibration of the pulse height spectra

The calibration of the recorded energy histograms is conducted by fast neutron irradiation tests, following a methodology developed by Ruddy et. al. [20]. The reaction $^{12}C(n,\alpha)^{9}Be$ produces a distinct peak in the recorded spectra. Thus this peak is studied to express the channel energy of the histogram. The $^{12}C(n,\alpha)^{9}Be$ reaction has a reaction energy (Q) of -5.71 MeV. Neutrons generated by the neutron generator at TUD leave the target with the maximum kinetic energy under 0°, i.e. in the same direction as the deuterium beam. The most commonly used deuterium beam energy during the tests is 125 keV resulting in a maximum neutron energy of 14.89 MeV at 0° direction and 14.12 MeV at 90°. The deposited energy (E_d) in the $^{12}C(n,\alpha)^{9}Be$ reaction is equal to the sum of the neutron's kinetic energy (E_n) and the reaction energy (Q):

$$E_d = E_n + Q. \tag{30}$$

The mean value of the full energy peak in the energy histogram refers to the E_d value. SiC detectors with few mm^2 scaled surface area are proper devices to perform measurements with high energy and spatial resolution. By comparing several hundred recorded pulse height spectra the maximum attainable mean value of the peak is identified, which refers to the signal at 0° position with respect to the deuterium beam. This measurement position has been chosen because of the symmetric energy distribution of neutrons around the z-axis with the maximum neutron energy value. Hence, narrower full energy peaks could be recorded at the side positions, 0° position has been considered to the calibration procedure. The reasons were the deflection of the deuterium beam and the un-known minimum energy of neutrons, which is still detectable with appropriate accuracy. The peak mean value has been established using double Gaussian fitting. This method has been found sufficient for the present histogram structure. Double fitting has been used due to the signal from $^{28}Si(n,\alpha 8/9)^{25}Mg$ reactions, which is partially covered by the $^{12}C(n,\alpha)^{9}Be$ reaction peak, see in Fig. 35. The maximum mean value position in case of the $^{12}C(n,\alpha)^{9}Be$ full energy peak has been stated at the 2656^{th} channel (the maximum channel number is 2^{14}). This results in a **3487 eV energy range for each channel**, which is applied to the energy binning of the recorded energy histograms.

As it follows, the energy calibration depends on particle thus it needs some approximation. Secondary ions with the same kinetic energy but with different atomic numbers emitted after reactions between neutrons and the target nuclei, will have slightly different ionization level in matter. This phenomenon is referred as pulse height defect [19, 29]. Therefore, not a perfect linearity between the mean value positions of the full energy peaks and the evaluated energy deposition could be established for reactions with different secondary nuclei. Heavier particles like ^{25}Mg lead to less energy deposition through the ionization of the detector material than in case of light charged particles like α-particles. This difference can be measured also for reactions including ^{9}Be and ^{25}Mg ions. In semiconductors, the ionization process in case of ^{9}Be with a certain

kinetic energy results in a larger energy loss in form of electron-hole pairs than for ^{25}Mg with the same kinetic energy due to the smaller size and atomic charge of ^{9}Be ion.

The pulse height defect produces a noticeable effect in the energy histogram. If the measured peak positions of ^{28}Si(n,α)^{25}Mg reaction for different excited states of the recoil nucleus and of the ^{12}C(n,α)^{9}Be reaction are taken from Fig.35 and they are plotted as a function of the channel number, the data points in Fig.36 are obtained (here, the 8th and 9th excited states of ^{28}Si(n,α)^{25}Mg reaction are referred to as one single peak due to their near reactions energy values, see in Table II.). Linear fitting has been performed only for the ^{28}Si(n,α)^{25}Mg reactions and separately including the ^{12}C(n,α)^{9}Be peak, as well. It becomes visible that the fitting curve has an offset of 84 channels if all the data points are considered and a negative offset of 89.83 channels is occured by applying data exclusively from ^{28}Si(n,α)^{25}Mg reactions. The peak position of ^{12}C(n,α)^{9}Be reaction is not located on the regression line determined by the peak mean values of ^{28}Si(n,α)^{25}Mg reactions. The measured peak position of ^{12}C(n,α)^{9}Be reaction occupies higher energy channel as predicted by the peak positions of ^{28}Si(n,α)^{25}Mg. In this context there is non-linearity. The data points have a maximum 2.12 % difference from the values predicted by the fitting curve including points from both reaction types in the examined energy range. The energy values of the certain peaks in Fig.36 are calculated applying the above stated channel energy value (3487 eV/channel).

A significant reference point on the recorded pulse height spectrum is served by the full energy peak of the ^{12}C(n,α)^{9}Be reaction, which appears on the energy histogram as a prominent peak around 8-9 MeV. In case of accurately known incident neutron energy distribution, the peak energy is well defined. In case of SiC detectors with small (~mm^2) surface area, a slight change of this peak position in the pulse height spectrum denotes also a change of the mean incident neutron energy thus the change of the deposited energy inside the detector, which can be detected with high accuracy. This is because of the high spatial resolution of small sensors, which encounter neutrons of varying maximum middle energy depending on their moving direction relative to 0°.The small uncertainty (~1 cm horizontal and ~1.5 cm vertical) of the deuterium ion beam position results in an asymmetric neutron energy distribution relative to the theoretical z-axis. To evaluate, how this asymmetric neutron energy distribution affects the recorded signal, measurements at 4 different positions have been simultaneously performed, as illustrated in Fig.37. In Fig.38 the ^{12}C(n,α)^{9}Be reaction full energy peak positions are recorded by four D2 type diodes at the four positions. At first the figure confirms that the small D2 SiC diodes are able to detect small differences of the ^{12}C(n,α)^{9}Be peak position corresponding to the change of the projectile neutron energy. At two exact extreme positions (90°- P1 and P2) and at theoretical 0° positions (P3 and P4) relative to the theoretical deuterium beam direction in laboratory frame (z-axis), the neutron energy experiences the same shift.

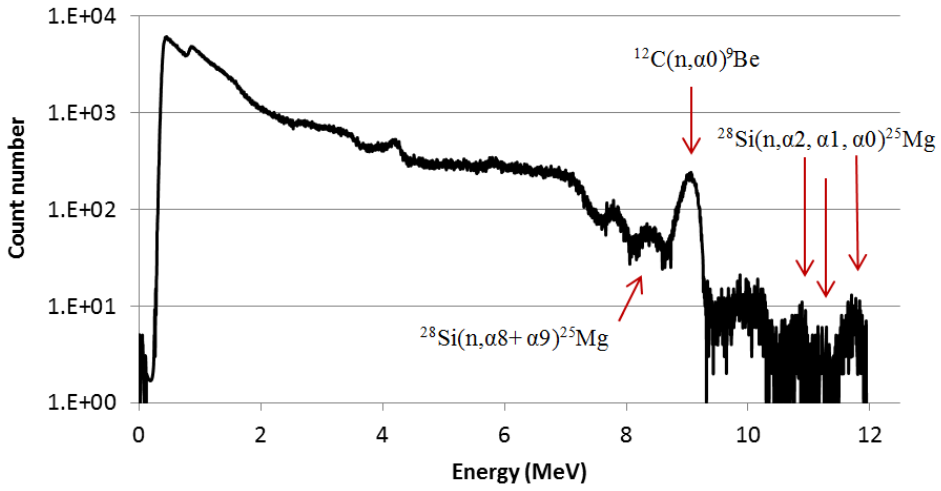

Fig.35 - Sensor counts as a function of the energy discretized channel number in a fast neutron spectrum to identify peak positions for the energy calibration

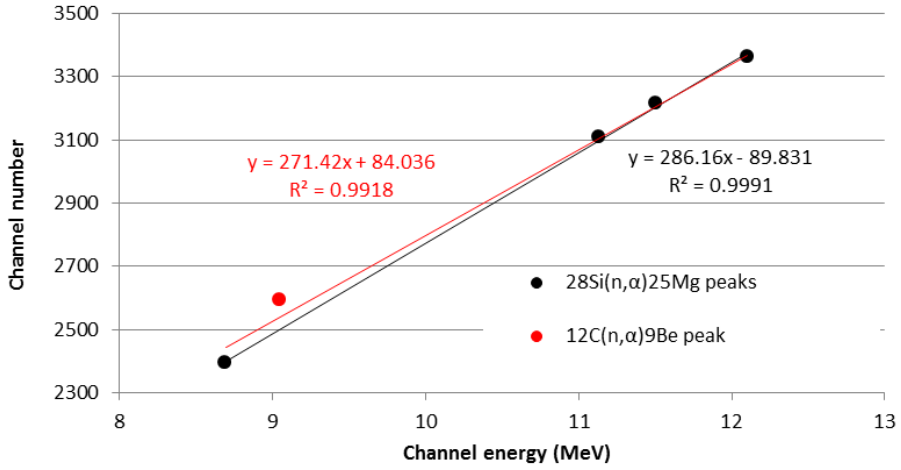

Fig.36 - Correlation of the measured peak positions and calculated channel energies. The red and black lines represent the linear fits of the data with and without the ^{12}C(n, α)^{9}Be reaction peak

The theoretical neutron energy value (T_n) at 90° angle position, can be evaluated by the following relation:

$$T_n = \frac{M_\alpha}{M_\alpha + M_n} * Q + \frac{M_\alpha - M_{{}^2_1H}}{M_\alpha + M_n} * T_{{}^2_1H} = \ 14.12\ MeV \ \ (Q = 17.6\ MeV, T_{{}^2_1H} = 0.125\ MeV)\ ,$$

where M values are the mass of the neutron, deuterium and tritium nuclei, Q is the reaction energy value and T represents the average energy of projectile deuterium ions and the emitted neutrons at 90°. Using this T_n value, the released energy (E), in the ^{12}C(n,α)^{9}Be reaction can be calculated:

$$E = Q + T_n(90°) = 8.42\ MeV \quad (Q = \ -5.70\ MeV).$$

The corresponding energy is marked by a black vertical line in Fig.38.

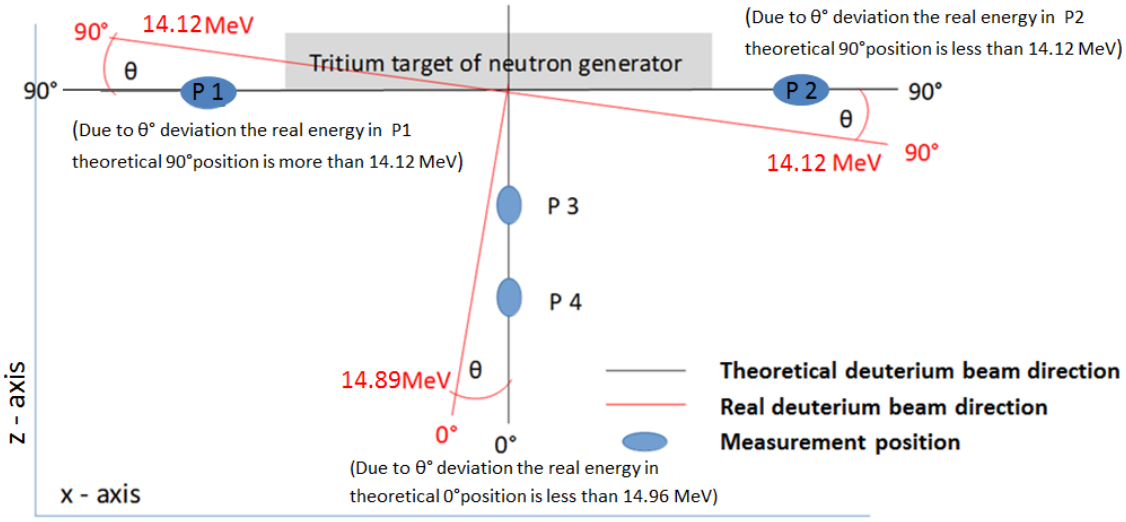

Fig.37 - Sketch of the measurement setup with four detector positions. P1, P2, P3 and P4 indicate the diode detector positions relative to the tritium target of the neutron generator. The black lines appoint the theoretical 0 degree oriented deuterium and neutron beam directions as well as the 90 degree neutron beam directions. The red lines mark the real positions during the measurements with an angular deviation of θ degree relative to the theoretical 0 degree and 90 degree directions. The angular deviation was occured by the uncertanty of the set-up of the positioning magnets of the DT-generator.

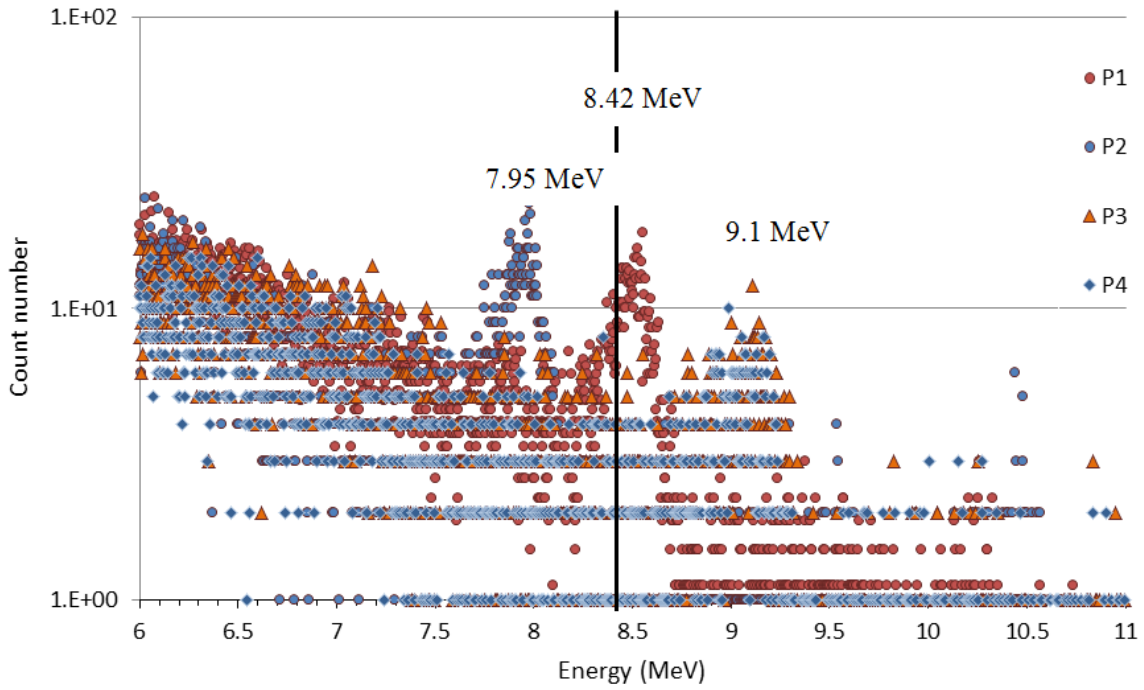

Fig.38 - $^{12}C(n,\alpha)^{9}Be$ peaks measured in different positions relative to the DT-target according to Fig.72.

The mean value of the resulting energy peak in P1 is slightly higher and in P2 lower than in the theoretical 90° position. The referring neutron energy, peak energy and angle values related to the deuterium beam direction in position P1 yield 14.22 MeV and 8.42 MeV at 82° and in position P2 13.65 MeV and 7.95 MeV at 128°. (The deviations of angle values from the 90° position are not equal, because of the uncertain position of the diode container boxes due to the arrangement difficulties of the four boxes simultaneously near to the tritium targets surface.) The results obtained at the side positions are important because it is clear that the peaks can be pinned to the average neutron energy and the diode position. The place of the $^{12}C(n,\alpha)^{9}Be$ reaction peak arising from 14.12 MeV (90°) neutrons should be located between the P1 and P2 peaks. Two additional D2 diodes are placed at 0° position. (Here, the positions of the aluminum boxes could be fixed.) The mean value channel of the measured $^{12}C(n,\alpha)^{9}Be$ peaks occupies the same energy channels in the higher energy region for both diodes, with a peak position at 9.10 MeV corresponding to the released energy generated by 14.80 MeV neutrons at ~26° relative to the real deuterium beam direction (red 0° direction in Fig.37). This neutron energy is higher than at the two side positions. This proves that forward direction neutrons with higher energy than at side direction generate a higher energetic signal. Thus accurate difference between the positions of full energy peaks can be observed on the recorded spectra. From the results it may be concluded that a small area SiC diode is able to detect small energy differences. This ability has an important role in the further examination of SiC diode detectors at elevated temperatures.

6.4 Special conditions for measurements at high temperature and in magnetic field

6.4.1 Measurements up to 155 °C

Tests up to 155 °C have been performed with D2 type detectors. The diodes are mounted in 3×5×4 cm^3 aluminum boxes. These measurements are conducted with Set-up 4. The boxes are connected to the CAEN A1422 four channel charge sensitive preamplifier through a 50 Ohm coaxial cable. The signal processing is performed by the 14 bit CAEN DT5780 multi-channel analyzer, of which voltage range was set to 9.5 V.

To heat the diodes, Al_2O_3 ceramic heating plates (from Rauschert GmbH) with platinum heating wire are used. The dimensions and geometry of the plates are shown in **Appendix B**. The maximum achievable temperature of the heater is 750 ± 30 °C, at maximum 24 V and 100 ± 12 W electric power.

Two heating plates are placed in a 5×6×7 cm^3 glass-ceramic, referred to as macor, house inside an aluminum box. The tested diode was at 6-7 cm distance from the tritium target. The sketch of the measurement arrangement in the x-z plane is shown in Fig.39. The figure depicts the sample holder aluminum box inside the macor house. The two heating plates are fully surrounded by the house and the aluminum box except at the entrance gap. A photograph of the described parts is shown in **Appendix B**.

The applied temperature range has been set from room temperature up to 150°C. Due to the low melting point of the tin/lead soldering (~170-180 °C) of the SiC diode's connectors higher temperatures could not be achieved during the first tests at elevated temperature.

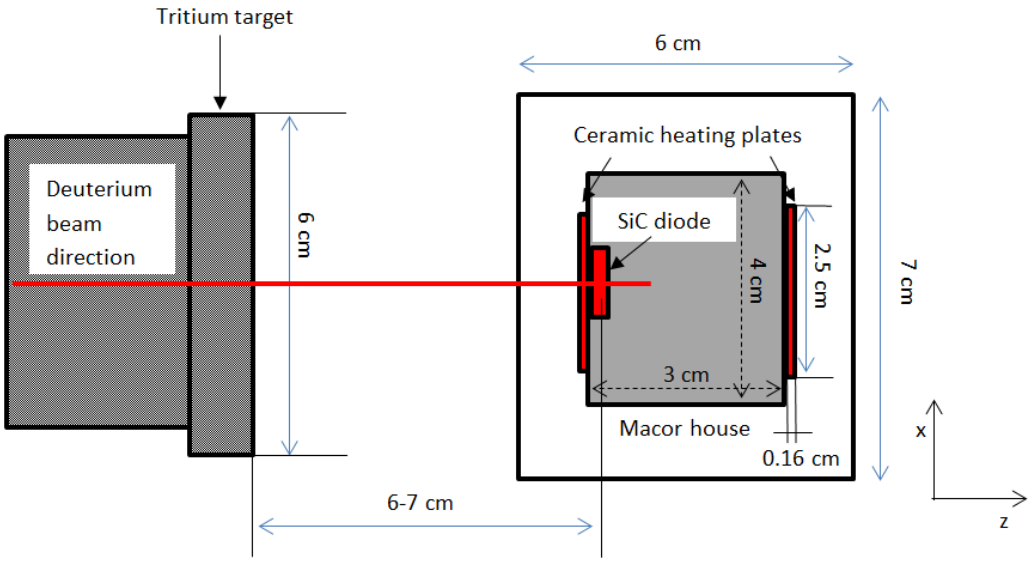

Fig.39 – Sketch of the measurement arrangement for high temperature tests up to 150 °C. The Al_2O_3 ceramic heating plates are inside the macor house, which is placed before the tritium target of the neutron generator.

6.4.2 Measurements up to 500 °C

The D5-type diodes are covered with heat-resistant gold-nickel ohmic contacts, which allow performing measurements up to 500 °C. To maintain such a high temperature special heating system has been designed. To achieve the highest possible neutron flux, the neutron irradiated sample should be placed near to the target surface of the DT- neutron generator. Therefore, a small volume, 4.5 × 4.2 × 2.4 cm^3 glass-ceramic heating box has been built (see in **Appendix C**). Inside this box two pieces of 2.5 × 3.7 × 1.6 cm^3 ceramic heating plates have been placed. Between them, the diode has been put in a small 2 × 1 × 1.2 cm^3 aluminum capsule serving as a Faraday cage during the tests.

To conduct the signal and to isolate the hot sample from the preamplifier, a stainless steel coaxial "cable" has been developed. The material of the inner signal wire and the outer shielding of the cable is also stainless steel. The steel wire is fixed by two macor rings inside the steel tube. A sketch of the coaxial cable is shown in **Appendix D**.

The resulting impedance of a coaxial cable can be evaluated by:

$$Z_L = \sqrt{\frac{\mu_0}{\varepsilon_0 \varepsilon_r}} \frac{1}{2\pi} ln\left(\frac{D}{d}\right) = \frac{376.73}{2\pi\sqrt{\varepsilon_r}} ln\left(\frac{D}{d}\right), \quad (31)$$

where μ_0 is the magnetic permeability of free space, ε_0 is the permittivity of free space, ε_r signs the relative dielectric constant of the isolator (here ε_{air} = 1.00059), *D* and *d* are the inner diameter of the steel tube and the diameter of the steel wire. Following from the foregoing the outer and inner tube diameters have been chosen as 10 mm and 7 mm. The air in the tube is the dielectric insulator between the tube and the wire. According to the ratio of the two diameters, the wire and the tube serves as a ~50 Ohm impedance coaxial cable.

The distance between the target surface of the neutron generator and the diode sensor is ~11 cm (This is more than for tests up to 155 °C because of the higher temperature, which could damage the target.) The neutron flux inside the macor house is measured with the niobium foil activation technique at room temperature. At elevated temperatures the relative change due to fluctuations in the flux compared to the measured value at room temperature is calculated from the signal of a silicon detector for the α-particles near to the tritium target of the DT-generator. The resulted neutron flux associated with the DT-reaction at the position of the detector varies between ~ 2.4 and ~3.1 × 10^7 $cm^{-2}s^{-1}$. Photographs of the typical measurement arrangement are shown in **Appendix D**. These measurements have been conducted with Set-up 4.

6.4.3 Fast neutron measurements in external magnetic field up to 1 Tesla

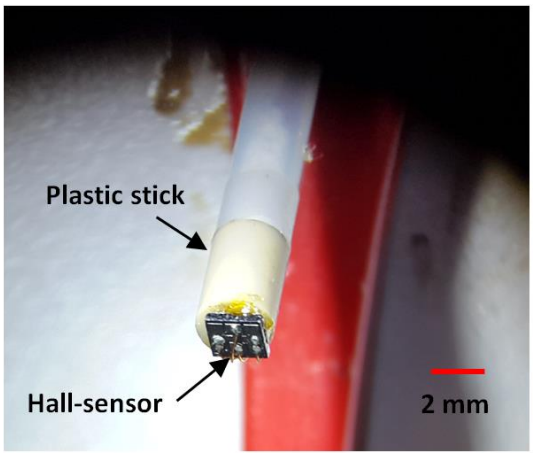

Fig.40 - Hall-sensor applied to measure the magnetic flux inside the central channel of a ring magnet. The sensor is attached to the end of a plastic stick

Tests with D5-type sensor were carried out in the permanent magnetic field up to 1 Tesla of neodymium magnets irradiated with DT neutrons at TUD. The cathode side of the SiC diode detector with 2.13 mm diameter was placed on a solder plate and a copper disk spring was contacted on the anode side (similar to that shown in Fig. 84). The disk spring was electrically insulated from the solder plate. The width of the solder plate was equal to the width of the SiC wafer in order to achieve the smallest possible area which could fit inside the ring magnet. Two N42 grade neodymium magnets with different magnetic field strength inside their central channels were applied for the measurements. The magnetic field strength has been measured with a Hall-sensor, see in Fig.40. For the small magnet 0.5592 ± 0.0025 Tesla and for the big magnet 0.9020 ± 0.0051 Tesla at the detector position were measured.

The two magnets were placed inside a T-shaped aluminum house adapting to the magnet shape, see in Fig.41 a-d. The technical drawings of the parts of this capsule can be found in **Appendix D**.

Fig.42 shows that in case of pn-diodes, the electrical field is established perpendicular to the junction's surface due to the electrodes contacted from the two sides of the diode; the electric field lines (black and white lines) inside the diode in the ring magnet. The magnetic field has the largest effect on the

movement of the electron-hole pairs and on charged particles if its field lines are perpendicular to the electric field. The orientation of magnetic field is set with the neodymium ring magnets with axial magnetization direction. At the center of the ring magnets the magnetic field lines are parallel to the wall of the inner cylinder hole. A diode placed in the center of the ring magnet with parallel surface to this wall fulfills this condition. The applied electric and magnetic fields induce electrostatic and Lorentz forces on moving charges

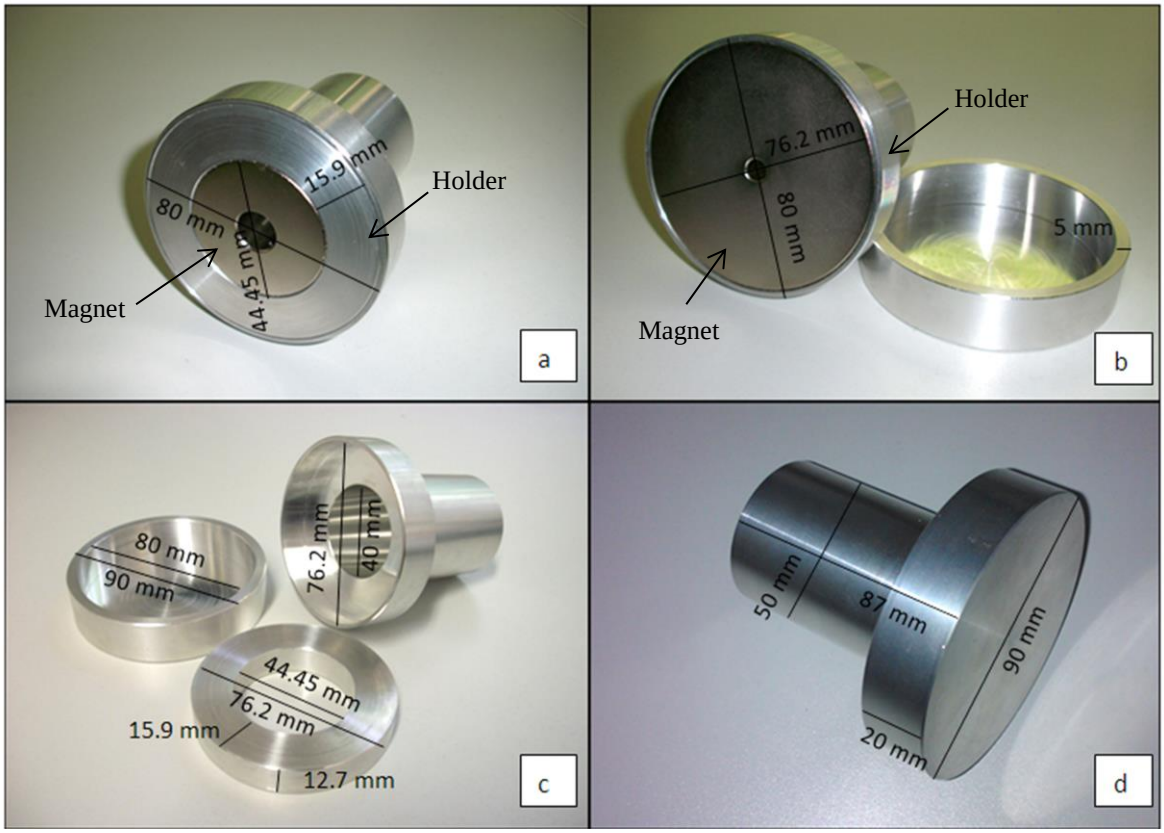

Fig.41 – **Aluminum housing and mounting set-up for measurements with SiC diode detector in permanent magnetic field:** *a* - aluminum house with the smaller magnet without lid; *b* - aluminum house with the bigger magnet without lid; *c* - the aluminum house, the small magnet fixing aluminum ring and the lid; *d* - aluminum house closed with lid

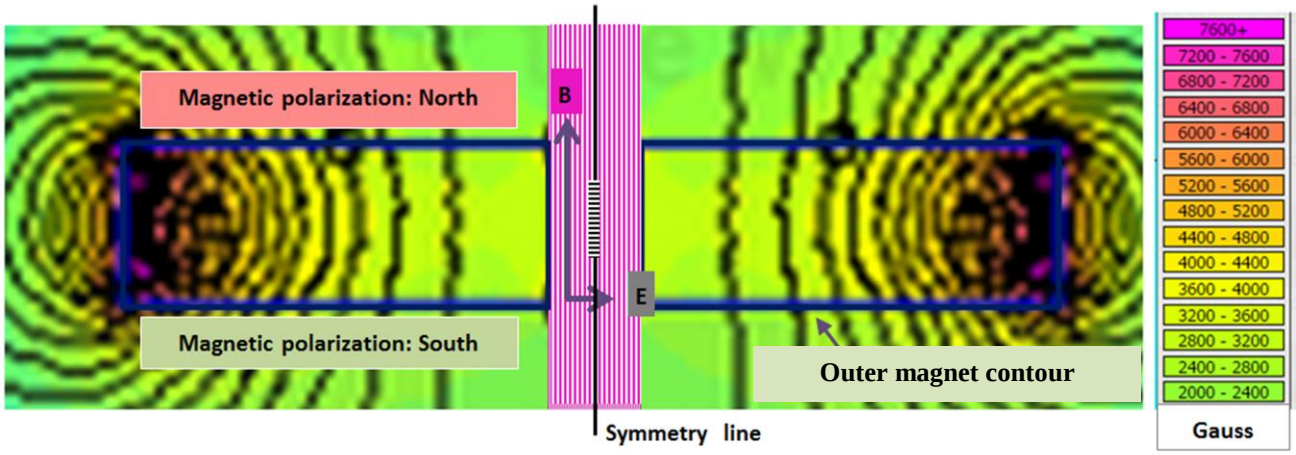

Fig.42 - Magnetic field lines (magenta lines) of a ring magnet (blue line) and a diode detector with perpendicular electric field lines (black and white lines in the middle of the magnet's hole) (The magnetic field was calculated and the background picture was generated at [98])

inside a crystal detector (Eq. (20)). In case of applying only built-in bias through the diode the magnetic field could change the direction and the velocity of the charge carriers. Magnetic field should be considered only in extreme cases using a high electric field through the space charge region, which is discussed detailed in **Appendix F**.

The magnet position has been chosen so that the SiC diode could experience the highest neutron flux during the measurements with the ring magnets. The angle between the tritium target's surface and the lid of the aluminum box is ~30°, thereby the largest available surface of the diode is faced to the tritium target un-shielded by the magnet. The distance between the target surface and the diode is ~13 cm, see in Fig.43. A neutron flux up to 2.3-2.4×10^7 $cm^{-2}s^{-1}$ at the diode's position has been calculated from niobium activation foil measurements. These tests have been conducted with electronics of Set-up 4.

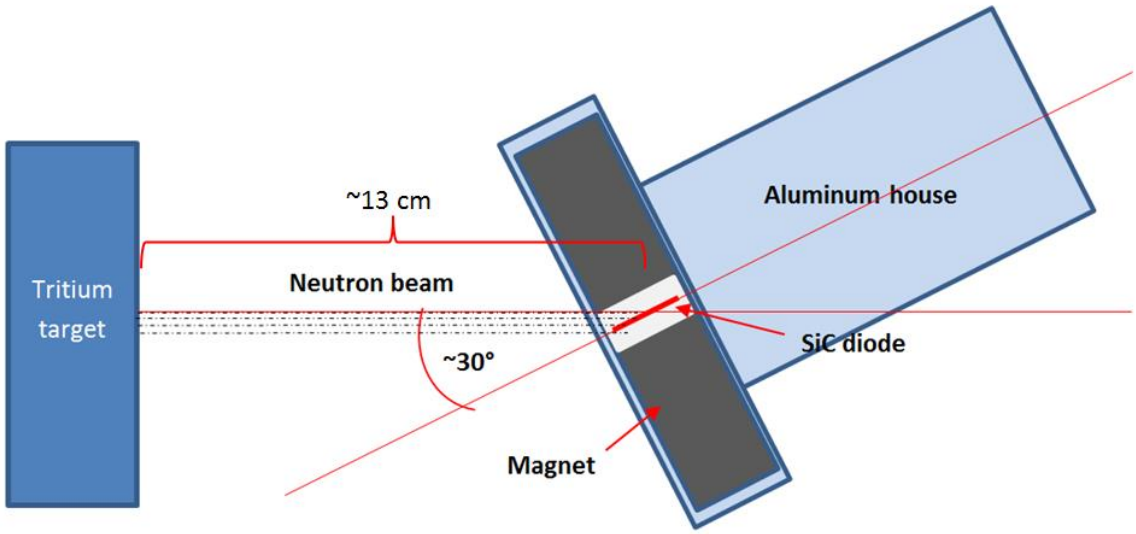

Fig.43 - Sketch of measurements arrangement for fast neutron measurements with encapsulated ring magnet with SiC diode inside of it

6.4.4 Epithermal neutron measurements in external magnetic field up to 8 Tesla

Screening tests with neutron irradiated SiC detector at higher magnetic field are performed at the Institut Laue-Langevin (ILL) in Grenoble in cooperation with the responsible group of the "*D3* – Spin Polarized Hot Neutron Beam Facility" [102]. The *D3* diffractometer is mostly applied for magnetic structure investigations, but due to its geometrical design other types of measurements can also be executed with the instrument. The epithermal neutrons for the tests were supplied by the 58,3 MW heavy water moderated High Flux Reactor (HFR) of ILL. Neutrons from the reflector part of HFR are lead through guide tubes to the measurement places. Additionally, the neutrons are polarized with a mono-chromator before they enter the guide field. Fig.44 and Fig.45 show the common set-up for high field tests, including the 10 T cryomagnet (CM) on the sample table (ST). The sample table is reached through a 2 meter long sample stick, which

terminates in the sample container capsule with a maximum diameter of 18 mm. For these tests, a D2 type SiC diode detector with ~ 0.98 × 0.88 mm^2 area has been chosen. The surface of the sample is set perpendicular to the polarized neutron beam and parallel with the magnetic field lines. Hence the magnetic and the electric field are at a 90° angle included. These measurements are also conducted with electronics Set-up 4.

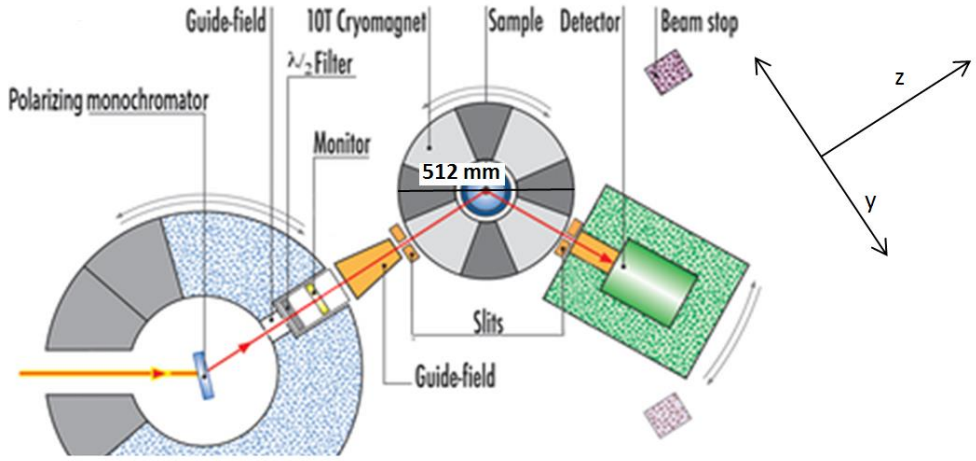

Fig.44 – Sketch of the D3 diffractometer at ILL Grenoble set-up for high magnetic field measurements including the 10 T cryomagnet (source: [102])

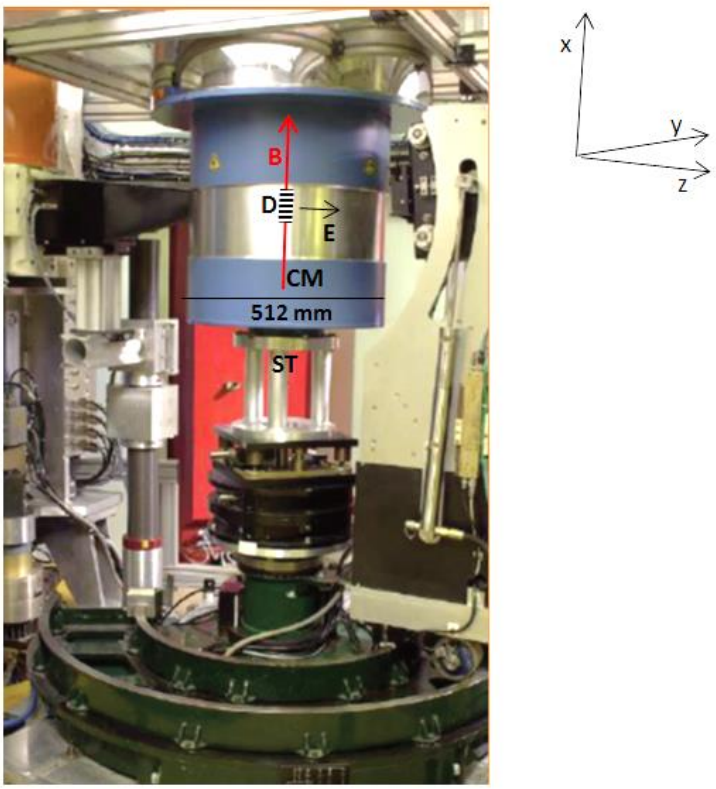

Fig.45 – The D3 facility mounted with the 10 T cryomagnet (CM) on the sample table (ST). The magnetic (B) and diode's (D) electric (E) field directions are indicated with the red and black arrows. (Source: [102])

6.6 Neutron source characterization

Thermal neutron measurements with SiC detectors are performed in the large central cavity of BR1 reactor at SCK-CEN. Inside the cavity the neutron spectrum is pure thermal with an average flux of ~10^8 $cm^{-2}s^{-1}$. The neutron flux as a function of the neutron energy at different locations in BR1 is shown in Fig.46.

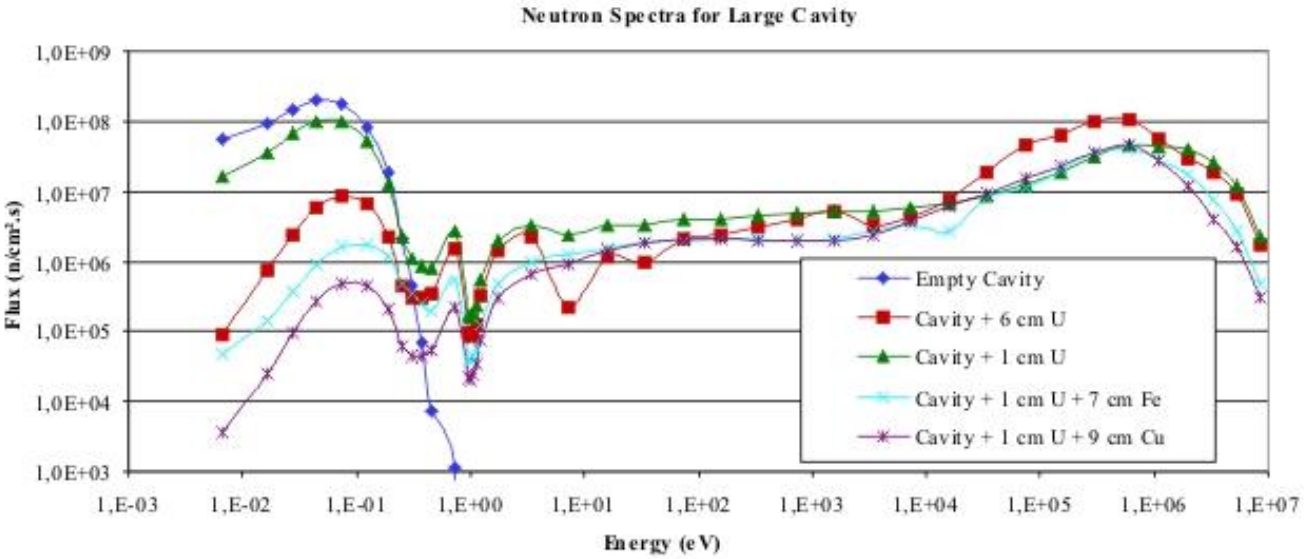

Fig.46 Neutron flux distribution as a function of the neutron energy in the central cavity of the BR1 reactor at SCK-CEN in Mol, Belgium. For the present work Empty Cavity has been applied. Source: [103]

Measurements with epithermal neutrons were carried out at the D3 facility in the HFR reactor of the Institut Laue Langevin, where an average neutron flux of ~5×10^6 $cm^{-2}s^{-1}$ can be obtained. The neutrons are extracted from the heavy water tank of the reactor, where a mixed neutron field is present. Fig.47 represents the measured and calculated neutron flux inside the heavy water tank as a function of distance from the core of the reactor. (Lines denoted with Ageron are calculation performed by P. Ageron.) [104]. For the present work ~4.69×10^6 $cm^{-2}s^{-1}$ average neutron flux in the measurement position has been established with gold foil activation method.

Fast neutron measurements with 4H-SiC diode detectors are carried out in the Neutron Laboratory of TU Dresden. Three neutron sources have been used:

- 14 MeV neutrons supplied by the DT-neutron generator with an average DT-neutron yield of 4.04×10^{10} - 5.25×10^{10} s^{-1} during the measurements
- $1.8*10^{11}$Bq AmBe isotope source with a neutron yield of $2*10^7$ s^{-1} and
- Cf-252 150 MBq isotope source with a neutron yield of 2.15×10^7 s^{-1}. Their neutron spectra are shown in Figs.48-51.

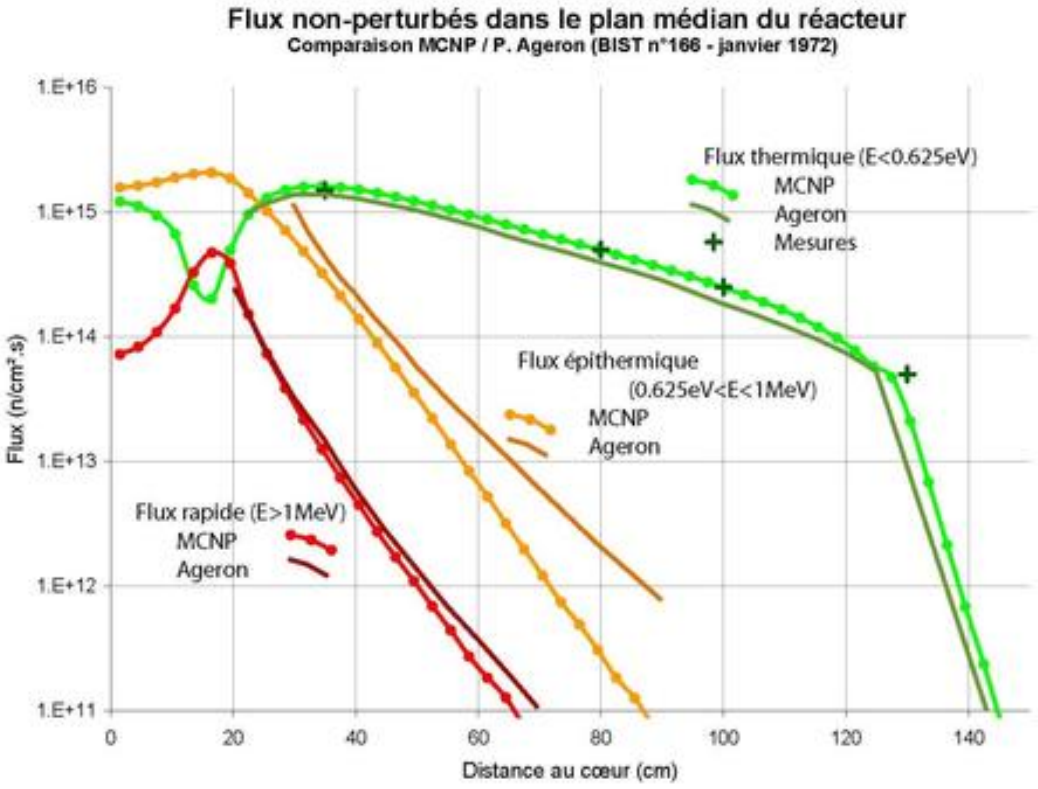

Fig.47 Neutron flux as a function of the distance from the core inside the heavy water tank of the HFR reactor at ILL in Grenoble, France. The green, brown and red lines represent the thermal, epithermal and fast neutron flux values. Source: [104]

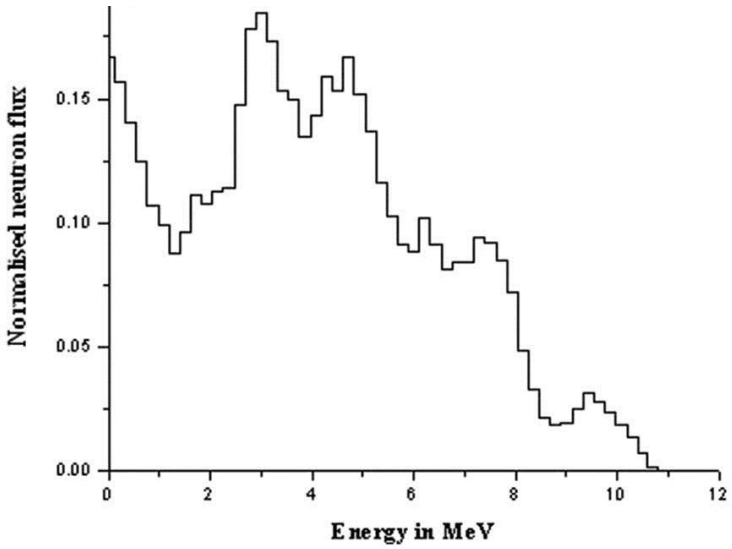

Fig.48 - ISO 8529-2 recommended ^{241}Am-Be neutron spectrum as a function of the incident energy. Source: [105]

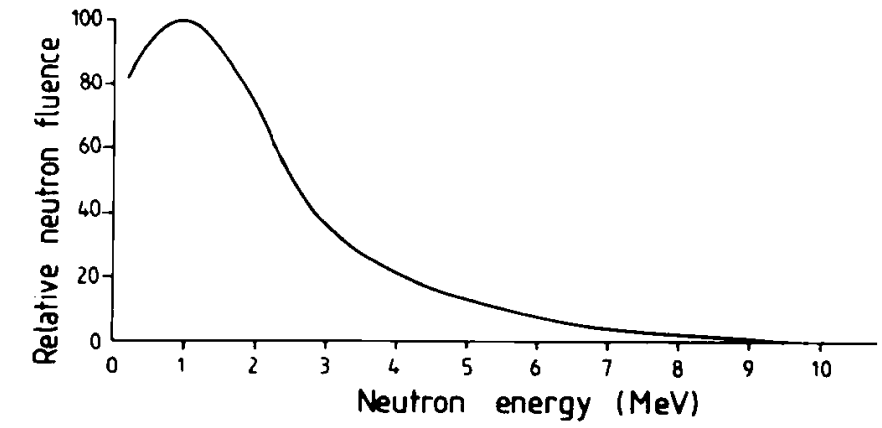

Fig.49 - Relative neutron fluence emitted from spontaneous fission of ^{252}Cf. Source: [106]

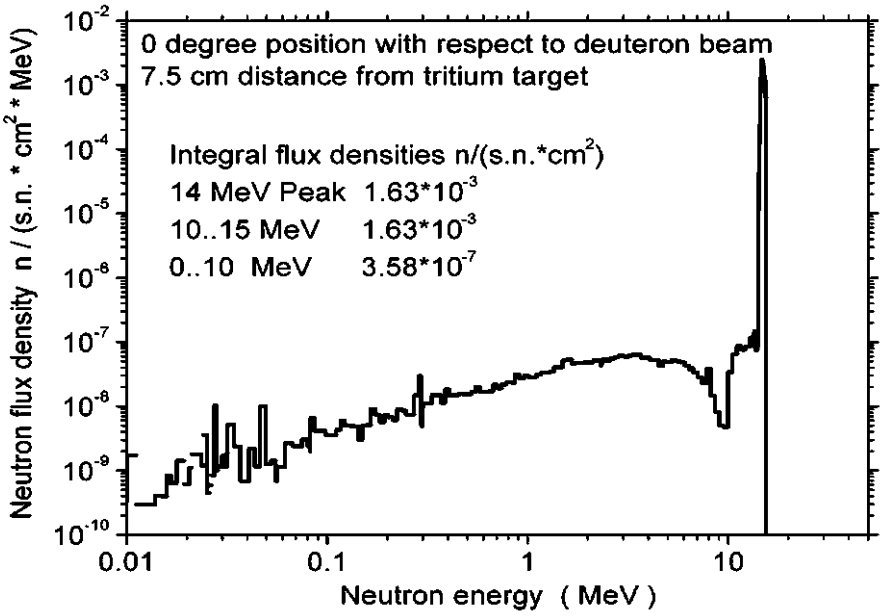

Fig.50 – Calculated neutron flux density as a function of the neutron energy in flight direction (0 degree) of TUD-NG. Source: [107]

The neutron flux in the SiC diode container box is measured at room temperature with niobium activation foils. This flux value is related to the count rate of a silicon detector (later in the text referred as NG monitor) for the α particles associated with the DT reaction in the tritium target. At elevated temperatures the neutron flux is calculated from the recorded count number of the alpha counter. The signal of the SiC diode detector is normalized to the change relative to the test performed at the lowest neutron flux.

7. THERMAL NEUTRON TESTS WITH SiC DIODE DETECTORS AT ROOM TEMPERATURE

In order to develop an appropriate semiconductor sensor to detect both fast and thermal neutrons a well-defined sensor geometry is needed. Detection of thermal neutrons is possible by introduction of an additional converter material into the sensor, since pure SiC does not produce electric signals from thermal neutrons. Materials with large nuclear cross sections for charged particle emitting reactions at low neutron energies, as boron-10 and lithium-6 are primary candidates for such a converter. In the present work sensors with boron-10 converter layer have been tested, which emits α- and ^{7}Li-ions unther thermal neutron irradiation:

$$^{10}B + n \rightarrow {}^{4}He\ (1.47\ MeV) + {}^{7}Li^{*}\ (0.84\ MeV) + \gamma\ (0.48\ MeV)\ , \tag{27}$$

$$^{10}B + n \rightarrow {}^{4}He\ (1.77\ MeV) + {}^{7}Li\ (1.015\ MeV). \tag{28}$$

The ^{4}He- and ^{7}Li-ions are stopped inside the crystal material due to ionization loss, in which they are producing electron-hole pairs. If these ions are able to enter the sensitive depleted volume of a diode detector, they can generate a detectable current signal. By implementing semiconductor diode detectors the converter layer should be localized very close or inside the diode to allow for the highest detection probability of the initial neutron. Due to the short mean free path of charged particles, only a few μm with energies of few MeVs in the solid material, both the position of the converter layer and also the concentration of the implanted boron-10 must be optimized. The short ranges facilitate small-scale detector design, as well.

Reactions occurring at low incident neutron energies result in isotropic outgoing particles in a 4π steradian. Considering a reference point „O" as a location of such a reaction as indicated in Fig.51, the ion starting from it will deposit energy inside a spherical volume with a radius equal to its path length and stops at the sphere's surface. Except D4 sensors, all studied diodes have ^{10}B-ion doped layer outside the sensitive volume of the diode. Events, which take place on the spherical cap lying inside the sensitive volume/depleted region of the diode can be detected, as R2 and R3 in Fig.51. Energy deposition outside the volume or with a radius less than the distance to the active volume (R1), will not contribute to the signal. Ions with larger ion masses and bigger sizes produce more crystal defects along their path in the crystal, thus inside the active volume as well. Therefore, ^{7}Li-ions leaving the above mentioned two reactions contribute to the diodes deterioration more significantly than the lighter and smaller α-particles; however, their mean free path is shorter than the path of alphas. The difference in the generated damages by the two light ions was investigated with a SRIM/TRIM calculation, which models the penetration of helium-4 and lithium-7 nuclei with the energies from Reaction 1 (Eq.27) into silicon-carbide. The simulation exhibits a vacancy number per ion of 140.5 for the ^{4}He (1.47 MeV) and 318 for ^{7}Li (0.84 MeV). Hence ^{7}Li exhibits two times more damage events than helium ions by the Reaction 1 in the silicon-carbide crystal.

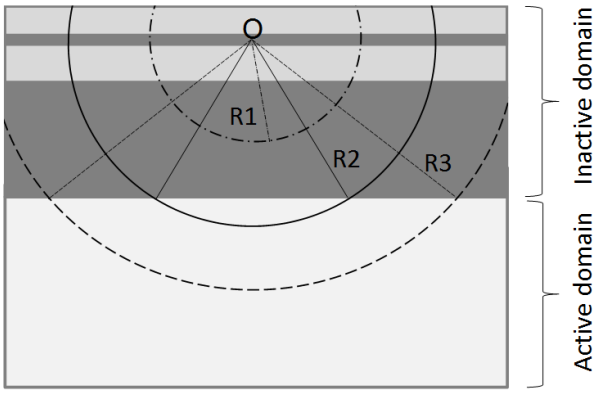

Fig.51 – Spherical cups determined by the secondary ions path range inside a diode detector. The "active domain" represents the sensitive volume of a diode detector, while the "inactive domain" the layers from where no detector signal can be collected.

In measurements at high thermal neutron flux, the proper size of the detector is crucial, since it determines the temporal signal resolution. The higher the flux the higher the probability is to encounter pile-up effects. This leads to the loss of counts. In an extreme case the measurement electronics is not capable of resolving the signal of large number of counts occurring simultaneously and a current or voltage pulse corresponding to the collective energy of the detected particles may appear on the output signal of the preamplifier. Therefore, in application associated with a very high neutron flux, sensors with small sensitive volumes and lower sensitivity become of interest.

Four geometries of ^{10}B-implanted 4H-SiC diodes are studied in thermal neutron irradiation. Table III. lists the average projected stopping ranges of α-particles and lithium ions inside the depleted region for the diodes investigated. The starting positions of the projected ions are the mid-positions of the boron implanted layers. These calculations were carried out by using SRIM software. In Table III. the "Ratio" columns mark the ratios of the surfaces of sphere cups lying in the sensitive layer relative to the whole sphere surfaces drawn by the ions. Due to the large distance between the boron implanted layer and the pn-junction, the D1- type diode can detect only α-particles from the two reactions. In contrast the D3 geometry diodes allow measuring both α-particles and lithium ions. In case of D2 diodes almost exclusively α-particles have sufficient energy to generate signal in the detector, the contribution of ^{7}Li is minor. It is important to note that Table III. lists idealized values in case of the projected situations. Lower energy contribution exhibits by the ions entering the sensitive volume under an angle, which differs from the perpendicular direction relative to the sensor surface (as it is also demonstrated with SRIM/TRIM calculations in Fig.52-a and-b).

Figure 52-a and b illustrate, how the path range inside the sensitive SiC volume shortens with the increasing incident angle. On the right side of Fig.52-a and b the ionization rates are depicted in the different diode layers decreasing with the larger incident angle. In Fig.52-c the recorded pulse height spectrum is shown as a function of the deposited energy by ionization loss inside SiC in thermal neutron irradiated D3 diode. The effect of different energy deposition in the sensitive zone of the sensor can be observed. Particular energy loss of ions happens inside the non-sensitive layers before they enter the sensitive zone. From that follows that no full-energy peaks can be recorded using a sensor with thermal neutron converter material placed outside the sensitive region.

TABLE III.
PROJECTED RANGES OF α- AND ^{7}LI IONS INSIDE THE SIC DETECTOR

	D1 diode		D2 diode		D3	
	Range [μm]	Ratio	Range [μm]	Ratio	Range [μm]	Ratio
In the region of Al-metallization						
Thickness between SL and BL	**3.53**		**1.78**		**0.39**	
1.47 MeV α range	3.78	3.31%	3.56	25.04%	3.37	44.22%
1.77 MeV α range	4.53	11.04%	4.31	29.40%	4.12	45.28%
0.840 MeV Li range	2.05	0.00%	1.83	1.54%	1.59	37.75%
1.015 MeV Li range	2.35	0.00%	2.06	6.82%	0.39	39.21%
In the region of SiO_2-layer						
Thickness between SL and BL			**2.21**			
1.47 MeV α range			3.56	19.00%		
1.77 MeV α range			4.31	24.41%		
0.840 MeV Li range			1.90	0.00%		
1.015 MeV Li range			2.11	0.00%		

SL – sensitive layer,
BL - boronized layer,
Ratio - percental ratio of the sphere cup with a radius of projected range of reaction products which reach the sensitive volume of the diode related to the whole sphere surface described by a certain residual ion with the same radius

7.1 Testing of the D1 diode geometry

First tests with 4H-SiC detectors irradiated with thermal neutrons have been performed with D1 geometry (Fig.17 in 4.1) with and without ^{10}B-converter layer. These preliminary tests serve as a reference to further investigations and help to understand the diode's behavior and signal characteristics.

The diodes have been produced with three different surface areas. The biggest diode has a 5 × 5 mm^2, the medium sized diode 5 × 2 mm^2 and the smallest diode 2 × 2 mm^2 area. Furthermore, four different designs of the thermal neutron converter layers have been applied. Diodes without converter layer, only with ^{10}B-ion implanted layer, only with B_4CN on the top of the detector and both with ^{10}B-ion implanted and B_4CN layers were tested, the positions of the boron containing layers on the D1 diode are indicated in Fig.53. It has been tested, which converter construction could improve the thermal neutron detection ability and efficiency. These tests are performed with electronics Set-up 1 (see in 6.2.1).

Two types of the biggest 25 mm^2 diode are examined. Both of them are covered with a 120-140 nm thick B_4CN film converter layer on the surface of the detector and one type also has an additional ^{10}B-ion implanted layer inside the aluminum metallization. Almost no secondary particles from the B_4CN layer can reach the sensitive volume. The layer has been tested only during the first experiments and it is mentioned here because of the exact description.

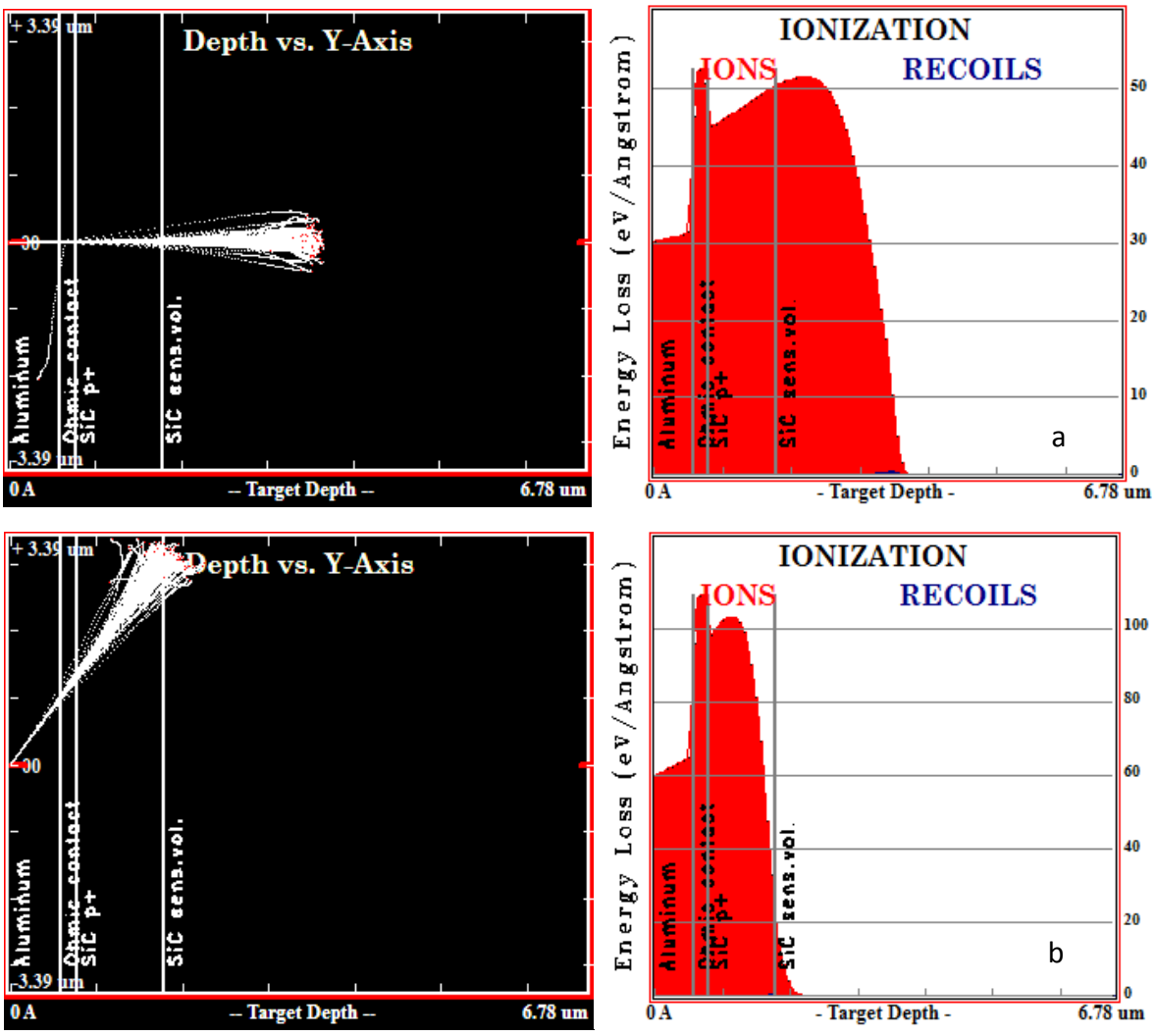

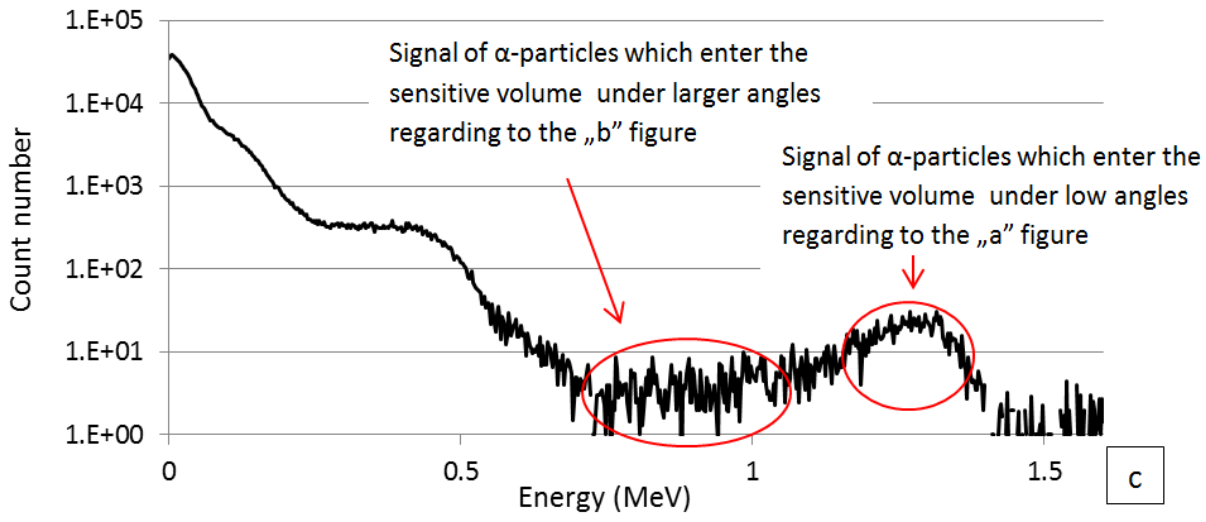

Fig.52 a-b – The SRIM/TRIM models of path and ionization of charged 1.47 MeV ^{4}He-nuclei in D2 type diode for 0°(a) and 60°(b) ion movement directions; c- Count number as a function of the deposited energy value in D3 diode measured in thermal neutron sprectum

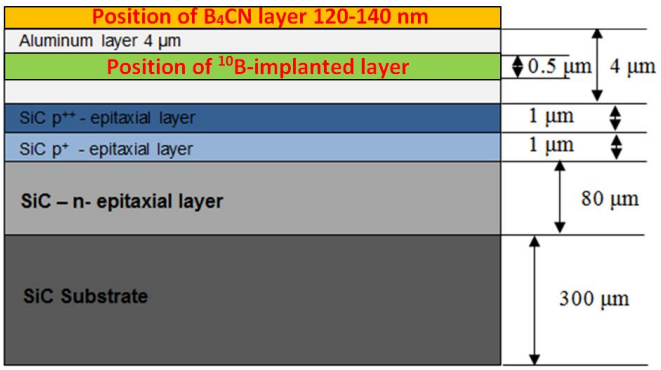

Fig.53 – Positions of the boron containing layers on the D1 type diode structure

The recorded pulse height spectra for measurement duration of 600 seconds (the most measurements have been carried out with 600 seconds collection time) are shown in Fig.54 and Fig.55. Because of the relatively large distance between the B_4CN neutron converter layer and the sensitive region, the diode supplied only with B_4CN converter film does not generate well-defined signal structures due to energy deposition of α-particles and ^{7}Li-ions. Diode implanted with boron could detect counts from α-particles. The resulting spectrum form has two plateaus, the first one from the α-particles of Eq.(27) (Reaction 1) is located in the lower energy channels, and the second one from Eq.(28) (Reaction 2) occupies the higher energy channels. A shift of the whole energy histogram to the higher energy channels at higher bias voltages occurs because of the larger energy deposition of the secondary α-particles in the thicker depleted region.

Signal of the medium size surface area diode with ^{10}B-ion implanted aluminum layer has been recorded for different bias voltages, see Fig56. The diode has been studied in a bias voltage range from 0 V to 130 V. A slight shift of the whole energy histogram and the plateau structures to the higher energy channels at higher bias voltage values is observed similar as in case of the bigger boron impanted diode; the α- particles starting from the reaction point and penetrating into the space charge region of the diode can deposit larger amount of their energy in the thicker sensitive volume at higher biases.

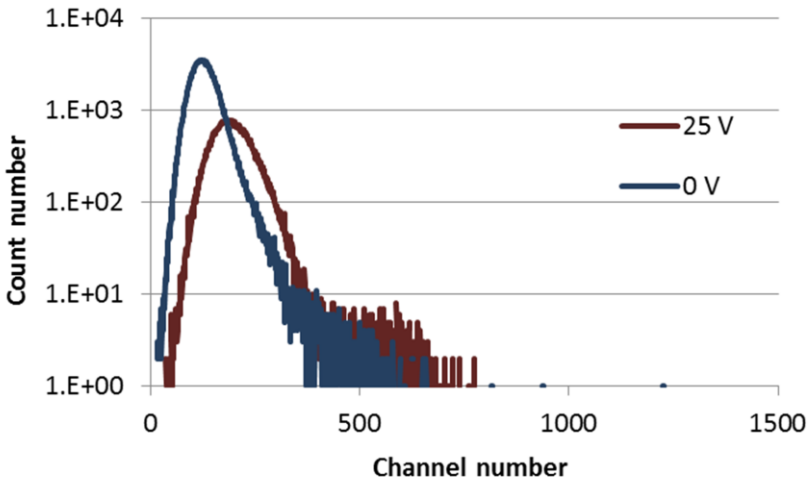

Fig.54 – Pulse height spectrum of the 5 × 5 mm^2 area D1 diode with B4CN converter film at two different bias voltages measured in a thermal neutron spectrum.

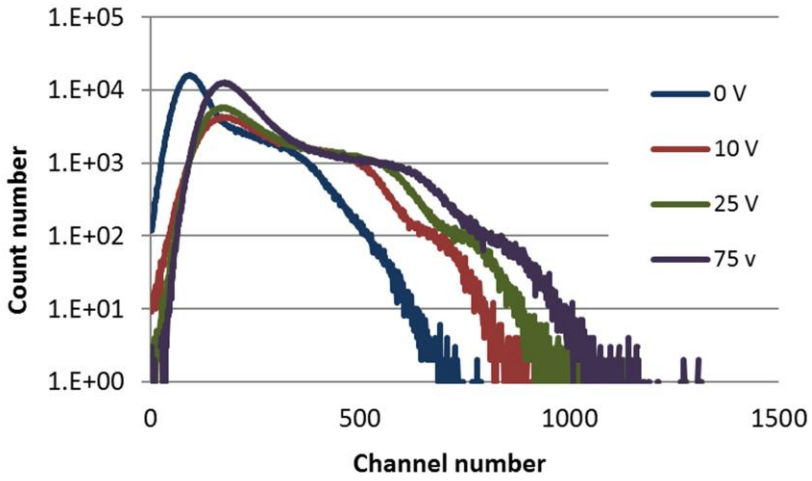

Fig.55 – Pulse height spectrum of the 5 × 5 mm^2 area D1 diode with B_4CN converter film and ^{10}B-implanted layer at four different bias voltages measured in a thermal neutron spectrum.

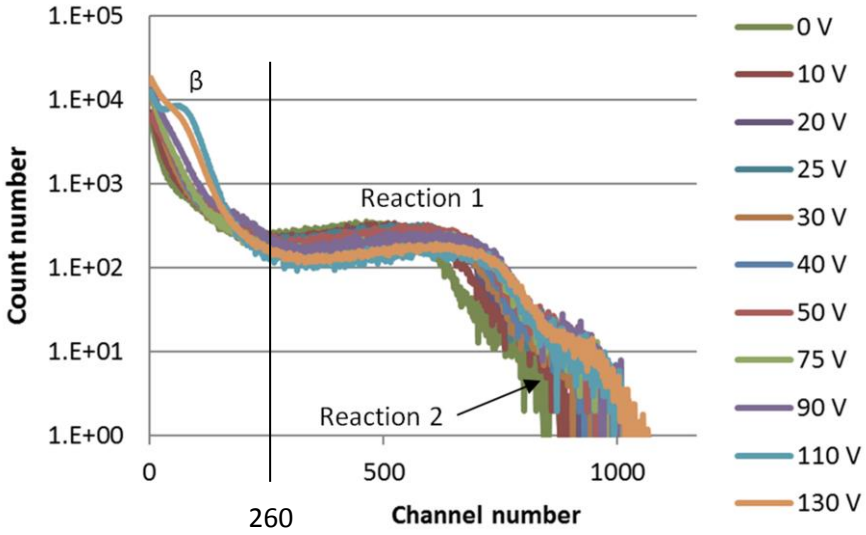

Fig.56 - Pulse height spectrum of the channel number of the 2 × 5 mm^2 area D1 diode with ^{10}B-implanted layer at different bias voltages measured in a thermal neutron spectrum.

An increased bias voltage yields a rise of the total count number for the whole pulse height spectrum, as shown in Fig.57. Furthermore, the integrated count number beyond the 260th channel (~0.5 MeV estimated) remains almost constant. The reason for this is that most of the signals below the 260th channel are generated by low energy events, of which number depends on the thickness of the depleted volume; these are the noise signal and signal of β- and photons, which can be collected in the whole depleted volume of the diode detector. Beyond this channel, most of the signal arises from α-particles, which are generated within the ^{10}B-implanted layer and have a specified range. If the depletion thickness stretches beyond this maximum range by increasing the bias voltage no additional events is recorded.

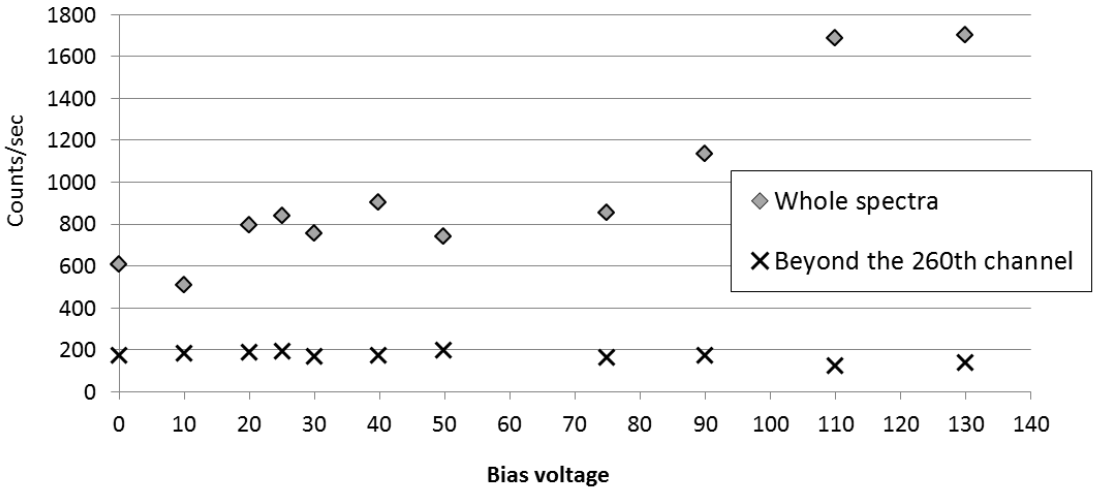

Fig.57 – Count rate dependence on bias voltage for all detector pulses and pulses caused by α-particles only for the medium sized (2 × 5 mm^2 area) D1 diode with ^{10}B implanted layer.

The smallest D1 diode is covered with a 120-140 nm thick B_4CN film as well as ^{10}B-ion implanted layer in the aluminum metallization. In Fig.58 the recorded pulse height spectra are depicted for thermal neutron irradiation. The diode exhibits a continuous count distribution in a wide energy range, which can be assigned to the energy deposition of α-particles from Eq.(27) (Reaction 1) and Eq.(28) (Reaction 2) starting from the metal contact. The structure in the lower energy channels indicated in Fig.58 by "β" are generated to a large extend by energetic β-particles released from the neutron reaction with aluminum of the sensor casing. For the smallest ^{10}B-implanted diode no shift of the pulse height spectrum at higher bias voltage values is observed.

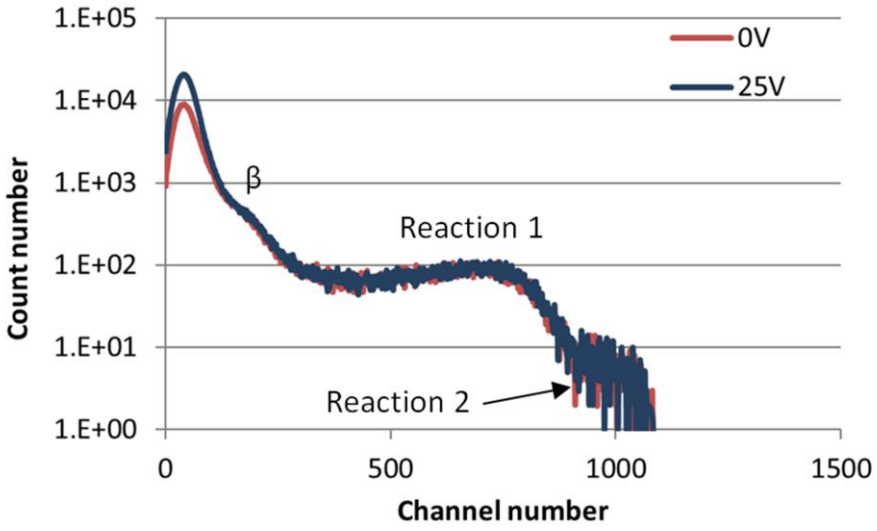

Fig.58 - Pulse height spectrum of the 2 × 2 mm^2 area D1 diode with B_4CN converter film and ^{10}B-implanted layer at different bias voltages measured in a thermal neutron spectrum.

Post experiment SIMS (Secondary Ion Mass Spectroscopy) measurements indicated that in the D1 diode ^{10}B-ions have penetrated from the aluminum contact into the SiC layer. This effect leads to an increased leakage current. During the diode fabrication process an annealing treatment has been applied following the ^{10}B-implantation step. Comparing the SIMS data of annealed and un-annealed diodes it has been demonstrated that in case of un-annealed samples the ^{10}B-ions do not penetrate from the aluminum layer in to the SiC layer. Leakage current measurements have shown leakage current density values of 10^{-9} – 10^{-8} Acm^{-2} before annealing and 10^{-4} – 10^{-3} Acm^{-2} after annealing for D1 diodes. The D1 diodes with smaller surface area have less leakage current than the bigger ones. Additional outcome is that the bigger diode, which produced a shift in the pulse height spectrum with the change of the bias voltage level, has the α-edge positions from the Eq.(27) and Eq.(28) in lower energy channels than in case of the smaller detectors, see in in Fig.59. It can be concluded that diodes with smaller surface have the lower leakage current and better charge collection efficiency even at lower bias voltage level.

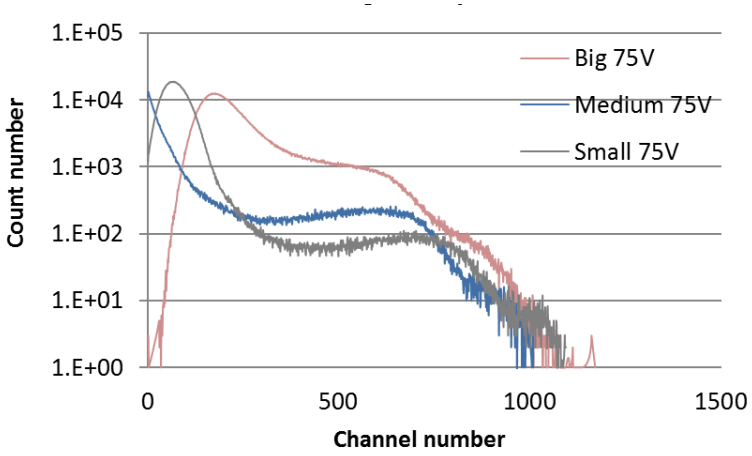

Fig.59 – Pulse height spectrum of the big, medium and small size D1-type SiC detectors with ^{10}B-implanted layer at 75 V biasing for 600 s measured in a thermal neutron spectrum.

7.2 Thermal neutron tests with the D2 diode detector

Further thermal neutron tests have been carried out with an improved D2 structure SiC diode applying only ^{10}B-ion implantation and a shorter distance between the neutron converter layer and the sensitive region of the diode (the sketch view of D2 diode is shown in Fig.60). Due to the shorter distance, larger amount of the secondary charged nuclei generated inside the boronized layer can be detected. The D2 type diode has two regions, both implanted with ^{10}B atoms at two different distances from the sensitive region. The doubled structure has been formed unintentionally during the diode preparation process. The depletion thickness for D2 geometry at -2.8 V built-in bias voltage (see Eq.(12)) is ~5.5 μm. This sensitive volume thickness overlaps the necessary volume, where ions starting from the ^{10}B doped layer can stop according to the calculated

projected ranges in Table III. Furthermore, the distances between the sensitive layer and the ^{10}B-implanted neutron converter layers are large enough to avoid most of the signal arising from the secondary ^{7}Li-ions. In Fig.60 the maximum path lengths of the secondary particles starting from the different boron containing layers are illustrated with red arrows.

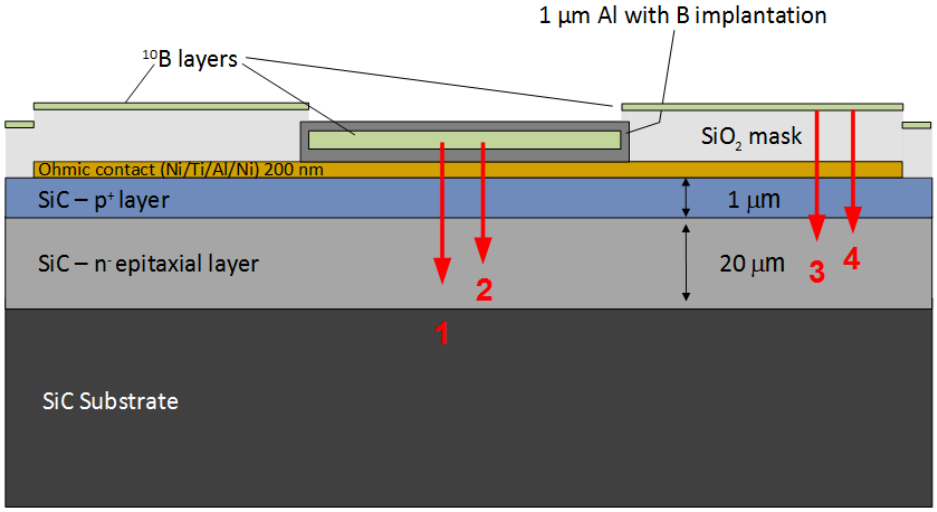

Fig.60– Sketch view of D2 diode (1- α-particle from Eq.28 from the Al-layer, 2- α-particle from Eq.27 from the Al-layer, 3- α-particle from Eq.28 from the SiO_2-layer, 4- α-particle from Eq.27 from the SiO_2-layer)

The signal structure expected to be obtained depends essentially on the layer structure of the sensor. Therefore it is described here in more detail. On SiC substrate wafer a rounded rectangle shaped diode is formed, see in Fig.61. On a 0.98 mm diameter whole rectangular surface (SiO_2 in figure) a 0.4 mm diameter ^{10}B-implanted aluminum metallization layer (M in figure) is realized and the rest of the surface is covered with ^{10}B-implanted SiO_2. Thereby, 83% of the diode surface is occupied by SiO_2 and only 13 % by aluminum. Due to the shorter distance of central boron implantation in the aluminum from the sensitive region a higher

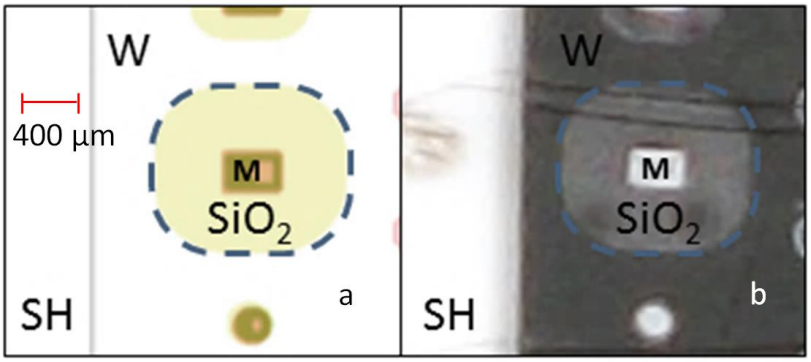

Fig.61-***a*** **-** Drawing of the mask's structure and; ***b*** **-** a photo about a realized D2 type diode. The dashed line marks the active diode area on the wafer (W) covered with ^{10}B-implanted SiO_2 layer (SiO_2) and with ^{10}B-implanted aluminum metallization layer (M). The wafer is attached by conductive glue on an alumina sample holder (SH).

energy deposition can be expected than by ions starting from the SiO_2. On the other hand due to the significantly larger size more events in the lower energy channels a likely to be detected, which arise from the ^{10}B in the SiO_2-layer.

A typical signal form recorded by the D2 detector is depicted in Fig.62. (A minimal external bias voltage, -3 V has been applied on the sensor to build the space charge region.) The measurement time is 5000 seconds. The signal domains indicated in Fig.62 denoted by roman numerals refer to individual reactions. The first domain "I" comprises to parts of the noise from the measurement electronics and to the not resolvable events below the noise level. The domain "II" is formed mostly by events depending on the bias voltage, photons, β-particles, fast Compton electrons, etc. originating from ^{28}Al decay. They scope also background radiation of the reactor. Furthermore, this signal section also incorporates counts generated by bias voltage independent events, such as low energy deposition of α-particles and ^{7}Li-ions as well as thermal neutron scattering events. Detailed analysis has been carried out to demonstrate that structure „III" is formed mainly by α-particles emitted from the SiO_2-layer of the diode and contain also counts of lower energy ^{7}Li-ions and α-particles released by nuclear reactions from the boron implanted metal layer. This latter is supported by two observations:

- In early measurements by D1 detectors with a single layer of ion-implanted ^{10}B nuclei, the signal structures have been generated by background β-particles, α-particles according to Eq.(27) and Eq.(28) and noise signal, while no additional distinct plateaus in the histogram have been observed, see in Fig.56 and 58.

- Complementary Monte Carlo simulations for the D2 detector type predict a structure "III" signal shape within a characteristic energy threshold as indicated in Fig.63. Therein, also the individual contributions of the layers to the collective signal are analyzed.

The structure "IV" occupying the higher energy domains is caused by α-particles from the Eq.(27) in the metallic layer. The last structure, "V" is formed by α-particles from the Eq.(28) originating from the aluminum metallic layer. "IV" and "V" cover the higher energetic α-particle signal from the Eq.(28) from the boron implanted SiO_2 layer.

Geant4 Monte Carlo simulations depicted in Fig.63 allow for a more detailed analysis of the signal structure of the pulse height spectra. The energy thresholds due to α-particles arising from the Eq.(27) from SiO_2 layer and from the Eq.(27) and Eq.(28) from the aluminum layer can be clearly identified in the "Collective signal". ^{7}Li-ions are detected only from the boron implanted aluminum layer, with a maximum energy deposition of ~70 keV. However in this energy domain the signal overlaps events caused predominantly by β-particles in the measurements, which is marked by "II" in the computed spectrum. Based on the calculations, no events from ^{7}Li-ions originating from the SiO_2layer are observed. Also no changes due to the energy deposition of ^{7}Li-ions are observed in the high energy tail of the histogram. Separated simulations are performed with thermal neutron-, γ- and with β sources.

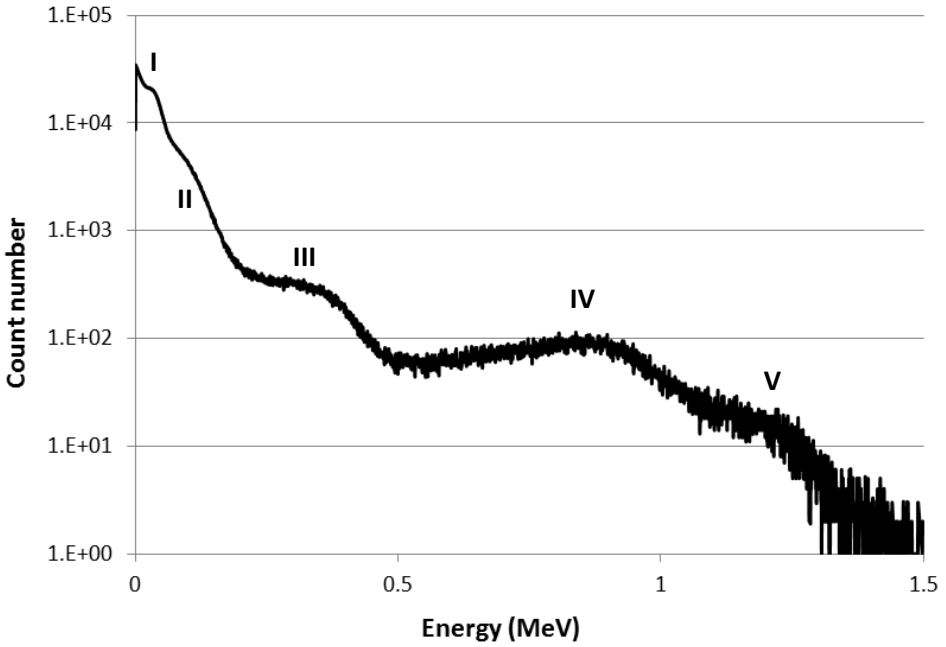

Fig.62 – Count number as a function of the channel number of D2 diode detector in thermal neutron spectrum. Origin of signal parts: „I"- noise and low energy events; „II"- β- and γ-particles; „III"- α-particles from Eq.(27) in the SiO_2 layer; "IV"- α-particles from Eq.(27) in the Al-metallization layer (see in Fig.40); "V" "- α-particles from Eq.(28) occurred in the Al-metal layer (see in Fig.40); "- the signal of α-particles from Eq.(28) in the SiO_2 layer are covered by "IV"

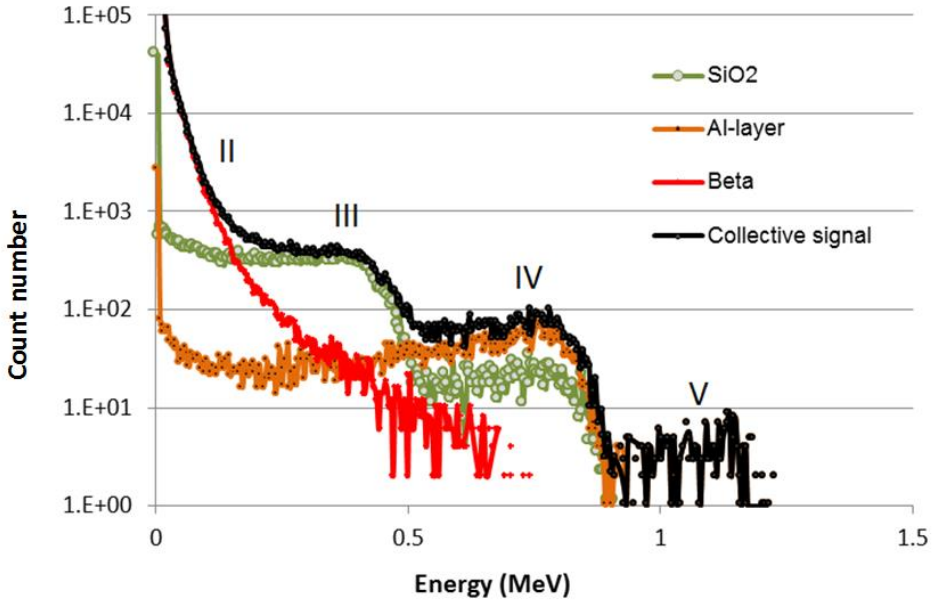

Fig.63 – Computed signal of D2 diode detector using Geant4. Origin of the signal parts: „III"- α-signal from Eq.(27) in the SiO_2 layer; „IV"- α-signal from Eq.(27) in the aluminum layer; „V"- α-signal from Eq.(28) in the borated aluminum layer. The α-signal from Eq.(28) arising due to the reaction within the SiO_2 layer is overlapping with „IV", as in case of the related measurement. In the „Collective signal" an additional effect of β-particle energy deposition is considered. The β-signal „II", serves an initial upsurge in the low energy channels.

To estimate the photon and β-particle flux inside the aluminum sample holder inside the central cavity of the BR1, an MCNP [108] computation has been conducted. The normalized flux spectra obtained by this are used as input in subsequent Geant4 calculations. Fig.64 illustrates the simulated energy histograms with β (from the activated aluminum sample box) and photon (generated inside the reactor) sources for 500 000 initial events. The corresponding collected count number values are in total about ~3800 for photon and ~210 000 for β irradiation. With respect to the photon-signal, a negligible energy deposition is obtained in the low energy range with a peak located around 10 keV. This is attributed to the thin active volume of the detector. Here, a much thicker detector would be necessary to deposit the energy of the charge neutral photons via electrons. Hence in this context no signals emerging from photons are considered. Due to the ~55 times higher generated event numbers caused by electron irradiation located in higher energy threshold between 10 and 300 keV, the β-signal is simulated during the signal analysis.

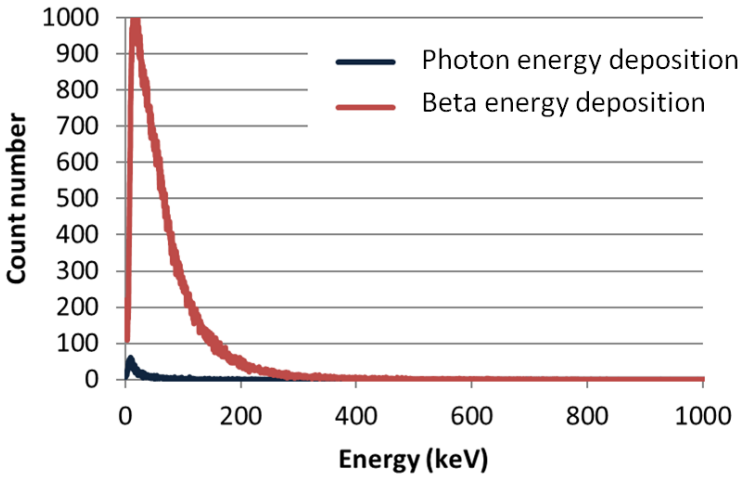

Fig.64 – Geant4 simulation of energy deposition of photons and β-particles for the BR1 reactor configuration in D2-type SiC diode detector

The applied geometry model for simulations is based on D2 geometry considering layer thicknesses and detector form. Because of the different surface areas of the studied diodes representative diameters have been used; 1 mm has been taken as diameter of the entire diode and 0.35 mm of the aluminum surface. Separated simulations are performed for the SiO_2 and aluminum layers containing the ^{10}B-layer. To obtain a "Collective signal" ^{10}B atoms have been assumed in both layers and also signals of β-particle events from the ^{28}Al decay. To the simulations a 200 nm thick ^{10}B-layer is assumed with ^{10}B concentration of 60%. The high concentration has been necessary because of the limited primary event number of Geant4, which is much less than the number of impinging neutrons in the real measurements; using the real doping concentration (^{10}B content of ~0.15% in detector's material) generates negligible recorded event number.

Further pulse height spectra have been recorded for different bias voltage values with three different D2 diodes using 600 seconds measurement time. The graphs are depicted in Fig.65 a-c. All three diodes

produce the same signal shape and count amplitude in the thermal neutron irradiation. No significant differences in the character of the histograms are observed. Compared to the measurement at -2.8 V built-in bias voltage, the spectra recorded at higher external bias voltage levels exhibit a slight shift to higher energy

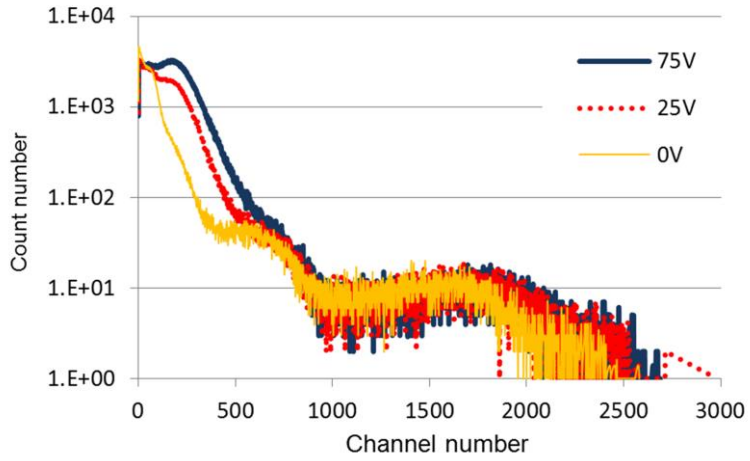

a (Sample #4)

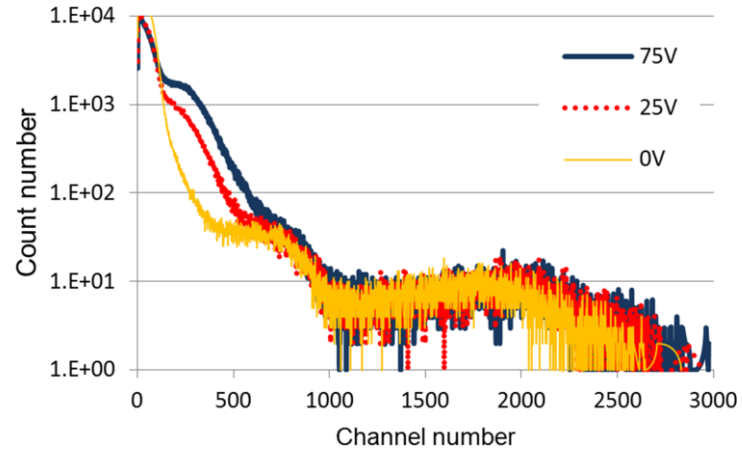

b (Sample #5)

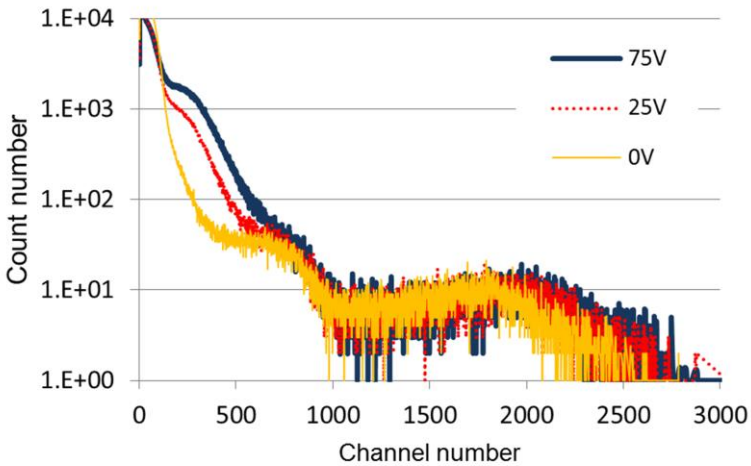

c (Sample #6)

Fig.65-a,b,c - Count number as a function of the channel number of three D2 diode detectors ^{10}B-implanted layer at different bias voltages measured in a thermal neutron spectrum.

channels. This effect appears because of the partial energy deposition without external biasing, in other words the thinner sensitive volume at zero bias voltage than the path range of secondary α-particles in SiC. Furthermore, the implantation profile of the pn-junction is not perfect planar and the implanted ^{10}B-nuclei have a concentration distribution within the aluminum normal to the interface. Beyond ~10 V absolute bias voltage value, signal parts arising from heavy charged particles are not influenced significantly by the external bias voltage due to the shorter stopping range of the generated ions than the distance between the reaction place and the bottom of the depleted region.

Fig.66 illustrates the collected count number values for three different diodes above the 1080th energy channel (0.5 MeV estimated deposited energy from amplification of CAEN A1422 preamplifier). Exceeding this energy domain all the detected events can be exclusively originate from charged ions released by nuclear reactions in the boronized layer. Due to the sufficiently large depletion, the collected counts are not significantly influenced by additional biasing at more than 10 V reverse bias voltage value. The relative differences normalized by the total count number exceeding 10 V bias above ~1080th energy channel are less than 3.47%. If the bias voltage falls below 10 V the relative difference increases to 8-13 %. This effect is caused by the above mentioned partial energy deposition.

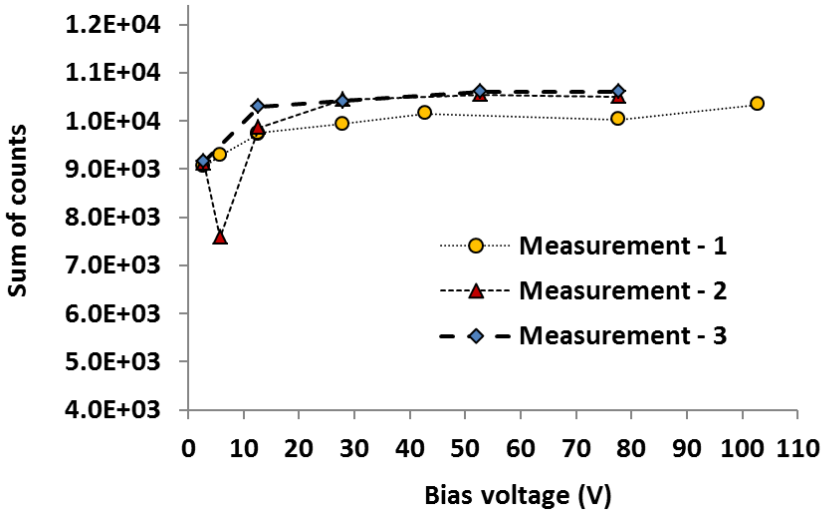

Fig.66 – Collected count number in the energy channels above the ~1080th energy channel a function of the bias voltage, recorded with three different D2 diode detectors in a thermal neutron spectrum.

In the low energy channels up to the ~600th energy channel, a well-defined signal structure is observed (marked with "II" in Fig.62). The signal height and count number of this structure increases with higher bias voltages, in other words with the volume of the depleted region. This indicates that this signal part is generated not exclusively by the energy deposition of α-particles and ^{7}Li-ions in the ^{10}B-implanted layer. They can deposit all energy inside the active volume of the diode, at least at higher biasing. Therefore, the bias dependent part of the counts can be attributed to external photons and β-particles, which have a longer

mean free path in the material. As shown in the Figs.65-a, b and c, the bias voltage dependent signal overlaps a part of the bias-independent signal (marked with "III" in Fig.62), which remains pronounced in the measurements performed up to 25 V bias voltage with a significant count drop exceeding the ~800th energy channel. For higher voltages, this bias independent signal part is masked by the bias-dependent signal and includes a constant amount of counts.

The depletion width of a diode has a linear correlation with the square root of the bias voltage value, as it is shown in Eq.(15). Ionizing radiation as β-particles from outside the sensor also generates counts with the same dependence on the bias. In Fig.67 the sum of the collected counts between the channels ~300 and 1000 is shown as a function of the square root of the applied absolute bias voltage, for the three D2 geometry diodes, which exhibits this linearity for bias voltages from 3 V to 40 V. At 40 V bias voltage the depletion reaches the interface of the 20 μm thick n-type epitaxial layer and the substrate. If the applied bias voltage is higher than required for the full depletion, the count number dependence on the bias voltage saturates.

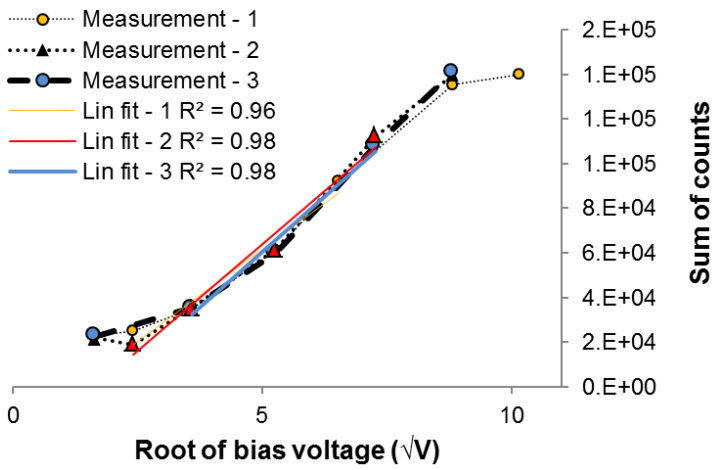

Fig.67 - Collected count number values in the energy channel region 300-1000 (~ 0.14-0.5 MeV estimated from amplification of the preamplifier) as a function of the square root of the absolute bias voltage in the range from 3 V to 40 V.

Measurements performed at built-in bias voltage have a higher count rate than predicted by linear fitting due to the offset caused by signals arising from heavy ions and neutron scattering events depositing small energy in the thin sensitive layer of the diode. The high energy secondary ions starting their movement near to the pn-junction cannot deposit all their energy inside the partially depleted volume at built-in bias. This volume can be thinner than the path range of these ions, thus the count rate in the low energy channels further increases because of the partial energy deposition.

The low energy tail signal part is studied by means of short term measurements to identify its origin. During the shutdown of the BR1 reactor 60 second tests are carried out. Signal parts arising from prompt events, as energy deposition of α- particles, ^{7}Li-ions, thermal neutron scattering events and Compton

scattering events from prompt photons immediately disappear in the absence of thermal neutrons in the central cavity of the reactor. The reactor power has been at 350 kW for minutes before the final off-state. In Fig.68 the signal count curves recorded in the 1st and 2nd minute depict the signal during the stable 350 kW reactor operation. In the 3rd minute the reactor is switched off which is reflected by a significant signal drop recorded in the 4th minute. The jump is caused by the disappearance of direct neutron irradiation. From the 4th minute the count number decreases exponentially in time, as illustrated by an exponential fit in Fig.69 based on one minute intervals. Half-life time ($T_{1/2}$) values can be calculated from the indices of the fitted exponential function and from measurement times which are $T_{1/2}$ = 2.46 min between the 4-9th minute and $T_{1/2}$ = 2.61 min between the 9-25th minute. The sensors are mounted in an aluminum box with 2 mm wall thickness, where γ- and β-particles are generated during ^{28}Al decay with $T_{1/2}$ = 2.25 min after neutron irradiation. This contributes

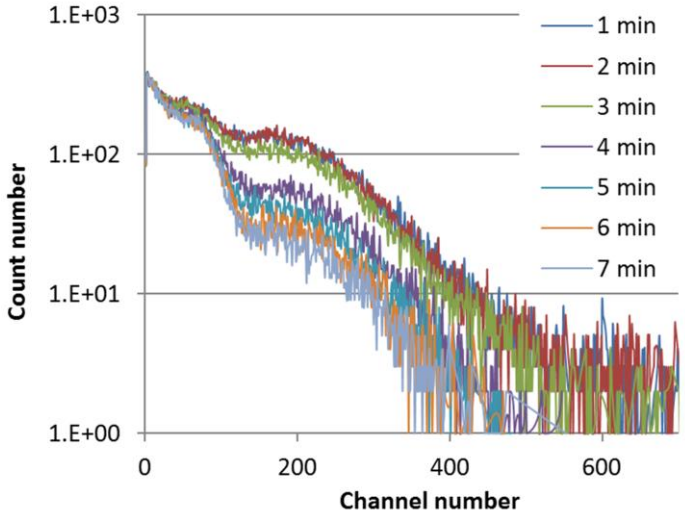

Fig.68 - Low energy signals occured by prompt events, which immediately dropped in the lack of neutrons (after the 3rd minute, when the reactor was completely swiched off); the different decay processes around the sensor lead to a continuous decreasing signal (from the 4th minute)

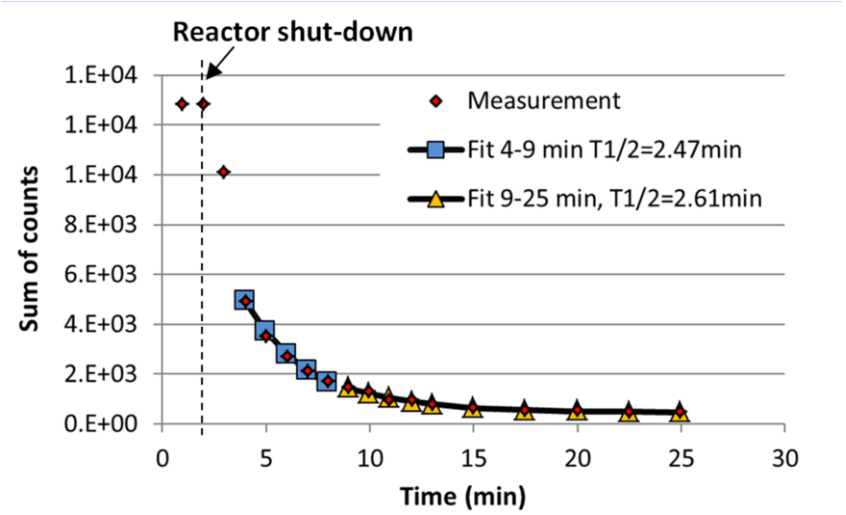

Fig.69 - Exponential fitting of the decreasing collected count number from the 4th minute, after the reactor's shut down

to the long term signal. Additional counts may be devoted to γ-photons of short lived fission products from the uranium fuel of the reactor, which also influence the signal.

7.3 Thermal neutron tests with the D3 diode detector

A cross sectional cut of the D3 diode is shown in Fig.19 in 4.3. The average 0.2 μm thick ^{10}B-ion implanted layer is located inside the p^+- layer of the 4H-SiC diode under the Ni/Ti/Al/Ni ohmic contact. The distance between the mid of the neutron converter layer and the pn- junction is ~0.3 μm. Therefore, D3 type diode is able to detect both α-particles and ^{7}Li-ions generated in the neutron converter layer. Due to the implantation profile, D3 diodes require several times higher bias voltage than the D2 diodes. According to Eq.(15) the maximum 15 μm depletion of the n-type epitaxial layer can be achieved at ~630 V.

Fig.70 shows the signal of D3 diode recorded at -250 V bias voltage (~9.5 μm space charge region thickness) with 5000 seconds measurement time in comparison with the D2 sensor (-25 V bias voltage, 600 seconds integration time) in order to demonstrate the difference between their signal. Here is worth to mention that the main differences between the two sensors are the thickness between the boronized layers and the sensitive region and the extra SiO_2-layer in case of D2-diode. The number of channels of the histogram is re-binned from 2^{14} (due to the 14 bit system of CAEN DT5780) to 3000 to make better visible the low count rate effects.

Structures in Fig.70 signed with roman numerals from I to VI are attributed to their origin, as noise, γ- and β-particles, ^{7}Li-ions and α-particles from reactions specified above in Eq.(27) and Eq.(28), according to the caption under the picture. The explanation is supported by complementary Geant4 Monte Carlo simulation, which is depicted in Fig.71. The simulation has been performed in the same way as in case of the D2 detector above applying the layer structure of D3 diode. The origin of counts at dedicated energies arising from α-particles and ^{7}Li-ions can be clearly identified. The experiments exhibit significant higher count rates in the energy domain, where the counts from ^{7}Li ions (III, IV) are expected than emerging from α-particles, while the simulation predicts marginal higher count rates by α-particles than those by ^{7}Li-ions. This difference is attributed to the non-comprehensive description of the β-radiation from the aluminum sample holder and γ-background in the BR1, which can cause an increased count rate in the same energy domain as ^{7}Li ions (III, IV), but it could not be found a satisfactory explanation to the phenomenon, thereby it cannot entirely be built-in to the simulations. To the calculations only approximations can be applied as the signal ratio of the α- and ^{7}Li-ion signal and their energy spectra. The measurements and simulation have proven that pulse height spectrum with more energy edges can be recorded with D3 diode than with D1 or D2 during thermal neutron irradiation. This effect enables more reference points for a spectroscopic use.

Fig.72 illustrates the recorded pulse height spectrum at different bias voltages. The secondary ions generated inside the boron layer have a longer stopping range than the thickness of the

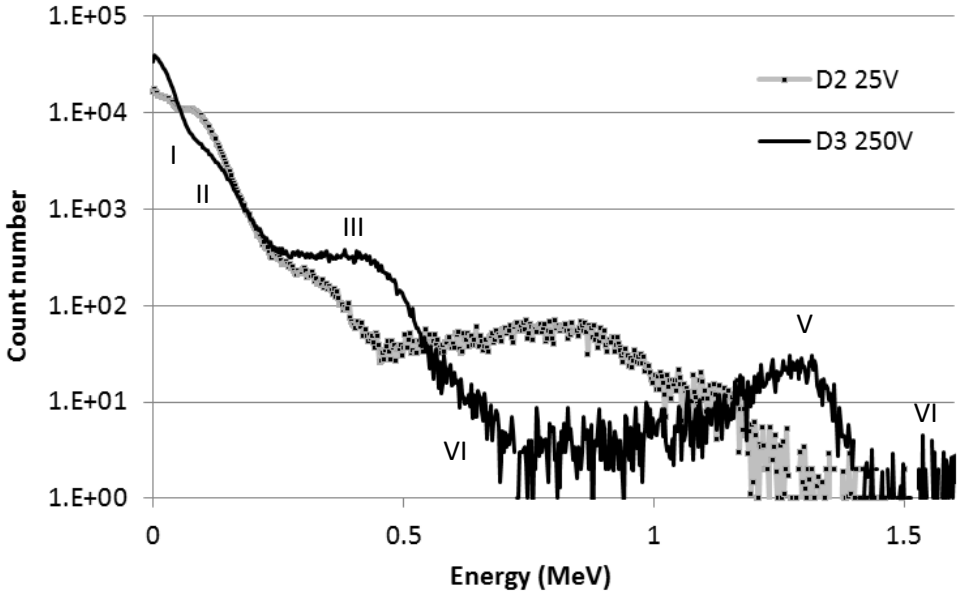

Fig.70 – Pulse height spectra of D3-type detector in thermal neutron spectrum compared to the D2 detector (in gray). Origin of the signal parts: "I"- signal of electronic noise and events below the noise level; "II" - γ- and β-particle events; "III" and "IV"- lithium signal from Eq.(27) and Eq.(28);"V" and "VI"- signal of α-particles from Eq.(27) and Eq.(28), respectively.

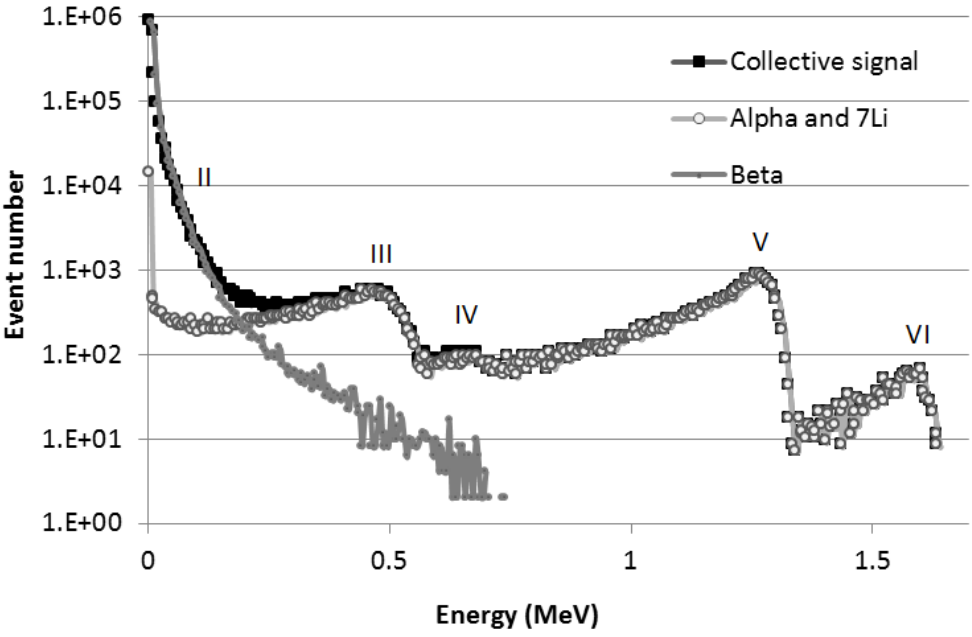

Fig.71 – The simulated signal of D3-type detector with thermal neutrons. Origin of the generated signal parts: "II" - β-particle events; "III" and "IV"- lithium signal from Eq.(27) and Eq.(28);"V" and "VI"- signal of α-particles from Eq.(27) and Eq.(28).

depleted volume at low biasing levels, according to Table III. A shift of the whole spectrum to the higher energy channels appears at higher bias voltages, which indicates increasing charge collection efficiency.

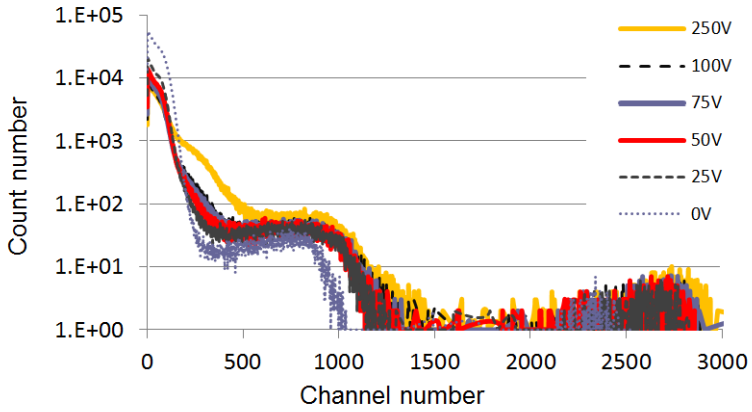

Fig.72 – Pulse height spectrum of the channel number of D3-diode at different applied bias voltage values measured in a thermal neutron spectrum.

7.4 Thermal neutron tests with the D4 diode detector

Finally measurements with D4 diode detector (in Fig.20 in 4.4) are performed. The pn-junction is realized by the implantation of the thermal neutron converter of ^{10}B-ions. Thus the boronized layer has a dual role. The D4-diode is a novel detector design; therefore, further developments are necessary to decrease high leakage currents, which impact measurements with thermal neutrons.

The recorded pulse height spectra of the D4 sensor at different bias levels are shown in Fig.73. Compared to the results obtained with other sensor geometries, a shift of the whole energy histograms to the

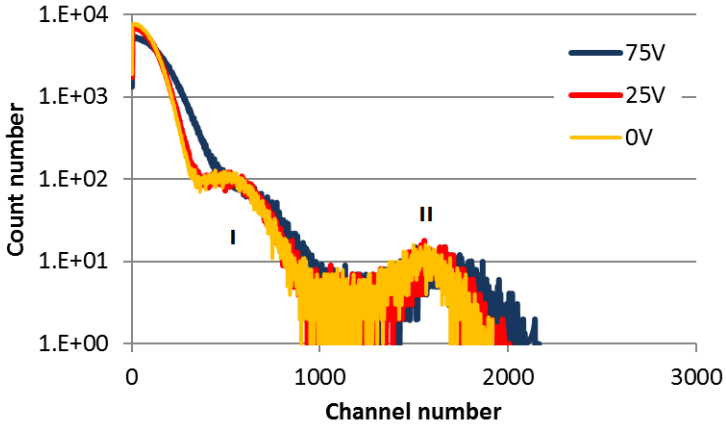

Fig.73 – Pulse height spectrum of D4 diode detector at different applied bias voltage values measured in a thermal neutron spectrum.

lower energy channels can be observed. However the distance between the ^{10}B-nuclei and the space charge region is reduced to zero. The two structures, marked in the figure with "I" and "II" arise from energy deposition of α-particles and ^{7}Li-ions generated in the two reactions Eq.(27), Eq.(28) between thermal neutrons and ^{10}B atoms, but more details about the signal structure could not be assigned to individual reactions.

7.5 Life-time considerations of thermal neutron detection with SiC detectors

Fig.74 shows the count rate values per cm^2 for the investigated diodes at a level of 7 × 10^8 s^{-1}×cm^{-2} thermal neutron flux including all the energy channels on the recorded pulse height spectra. The sample numbers designates the samples from Table IV. D3-type detector set-up exhibits large variations. The results indicate that the highest count number can be obtained with D2 and D4 type detectors applying the same large surface area. The high count number per square centimeter for the D4 detectors is attributed to the short distance between the ^{10}B-implanted layer and the sensitive volume of the detector, although the leakage current of these sensors is quite high.

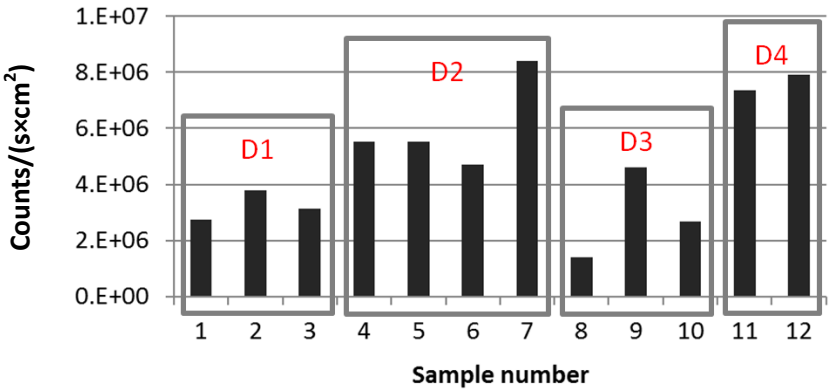

Fig.74 - Count rate values for four different tapes SiC diodes for 12 samples at the same thermal neutron flux of 7E8 s^{-1}×cm^{-2}

The thermal neutron detection efficiencies (count number per impinging neutron for a certain detector surface area) of the four types of investigated 4H-SiC detectors are collected in Table IV. To the calculation the regions of pulse height spectra are used, which can be obviously attributed to the reactions in Eq.(27) and Eq.(28). Counts above the adequate threshold channels are collected. Below these channels, the low energetic however, large number of events mostly generated by β-particles masks the signal. The average efficiencies are between 2×10^{-4} and 10^{-3} % for all the detectors. The highest values are observed for the D4 detectors and for the smallest D2 detector. The quiet low efficiency values are caused by the low capture probability of thermal neutrons in the thin ^{10}B-implanted converter layers. Greater efficiency values can be achieved by applying a higher concentration of converter ions or shorter distances between the neutron converter layer and the pn-junction. However, this causes more crystal defects, as observed for D3 and D4 diodes. Due to the low

TABLE IV.

THERMAL NEUTRON DETECTION EFFICIENCY OF DIFFERENT SIC DIODE DETECTORS

	Sample	A (cm2)	TH Ch.	η-0 V (%)	η-10 V (%)	η-25 V (%)	η-50 V (%)
D1	#1	4.00E-2	180^{th}	3.90E-04	3.98E-04	4.03E-04	4.12E-04
	#2	1.00E-1	180^{th}	5.39E-04	5.64E-04	5.96E-04	6.10E-04
	#3	2.50E-1	180^{th}	4.47E-04	7.16E-04	8.64E-04	1.34E-03 *
D2	#4	7.50E-03	435^{th}	7.90E-04	8.50E-04		
	#5	7.50E-03	435^{th}	7.90E-04	9.10E-04		
	#6	8.60E-03	435^{th}	6.70E-04	7.70E-04		
	#7	3.30E-03	435^{th}	1.20E-03		1.30E-03	
D3	#8	4.90E-04	435^{th}	2.00E-04		2.60E-04	4.50E-04
	#9	1.30E-03	435^{th}	6.60E-04		7.30E-04	7.40E-04
	#10	7.90E-03	435^{th}	3.80E-04		7.10E-04	7.60E-04
D4	#11	8.60E-3	368^{th}	1.05E-03	1.05E-03	1.05E-03	1.13E-03
	#12	7.50E-3	368^{th}	1.13E-03	1.15E-03	1.17E-03	

A-surface, TH Ch – Threshold channel, η-efficiency ({count number per impinging neutron per area} x 100)

*measured at -75 V

detection efficiency values, these small volume diodes may be proper for measurements in intense radiation, such as in case of the TBM module of the ITER fusion reactor, where the thermal neutron flux will be higher by orders of magnitude than the applied flux in the present measurements.

The estimated thermal neutron flux in the blanket module can reach up to 10^9-10^{13} $s^{-1}cm^{-2}$. Applying this neutron flux range, the average event number per second in a SiC detector can be expressed by:

$$R = \Phi \cdot V \cdot N \cdot \sigma, \tag{32}$$

where R is the reaction rate, Φ is the flux of thermal neutrons, σ designates the thermal neutron capture cross section of ^{10}B-nuclei, V indicates the volume of the boron implanted layer of the investigated diodes and N is the number of ^{10}B-nuclei in the certain volume. For all the diodes except D4 400 nm thickness of boron implanted layer are used. The number of events generated by neutron capture increases proportional to the increase of the neutron flux, see in Fig.75. At 10^{11} $s^{-1}cm^{-2}$ neutron flux only the smallest #7, #8 and #9 (D3 samples) detectors generate less than 10 000 counts of $^{10}B(n, \alpha)^7Li$ events per second. Beyond this point, the D1 type detectors exceed more than 1 million events per second, and from 10^{13} $s^{-1}cm^{-2}$ neutron flux in the D2 detectors also ~1 million events are generated. The higher reaction rate the more inevitable crystal defects by secondary charged ions in the sensitive detector volume are produced. These crystal defects lead to an increased leakage current of the diode detector. Thereby, for tests in high flux irradiation field, detectors should be used having a larger distance between the ^{10}B-implanted thermal neutron converter layer and the sensitive detector volume. Diodes with the smallest possible surface area may help to avoid pile-up of the detector signal during measurements at high neutron flux; furthermore small size is beneficial in case of very

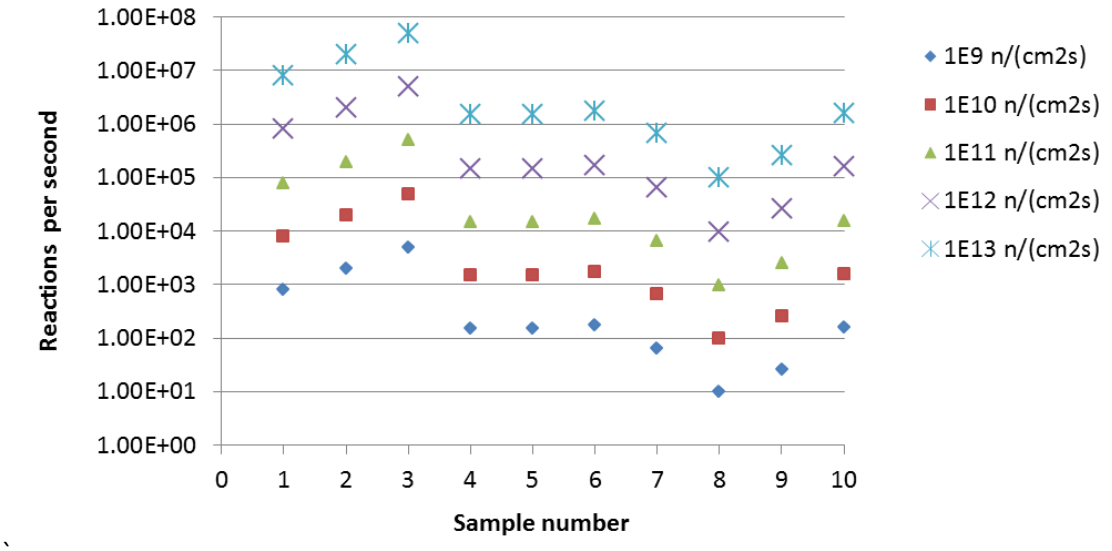

Fig.75 – Generated reaction number per second for the studied SiC diode types at different thermal neutron fluxes. The sample numbers agrees with that in Table IV.

limited place to be built-in as for the ITER TBM. D1 and D2 detectors have the largest distance between the converter layer and the space charge region. The smallest surface area have D2 and D3 diodes. Combining the observations the most suitable detector for future thermal neutron measurements in the TBM of the ITER reactor among the studied sensors is the D2 detector.

During continuous thermal neutron irradiation, ^{10}B-nuclei burn-up in time. Since the burnup is linear with neutron flux, we can define a limit for the minimum remaining ^{10}B concentration in terms of fraction of the initial one and calculate a neutron fluence to reach this limit. An estimated life-time of such detectors as a function of neutron flux and for various burned-up ^{10}B concentration is shown is Fig.76. In order to estimate the number of ^{10}B nuclei in the converter layers an exponential decay of them is assumed. The 1% of the original number of ^{10}B-nuclei breaks within ~3 days at 10^{13} $s^{-1}cm^{-2}$ neutron flux, this corresponds to the neutron fluence of ~2.5×10^{18} cm^{-2}. The number of ^{10}B-nuclei in the certain diodes can be estimated from the doping concentration and the dimensions of the implanted layer. The original number of boron atoms in sample #3 without irradiation corresponds to 1.25×10^{15}, and to 1.65×10^{13} in sample #7. Therefore, the 1% of boron atoms resulted as 1.25×10^{13} and 1.65×10^{11}, respectively. The secondary particles after burnup remain inside the SiC crystal and appear as crystal defects.

In Table III. it has been shown, that due to the position of the thermal neutron sensitive layer only a fraction of the generated secondary ions enter the sensitive volume of the detector. If we assume that only 20 % of the secondaries reach this volume, 2.5×10^{12} light ions (mostly α-particles) in sample #3 and 3.3×10^{10} ions in sample #7 enter and remain in the sensitive volume. These ions will appear as interstitial atoms and

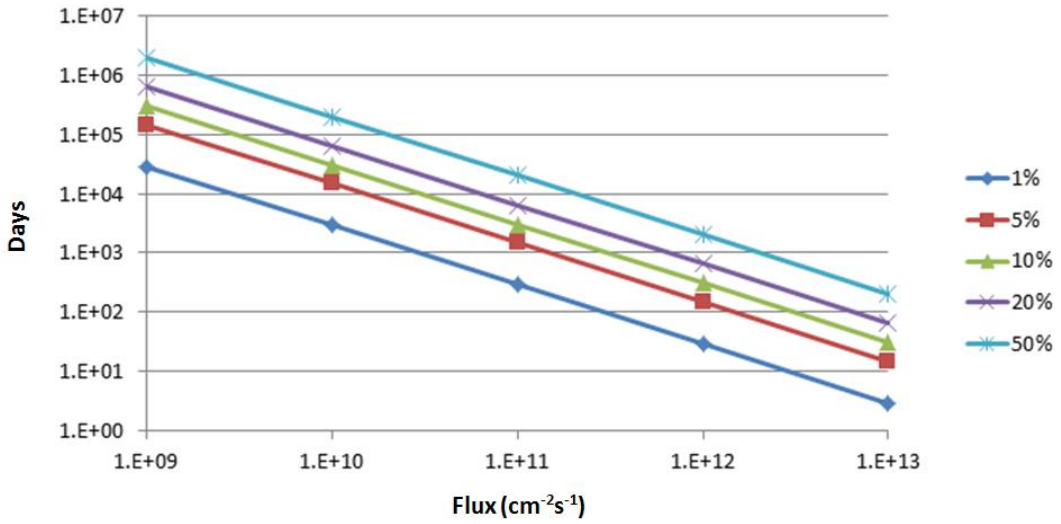

Fig.76 – Fraction of the ^{10}B-ion transmutation in days as a function of the thermal neutron flux. It is shown that at a certain flux how much time it takes to burn up different amount of the original ^{10}B concentration.

they produce vacancies inside the sensitive volume of the SiC sensor. These defects contribute to the deterioration of the crystal structure and worsening of the recorded signal.

Seshadri et al. [16] have examined the effect of high thermal neutron fluence up to 3.4×10^{17} cm^{-2} on the signal process of 4H-SiC Schottky detectors at room temperature. A thermal neutron converter LiF containing foil was placed above the Schottky diode. They found that the energy edge maximum position of charged secondary ions from ^{6}Li(n, ^{3}H)^{4}He reaction shifted to the lower energy channels after irradiation with different thermal neutron fluences (from ~310th to ~20th channel after applying 3.4×10^{17} cm^{-2} fluence). This means the charge collection efficiency due to the deep level defects in the crystal induced by ^{3}H and ^{4}He ions degraded. This in turn leads to higher trapping probability of minority charge carriers before they could be collected on the diode's electrodes. It should be mentioned that after application of higher neutron fluence the reverse bias voltage has to be increased in order to collect the generated electron-hole pairs. Above a neutron fluence of 1.5×10^{16} cm^{-2} a self-biased operation was no more possible. An illustrative figure about Seshadri's results from [17] is shown in Fig.77. In case of their measurements, the applied converter layer contained 50 % of thermal neutron sensitive ^{6}Li atoms. Thereby a larger amount of generated crystal defects occurs for the same neutron fluence than for diodes implanted with much smaller converter atom content as in this work (around 0.15 %). Based on this, the investigated diodes should be capable to operate properly up to extreme high flux of thermal neutrons, due to the low number of generated crystal defects even at higher neutron yield than the published values.

A much longer life-time of ^{10}B-implanted diode detectors is predicted for lower neutron fluxes, as 10^{9}-10^{10} s^{-1}cm^{-2}, where the decay of 1% of ^{10}B-ion occurs in several thousands of days, after having 2.5×10^{18} cm^{-2} thermal neutron fluence. Due to the much shorter available irradiation time with thermal

neutrons at 7×10^{8} $s^{-1}cm^{-2}$ flux in the BR1 reactor, no change in the signal quality due to crystal defects has been observed.

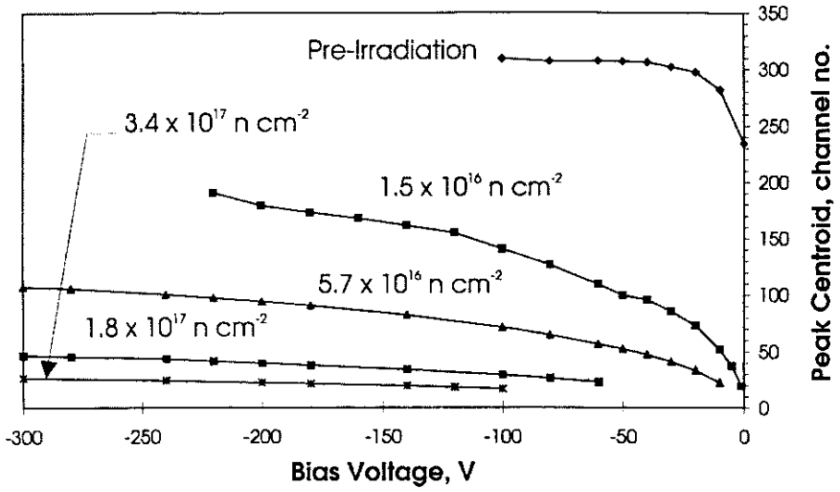

Fig.77 - Peak centroid versus bias voltage for a SiC Schottky diode before and after exposure to a range of thermal neutron fluences from Ref. [17]

8. FAST NEUTRON TESTS WITH SiC DIODE DETECTORS AT ELEVATED TEMPERATURES

In reactor technology and several industrial applications the detection of fast neutrons plays a crucial role to obtain relevant information about the reactor status, neutron yield or the neutron field in general. But, in many cases elevated temperatures make neutron measurements challenging. With respect to the currently available semiconductor crystals 4H-SiC seems to be one of the most suitable neutron detector materials for these harsh conditions due to its high heat and radiation resistance, large band-gap energy and low production cost compared to the competing diamond detectors.

A detailed examination of the temperature dependence of the detector signal has been performed with silicon carbide diode detectors. Two temperature ranges have been investigated with two similar set-ups. During the first high temperature tests D2 geometry diodes with ~1 mm^2 surface area have been tested with 14 MeV DT neutrons from room temperature up to 150 degrees Celsius. Measurements up to 500 degrees Celsius have been conducted with larger area SiC diodes with enhanced D5 and D6 geometry diodes. Because of the significant higher temperature the influence of the thermal noise and the change in the band-gap and ionization energy of 4H-SiC as discussed in 3.2 have been taken into account.

8.1 TestingD1 diodes in fast neutron field

The first room temperature tests with D1 type 4H-SiC diode detectors have been carried out with 14 MeV neutrons supplied by the DT neutron generator in the Neutron Laboratory of TU Dresden. The neutron generator had an average fast neutron yield of 4.04 x 10^{10} - 5.25 x 10^{10} s^{-1} during the measurements. Some of the tests were performed with an AmBe and a Cf-252 isotope sources, see in Chapter 6.

An example pulse height spectrum of a 0.25 cm^2 area D1 detector with the three different sources measured with Set-up 3 are shown in Fig.78. The spectrum has been compared with the histograms in the work of Ruddy et al. [19], which publication has been used as a reference to identify the main signal structures. These tests exhibit that the developed diode is able to detect fast neutrons with information on energy. AmBe and Cf-252 sources have main neutron energies at ~3-8 MeV and ~2 MeV but a very broad distribution up to ~11 MeV and ~10 MeV, respectively. Hence, nuclear reactions with high threshold energies above a few MeV do not appear compared to the pulse height spectra recorded with 14 MeV DT-neutrons. The obtained signal with isotope sources mostly attributed to inelastic scattering reactions of neutrons with carbon and silicon nuclei. The energy histogram recorded with 14 MeV fast neutrons exhibits several signal domains from various nuclear interactions. Well-defined full energy peak can be assigned to the reactions of $^{12}C(n, \alpha)^{9}Be$ and $^{28}Si(n, \alpha 0)^{25}Mg$. These first tests served as proof of principles for later measurements, therefore no energy calibration or detailed examination has been carried out.

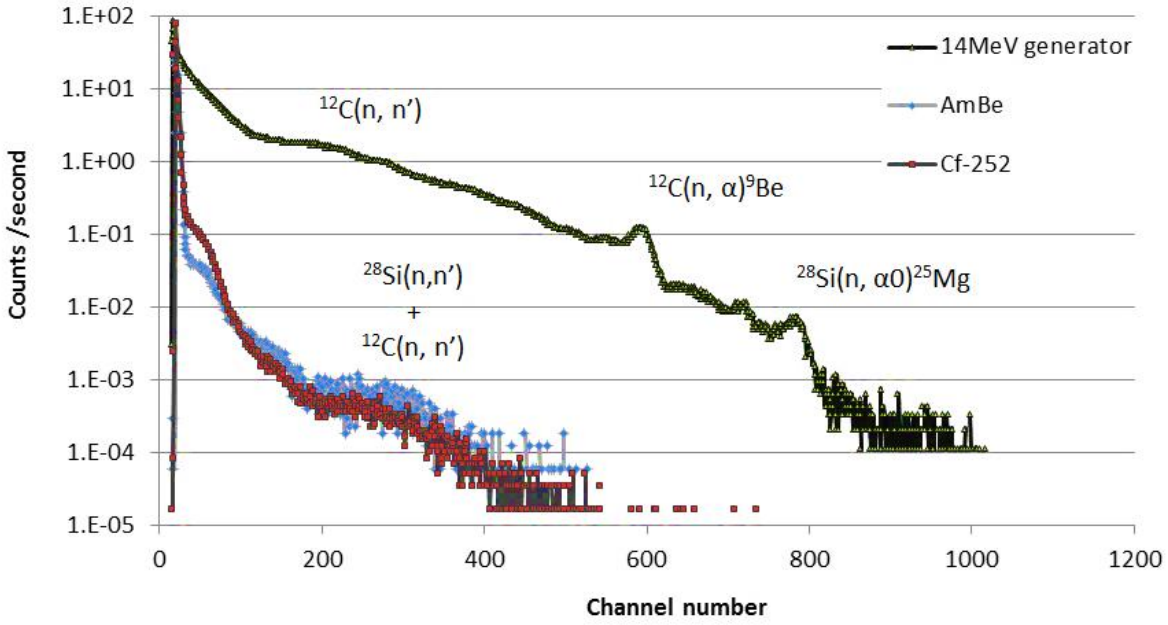

Fig.78 – Measured pulse height spectra of the D1 detector irradiated with different fast neutron sources.

8.2 Tests with D2 type SiC neutron detectors in the temperature range of 20-155 °C

Measurements with D2 geometry diodes are performed from room temperature to 155 °C with electronics Set-up 4. At this higher temperature a slightly higher detector signal is expected for the same energy deposition due to the larger number of generated electron-hole pairs at lower band gap according to Eq.(6) and Eq.(7). For example, an incident 1 MeV particle generates 127149 electron-hole pairs at 20 °C and 0.54 % pairs more at 150 °C in the sensitive region. Assuming a good quality 4H-SiC crystal detector, this small difference causes only a hardly measureable signal change.

Pulse height spectra of D2 detectors recorded in the temperature range of 20-155 °C are presented in Fig.79-a and b. The diodes have been located in the 0°direction relative to the theoretical deuterium beam direction (z-axis). The first detector has been tested between 50 °C and 155°C and the second between room temperature and 150 °C. The average measurement time has been 1800 seconds at each temperature; the applied reverse bias has been 40 V. Both figures exhibit an insignificant influence of the temperature on the detector signal up to 155 °C. The central energy channels of α-peak in the recorded histograms at different temperatures are fitted with a Gaussian curve. Following the methods in literature, mostly double and single Gauss fitting has been applied to establish the mean values of the measured energy peaks. This process proved to be good enough for calculations taking into account the not too high number of detector counts in the given energy region for less than half an hour measurement time. The resulting central channel values are listed in Table V. The channel shift remains for all the cases below 0.5 % compared to the reference low temperature

tests. This agrees well with the predicted behavior considered above. From that it can be concluded that due to this negligible change the generation of electron-hole pairs by temperature rise does not lead to an altered signal quality up to 155°C.

The sample #2 in Fig.79 is the same diode at 0° position as P1 in Fig.32 and Fig.33 at 90° position. To verify that the measured peak positions are not caused by any electrical effect, the two histograms of the same diode in the two positions are compared in Fig.80. The angle relative to the real deuterium beam direction and the mean value of projectile neutron energy at this angle, 18°- 14.92 MeV and 85° - 14.20 MeV in the figure are established from the measured peak positions. The measured spectra prove that D2 diode has a sufficient energy resolution to detect the differences in the mean DT neutron energy. The constant $^{12}C(n,\alpha)^{9}Be$ reaction peak position during the tests up to 150 °C is a real physical effect.

8.3 Tests with D5 and D6 diode detectors in the temperature range of 20-500 °C

First of all, prior examinations with D5 and D6 detectors are conducted to investigate the behavior and limitations of the diode types up to the temperature of 500 °C with Set-up 4. The main differences between D5 and D6 detectors are the material of the ohmic contact and the D6 detectors are implanted with ^{10}B nuclei inside the p+ epitaxial layer of the diode. Typical pulse height spectra of the two diode types are presented in Fig.81 and Fig.82 for different temperatures. All the spectra have 1800 seconds measurement time for 14 MeV fast neutron irradiation, except the 400 °C measurement with D6 diode for 1200 seconds. The maximum bias voltage values at higher temperatures have been set so that the noise level does not increase. In case of D5 diode with 2.13 mm^2 surface area tests at room temperature and at 100 °C are performed at the same bias voltage level; the applied 110 V is an optional choice in the present measurements and it is applied only for the first examination period.

It has to be noted that the structure of the full energy peak from the reaction of $^{12}C(n, \alpha)^{9}Be$ is only observed at 90 V and 200 °C for the D5 diode and at 50 V and 100 °C for D6 diode. Below these bias values the structure disappears. In later measurements it has been observed that following a longer thermal treatment at lower temperatures (~150-200 °C) the peak could be present even at lower bias values and at higher temperatures. In case of measurements with ^{10}B-implanted D6 diode the bias voltage has to be decreased to 50 V already at 100 °C; from 200 °C almost zero bias has to be applied, due to the high noise level. Thereby less structured spectra with D6 sensor can be recorded at higher temperatures, as it is visible in Fig. 82.

The appropriate maximum bias voltage values at different environmental temperatures were established in further tests with D5 diodes. Beyond these bias values the diodes suffered a permanent damage due to thermal run-away and breakdown effects. At room temperature and at 100 °C a bias voltage of 280 V is sufficient to deplete the whole n-type epitaxial layer. At 200 °C the proper bias is found at 90 V, at 300 °C, 400 °C and 500 °C the biasing has to be changed to 50 V, 20 V and 20 V. These bias voltage value are the

TABLE V.
CENTRAL ENERGY CHANNELS OF THE MEASURED PEAK FROM THE $^{12}C(n,\alpha)^{9}Be$ REACTION

SAMPLE #1			SAMPLE #2		
T (°C)	Central E (MeV)	Diff. of peak position (%)	T (°C)	Central E (MeV)	Diff. of peak position (%)
50	9.11	0	RoomT	9.22	0
100	9.07	-0.35	50	9.22	-0.05
150	9.09	-0.18	100	9.25	0.32
155	9.12	0.17	150	9.26	0.39

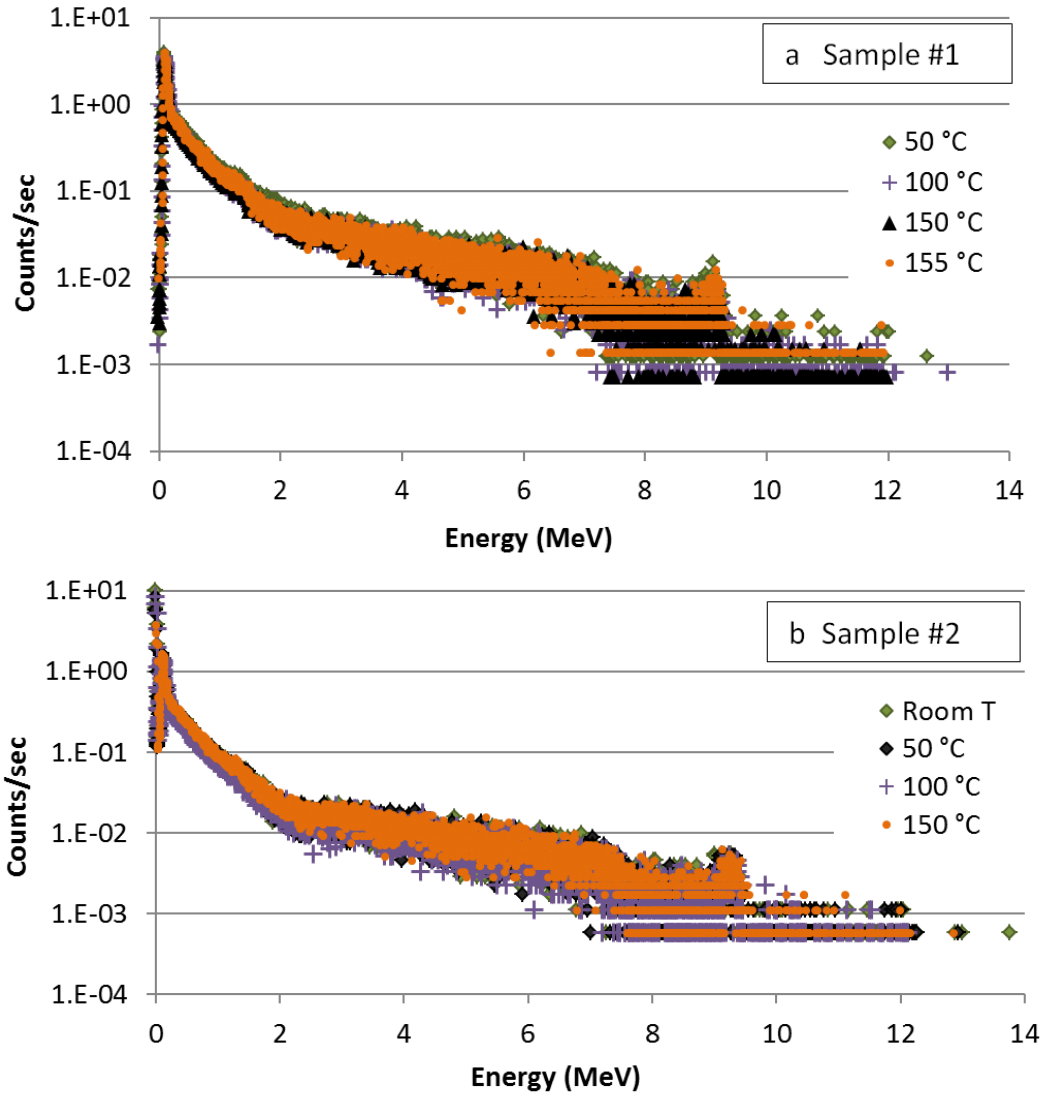

Fig.79-a,b – Energy histograms of two D2 diode detectors irradiated with 14 MeV fast neutrons at high temperatures up to 155 °C (normalized for one second). Energy calibration for the histograms is carried out according to Section 3.2.

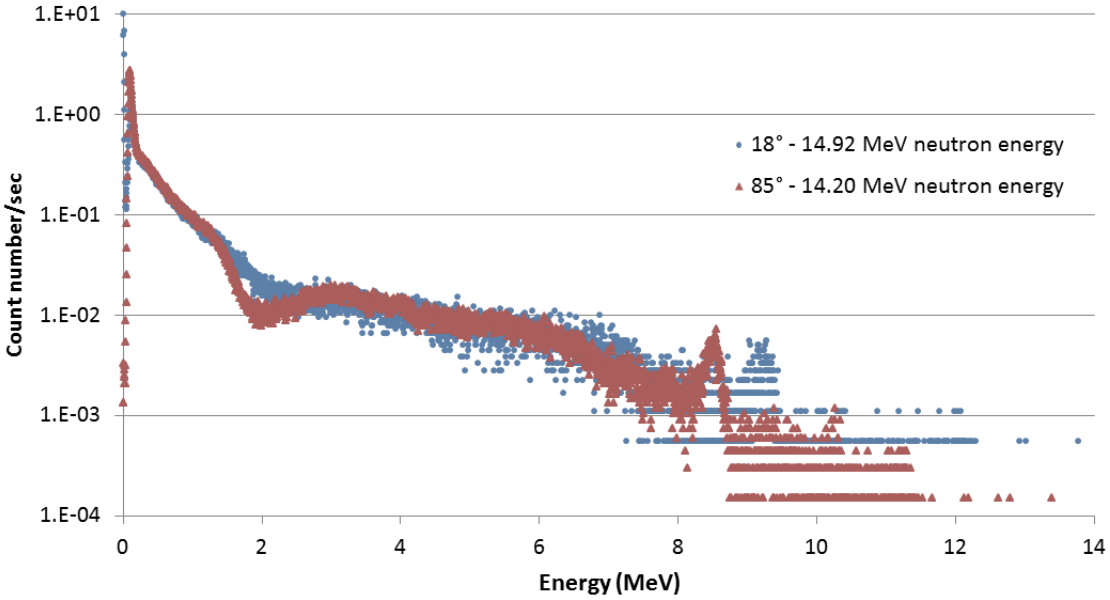

Fig.80 – Energy histograms recorded at room temperature with the same D2 diode detector in two positions relative to the tritium target of the DT-neutron generator. The two spectra have been recorded placed the diode 18°and 85°relative to the real deuterium beam direction (at 0°and 90° position relative to the theoretical beam direction).

maximum reverse biases which can be applied at the individual temperatures so that the diode does not experience any permanent damage. The spectra presented in Fig.83 are recorded at these biasing levels. D6 type diode was not proper for high temperature tests due to its high noise level at elevated temperature.

A more detailed investigation with a D5 diode (2.13 mm^2 area) has been performed up to 500 degrees Celsius. Measurements at each temperature have been carried out in two main time periods, at first for 6000 seconds and then for 1800 seconds, with 2-3 hours continuous heating without neutron irradiation between them. During both irradiation periods the recorded spectra were saved after every 600 seconds to allow for sensor stability studies. The summarized energy histograms for the first 6000 seconds time period at different temperatures are shown in Fig.83. The spectra are normalized with respect to the relative change in the neutron yield in time of the neutron generator. A well distinguishable peak is formed in the $^{12}C(n,\alpha)^{9}Be$ reaction in the ~9 MeV region. Additional peaks are formed by excited states of the reactions of $^{28}Si(n,\alpha)^{25}Mg$ in the ~8-12 MeV region, $^{28}Si(n,p)^{28}Al$ in the ~8-11 MeV region, etc.

Large part of the histogram (up to ~4 MeV) is occupied by counts from inelastic scattering events between neutrons and the silicon and carbon atoms of the crystal. In the mid-energy region the four-body reaction group, $^{12}C(n,3\alpha+n)$ is contributing to the signal and creates a plateau from ~2 MeV to ~7 MeV.

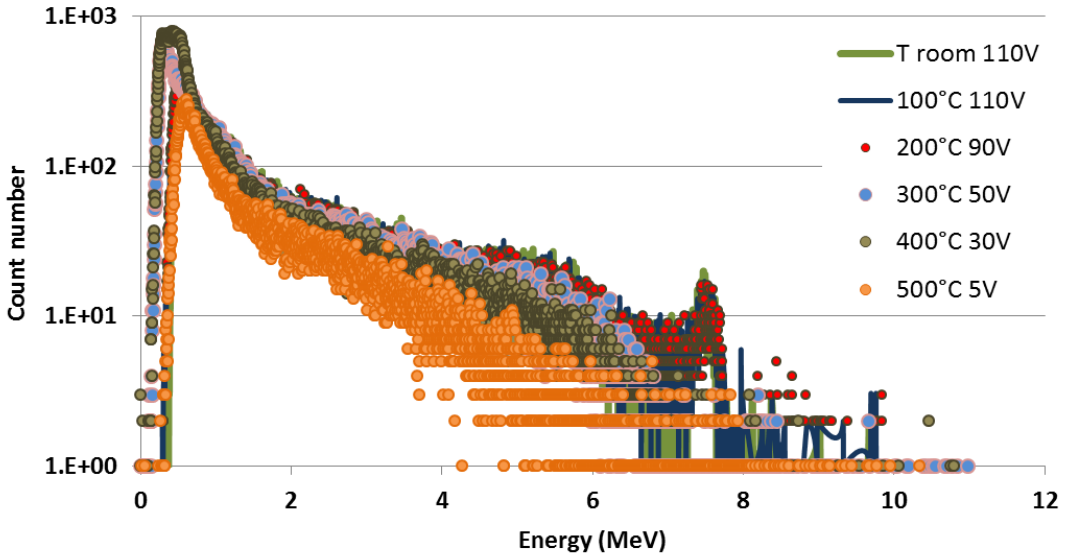

Fig.81 – Pulse height spectra of D5 diode detector irradiated with 14 MeV neutrons at different temperatures

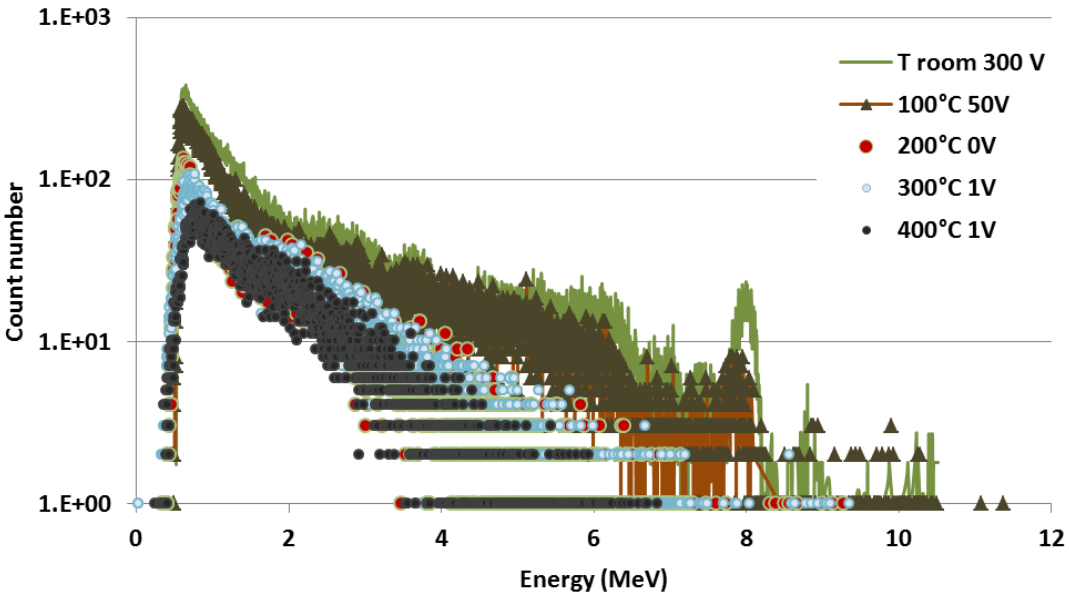

Fig.82 – Pulse height spectra of D6 diode detector irradiated with 14 MeV neutrons at different temperatures

The main difference in the signal shapes is represented by the falling count numbers at higher energy channels, which is caused by the thinner depletion thickness and hence a smaller sensitive volume due to the lower bias voltages in case of higher temperature measurements. Additional energy peaks from the α-particle and proton producing reactions with silicon atom are blurred at lower bias voltages. Hence an effect of temperature on them cannot be detailed discussed in the present work.

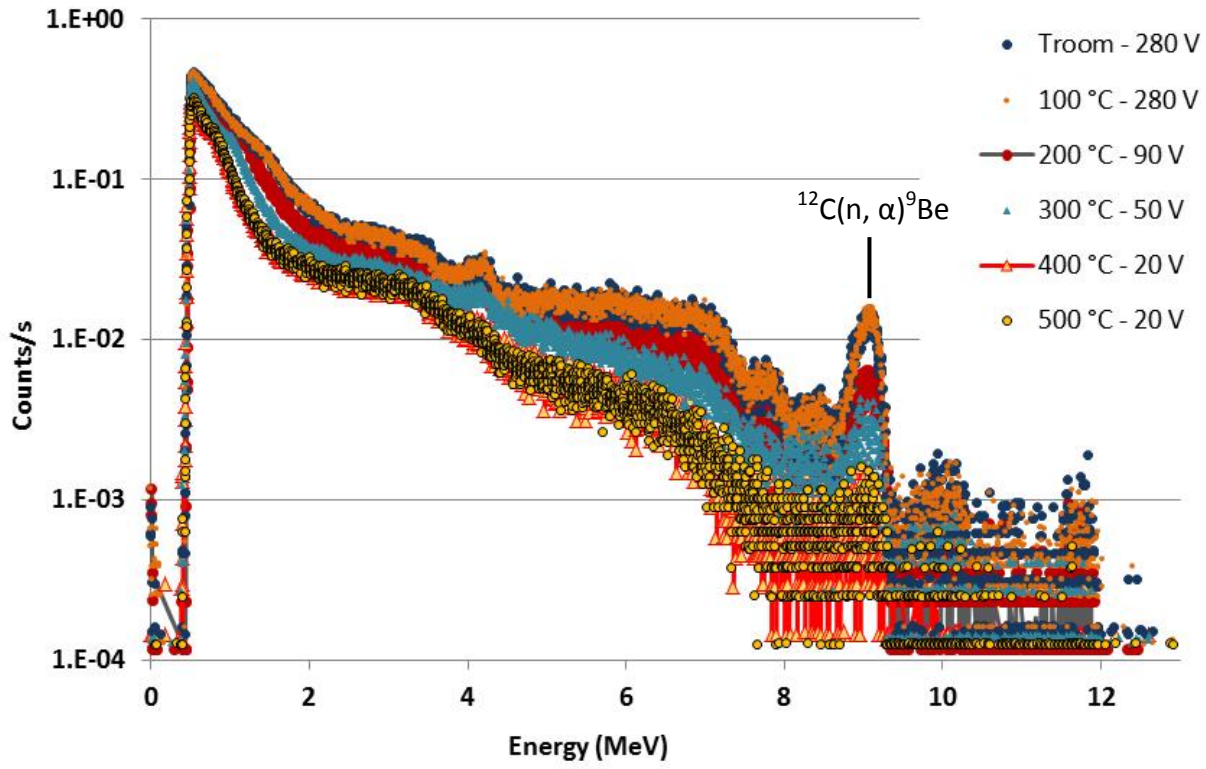

Fig.83 – Energy histograms recorded with D5 diode detector irradiated with 14 MeV neutrons at different temperatures

After the repeated heating at 500 °C temperature, the amplified detector signal became unstable and noisy, but the reverse current of the diode measured with the MCA (see DC-current in 6.2) remained low (0.06-0.07 μA). These results indicate that the metallic contacts on the electrodes of the sensor lost their integrity. After removing the detector from the alumina sample holder and re-contacting with a test spring contact, the measured detector signal recovered and became stable. Therefore the quality of crystal layers of the SiC diode seem to be unaffected by the applied thermal, irradiation and biasing conditions. A photo of the heated wafer marked with "1"with the spring contact on the investigated diode is shown in Fig.84. The different colors of the metallic surfaces on the two wafers are caused by the oxidation of the ohmic contact at high temperatures. The second wafer signed with "2" has not been heated and still has the original color of its metallic parts.

In Fig.85 two energy histograms are depicted. They were recorded at two different positions relative to the target surface of the neutron generator. One was set in the front of the tritium target surface at a distance of ~6 cm and the second one at the target surface at an angle of more than 90°, after thermal treatment and changing the electrodes. The maximum applicable reverse bias voltage at room temperature decreases to 220 V, which could be caused by the imperfect contact between the surfaces of the bottom contact and the diode or by some deterioration of the ohmic contact itself on the diode.

Fig.84 – Photo of the thermal treated wafer with purple surface on the metallic contact (denoted with **1**) and of the not heated SiC wafer (denoted with **2**). Both wafers are attached to a conductive plate with a spring contact. The plate and the spring are electrically isolated from each other.

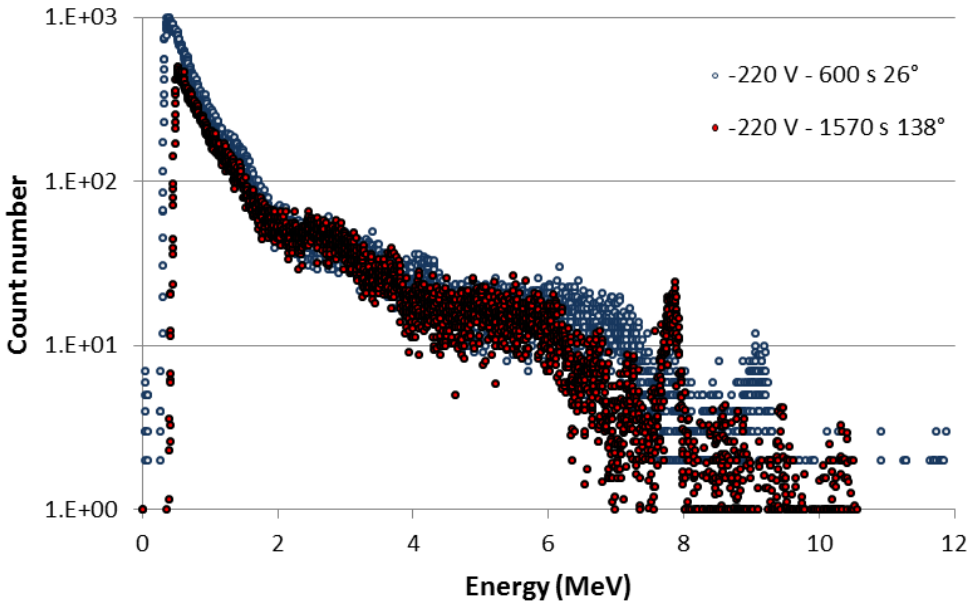

Fig.85 – Energy histograms recorded at room temperature with D5 type detector supplied with new spring contacts after extended heating up to 500 °C in two different positions, at 26°and 138° relative to the real deuterium beam direction. The illustration of the deflection of the deuterium beam direction is shown in Fig.37.

The position of the full energy peak of $^{12}C(n, \alpha)^{9}Be$ reaction moved corresponding to the change in the neutron energy at certain angles (~26°and ~138°) with respect to the deuterium beam of the neutron generator. In contrast with the preliminary tests performed with D5- and D6-type detectors, these results represents that choosing the proper biasing set-up at high temperatures, the D5-type SiC diode detector does not suffer thermal run-away and breakdown effects and the sensor can be used repeatedly after thermal treatments.

8.4 Noise evolution during the thermal treatment of 4H-SiC diode detector

It is noteworthy that the reverse current of the diode measured on the preamplifier output, in other words the noise of the diode (leakage current + current generated by irradiation and heating) was decreased after long term heating at 100 °C and at 200 °C. This effect is not observed in case of the prior measurements, where the detector signal has recorded at different temperatures directly after each other, with shorter measurement times. The decrease in the noise level of the diode after long term heating at 200 °C is due to the thermal annealing effect, which is also applied as a common process during the semiconductor device preparation [109, 110]. Between the tests at 100 and 200 °C, the diode has been continuously heated at 100 °C for ~20 hours, which serves as a slight annealing effect of the diode. After the tests at 200 °C, the reverse current from the preamplifier measured with the CAEN MCA decreases at room temperature and at 280 V from the diode before irradiation 0.24 μA to 0.11 μA. After the tests at 300 °C and with a bias of 50 V the reverse current value stabilized at 0.06 μA even for the measurements at 400 °C and at 500 °C with 20 V biasing. This small current was close to the limit of current measurement with the CAEN MCA.

At elevated temperatures free charge carriers acquire thermal energy and the leakage current increases, thereby the same amount of the released energy to the material results in higher energy scattering at high temperatures than at lower ones [45, 49]. The examination of the change in the energy resolution has been carried out with Gaussian fitting method on the full energy peak of $^{12}C(n,\alpha)^{9}Be$ reaction. A double Gaussian curve has been fitted to the measurement results, because the signal arising from $^{28}Si(n,\alpha 8)^{25}Mg$ (Q=-6.055 MeV) and $^{28}Si(n,\alpha 9)^{25}Mg$ (Q=-6.064 MeV) reactions is close to the full energy peak of $^{12}C(n,\alpha)^{9}Be$ (Q=-5.70 MeV) reaction and hence it is masked by that one. This fitting method was eligible to determine the peak mean energy channels.

As mentioned before, the optimum bias voltage values for the different temperatures have been chosen in preliminary tests with D5-type SiC detectors. The prior tests with a constant 60 V bias voltage temperatures up to 400 °C exhibit a histogram shift to higher energy channels as illustrated in Fig.86. The central-channel position of the reaction $^{12}C(n,\alpha)^{9}Be$ is detected at room temperature at 7.8 MeV and a shift equivalent to 0.09 MeV energy difference of this position occurs at 400 °C corresponding to 7.89 MeV. This denotes a ~1.1 % difference in the average measured energy. This change is less than predicted in the work of Garcia et al.in [45], where in the temperature range of 23-400 °C, a 2.7 % change in the central energy value has been observed. From the fitted σ-value of the Gauss function, a 38 % increase in the full width at half maximum (FWHM) is found, from 0.23 MeV to 0.32 MeV, which is most likely caused by an increased leakage and thermal noise of the semiconductor diode at higher temperatures. Diode in Fig. 86. tested at constant and higher bias voltage (60 V) at temperatures up to 400-500 °C suffered breakdown events and thermal runaway [49].

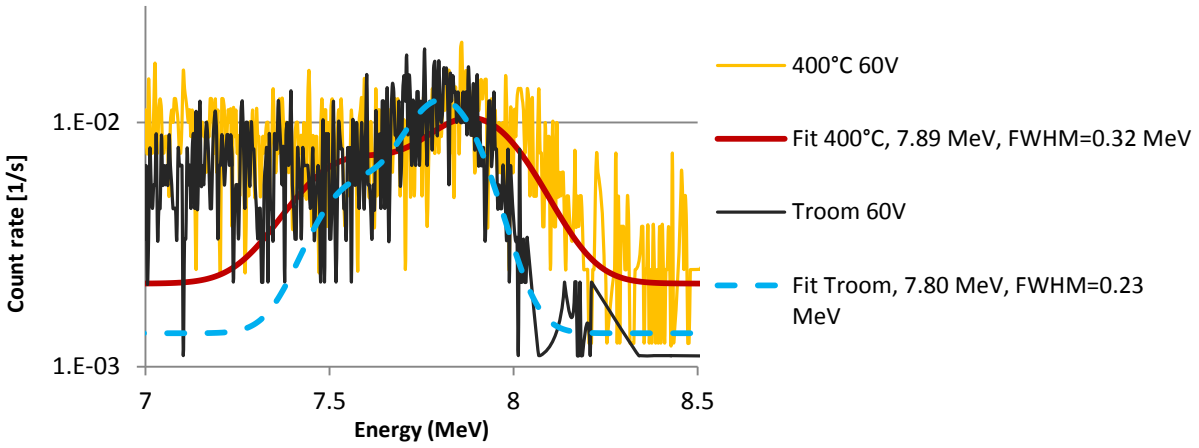

Fig.86 – Gaussian fitting of the full energy peak from the $^{12}C(n,\alpha)^{9}Be$ reaction at room temperature and at 400 °C applying -60 V bias on D5-type SiC diode. FWHM: Full Width at Half Maximum

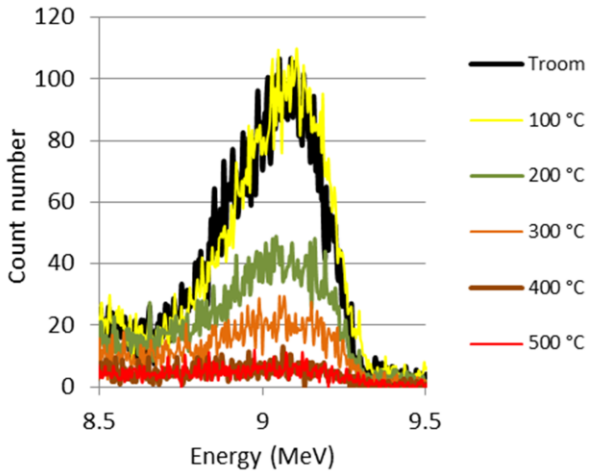

Fig.87 –The measured full energy peaks of the reaction $^{12}C(n,\alpha)^{9}Be$ at different temperatures up to 500 °C

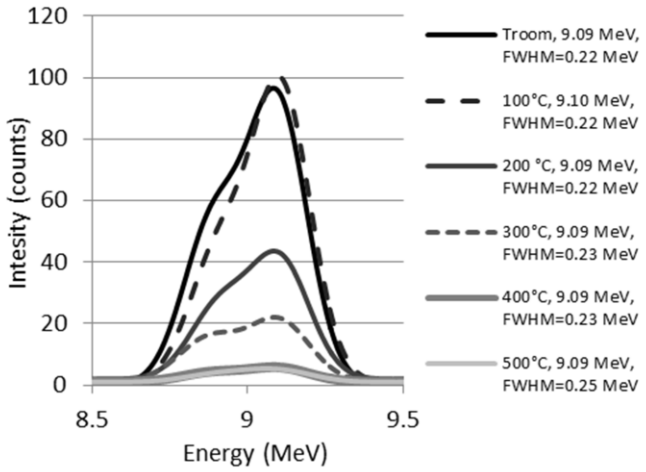

Fig.88 – Double Gaussian fitting curves of the recorded full energy peaks of the reaction $^{12}C(n,\alpha)^{9}Be$ at different temperatures

To avoid the deterioration of the diode detectors in the following measurements, the applied bias voltage values have been chosen for the temperature values up to 500 °C so that no increase of the noise, thus the reverse current measured by the CAEN MCA appears compared to the current value at room temperature. Due to this continuous low noise level, the energy resolution of measured histograms does not change significantly during the measurements up to 500 °C. The recorded energy peaks of $^{12}C(n,\alpha)^{9}Be$ reaction are shown in Fig.87 and the resulted fitting curves and values of the Gauss fitted parameters are illustrated in Fig.88. The position of the central energy channels are not shifted to the higher energy channels and they remain at 9.09 MeV. A slight increase in the FWHM values of the fitted peaks is observed at higher temperatures. 0.22 MeV FWHM was established at room temperature, for 100 °C and 200 °C it is near to 0.23 MeV. At 300 °C and 400 °C 0.23 MeV FWHM was obtained from the fitted σ parameters. At 500 °C 0.25 MeV are found. In total a 11.8 % increase relative to the value at room temperature is obtained.

8.5 Detector Signal Stability at Elevated Environmental Temperature

Sufficient stability is a requirement for radiation flux detector, because it informs about the measured radiation field and also about the quality of the sensor. In case of a known flux of neutrons, the stability of the diode detector can be validated at given conditions. A significant count rate change at continuous irradiation conditions indicates a deterioration of detector or the signal processing electronics. To investigate the detector stability repeated irradiation tests are performed at all temperatures in two steps with 2-3 hours long time between them maintaining the same temperatures. In the first test run (Run1) ten times 10 minutes and during the second run (Run2) three times 10 minutes measurements are performed, except at room temperature, which serve as reference. During the waiting time between the two runs the neutron irradiation was stopped.

For 10 minute long measurement periods the change in the average count rate normalized by the signal of the NG monitor has been recorded for different temperatures. The results are plotted in Fig.89 for the 10+3 test periods. The smallest significant difference relative to the average count number is observed for 300 °C, amounting to ±0.5%. The largest deviation in the count rate is seen for 400 °C with ±1.8 % is found

For all the measurements, the neutron generator has been stopped between two runs and in case of the 500 °C test between the first four and the additional two tests. In case of the Run 2 measurements (100 °C - 400 °C) and in the 500 °C test a slight increase in the count rate is observed after restarting the neutron generator. The main difference of Run 2 is at 400 °C, where an increased count rate from 62 to 65 corresponding to a 5% difference appeared. For the latter two 500 °C tests (Fig.90), these values are 70 and 73 counts per second, which is a 4.2 % difference. At first, this increase in the count number has been associated with the annealing of the crystal defects, but it was not found during subsequent investigations at 500 °C. In the later tests the neutron generation is stopped only for 2 minutes, being less than the 2-3 hours in the previous measurements. Nonetheless the detector count rate increased. This suggests that the count rate change is generated not by the annealing of the crystal defects but by the slightly non-linear answer of the α-particle counter detector near to the tritium target (the signal of the silicon α-counter is used to normalize the recorded histograms corresponding to the change in the neutron flux).

8.6 Diffusion length calculations for fast neutron irradiated SiC diode detectors

The square of intrinsic charge carrier concentration $n_i^2 = n \cdot p$ in semiconductor materials is a constant value at a given temperature. This was detailed in Section 3.2. Depending on the doping conditions, the crystal material can be intrinsic (n=p), p or n-type. For a p-type material, acceptor atoms are implanted in to the crystal and the hole concentration is increased, thus holes are referred as majority carriers and electrons as minority carriers. For n-type material the concentration of donor atoms in increased, thereby electrons are the majority and holes are the minority charge carriers.

Any impinging particle or radiation (e.g. gamma), which has larger energy than the band-gap, could generate electron-hole pair, thus both minority and majority charge carriers simultaneously, and their concentration already differs from the equilibrium level. The deviation from equilibrium is more pronounced for minority carriers because it follows the change in the majority carrier concentration. If the minority carrier concentration is 0.1 % of the majority carrier concentration, 0.1 % change in the latter one causes 100 % change in the minority carrier concentration [111]. Forward biasing on a pn-diode leads to current flow generated by the majority carriers, and in the opposite case for reverse biasing a current flow of the minority carriers occurs [31]. In case of the semiconductor particles detectors, reverse biasing is applied, thereby the contribution of minority charge carriers has to be considered in the present work.

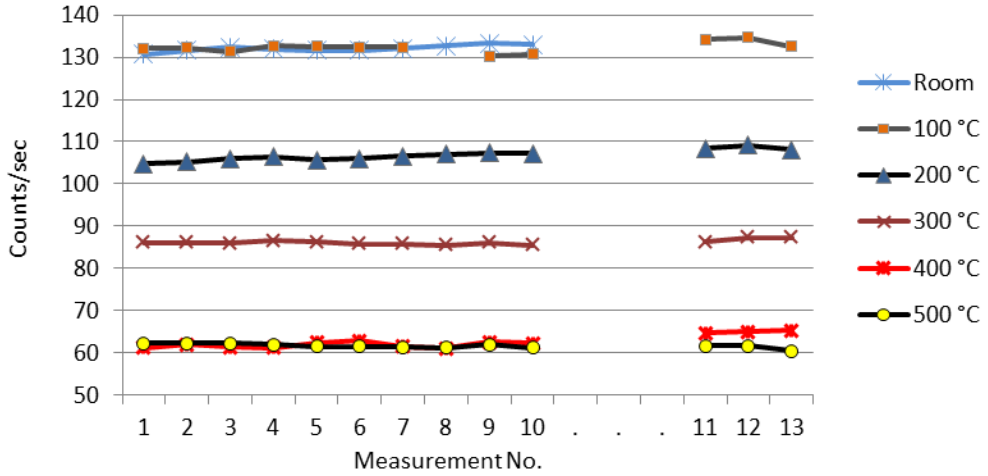

Fig.89 – Measured count rates at different temperatures at irradiation with 14 MeV neutrons in two main runs: 10 times 10 minute and 3 times 10 minutes with 1-3 hours interruptions between them

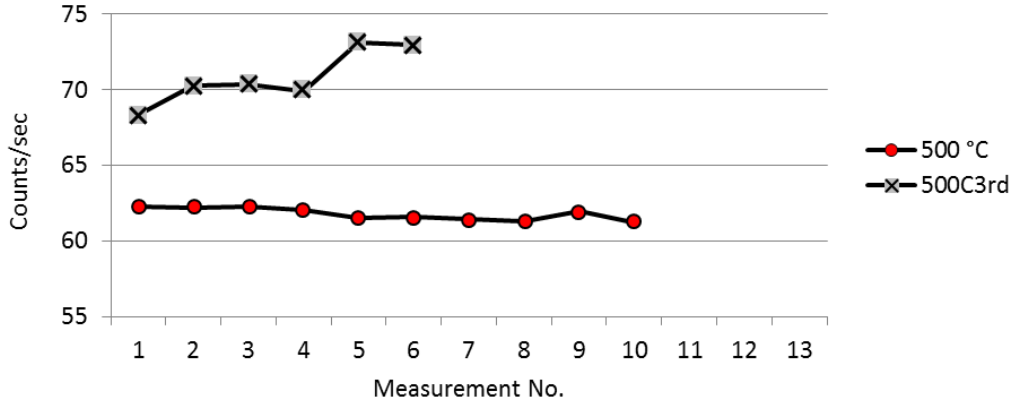

Fig.90 – Count rate as a function of the measurement runs at 500 °C during the first and third thermal treatments

The life time (τ) and diffusion length (L_d) of the minority charge carriers in semiconductor devices determines the quality of the crystal material itself. The life time indicates the average time after minority carriers will be recombined in matter after they are generated. In perfect indirect gap semiconductors, such as 4H-SiC, its value can reach several milliseconds for electrons, but different defects in the crystal as impurities can lead to lower life time values [111]. The diffusion length determines how far a charge carrier with diffusion movement due to charge concentration difference can travel in a crystal material before recombination. It is worth to note that in high quality silicon the diffusion length of electrons can reach up to several millimeters. The connection between the life time and the diffusion length can be written as

$$L_d = \sqrt{D\tau} \tag{33}$$

where

$$D = \frac{k_B * T}{q}\mu \tag{34}$$

is the Einstein relation, D is referred as diffusion coefficient, q denotes the elementary charge and μ is mobility of the minority carrier. The minority charge carriers generated outside the space charge region of a pn-diode, for example in the detector layer which could be still depleted at higher bias voltage level, have smaller velocity than inside, due to the lack of electric field. Their movement is influenced only by the concentration difference of the charge carriers between the two regions [34]. The higher L_d value allows possible to collect more charges and thus a larger sensor signal.

The diffusion length of minority charge carriers in 4H-SiC has been investigated by several research groups earlier [112-122]. There mono-energetic light ions such as α-particles, ^{16}O and ^{12}C nuclei are applied, which generate peaks in the recorded pulse height spectra. The position of these peaks can be used to calculate the diffusion length and charge collection efficiency of a given diode sensor. It is known that the diffusion length at elevated temperatures increases compared to lower temperatures. In this context two new methods to establish the L_d value of the minority carriers in 4H-SiC from 14 MeV neutron measurements were elaborated, which are introduced in the following.

After irradiation of D5 SiC diode detectors with 14 MeV neutrons at elevated temperatures, the relative change in the count rates for the whole energy histogram have been examined. The values compared to those at room temperature show a decreasing behavior (see in Fig.91) at higher temperatures and at lower bias voltages. The count rate is reduced by 53.2 % at 500 °C. The relative changes of the collected count rate in 1 μm thick detector volumes with respect to room temperature show an increasing behavior at higher temperatures. It reaches ~ +42 % for the tests at 400 °C and 500 °C at 20 V biasing. The count rate per micrometer (CPS/μm) are also depicted in Fig.91. The explanation of this increase of the CPS/μm value is served by the diffusing minority charged carriers – in case of the present diode, the holes. It means that not only the charge carriers generated inside the depleted part of the n-type epitaxial layer of the diode are

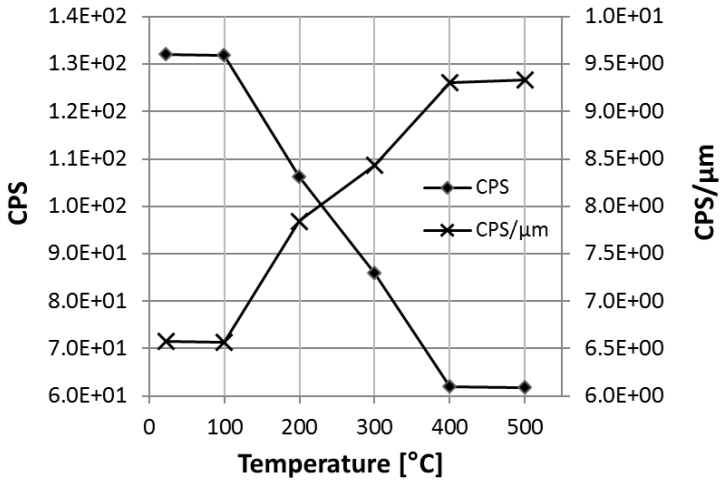

Fig.91 - Count rate (CPS - count per second) for the measurements prepared at lower bias voltage values and at higher temperatures (CPS) and the simultaneous increase of the count rate per micrometer (CPS/µm) at higher temperatures; Bias/temperature values: 280 V/ Troom, 280 V/100 °C, 90 V/200 °C, 50 V/300 °C, 20 V/400 °C 20 V/ 500 °C

collected, but also some minority carriers, which are generated externally in the electrically neutral region. Depending on the crystal quality these minority carriers have an average diffusion path length till recombination. From the distance equal or less than this length, the carriers are able to reach the sensitive region by diffusion movement. Thereby the detected signal arises from the space charge region and from an additional external detector volume, which has an average thickness of the diffusion length of the minority charge carriers.

To validate the results further experiments with D5 diodes have been performed. The same detector (area: 2.13 mm^2) hereinafter referred as "D#1", after thermal treatments and an additional diode, "D#2", with 0.2 mm^2 surface area have been tested. They have been irradiated with 14 MeV neutrons at room temperature at different bias voltages and the count rates are recorded. The same effect has been experienced as at high temperature tests; the count rate value decreases and the count rate per µm value increases (see in Table VI.) at lower bias values. To establish the values in Table VI., the temperature dependency of some physical parameters, as in case of the depletion width from Eq.16 in 3.2 has also been taken into account.

For the first method to estimate the diffusion length of the holes the count rate values are applied. The following equation has been used to express the effective detector thickness (D_{eff}) from where the signal is collected:

$$D_{eff} = \frac{D_{ref}}{CPS_{ref}/CPS_x} \ . \tag{35}$$

where D_{ref} = 20.9 µm is the reference depletion, so the full depletion width of D5-type detector, CPS_{ref} is the reference count rate value at room temperature with full depletion, finally CPS_x indicates the measured count rate values at different bias voltages. The difference of the effective thickness and the theoretical thickness of

the space charge region at a given bias voltage (SCR_x) results the missing thickness from where counts could originate, now this value is referred as "effective diffusion length" (L_d):

$$L_d = D_{eff} - SCR_x \,. \tag{36}$$

TABLE VI.
EFFECTIVE DIFFUSION LENGTH VALUES I.

Bias (V)	Depl.(μm)	D#1 at high T (μm)		D#1 at room T (μm)		D#2 at room T (μm)	
		CPS/μm	Eff. L_d (μm)	CPS/μm	Eff. L_d (μm)	CPS/μm	Eff. L_d (μm)
2.96	2.42			18.56	**1.58**	6.38	**7.79**
22.96	6.74	9.33	**3.14** (400°C)	13.45	1.32	3.22	7.60
22.96	6.74	9.31	3.15 (500°C)				
52.96	10.24	8.43	3.40 (300°C)	12.92	1.53	2.52	6.82
82.96	12.82			13.26	2.30		
92.96	13.57	7.85	3.26 (200°C)			2.06	4.86
102.96	14.28			13.02	2.26		
122.96	15.60			13.12	2.61	1.93	4.16
152.96	17.40			12.83	2.46	1.80	3.30
182.96	19.03			12.42	1.99	1.65	1.74
202.96	20.05			11.68	0.78	1.60	1.11
222.96	21.01			11.24	0.00	1.51	-0.11*
252.96	21.01					1.42	-1.43*
282.96	21.01	6.56	0 (Troom)			1.33	0.00
282.96	21.01	6.58	-0.04 (100°C)				

Depl. – Thickness of the sensitive volume of the diode detector
Eff. Ld – Effective diffusion length, the missing thickness from where counts could originate
* negative values are resulted only by calculation and they have no physical meaning

A detailed list of the obtained possible diffusion length values with the first calculation method is shown in Table VI. The maximum bias voltage values have been differently set for D#1 diode because of its elevated noise level after high temperature tests. It is important to note that the diffusion length do not have bias voltage dependence, in Table VI. its possible values are listed, which are calculated from the data at different bias levels thus with different depletion thicknesses. A further method has been developed to establish the appropriate L_d value. It will be shown that the "effective diffusion length value" calculated from the data at built-in bias corresponds to it.

The calculated values of effective L_d for the D#1 diode at the same bias voltages at room temperature slightly decreases compared to those at higher temperatures, e.g. at 22,96 V (2.96 V built-in bias + 20 V external bias) from 3.15 μm (500 °C) to 1.32 μm (room temperature). This effect can be caused by the

collective action of the increasing minority carrier lifetime (τ) [123,124] and its decreasing mobility (μ) [125] with rising temperature [126] in the bias voltage independent expression from Eq.(32) and (33):

$$L_d = \sqrt{\frac{k_B * T}{q} \mu\tau} \ , \tag{37}$$

The increase of diffusion length at higher temperature is also discussed in [127], [128] and [129]. Tests with a smaller area D#2 result about four times higher values of effective L_d than with the D#1 detector at room temperature. The maximum value of 7.78 µm is observed at 0 bias voltage. The different L_d value of the two diodes is likely caused by the different density of intercrystalline defects formed during the implantation process of the p-type dopant into the n-type epitaxial layer. A clarification, however, would require additional material testing.

The second method to evaluate the diffusion length of minority charge carriers is based on the work of Breese [130]. Breese applied his calculations to model the measured charge pulse height in keV. In later works [112-122] his equation is applied to establish the contribution of the signal from drift and diffusion processes to the charge collection efficiency of SiC detectors. In Breese's study, in the damage-free approximation the diffusion length is assumed as a uniform depth in the crystal. Thereby it is a constant, the pn-diode is considered as quasi-infinite in horizontal direction with finite vertical width. The fitting formula of charge pulse height value (H) reads to:

$$H = \int_0^{z_d} \frac{dE}{dz}\, dz + \int_{z_d}^{R_i} \frac{dE}{dz} e^{\frac{-(z-z_d)}{L(z)}}\, dz \ , \tag{38}$$

where z is the depth and dz the integration variable, E signs the energy and dE/dz the ion energy loss per unit length. Finally, R_i refers to the range of ions (Breese in [130]) or the active detector thickness (in [112-122]). The first term is the contribution of the charge carriers (electrons and holes) generated inside the space charge region with the thickness of z_d, and the second term is the contribution of the minority charge carriers, which penetrate by diffusion from the electrically neutral region to the space charge region. Later in [112-122], mono-energetic ion sources are applied to irradiate the detector and the position of the single energy peak on the energy histogram has been studied.

Here, an additional interpretation of Breese's equation is applied to calculate the diffusion length of the minority charge carriers from measurements with neutron irradiated SiC detectors. The main differences between the earlier studies and the present one are both the type of impinging particle and the location of the electron-hole pair generation inside the detector. In the early experiments charged ions starting from a given distance from the diode's surface and from a well localized position enters the diode detector. The position of the energy peak maximum on the recorded histogram depends mainly on the thickness of the space charge region, thus on the bias voltage. A thinner depletion yields maximum peak positions in the lower energy channels, because of the shorter distance of ions inside the sensitive region of the diode than the full stopping

range. This also means that in case of a partial energy deposition the rest of the ion path overlaps with the electrically neutral detector region. A part of the energy of the moving ions is deposited outside the sensitive volume, as it is illustrated in Fig.92-a. At sufficient large depletion these ions can be fully stopped inside the sensitive region and no further shift of the energy peak maximum on the energy histogram is observed even at higher biases. “Peak centroid positions” in Fig.93. represent this shifting effect with increasing bias.

Fast neutrons entering the detector volume cause nuclear reactions inside the whole crystal. Thus the direction of the moving secondary ions and the position from where they start their movement are not well-defined and they are homogenously distributed inside the diode. Every reaction can occur at any point inside the detector and the maximum collectable charge number depends on the thickness of the sensitive detector layer, here the depleted n-type epitaxial layer, see in Fig-92-b. This predicts that a full energy deposition of secondary ions can occur at lower bias values, because they can be ejected in any direction inside the sensitive layer. In case of using a point ion source perpendicularly faced to the detector full energy deposition preferably occur for thicker depletion. Additionally, also events outside the space charge region but close to it could contribute to the signal if secondary particles (protons, neutron, α-particles, etc.) are emitted and they enter the sensitive region. Minority charge carriers are also capable to reach the electrically active layer by diffusion from the electrically neutral region and to be collected. The next calculation is important due to the contribution of these minority carriers to the measured detector signal.

In the above mentioned [112-122] works the mean values of the edge positions on the energy histograms are examined after irradiation with mono-energetic ions at different biasing and a maximum edge

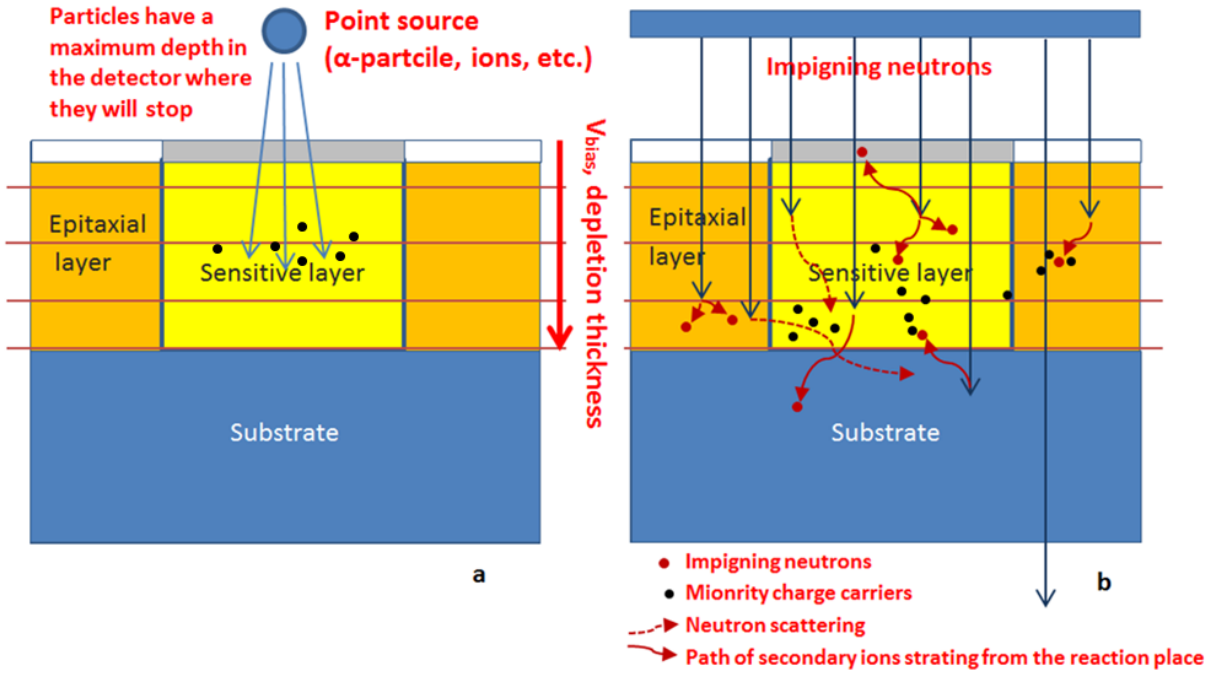

Fig.92-a - Diode detector irradiated with charged particles from a point source; b - Diode detector irradiated with neutrons from a plane source

position is observed beyond a certain voltage, which already does not shift to higher energy channels with the increasing bias voltage, as shown in Fig.93. The diffusion length of the minority charge carriers is established by fitting Bresse's equation to these mean values, in other words to the signal maximum, which compliances the collected charge number. Here, the count rate values at different bias voltages are taken to calculate the diffusion length. The saturation of the count rates is observed beyond a bias voltage level for all the examined diodes. The saturation of the edge position in [112-122 and 130] beyond an applied bias voltage level behaves similar to the saturation of the count rate of our sensors. A non-linear change with the thickness of the depleted region is observed, as it can be seen in Table VI., the count rate per μm values increase for the thinner depleted layers. Similar to the saturation edge position in [112-122 and 130,131], a saturation of the count rate represents the 100 % detectable event number with the applied diode in case of a given neutron flux. An example diagram in Fig.94 illustrates the saturation effect of the count number, which is the signal of the small area D#2 diode discussed above. If the count rate value would change linear with the thickness of the sensitive layer, the trend line should change with the square root of the bias voltage according to Eq.(15) in 3.2, but here the indices is less than 0.5. The saturation of the count number is caused by the detection of the maximum collectable events in the detector volume at a given neutron flux. As mentioned before, these events are generated inside the space charge region of the diode and in the electrically neutral nearby region. Thereby, one part of the detected signal is caused by drifting electrons and holes and the second part by the diffusion of minority charge carriers, presently of holes.

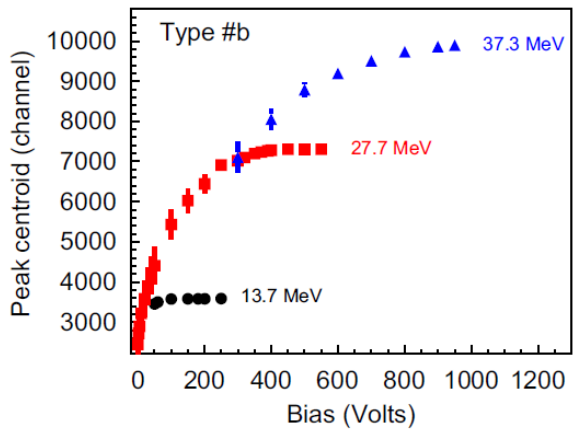

Fig.93 – Study of charge collection efficiency of 4H–SiC Schottky diodes irradiated with ^{12}C-ions from DeNapoli [118]

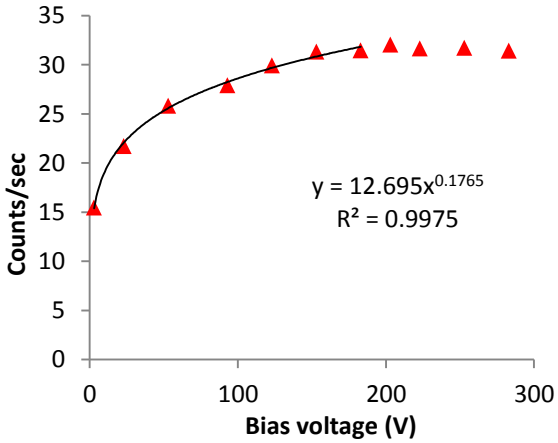

Fig.94 – Count rate for the D#2 diode at different bias voltages

Accordingly, the different terms of Eq.(38) related to energy deposition correspond to the collected and produced count number values. Despite *dE/dz*, the average count rate inside a unit thickness is considered signed with *dC/dx*; this value depends on the number of carriers from the space charge region and on the additional charge carriers coming from the neutral region. Averaging of count rate is necessary due to several different sources of counts in a neutron irradiated detector, where many types of ionizing particles and radiation are generated and they contribute to the signal. x_d (z_d in Eq.(38)) corresponds to the thickness of the

depleted layer regarding to Eq.(15) at given bias voltage. D (R_i in Eq.(38)) marks the thickness of the active detector volume (20.9 μm). x and L_d (z and $L(z)$ in Eq.(38)) are the integration variable and the diffusion length. Applying the notations, the fitting function for the count rate reads to:

$$C = \int_0^{x_d} \frac{dC}{dx}\, dx + \int_{x_d}^{D} \frac{dC}{dx} e^{\frac{-x-x_d}{L_d}}\, dx \quad , \tag{39}$$

where C represents the count rate values. The resulting count rates are approximated by the integrated form of Eq.(39) applying the Solver application of LibreOffice 4.4 Calc [132] with the fitted parameters of dC/dx and L_d, x_d is calculated using Eq.(15).

The resulting fitting curves and parameters for D#1 diode with and without heating and for D#2 diode are shown in Fig.95 a-c. The data series „Experiment" are the measured count rates. The „Drift count" curve arises from the first term of the equation indicating the signal contribution of the charges generated inside the detectors space charge region. The „Diffusion count" curve comes from the second term of the equation and provides the signal contribution of the diffusing minority charge carriers from the electrically neutral region of the diode. The sum of the count rate values from drift and diffusion signal is marked with „Drift + Diffusion". The fitted L_d parameters with D#1 diode at room temperature yields 0.96 μm and for the heated diode to 3.19 μm. These are close to the ones obtained with the first method at low bias voltage values (at -20 V, 1.32 μm at room temperature and 3.15 μm at 500 °C in Table VI.). A value of L_d of 8.67 μm is obtained for the D#2 diode, closest to the 7.78 μm calculated with the first method at 0 V. The differences of values between the two methods are less than 1 μm. In the figures it is also visible, that only the count number arising from drifting charge carriers increases linearly with the thickness of the space charge region. The signal for diffusing charge carriers behaves non-linear and its contribution to the collective signal increases with the calculated diffusion length.

Finally, applying the resulting diffusion lengths of 0.96 μm and 3.19 μm from the second method for the D#1 detector, the multiplication of the mobility and lifetime (μ*τ) in Eq.(37) can be calculated at different temperatures. Thus one obtains 35.76 $\mu m^2/V$ at room temperature and 152.79 $\mu m^2/V$ at 500 °C.

8.7 Simulation of the SiC detector signal for 14 MeV fast neutron irradiation

For fast neutron measurements with SiC semiconductor detector neutron converter layers are not required because several available reactions emitting charged particles, between fast neutrons and silicon and carbon nuclei exist. Thereby, the obtainable signal originates from the inner volume of the crystal and not from an additional neutron converter layer. The signal can have contributions from events inside and outside the sensitive volume depending on the path of the secondary charged particles. This consideration of the energy deposition is restricted to the generated secondary charged particles of a nuclear reaction and does not include the electron-hole pair generation processes inside the semiconductor material. Furthermore it localizes all the signal generation to the path of the secondary particles.

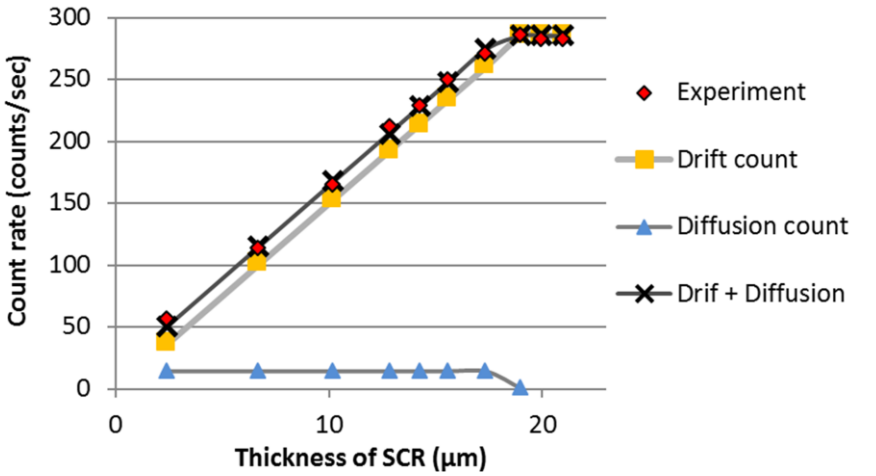

L_d = 0.96 µm

dC/dx = 14.98

D#1 diode at room temperature

a

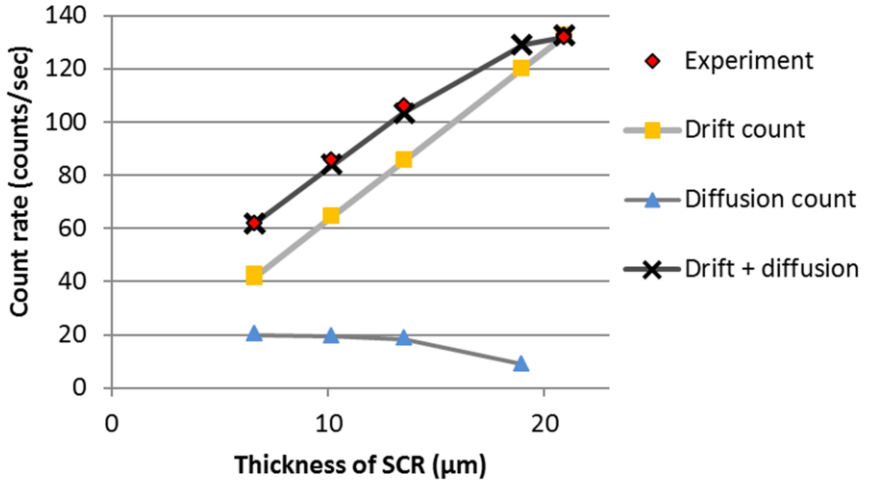

L_d = 3.19 µm

dC/dx = 6.32

D#1 diode at elevated temperatures

b

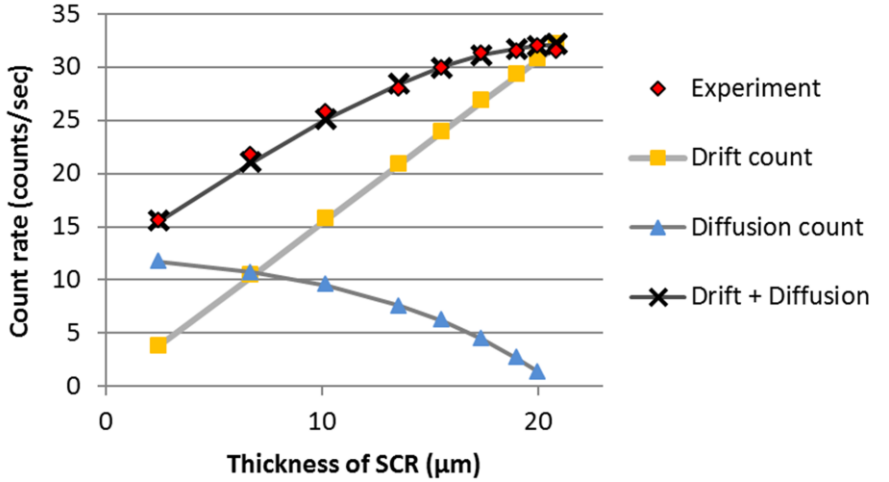

L_d = 8.67 µm

dC/dx = 1.53

D#2 diode at room temperature

c

Fig.95-a,b,c - Fitting of the experimental count rate values for D5-type diodes. The measured data are fitted with the sum of the calculated count rate contributions of drift and diffusion signal.

To support the analysis of the detector signal, Geant4 Monte Carlo simulations are developed. Although in the simulation the kinetic energy of the secondary particles is converted through ionization processes to detectable signals, these processes differ from the electron-hole pair creation process and collection in a real semiconductor sensor. The effect of the different concentration of charged carriers in the crystal on the carrier movement is also not included in the present simulations. Therefore, these Monte Carlo simulations provide information on the directly deposited kinetic energy of the secondary particles in the detector material, which could be detected with an idealized noise-less diode and electronics. The aim of these calculations is to understand the basic structures of the recorded pulse height spectra, the generating reactions and the contribution of the different sensor layers to the detector hits.

Here, the effect of the different detector thicknesses and detector layers on the signal with SiC is studied. The investigated diodes are not separated from the substrate wafer, on which they are formed, hence the impact of the surrounding wafer material is also considered in the calculations.

To create the initial set-up in Geant4 version 10.00, a macro file is used and the neutron source is described by the General Particle Source class (GPS) of the Geant4 code. The initial parameters of the calculations are set-up corresponding to real measurements. Regarding the detector position a neutron source ejects neutrons perpendicular to the surface of the sensor. A Gaussian distribution for neutron energy (mean value: 14.79 MeV, FWHM: 0.22 MeV, σ: 0.0934 MeV) has been applied. The neutron source is defined as a beam with circular cross-section and with 2 mm diameter. This beam fully overlaps with the applied active detector surface in the simulation. To check the developed geometry and source position VRML graphics are generated and displayed with Cortona3D software [85]. Using vector graphics enables to view all parts of the modelled sensor even if the layers have orders of magnitude difference in their spatial dimensions (e.g. more mm diameter of the sensor versus 250 nm thick gold layer).

The detector model for D5-type diode is a circular shaped detector with 2 mm diameter with different thicknesses. The detector is mounted inside a 200 μm thick SiC substrate volume with 2.2 mm diameter. Beyond the detector a 1 μm thick SiC layer with 2 mm diameter area is generated representing the p+ epilayer of the diode. The larger surface substrate is provided by a border ring around the active detector volume. A sketch of the D5 detector is shown in Fig.96.

8.7.1 Detector signal simulation

To reproduce the energy histogram a 20 μm thick sample of SiC detector is investigated with 14.8 MeV neutron irradiation using more than 256 million initial events. The obtained spectrum is compared to high count rate room temperature test results from Fig.83. The simulated and the measured pulse height spectra are depicted in Fig.97; both spectra have the same energy bin structure. The full energy peak of the reaction of $^{12}C(n,\alpha)^{9}Be$ occupies the same energy channels in both cases. The yellow color indicating the difference between measured and computed data displays a missing feature in Geant4 Monte Carlo

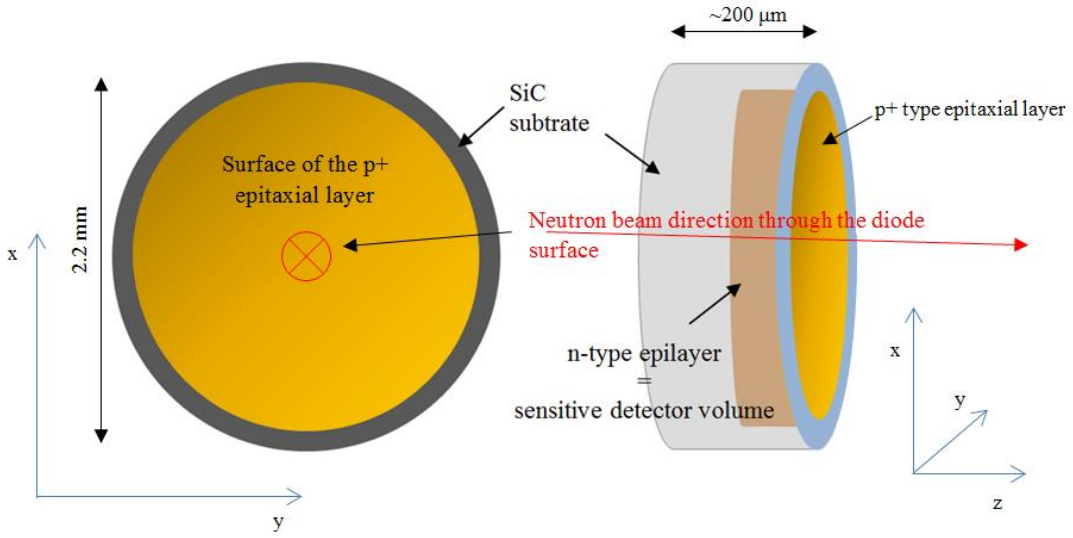

Fig.96 - Frontal and lateral view of the detector for fast neutron signal simulations. The thickness of the n-type epilayer/sensitive detector volume can vary from zero to 200 µm.

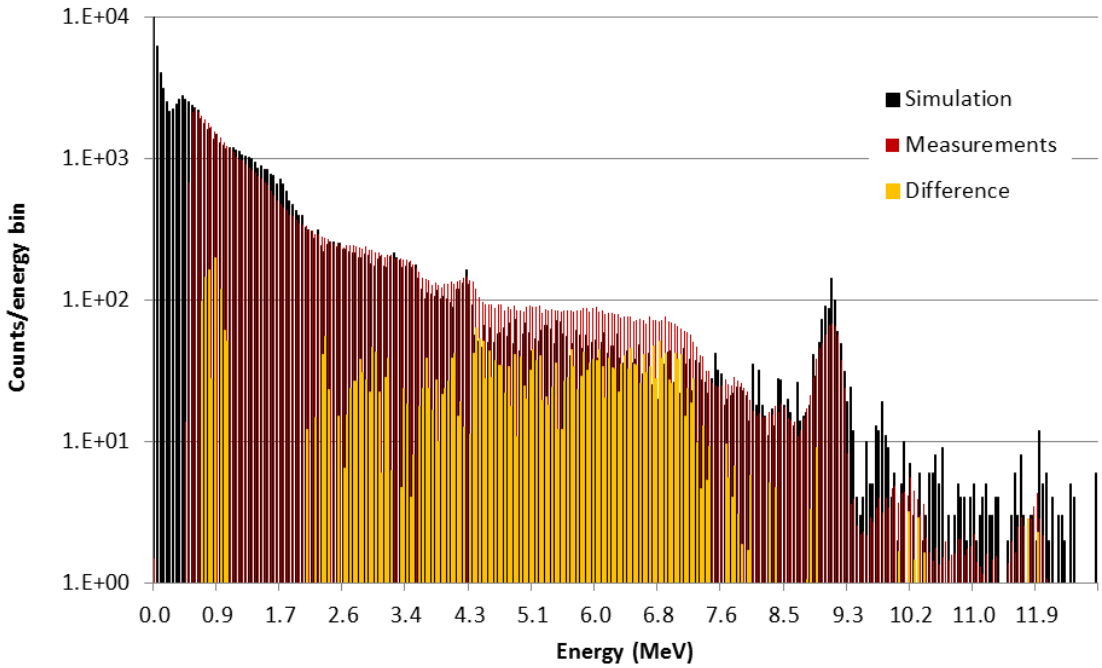

Fig.97 - Geant4 simulation of the signal of fast neutron irradiated SiC detector with high initial event number

simulation. This is the evaluation of the four-body reaction group of $^{12}C(n, n')3\alpha$ and also some excited state events from $^{28}Si(n,\alpha)^{25}Mg$. The additional signal structures are visible on the simulated histogram.

For a more detailed examination of the origin of the distinct signal parts, further calculations with a significantly larger, 1×1×1 cm^3 detector volume are carried out. The generated signal structures by the different main types of reactions are depicted separately for silicon, carbon and silicon-carbide target in

Fig.98, Fig.99 and Fig.100. The most striking structure is provided by the ground state $^{12}C(n,\alpha)^{9}Be$ reaction, as before. Although, the model of the cascade reaction $^{12}C(n,n')3\alpha$ is not included in Geant4, the reaction itself is existing in the neutron data library. Therein, the reaction is handled as a one-step inelastic event terminating in an excited state $^{12}C^*$ nucleus, which does not break further into three α-particles, [87]. The latter in reality can provide additional counts in the lower energy channels by the release of neutrons instead of three α-particles and one neutron at the same time. The generated structures by energy deposition of neutrons in the $^{12}C(n,n')3\alpha$ four body reactions are discussed in detail in [64]. The full energy peak associated with carbon nuclei at the highest energy is produced in the $^{13}C(n,\alpha)^{10}Be$ reaction. The inelastic neutron scattering reaction $^{12}C(n,n')^{12}C^*$ creates a well-defined edge with the threshold energy of ~4.2 MeV. This structure was also observed in the real measurements. Furthermore, these reactions significantly contribute to the count number in the lower energy channels up to ~7 MeV.

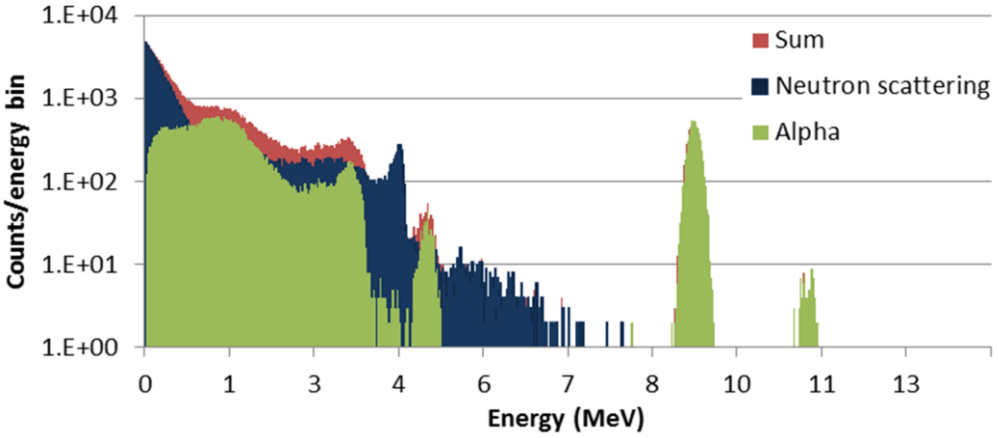

Fig.98 – Geant4 simulation of the computed count numbers and the corresponding energy deposition for 14.8 MeV incident neutron energy deposited in 1 cm^3carbon cube

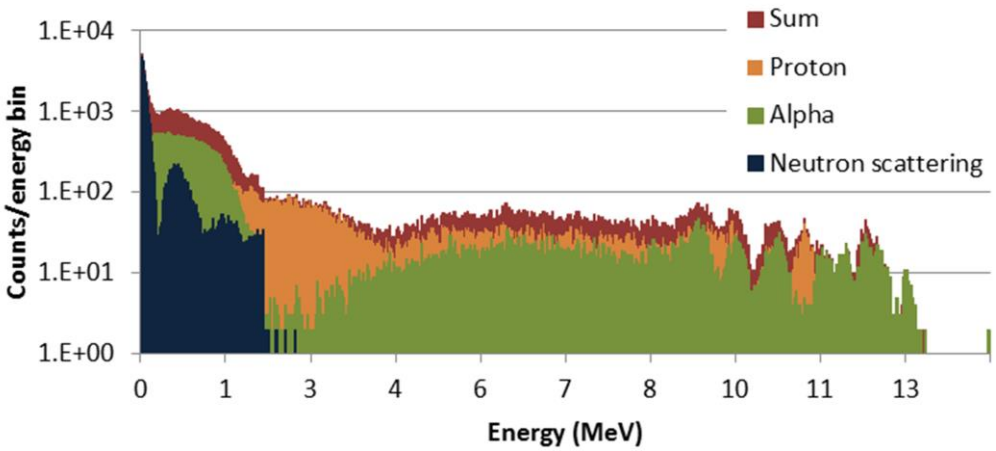

Fig.99 – Geant4 simulation of the computed count numbers and the corresponding energy deposition for 14.8 MeV incident neutron energy deposited in 1 cm^3silicon cube

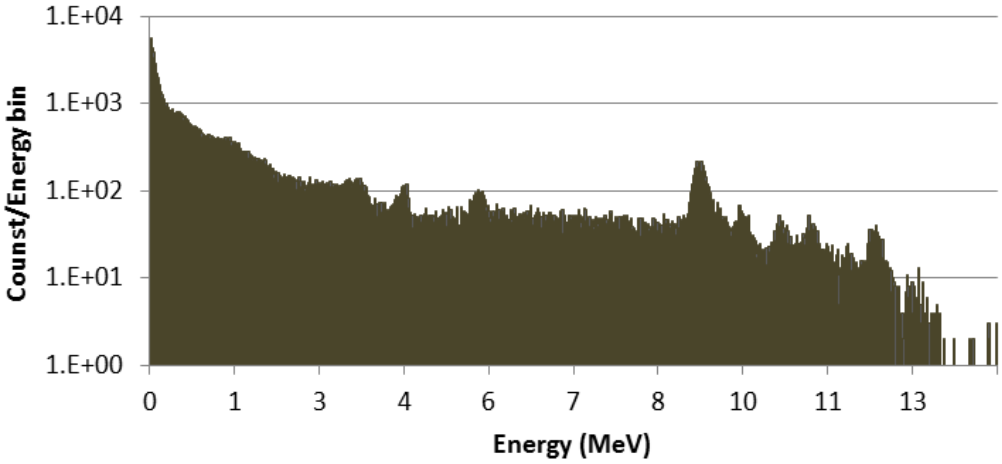

Fig.100 – Geant4 simulation of the computed count numbers and the corresponding energy deposition for 14.8 MeV incident neutron energy deposited in 1 cm^3silicon-carbide cube

Fast neutron reactions with silicon nuclei create several signal shapes in the energy histogram. At the low energy channels, some characteristic threshold energies can be identified due to scattering events. Beyond 0.2 MeV a distinct drop is observed. In case of low noise measurements with low signal discrimination level this structure can likely be observed. The main "body" of the simulated histogram is provided by events in the mid energy domain up of ~4-9 MeV and in the higher energy channels beyond 9 MeV, due to the (n, p) and (n, α) reactions with ^{28}Si. The mentioned higher energy peaks are clearly visible only in case of measurements using large area detectors (~20-25 mm^2) or with small detector areas at long irradiation times or at high neutron flux.

8.7.2 Influence of the reactions in surrounding wafer on the detector signal

Calculations are performed with and without SiC (SiC wafer in the real diode) around the active detector volume (n-type epilayer in the real diode). Sensitive volume thicknesses in the range of 1 μm up to 20 μm embedded inside the 200 μm thick substrate material are considered. Applying the accurate layer structures of the diodes including the wafer layer, more events are detected due to the secondary particles produced outside the sensitive volume and reaching it depending their kinetic energy. The ratio of the count number for 30 million source neutrons is compared for the different thicknesses. The computed count numbers without and with substrate and their ratios are depicted in Fig.101 and Fig.102.

The obtained count number for smaller sensitive volume thickness is mainly influenced by the events generated outside this volume and not by the inner events. In case of a 1 μm thickness only 26 % while with 20 μm thickness 79 % of the generated events arises from the sensitive volume. This effect occurs because in different nuclear reactions between 14 MeV neutrons and SiC, secondary particles (α, β, proton, neutron) with high kinetic energy are generated having several μm long path range. They can enter the sensitive region from outside.

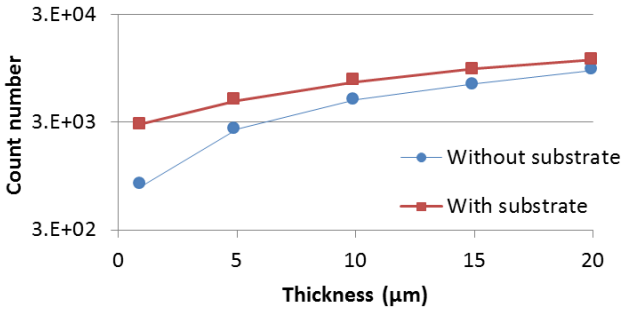

Fig.101 - Simulated count numbers as a function of the sensitive volume thickness with and without substrate layer (30 million simulated initial events).

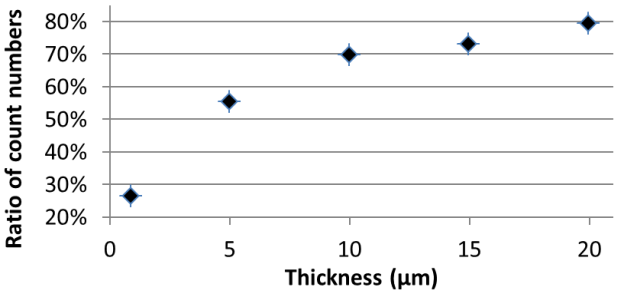

Fig.102 - Ratios of the simulated count numbers without and with SiC wafer around the sensitive detector

8.8 Summary of the measurements of fast neutrons at high temperatures

Several tests with 4H-SiC pn-diode detectors are conducted. The main goal is to clarify if 4H-SiC are an adequate detector material to perform neutron field characterization measurements at high temperatures as in a fusion reactor in particular in the ITER TBM. The change in the signal form, quality and stability at elevated temperatures is studied.

First tests with SiC detectors use a 1 mm^2 area D2-type pn-diode sensors up to 150 °C. Due to the small detector area neutrons leaving a DT neutron generator are detected in a narrow and defined energy range. The energy resolution of the recorded detector signal exhibits negligible differences throughout the temperature range and no signal shift in the energy histogram is observed.

Larger surface D5- and D6-type diodes are tested up to 500 °C. The D5-type diodes are supplied with a temperature resistant gold contact. The recorded energy histograms indicate different signal features arising from high energetic deep inelastic nuclear reactions, such as the full energy peak of $^{12}C(n,\alpha)^{9}Be$ reaction. An increasing thermal noise at high temperatures requires a reduced bias voltage to prevent the deterioration of the sensor. A stable energy resolution of the recorded histograms is obtained for all test temperatures. Nonetheless, applying the same -60 V biasing at all temperatures leads to a shift of the $^{12}C(n,\alpha)^{9}Be$ reaction

peak to higher energy channels and it suffers a broadening. A decrease of the count rate is obtained at higher temperatures and thinner depleted volumes. Simultaneously, a significant increase of the count rate per micrometer values is measured due to diffusion of the minority charge carriers, generated outside of detector space charge region. To evaluate the diffusion length of the minority carriers at different temperatures two methods are developed. Less than 1 μm difference of the diffusion length has been found between the two approaches. An increased diffusion length is observed at higher temperatures corresponding to results reported in literature. The stability of the detector count rate of the detector studied in a temperature range from 22 °C to 500 °C reveals a stable behavior. After repeated thermal treatments at 500 °C a deterioration of the metallic contacts on the diode electrodes is observed causing instability of the detector signal. This instability disappears after preparing new spring contacts on the two electrodes of the diode.

At the same bias voltages at different temperatures the D5-type diode exhibits almost equal count rates, as it is shown in Fig. 89 and Fig. 90. The number of counts at fixed neutron flux in the detector volume is determined by the applied bias voltage. In other words the thickness of the space charge region and less is hardly affected by the temperature level, although enough effect on the count rate occurs at higher temperature. Thereby it has been possible to identify the difference in the diffusion length, as well.

On the basis of the results obtained SiC detectors are capable to operate under harsh environmental conditions, such as long term thermal treatment at 500 °C. This supports future investigations of 4H-SiC devices as a prominent candidate detector material for industrial and scientific applications. The obtained results confirm that SiC detectors can be suitable devices for tritium yield measurements and neutron field characterization in ITER TBM during DD cycles and early low duty DT cycles.

9. MEASUREMENTS WITH 4H-SiC DETECTOR IN PERMANENT MAGNETIC FIELD

Detectors for application is fusion reactors should tolerate also high magnetic fields. The predicted strength of the magnetic field varies from inside the TBM up to the outer surface of the blanket between 4 Tesla and 11 Tesla. In the present work preliminary tests are performed to investigate the influence of the Hall-effect inside the detector on the recorded signal. In a magnetic field, semiconductors may behave as a Hall sensor due to the Lorentz force, which interacts with electrically charged particles. The higher the magnetic flux the stronger the Lorentz force gets. Tests in magnetic field up to ~1 Tesla are carried out with 14 MeV DT neutrons at the Neutron Laboratory of TU Dresden and up to 8 Tesla field with epithermal neutrons at the D3 facility of the Institut Laue-Langevin in Grenoble, France.

9.1 Fast neutron measurements under magnetic field up to 1 Tesla

Tests with D5 detector have been performed in three runs. In the first, the SiC diode has been irradiated without magnets inside the aluminum house. This measurement poses the reference to the further ones. In the second and third runs the magnet has been placed inside the box. The SiC diode has been positioned in the mid of the magnet central channels. For all the three runs measurements at three bias voltage levels, 0 V, 80 V and 200 V have been conducted.

Pulse height spectra at different bias voltage values and with different magnetic fields are shown in Fig.103 a, b and c. No remarkable difference with respect to the signal structure is observed by the existence of the magnetic field. Additionally, the count rate is examined for three magnetic conditions. In Fig.104 the measured count rates at different bias voltage values are shown, with and without neodymium ring magnets. The ratios of the count numbers from the measurements at -200 V and -80 V for the three magnetic fluxes are slightly increased. The ratio CPS_200V/CPS_80V without magnet is 1.335 and with the bigger magnet 1.403. The stability of the signal predicts that the velocity of the charge carriers in the depleted volume is near to or beyond the saturation velocity (the maximum velocity of a charge carrier in a semiconductor in the presence of high electric fields) [100, 101] thus the carriers from the sensitive volume are collected on the electrodes without loss. Small differences of the count numbers are attributed to the minority charge carriers from the surrounding crystal material without any external electric field. Due to the deflection and deceleration of electrons and holes in magnetic field, as well as the change in the diffusion length of the minority carriers, the recorded count number can change. To investigate the diffusion length values at the different magnetic fields, the same calculations are performed as in Eq.(39) for the count rates. The values of the diffusion length (L_d) decreases during the tests at higher magnetic field strength. Without any external magnetic field L_d is 1.99 μm. With the small magnet it decreases to 1.91 μm and with the bigger magnet to 1.78 μm. The results let conclude that the signal contribution of the minority charge carriers diffusing from the electrically neutral layers is slightly less at higher magnetic field strength values. From these results, it has been concluded that no significant effect of the external magnetic field on the diode signal can be observed up to ~1 Tesla.

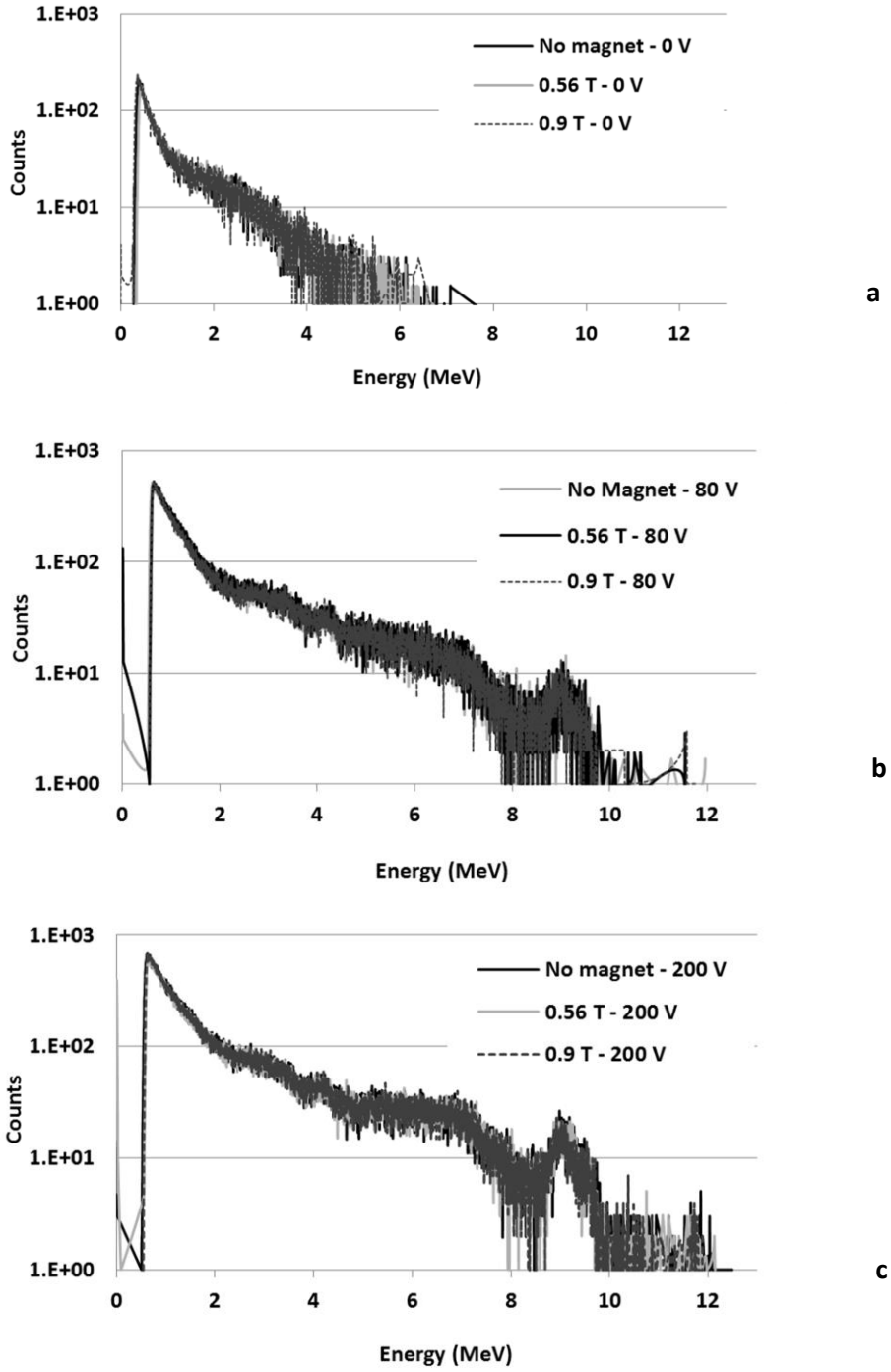

Fig.103 – Energy histograms recorded with SiC diode detector irradiated with 14 MeV fast neutrons in permanent magnetic field: *a* – with zero biasing on the diode; *b* – at -80 V bias voltage; *c* – at -200 V bias voltage

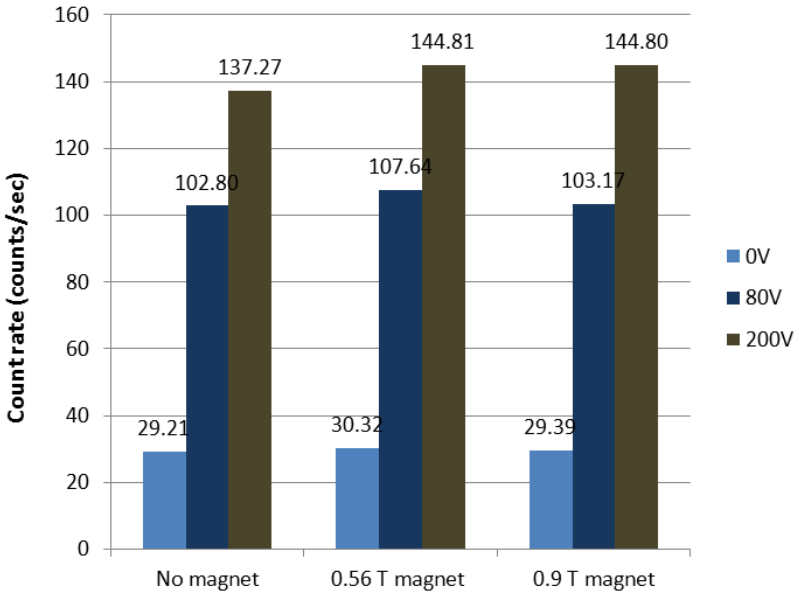

Fig.104 – Count rates for different magnetic field strength at three bias voltages.

9.2 Detector behavior in magnetic field up to 8 Tesla

During these tests the magnetic field has been set to 0, 5 and 8 Tesla. 40 V reverse bias voltage on the sensor have been supplied, which is enough to deplete the 20 μm thick n-type epitaxial layer of the boron doped D2 type diode used for these experiment. Significant noise was generated by the surrounding electronics, vacuum pump and stray capacitances. The amplified noise level from the diode was ~50 mV and can reach up to 200 mV, which is quite high. The applied low signal threshold level (5-8 mV) is not suitable to obtain a good quality signal, thereby only the nearly identical signal of epithermal neutrons at the different magnetic fluxes can be obtained from the recorded pulse height spectra. . Because of the noise, tests with lower threshold level lead to long measurement dead time around 50 %. In Fig.105 the bare energy histograms and in Fig.106 the histograms for 400 minutes recorded at 0, 5 and 8 T field are shown. The domain between the ~100th and ~350th channels appears in the presence of neutrons and does not change its position at higher magnetic fluxes. This structure is attributed to the energy deposition of α-particles from Reaction 2 (see in Section 6.4). The integrated count rate remains almost constant (~0.02-0.03 s^{-1}) for the energy channel range of the edge as well as for the whole histogram beyond the 120th channel. No clear correlation with respect to the magnetic strength is observed as illustrated in Fig.107.

The tests shows that even at high magnetic strength the SiC detector signal does not change significantly compared to the tests without external magnetic field.

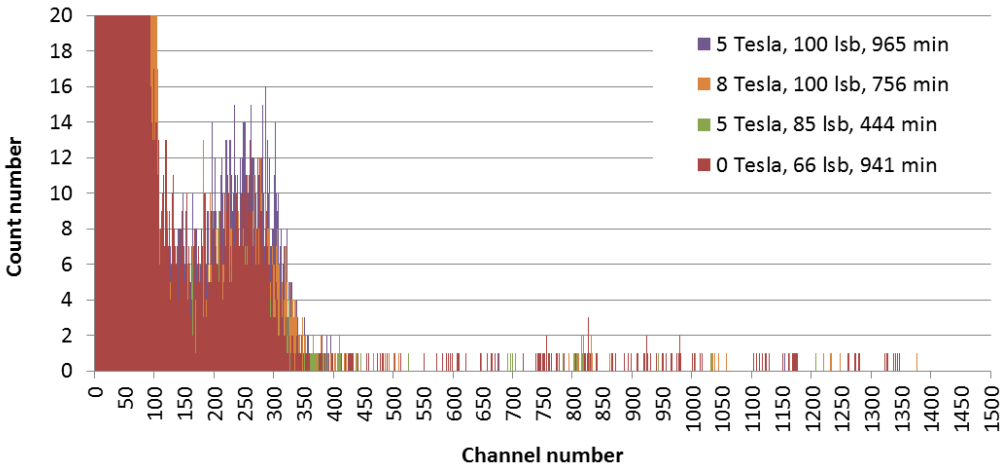

Fig.105 – Bare pulse height spectra with original measurement times recorded with epithermal neutron irradiated SiC diode detector at 0, 5 and 8 T magnetic field; lsb: least significant bit, which agrees with the threshold channel number

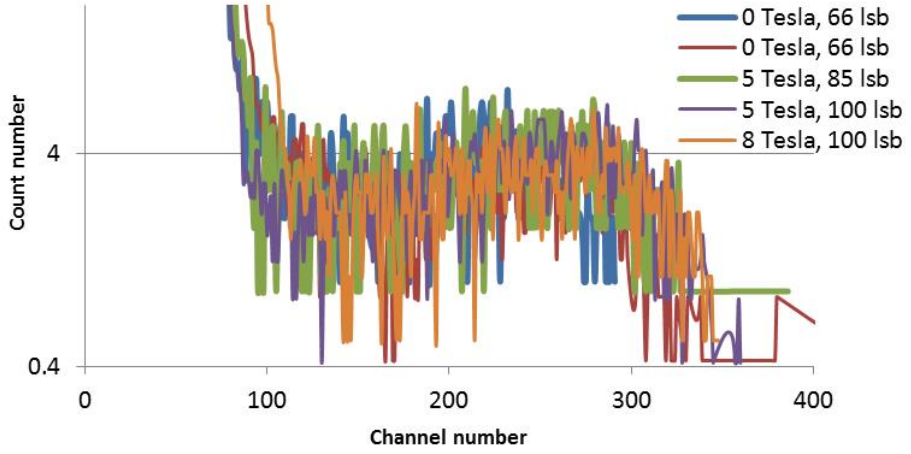

Fig.106 – Pulse height spectra normalized to 400 minute measurement time recorded with epithermal neutron irradiated SiC diode detector at 0, 5 and 8 T magnetic fields

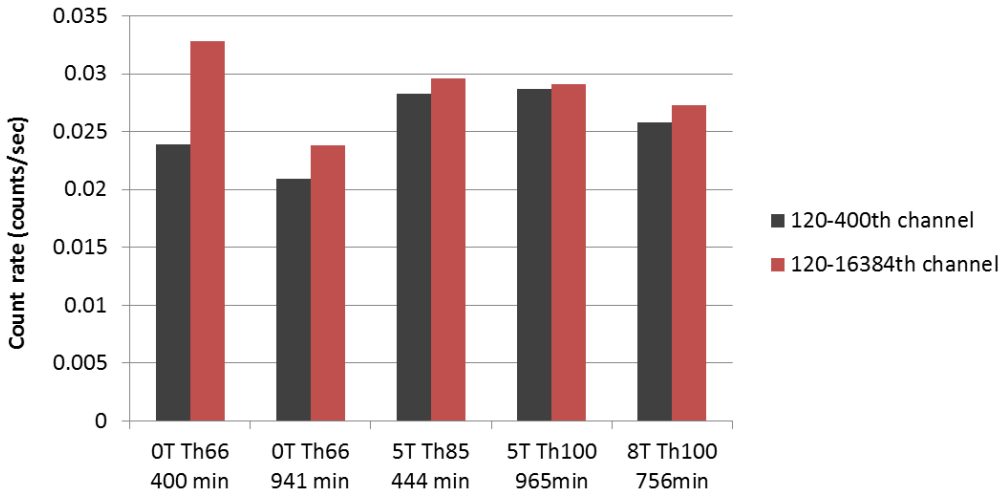

Fig.107 – Count rates for epithermal neutron irradiated SiC diode detector at 0, 5 and 8 T magnetic fields

9.3 Summary of the measurements in permanent magnetic field

The last two points show neutron irradiation experiments for 4H-SiC detector in permanent magnetic fields up to 8 Tesla. No remarkable differences between the recorded energy histograms with and without magnets have been observed. This meets the expected diode behavior in case of applying reverse bias. Even for low bias voltage a very high electric field is built through a thin volume. In case of 40 V the electric field is 2 MV/m in a 20 μm thick volume. According to the equations in Section 3.2 and in **Appendix F**, 8 Vsm^{-2} magnetic field strength is negligible compared to this high electric field and it is not enough to deflect electrons and holes.

The obtained pulse height spectra do not show any change of the signal caused by the high external magnetic field. Furthermore, the count number values remained stable during the tests.

CONCLUSIONS

The dissertation work contributes to a better understanding of signal processing of wide band-gap SiC nuclear detectors in harsh environmental conditions with the aim to development an adequate neutron diagnostics for applications in nuclear fusion reactors.

The main achievement of the present work is the successful demonstration of detector operation at 14 MeV fast neutron irradiation with 4H-SiC pn-diode sensor at temperatures up to 500 °C. With the application of the proper biasing conditions and long term thermal treatments up to 300 °C, several beneficial signal and sensor properties are observed. From the obtained results the following experiences are deduced:

1. The leakage current (in the present case the feedback DC-current measured with the applied detector electronics) of the sensor is decreased due to the long term annealing effect on the crystal defects in the SiC pn-diode. Additionally, the annealing process also may further improve the metallic contact's quality.
2. Limiting the high bias voltage on SiC pn-diode at all the external temperatures that the measured reverse current (the collective current generated by leakage, irradiation and thermal currents inside the diode) is maintained at the same low level, results in stable detector operation without breakdown and thermal run-away effects through the junction of the diode.
3. A further consequence of the regulated biasing at higher temperatures ensures stable signal structures in the recorded energy histograms for all temperatures up to 500°C. Thereby, a better signal resolution and smaller FWHM values are attained compared to the application of higher biasing and thus higher leakage current levels.
4. Even at 500°C ambient temperature the recorded energy histogram with 4H-SiC diode irradiated with 14 MeV neutrons has defined structures. Different signal parts originating from characteristic nuclear reactions can be identified and the still prominent $^{12}C(n,\alpha)^{9}Be$ full energy peak can be used to obtain information on the fast neutron spectrum.
5. Due to repeated high temperature thermal treatments the metallic contacts on the ohmic contacts of the diodes can irreversibly deteriorate and detach from the diode surface. After preparation of metallic contacts on the diode the normal detector operation can be restored.

The signal contribution of the minority charge carriers due to their diffusion motion from the electrically neutral region into the space charge region is observed for the fast neutron measurements. The effect is investigated and detailed in earlier research works with light ion irradiation of SiC detectors, where the recorded peak positions at different bias voltage values are studied and the diffusion length of the minority charge carriers are derived via a fitting function for charge pulse height calculations developed by M.B.H. Breese. Here, a new form of Breese's function is developed and applied to assess the diffusion length of holes in the n-type epitaxial SiC layer of the diodes. A new consideration of the evaluation of the diffusion length and fitting procedure for the collected counts at different biasing is developed. Applying the new fitting

function one can show that minority charge carriers in SiC pn-diode detector have ~2-3 times longer diffusion path length at 500°C than at room temperature; which is supported by observations reported in literature. This effect increases the charge collection at high temperature but at low bias voltage compared to the room temperature case with the same biasing.

In order to prepare more accurate simulation of the physical environment in the ITER-TBM, the investigations of 14 MeV fast neutrons with SiC detector have been expanded by measurements in permanent magnetic fields. Up to ~8 Tesla magnetic field perpendicularly arranged to the applied electrical field through the diode exhibit no significant change on the recorded detector signal. Furthermore, in tests with 14 MeV fast neutrons up to 1 Tesla field a slight decrease of the diffusion length value at higher magnetic fields is found.

A wide range of experiments with SiC diode detectors in thermal neutron field has been conducted. New types of thermal neutron sensitive SiC sensors supplied with ^{10}B-ion implanted neutron converter layer outside the electrically active diode layers are studied. Here, the D2-type detector with a small surface area has shown to be a proper thermal neutron sensor due to its geometrical conditions, low noise and good quality signal. The distance of the ^{10}B-ion implanted layer and the pn-junction in D2-type detector is large enough to avoid the penetration of secondary ^{7}Li-ions in to the sensitive n-type detector layer and the large part of the detector signal from $^{10}B(n,\alpha)^{7}Li$ reactions is generated only by α-particles. Thereby, less crystal defects can occur and a longer detector lifetime is achieved.

To support the explanation of the recorded signal of the different detectors, a library of the developed Geant4 Monte Carlo simulations is created, which contains the geometrical models of five investigated SiC diode sensor types, the applied physical processes, the output file creator code and macro files with different source conditions and graphical output ability. The code package is currently unique and represents a comprehensive collection of Geant4 Monte Carlo models of SiC nuclear detectors. Applying the developed models allows to predict the energy histograms which enables by comparison with experimental data to analyze the sensor results. Furthermore, these simulations can also be useful for SiC diode detector calibration procedure.

OUTLOOK

Despite the wide range of performed investigations with neutron irradiated SiC detectors, some interesting problem could not be examined in the present work, thereby further efforts and tests are still needed to the fully understand of wide band-gap nuclear detectors between different harsh environmental conditions. The measurements carried out during the three years of the dissertation work for the basis and indicate the direction of further developments and experiments.

In the point of view of fusion diagnostics important tasks what should be investigated in the future works are:

- Thermal and epithermal neutron detection at elevated temperatures, in addition the proper position and formation of the thermal neutron converter layer on or inside the SiC sensor

- The effect of high temperature on SiC diode detector beyond 500°C, which requires professional high temperature standing sensor encapsulation and diode contacts

- The effect of high neutron flux and yield at elevated temperatures on SiC detectors; these measurements should be carried out in high performance irradiation facilities

- Precise examination of neutron irradiated SiC diode detectors in high magnetic field up to 10-11 Tesla

- The effect of alternating high magnetic field on the SiC detector signal

To perform these tests, several diverse environments and developments are necessary, but after creating them we could have a comprehensive view about the possibilities and limitations of the application of SiC diode detectors in fusion diagnostics.

REFERENCES

[1] https://www.iter.org/ , last accessed on 9th March, 2019

[2] "On the way to fusion power Energy news", Newsletter of the KIT Energy Center, Issue 1, pp. 16-17, 2014, available on: https://www.energy.kit.edu/downloads/08_ENERGYNEWS_-_Version_1-2014_(Internet).pdf, last accessed on 9th March, 2019

[3] "Tritium: Changing, Lead Into Gold", ITER Organization Magazine, Febr. 2016, available on: https://www.iter.org/doc/www/content/com/Lists/Mag%20Issue%20Index/Attachments/14/magazine_8_feb_2016.pdf, last accessed on: 9th March, 2019

[4] A. Klix, M. Angelone, U. Fischer, D. Gehre, B. Ghidersa, A. Lyoussi, P. Raj, Th. Reimann, D. Szalkai, K. Tian "Neutron Measurement Instrumentation Development at KIT for the European ITER TBM", 2015 4th International Conference on Advancements in Nuclear Instrumentation Measurement Methods and their Applications (ANIMMA), Lisbon Congress Center, Lisbon, Portugal, 20-24. April 2015, Presentation ID: #339, doi: 10.1109/ANIMMA.2015.7465635, May 2016

[5] http://www.agence-nationale-recherche.fr/Project-ANR-12-EITE-0004, last accessed on: 9th March, 2019

[6] L.M. Giancarli, M. Abdou, D.J. Campbell, V.A. Chuyanov, M.Y. Ahn, M. Enoeda, C. Pan, Y. Poitevin, E. Rajendra Kumar, I. Ricapito, Y. Strebkov, S. Suzuki, P.C. Wong, M. Zmitko "Overview of the ITER TBM Program", Original Research Article, Fusion Engineering and Design, Vol. 87, Issues 5–6, pp. 395-402, Aug. 2012

[7] L. V. Boccaccini, A. Aiello, O. Bede, F. Cismondi, L. Kosek, T. Ilkei, J. -. F. Salavye, P. Sardain, L. Sedano "Present status of the conceptual design of the EU test blanket systems", Fusion Engineering and Design, Vol. 86, Issues 6–8, pp. 478-483,Oct. 2011

[8] C. Mistrangelo, L. Bühler "Influence of helium cooling channels on magnetohydrodynamic flows in the HCLL blanket", Fusion Engineering and Design Vol. 84, Issues 7–11, pp. 1323–1328, June 2009

[9] P. Raj, M. Angelone , U. Fischer, A. Klix "Computational study of a chromium self-powered detector for neutron flux monitoring in the test blanket module of ITER", Nuclear Inst. and Methods in Physics Research A, Vol. 908, pp. 10–17, Aug. 2018

[10] G. F. Knoll "Radiation Detection and Measurement", Third edition, Wiley India Pvt. Ltd., ISBN: 978-81-265-2260-6, pp. 528-533, 2012

[11] B. Gudden, R. Pohl "Das quantenaquivalent bei der lichtelektrischen Leitung", Zeitschrift für Physik Vol. 17, Issue 1, pp. 331–346, Dec. 1923

[12] D. R. Kania "Diamond Radiation Detectors I. Detector Properties for IIa Diamond", Proceedings of the International Summer School of Physics “Enrico Fermi”, Bologna, Italy, July 30-August 2, 1996, Lawrence Livermore National Lab., UCRL-JC-127288-Pt.1 Preprint, May 1997

[13] D. R. Kania, M. I. Landstrass, M. A. Plano, L. S. Pan, S.Han "Diamond radiation detectors", Diamond and Related Materials, Vol. 2, Issues 5–7, pp. 1012–1019, April 1993

[14] R.V. Babcock, H.C. Chang "SiC Neutron Detectors for High Temperature Operation, Neutron Dosimetry", Proceedings of the Symposium on Neutron. Detection, Dosimetry and Standardization, Vol. 1, IAEA, Vienna, pp. 613-622, Dec. 1962

[15] Dr. W. Windl, T. Blue "SiC Schottky Diode Detectors for Measurement of Actinide Concentrations from Alpha Activities in Molten Salt Electrolyte" NEUP 09-842 project final report, Project Period: October 1, 2009 through October 31, 2012; published at IAEA-INIS, Instrumentation related to nuclear science and technology (S46), INIS Vol. 47, INIS Issue 21, Reference Number: 47066545, 2013

[16] E. V. Kalinina, A. M. Ivanov, N. B. Strokan, A. A. Lebedev "Structure and characteristics of the high-temperature SiC detectors based on Al ion-implanted p+–n junctions", Semiconductor Science and Technology, Vol. 26, Issue 4, doi: 10.1088/0268-1242/26/4/045001, Febr. 2011

[17] S. Seshadri, Abdul R. Dulloo, Frank H. Ruddy, John G. Seidel L. B. Rowland "Demonstration of an SiC Neutron Detector for High-Radiation Environments", IEEE Transactions on Electron Devices, Vol. 46, Issue 3, pp. 567 – 571, March 1999

[18] Z. Lin, Z. Yimen, Z. Yuming, H. Chao "Neutron radiation effect on 4H-SiC MESFETs and SBDs", Journal of Semiconductors", Vol. 31, Issue 11, doi: 10.1088/1674-4926/31/11/114006, Nov. 2010

[19] F. H. Ruddy, A. R. Dulloo, J. G. Seidel, M. K. Das, S.-H. Ryu, A. K. Agarwal "The Fast Neutron Response of 4H-Silicon Carbide Semiconductor Radiation Detectors", IEEE Transactions on Nuclear Science, Vol. 53, Issue 3, pp. 1666 – 1670, June 2006

[20] F. H. Ruddy, J. G. Seidel, A. R. Dulloo "Fast Neutron Dosimetry and Spectrometry Using Silicon Carbide Semiconductor Detectors", Journal of ASTM International, Vol. 3, Issue 3, doi: 10.1520/JAI13452, March 2006

[21] D. S. McGregor ,M.D. Hammig, Y.-H. Yang, H. K. Gersch, R.T. Klann "Design considerations for thin film coated semiconductor thermal neutron detectors—I: basics regarding alpha particle emitting neutron reactive films", Nuclear Instruments and Methods in Physics Research Section A: Accelerators, Spectrometers, Detectors and Associated Equipment, Vol. 500, Issues 1–3, pp. 272–308, March 2003

[22] D. S. McGregor, R. T. Klann, H. K. Gersch, J. D. Sanders, "Designs for thin-film-coated semiconductor thermal neutron detectors", 2001 IEEE Nuclear Science Symposium Conference Record (Cat. No.01CH37310), San Diego, CA, USA, 4-10 Nov. 2001, Presentation ID: R16-4, Vol.4, pp. 2454-2458, Aug. 2002

[23] D. S. McGregor, S. M. Vernon, H. K. Gersch, S. M. Markham, S. J. Wojtczuk, D. K. Wehe "Self-biased boron-10 coated high-purity epitaxial GaAs thermal neutron detectors", IEEE Transactions on Nuclear Science, Vol. 47, Issue 4, pp. 1364 – 1370, Aug. 2000

[24] A. Dulloo, F. Ruddy, J. Seidel, J. Adams, J. Nico, D. Gilliam "The Thermal Neutron Response of Miniature Silicon Carbide Semiconductor Detectors", Nuclear Instruments and Methods in Physics Research A, Vol. 498, Issues 1-3, pp. 415-423, Febr. 2003

[25] H. S. Kim, J. H. Ha, S. Park, S. W. Lee, M. K. Moon, G. Sun, C. H. Lee "Characteristics of Fabricated Neutron Detectors Based on a SiC Semiconductor", Journal of Nuclear Science and Technology, Vol. 48, Issue 10, pp. 1343-1347, Jan. 2012

[26] F. Franceschini, F. H. Ruddy "Silicon Carbide Neutron Detectors" in "Properties and Applications of Silicon Carbide" edited by Prof. R. Gerhardt, InTech, available on: http://www.intechopen.com/books/properties-and-applications-of-silicon-carbide/silicon-carbide-neutrondetectors, ISBN: 978-953-307-201-2, pp. 275-296, April 2011

[27] R. F. Pierret, G. W. Neudeck "Modular Series on solid state devices, Volume VI: Advanced Semiconductor Fundamentals", Second Edition, Purdue University, ISBN: 978-0130617927, pp. 8-13, Aug. 2002

[28] http://www.xtal.iqfr.csic.es/Cristalografia/parte_03_4-en.html, last accessed on 9th March 2019

[29] M. De Napoli "Silicon carbide radiation detectors", Nova Science Publisher, Inc., ISBN: 9781612096001, pp.18 and 87, 2011

[30] M. Wijesundara, R. Azevedo "Silicon Carbide Microsystems for Harsh Environments", Springer-Verlag New York, Prentice, ISBN: 978-1-4419-7120-3, pp. 15, 2011

[31] C. Kittel "Introduction to solid state physics", Eighth edition, John Wiley & Sons, Inc., ISBN: 0-471-41526-X, pp. 163-183, 2005

[32] S. M. Sze, Kwok K. Ng "Physics of Semiconductor Devices", Third Edition, John Wiley & Sons, Inc. ISBN: 978-0-471-14323-9, pp. 51-54, 2007

[33] M. Fox "Optical Properties of solids", Oxford University Press, ISBN 0 19 850613 9, pp. 51, 2001

[34] H. Spieler "Semiconductor Detector Systems", Oxford University Press, ISBN: 978–0–19–852784–8, pp. 85, 2005

[35] "SiC Power Devices and Modules", Application Note, Rev.001, ROHM Semiconductor, June 2013, available on: https://www.rohm.com/documents/11303/2861707/sic_app-note.pdf, last accessed on: 9th March 2019

[36] L. S. Pan, D. R. Kania "Diamond: Electronic Properties and Applications", Springer Science & Business Media, Technology & Engineering, ISBN: 978-1-4613-5951-7, pp. 1-29, 1995

[37] http://www.ioffe.ru/SVA/NSM/Semicond/Ge/electric.html, last accessed on: 9th March 2019

[38] http://www.ioffe.ru/SVA/NSM/Semicond/InP/electric.html, last accessed on: 9th March 2019

[39] A. Kumar, M S Aspalli "SiC: An advanced semiconductor material for power devices", IJRET: International Journal of Research in Engineering and Technology, Vol. 3, Special Issue: 3, NCRIET-2014, pp. 248-252, May 2014

[40] M. Willander, M. Friesel, Q. Wahab, B. Straumal "Silicon carbide and diamond for high temperature device applications", Journal of Materials Science: Materials in Electronics, Volume 17, Issue 1, pp. 1-2, Jan. 2006

[41] B. Ozpineci, L. M. Tolbert "Comparison of Wide-Bandgap Semiconductors for Power Electronics Applications", Technical Report, Oak Ridge National Laboratory, ORNL/TM-2003/257, doi: 10.2172/885849, Jan. 2004

[42] M. E. Levinshtein, S. L. Rumyantsev, M. S. Shur "Properties of Advanced Semiconductor Materials GaN, AlN, SiC, BN, SiC, SiGe", John Wiley & Sons, Inc., New York, ISBN: 978-0-471-35827-5, pp. 93-148, Jan. 2001

[43] DI M. Friedl "The CMS Silicon Strip Tracker and its Electronic Readout", doctoral thesis, Department of Electrical Engineering ,Vienna University of Technology, Vienna, pp. 14, May 2001

[44] M. V. S. Chandrashekhar, C. I. Thomas, M. G. Spencer "Measurement of the mean electron-hole pair ionization energy in 4H SiC", Applied Physics Letter, Vol. 89, Issue 4, 042113, doi: 10.1063/1.2243799, July 2006

[45] T. R. Garcia, A. Kumar, B. Reinke, T. E. Blue, W. Windl "Electron-hole pair generation in SiC high-temperature alpha particle detectors", Applied Physics Letters, Vol. 103, Issue 15, 152108, doi: 10.1063/1.4824774, Oct. 2013

[46] S. K. Chaudhuri, K. J. Zavalla, K. C. Mandal "Experimental determination of electron-hole pair creation energy in 4H-SiC epitaxial layer: An absolute calibration approach", Applied Physics Letters, Vol. 102, Issue 3, 031109, doi: 10.1063/1.4776703, Jan. 2013

[47] A. L. Giudice, F. Fizzotti, C. Manfredotti, E. Vittone, F. Nava "Average energy dissipated by mega-electron-volt hydrogen and helium ions per electron-hole pair generation in 4H-SiC", Applied Physics Letters Vol. 87, Issue 22, 222105, doi: 10.1063/1.2135507, Nov. 2005

[48] G. Bertuccio, R. Casiraghi "Study of silicon carbide for X-ray detection and spectroscopy", IEEE Transactions on Nuclear Science, Vol. 50, Issue 1, pp. 175-185, Febr. 2003

[49] C. A. Klein "Bandgap Dependence and Related Features of Radiation Ionization Energies in Semiconductors", Journal of Applied Physics, Vol. 39, Issue 4, pp. 2029-2038, March 1968

[50] U. Fano "On the Theory of Ionization Yield of Radiations in Different Substances", Physical Review, Vol. 70, Issues 1-2, pp. 44-52, July 1946

[51] U. Fano "Ionization Yield of Radiations. II. The Fluctuations of the Number of Ions", Physical Review, Vol. 72, Issue 1, pp. 26-29, July 1947

[52] F. Ren, J. C. Zolper "Wide Energy Bandgap Electronic Devices", World Scientific, ISBN: 981-238-246-1, pp. 344, Jan. 2003

[53] B. Jayant Baliga "Fundamentals of Power Semiconductor Devices", Springer, ISBN: 978-0-387-47313-0 pp. 26, Apr. 2010

[54] T. Erlbacher "Lateral Power Transistors in Integrated Circuits", Springer, ISBN: 978-3-319-00500-3, pp. 182-183, Oct. 2014

[55] "Silicon Carbide Power Device Projects", Technical report of SAMCO http://www.samcointl.com/tech_notes/pdf/TechnicalReport73.pdf, last accessed on 12th March 2019

[56] https://upload.wikimedia.org/wikipedia/commons/f/fa/Pn-junction-equilibrium-graphs.png, last accessed on 12nd March 2019

[57] http://www.globalsino.com/micro/1/1micro9833.html, last accessed on 12nd March 2019

[58] K. Sheng "Maximum Junction Temperatures of SiC Power Devices", Electron Devices, IEEE Transactions on Electron Devices , Vol.56, Issue 2, pp. 337-342, Febr. 2009

[59] C. Buttay , C. Raynaud , H. Morel , M. Lazar, G. Civrac , D. Bergogne "High-temperature behavior of SiC power diodes," Proceedings of the 2011-14th European Conference on Power Electronics and Applications, Power Electronics and Applications (EPE 2011), Birmingham, UK, 30 Aug.-1 Sept. 2011, Presentation Id: 191, pp. 1-9, Sept. 2011

[60] V. V. N. Obreja "On the Reliability of Power Silicon Rectifier Diodes above the Maximum Permissible Operation Junction Temperature", 2006 IEEE International Symposium on Industrial Electronics, IEEE ISIE, Montréal, Québec, Canada, July 9-12. 2006, doi: 10.1109/ISIE.2006.295743, Jan. 2007

[61] G. Lutz "Semiconductor Radiation Detectors Device Physics", Springer, 2nd printing of the 1st ed., ISBN: 978-3-540-71678-5, pp. 7-37, 1999

[62] K. N. Muhin "Experimental Nuclear Physics: Physics of Atomic Nucleus", Volume I, Volume II, Mir Publishers, Nuclear models, ISBN: 978-0714724577, Chapter V, Sections 28-30, 1987

[63] W. D. Loveland, D. J. Morrissey, G. T. Seaborg "Modern Nuclear Chemistry", John Wiley & Sons, Inc., ISBN: 978-0-471-11532-8, pp. 249-253, 2006

[64] K. Kondo, I. Murata , K. Ochai, N. Kubota, H. Miyamaru, C. Konno, T. Nishitani "Measurement and Analysis of Neutron-Induced Alpha Particle Emission Double-Differential Cross Section of Carbon at 14.2 MeV", Journal of Nuclear Science and Technology, Vol. 45, Issue 2, pp. 103-115, Febr. 2008

[65] Y.-C. Hsu, C.-Y. Huang, S.-Y. Lin, Y.-C. Hsu, M.-C.Chou "$^{12}C(n,a)^{9}Be$ Reaction at 14.1 MeV", Chinese Journal of Physics, Vol.7, Issue 1, pp. 1-6, Apr. 1969

[66] http://www.nndc.bnl.gov/endf/b7.1/, last accessed on 12nd March 2019

[67] J.K. Shultis, D.S. McGregor "Calculation of ion energy-deposition spectra in silicon, lithium-fluoride, boron, and boron-carbide", Report 299 Engineering Experiment Station, Department of Mechanical and Nuclear Engineering Kansas State University Manhattan, July 2007, available on: https://www.mne.k-state.edu/~jks/papers/EESrpt299.pdf, last accessed on 12nd March 2019

[68] G. Leinweber, D. P. Barry, M. J. Trbovich, J. A. Burke, N. J. Drindak, H. D. Knox, R. V. Ballad, R. C. Block, Y. Danon, L. I. Severnyak "Neutron Capture and Total Cross-Section Measurements and Resonance Parameters of Gadolinium", Nuclear Science and Engineering, Vol. 154, Issue 3, pp. 261–279, Apr. 2006

[69] D.I. Garber and R.R. Kinsey "Neutron Cross Sections", Third edition, BNL-325 Report, Vol. 2, 1976

[70] "Neutron Yield Measurements via Aluminum Activation", Technical Report Resource Relation, Brookhaven National Lab., Upton, NY (US), reference number at INIS-IAEA: 32061890, INIS Vol. 32, INIS Issue 48, doi:10.2172/762101, Dec 1999, available on: https://www.osti.gov/servlets/purl/762101-9atmIP/webviewable/, last accessed on 12nd March 2019

[71] "ENSDF Decay Data in the MIRD (Medical Internal Radiation Dose) Format for ^{28}Al", Oct. 2013, available on: https://www.nndc.bnl.gov/useroutput/28al_mird.html, last accessed on 12nd March 2019

[72] H. T. Motz, D. E. Alburger "Beta- and Gamma-Radiation of Al^{28}", Physical Review, Vol. 86, Issue 2, pp. 165-167, April 1952

[73] "Review of the Physics of Semiconductor Detectors" ORTEC, available on: https://www.ortec-online.com/-/media/ametekortec/other/review_of_the_physics_of_semiconductor_detectors.pdf, last accessed on 12nd March 2019

[74] F. Issa1, L. Ottaviani, V. Vervisch, D. Szalkai, L. Vermeeren, A. Lyoussi, A. Kuznetsov, M. Lazar, A. Klix, O. Palais, R. Ferone, A. Hallén "Study of the stability of 4H-SiC detectors by thermal neutron irradiation", Materials Science Forum, Main theme: Silicon Carbide and Related Materials 2014, Vol. 821-823, pp. 875-878, June 2015

[75] F. Laariedh, M. Lazar, P. Cremillieu, J. Penuelas, J.L. Leclercq, D. Planson "The role of nickel and titanium in the formation of ohmic contacts on p-type 4H–SiC", Semiconductor Science and Technology, Vol. 28, Issue 4, doi: 10.1088/0268-1242/28/4/045007, Febr. 2013

[76] F. Issa, V. Vervisch, L. Ottaviani, D. Szalkai, L. Vermeeren, A. Lyoussi, A. Kuznetsov, M. Lazar, A. Klix, O. Palais, A. Hallen "Radiation Silicon Carbide Detectors Based on Ion Implantation of Boron", IEEE Transaction on Nuclear Science, Vol. 61, Issue 4, pp. 2105-2111, Aug. 2014

[77] V. Vervisch, F. Issa , L. Ottaviani, D. Szalkai, L. Vermeeren, A. Klix, A. Hallen, A. Kuznetsov, M. Lazar, A. Lyoussi "Nuclear radiation detector based on ion implanted p-n junction in 4H-SiC", 3rd International Conference on Advancements in Nuclear Instrumentation (ANIMMA), Measurement Methods and their Applications, 23-27. June 2013, Marseille, France, Conference Record, IEEE, doi: 10.1109/ANIMMA.2013.6728002, Jan. 2014

[78] F. Issa, L. Ottaviani, D. Szalkai, L. Vermeeren, V. Vervisch, A. Lyoussi, R. Ferone, A. Kuznetsov, M. Lazar, A. Klix, O. Palais "4H-SiC Neutron Sensors Based on Ion Implanted ^{10}B Neutron Converter Layer", IEEE Transactions on Nuclear Science, Vol .63, Issue 3, pp. 1976 – 1980, June 2014

[79] http://geant4.web.cern.ch/geant4/, last accessed on 12nd March 2019

[80] http://geant4-userdoc.web.cern.ch/geant4-userdoc/UsersGuides/IntroductionToGeant4/html/index.html, last accessed on 12nd March 2019

[81] http://www.srim.org/, last accessed on 12nd March 2019

[82] J. F. Ziegler, J. P. Biersack, M. D. Ziegler "SRIM - The Stopping and Range of Ions in Matter", Version no. 7, SRIM Co., ISBN: 978-0-9654207-1-6, pp. 7-1 – 7-35, 2008

[83] https://www.visualstudio.microsoft.com/, last accessed on 12nd March 2019

[84] http://www.cmake.org/, last accessed on 12nd March 2019

[85] http://www.cortona3d.com/en/products/authoring-publishing-solutions/cortona3d-viewers, last accessed on 12nd March 2019

[86] http://hypernews.slac.stanford.edu/HyperNews/geant4/cindex, last accessed on 12nd March 2019

[87] Z. S. Hartwig , P. Gumplinger "Simulating the optical physics of nonlinear scintillation detectors with Geant4", Nuclear Instruments and Methods in Physics Research Section A, Vol. 737, pp. 155-162, Febr. 2014

[88] http://www.virginia.edu/ep/SurfaceScience/ion-surf.html, last accessed on 14th March 2019

[89] Kinchin, R. S. Pease "Reports on Progress in Physics", Vol. 18, pp. 1-48, 1955

[90] J. V. der Auwera, G. Stiennon, J. Goens, L. de Heem, baron E. M. de Dorlodot, P. Marien, C. Gerard, F. Léonard, Brochure of the "50th anniversary BR1", report number: CL-3, 2006, available on: http://science.sckcen.be/~/media/Files/Public/Publications/BR1_historybrochure.pdf?la=en, last accessed on: 14th March 2019

[91] J. Wagemans, E. Malambu, L. Borms "The Neutron Standard Fields at the BR1 Reactor at SCK•CEN", Journal of ASTM International, Vol. 9, Issue 3, pp. 1-7, March 2012

[92] http://www.fastcomtec.com/fwww/datashee/amp/ta1000b.pdf, last accessed on: 14th March 2019

[93] https://mirion.s3.amazonaws.com/cms4_mirion/files/pdf/spec-sheets/2004-semiconductor-detector-preamplifier.pdf?1523635306, last accessed on: 14th March 2019

[94] https://www.caen.it/sections/, last accessed on: 14th March 2019

[95] http://www.ortec-online.com/products/electronics/power-supplies-and-nuclear-instrument-module-nim-bins/660, last accessed on: 14th March 2019

[96] https://www.fastcomtec.com/, last accessed on: 14th March 2019

[97] "Application Note AN250-2, Rev. 3.", available on: http://amptek.com/a250-charge-sensitive-preamplifier-application-note/, last accessed on: 14th March 2019

[98] https://www.kjmagnetics.com/calculator.asp, last accessed on: 14th March 2019

[99] J Woźny, Z Lisik, J Podgórski "Hall Mobility Maps for 4H-Silicon Carbide by Monte Carlo Simulations", MicroTherm'2013 — Microtechnology and Thermal Problems in Electronics, Lodz, Poland, on 25–28. June 2013, Institute of Physics Publishing (IOP), Journal of Physics: Conference Series, Vol. 494, conference 1, ISBN: 978-1-63266-719-9, doi: 10.1088/1742-6596/494/1/012005, Aug. 2014

[100] R. K. Willardson, E. R. Weber, Y. S. Park, "SiC Materials and Devices – Semiconductors and semimetals", Academic Press, ISBN: 0-12-752160-7, Vol. 52, pp. 77-81, 1998

[101] S. Selberherr "Analysis and Simulation of Semiconductor Devices", Springer, ISBN: 978-3-7091-8754-8, pp. 93, 1984

[102] "The Yellow Book 2005 Guide to Neutron Research Facilities", available on: http://rencurel.essworkshop.org/documents/YellowBookCDrom/data/5_1_1.pdf, last accessed on 15th March 2019

[103] http://science.sckcen.be/en/Services/Irradiations/Neutron_gamma_BR1, last accessed on 15th March 2019

[104] S. G. Arutunian, J. Bergoz, M. Chung, G. S. Harutyunyan, E. G. Lazareva "Proposal of thermal neutron flux monitors based on vibrating wire", arxiv.org, arXiv:1502.04050, Feb. 2015

[105] L. Lebreton, A. Zimbal, D. Thomas "Experimental comparison of 241Am-Be neutron fluence energy distributions", Radiation Protection Dosimetry, Vol. 126, Issues 1 – 4, pp. 3–7, May 2007

[106] C.- K. C. Wang "Progress in Californium-252 Neutron Brachytherapy", in K. Kishi "Brachytherapy", IntechOpen, ISBN: 978-953-51-0602-9, doi: 10.5772/34172, Apr. 2012

[107] A. Klix, U. Fischer, D. Gehre "Analysis of Induced Gamma Activation by D-T Neutrons in Selected Fusion Reactor Relevant Materials with EAF-2010", 2016 ISRD 15 – International Symposium on Reactor Dosimetry, Aix-en-Provence, France, 18-23 May 2015, Presentation ID: E155, EPJ Web of Conferences, Section: Cross Sections, Nuclear Data and Uncertainties, Vol. 106, ISBN: 9781510819405, doi: 10.1051/epjconf/201610604016, Feb. 2016

[108] X-5 Monte Carlo Team " MCNP — A General Monte Carlo N-Particle Transport Code, Version 5, Vol. I: Overview and Theory", LA-UR-03-1987, Apr. 2003

[109] V. Borisenko, P. J. Hesketh "Rapid Thermal Processing of Semiconductors", Springer US, ISBN: 978-0-306-45054-9, 1997

[110] H. Fukuda "Rapid Thermal Processing for Future Semiconductor Devices", Elsevier B.V, ISBN: 9780444513397, Apr. 2003

[111] Prof. Dr. Helmut Föll "Semiconductors I", online university course book, University of Kiel, Faculty of Engineering, AMAT, available on: https://www.tf.uni-kiel.de/matwis/amat/semi_en/index.html, last accessed on 19th March 2019

[112] F. Nava, G. Wagnerb, C. Lanzieric, P. Vannia, E. Vittone "Investigation of Ni/4H-SiC diodes as radiation detectors with low doped n-type 4H-SiC epilayers", Nuclear Instruments and Methods in Physics Research A, Vol. 510, Issue 3, pp. 273–280, Sept. 2003

[113] F. Nava et al. "Silicon carbide and its use as a radiation detector material", IOP Publishing Ltd., Measurement Science and Technology, topical review, Vol.19, Issue 10, doi: 10.1088/0957-0233/19/10/102001, Aug. 2008

[114] F. Moscatelli, A. Scorzoni, A. Poggi, M. Bruzzi, S. Lagomarsino, S. Mersi, S. Sciortino, M. Lazar, A. Di Placido, R. Nipoti "Measurements of Charge Collection Efficiency of p+/n Junction SiC Detectors" Materials Science Forum Vols. 483-485, pp. 1021-1024, May 2005

[115] C. Manfredottia, F. Fizzottia, A. Lo Giudicea, C. Paolinia, E. Vittonea, F. Nava "Investigation of 4H–SiC Schottky diodes by ion beam induced charge (IBIC) technique", Applied Surface Science, Vol. 184, Issues 1-4, pp. 448–454, Dec. 2001

[116] T. Ohshima, T. Satoh, M. Oikawa, T. Yamakawa, S. Onoda, T. Wakasa, J.S. Laird, T. Hirao, T. Kamiya, H. Itoh, A. Kinoshita,1, R. Tanaka,I. Nakano, M. Iwami, Y. Fukushima "Characterization of charge generated in silicon carbide n+p diodes using transient ion beam-induced current", Nuclear Instruments and Methods in Physics Research A, Vol. 541, Issues 1-2, pp. 236–240, Apr. 2005

[117] I. Ishikawa, W. Kada, F. Sato, Y. Kato, T. Tanaka, T. Iida "Development of a Radiation Detector Based on Silicon Carbide", Journal of Nuclear Science and Technology, Vol. 45, Supplement 5, pp. 489-491, June 2008

[118] A. M. Ivanov, M. G. Mynbaeva, A. V. Sadokhin, N. B. Strokan, A. A. Lebedev "Observation of impact ionization in 4H-SiC radiation detectors", Nuclear Instruments and Methods in Physics Research A, Vol. 606, Issue 3, pp. 605–607, July 2009

[119] M. De Napoli, F. Giacoppo, G. Raciti, E. Rapisarda "Study of charge collection efficiency in 4H–SiC Schottky diodes with ^{12}C ions", Nuclear Instruments and Methods in Physics Research Section A, Vol. 608, Issue 1, pp. 80–85, Sept. 2009

[120] M. De Napoli,G. Raciti, E. Rapisarda, C. Sfienti "Light ions response of silicon carbide detectors", Nuclear Instruments and Methods in Physics Research Section A, Vol. 572, Issue 2, pp. 831-838, March 2007

[121] M. De Napoli, F. Giacoppo, G. Raciti, E. Rapisarda "Dopant concentration dependence of the response of SiC Schottky diodes to light ions", Nuclear Instruments and Methods in Physics Research Section A, Vol. 600, Issue 3, pp. 618–623, March 2009

[122] A. A. Lebedev, A. M. Ivanov, N. B. Strokan "Radiation Resistance of SiC and Nuclear-Radiation Detectors Based on SiC Films", Review in Semiconductors, Vol. 38, Issue 2, pp. 125–147, 2004

[123] P. B. Klein, R. Myers-Ward, K.-K. Lew, B.L. VanMil, C. R. Eddy, Jr., D. K. Gaskill, A. Shrivastava, T. S. Sudarshan "Recombination processes controlling the carrier lifetime in n^- 4H–SiC epilayers with low $Z_{1/2}$ concentrations", Journal of Applied Physics, Vol. 108, Issue 3, doi: 10.1063/1.3466745, Aug. 2010

[124] O .Kordina, J.P. Bergman, C. Hallin, E. Janzen "The minority carrier lifetime of n-type 4H- and 6H-SiC epitaxial layers", Applied Physics Letter, Vol. 69, Issue 5, pp. 679-681, July 1996

[125] T. Kimoto, J. A. Cooper "Fundamentals of Silicon Carbide Technology: Growth, Characterization, Devices and Applications", John Wiley & Sons, Technology & Engineering, ISBN: 978-1-118-31352-7, pp. 333-337, Nov. 2014

[126] P. Ščajev, K. Jarasiunas "Temperature- and excitation-dependent carrier diffusivity and recombination rate in 4H-SiC", Journal of Physics D Applied Physics, Vol. 46, Issue 26, doi: 10.1088/0022-3727/46/26/265304, June 2013

[127] A. Ivanov, E. Kalinina, G. Kholuyanov, N. Strokan, G. Onushkin A. Konstantinov, A. Hallén, A. Kuznetsov "High Energy Resolution Detectors Based on 4H-SiC", Materials Science Forum, Vols. 483-485, pp. 1029-1032, May 2015

[128] E. Kalinina, N. Strokan, A.M. Ivanov, A. Sadohin, A. Azarov , V. Kossov, R. Yafaev, S. Lashaev "4H-SiC High Temperature Spectrometers", Materials Science Forum, Vols. 556-557, pp. 941-944, Sept. 2007

[129] A. M. Ivanov, E. V. Kalinina, N. B. Strokan, A. A. Lebedev "4H-SiC Nuclear Radiation p-n Detectors for Operation up to Temperature 375 °C", Materials Science Forum, Vols. 615-617, pp. 849-852, March 2009

[130] M. B. H. Breese "A theory of ion beam induced charge collection", Journal of Applied Physics, Vol. 74, Issue 6, pp. 3789-3799, Sept. 1993

[131] L. Berluti, C. Canali, A. Castaldini, A. Cavallini, A. Cetronio, S. D'Auria, C. del Papa, C. Lanzieri, G. Mattei, F. Nava, M. Proia, P. Rinaldi, A. Zichichi "Gallium arsenide particle detectors: a study of the active region and charge-collection efficiency", Nuclear Instruments and Methods in Physics Research Section A: Accelerators, Spectrometers, Detectors and Associated Equipment, Vol. 354, Issues 2–3, pp. 364-367, Jan. 1995

[132] https://wiki.documentfoundation.org/ReleaseNotes/4.4, last accessed on 19th March 2019

APPENDIXES

APPENDIX A: THE THICKNESS OF SPACE CHARGE REGIONS OF THE INVESTIGATED SIC SENSORS

APPENDIX B: CERAMIC ELEMENTS FOR MEASUREMENTS UP TO 155 °C IN FAST NEUTRON SPECTRUM

APPENDIX C: TECHNICAL DRAWINGS ABOUT THE PARTS OF THE MACOR HEATING HOUSE FOR HIGH TEMPERATURE TESTS

APPENDIX D: TECHNICAL DETAILS FOR MEASUREMENTS UP TO 500 °C IN FAST NEUTRON SPECTRUM

APPENDIX E: TECHNICAL DRAWINGS OF THE PARTS OF THE MAGNET CONTAINER CAPSULE

APPENDIX F: CHARGE CARRIER VELOCITY IN MAGNETIC FIELD

APPENDIX A: THE THICKNESS OF SPACE CHARGE REGIONS OF THE INVESTIGATED SIC SENSORS

The following graphs illustrate the space charge region thickness values in the function of the absolute bias voltage values for the developed SiC diode sensors. To the calculations, Eq.(15) was applied for room temperature conditions.

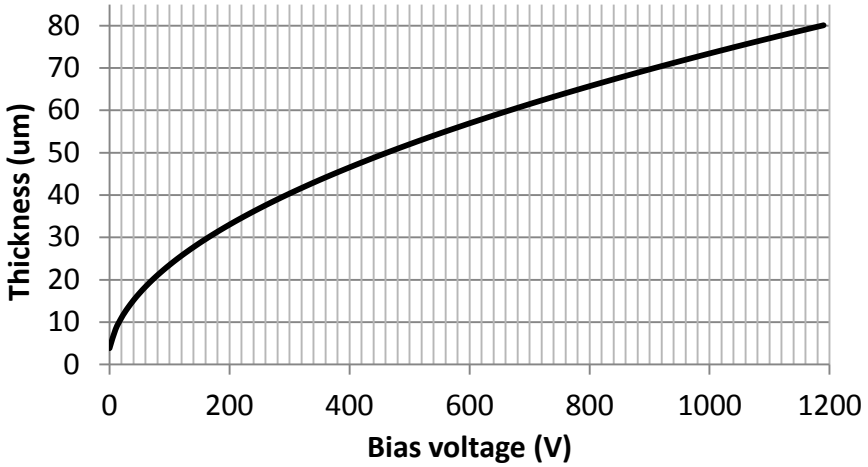

Sensitive layer thickness at different bias voltage values for D1 diode geometry

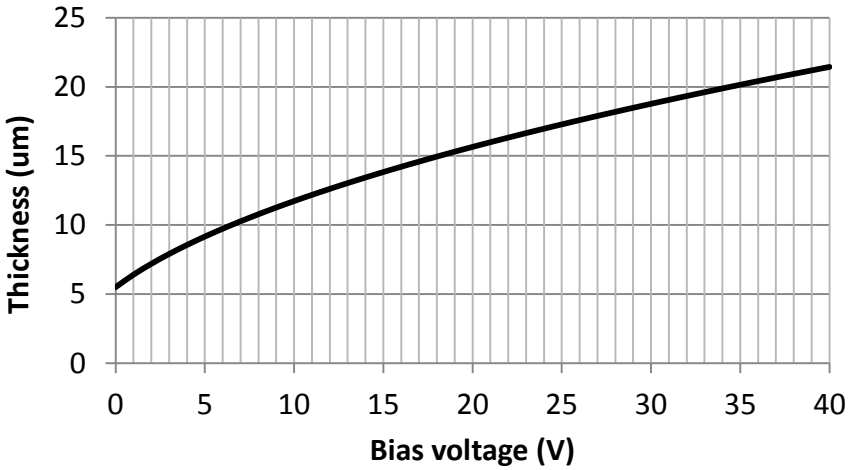

Sensitive layer thickness at different bias voltage values for D2 and “+1” diode geometry

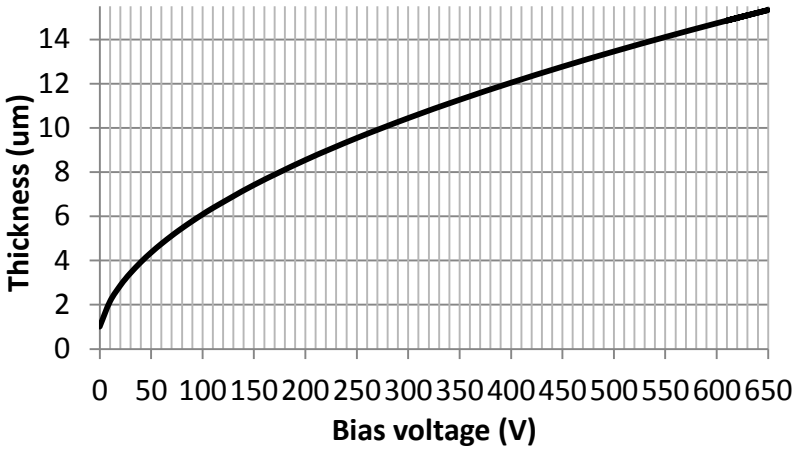

Sensitive layer thickness at different bias voltage values for D3 diode geometry

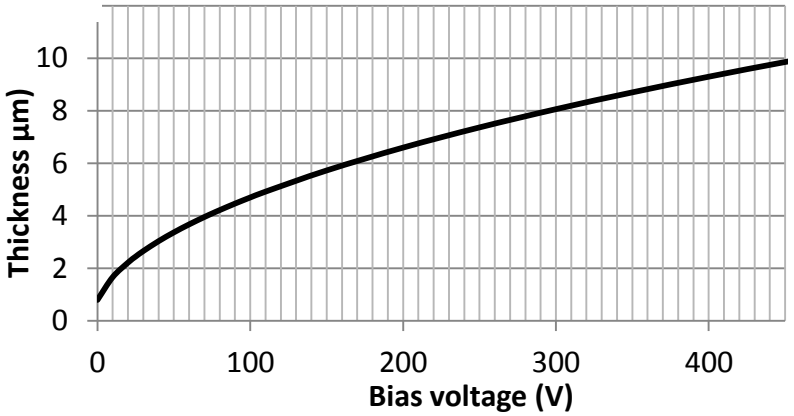

Sensitive layer thickness at different bias voltage values for D4 diode geometry

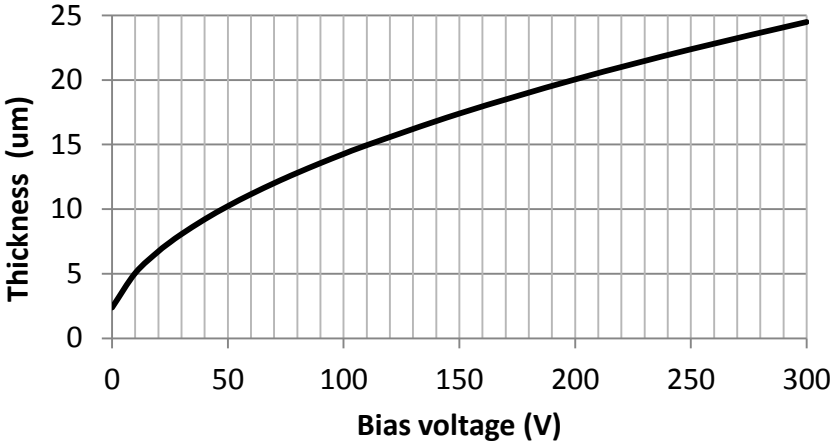

Sensitive layer thickness at different bias voltage values for D5 and D6 diode geometry

APPENDIX B: CERAMIC ELEMENTS FOR MEASUREMENTS UP TO 155 °C IN FAST NEUTRON SPECTRUM

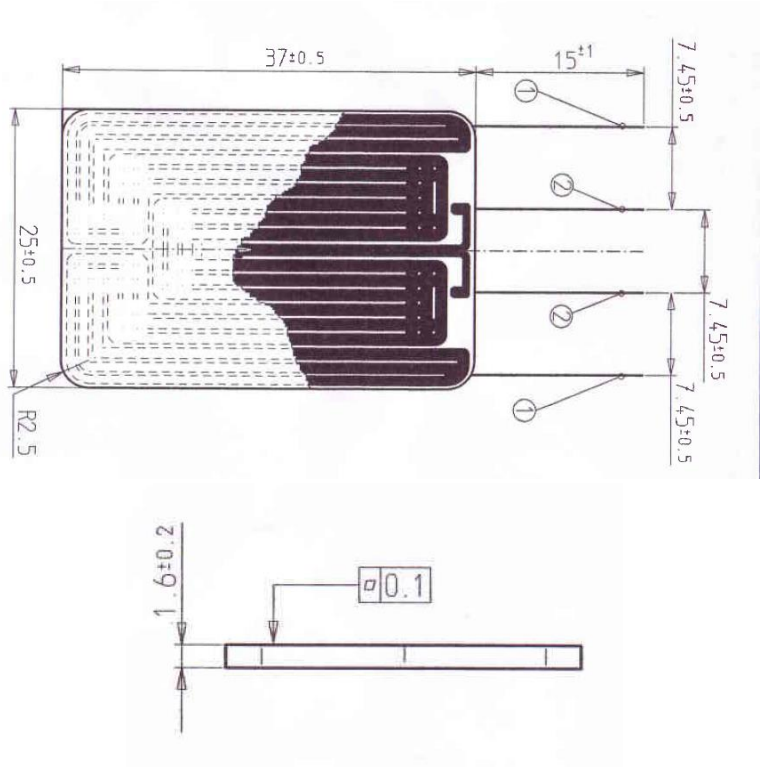

Technical drawing of the Al_2O_3 ceramic heating plate. 1 – platine connection to the heating circle, 2 – platine connection to the temperature sensor circle

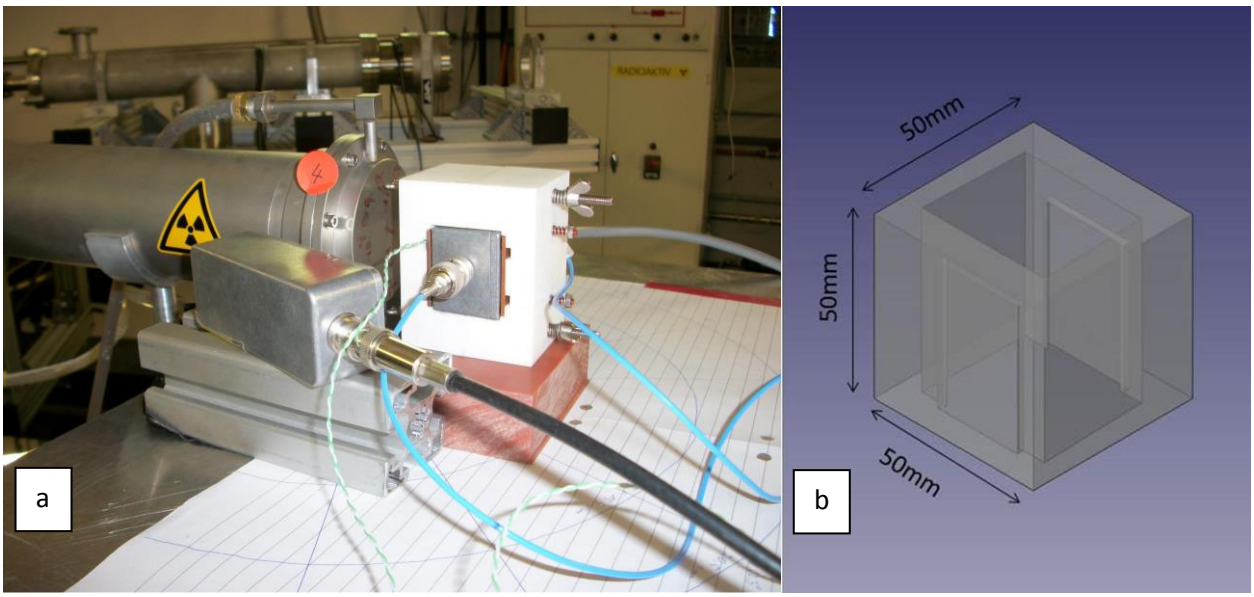

a - Macor heating box for high temperature tests with 14 MeV neutron irradiated SiC diode detectors, b - the transparent CAD model of the macor heating house

APPENDIX C: TECHNICAL DRAWINGS ABOUT THE PARTS OF THE MACOR HEATING HOUSE FOR HIGH TEMPERATURE TESTS

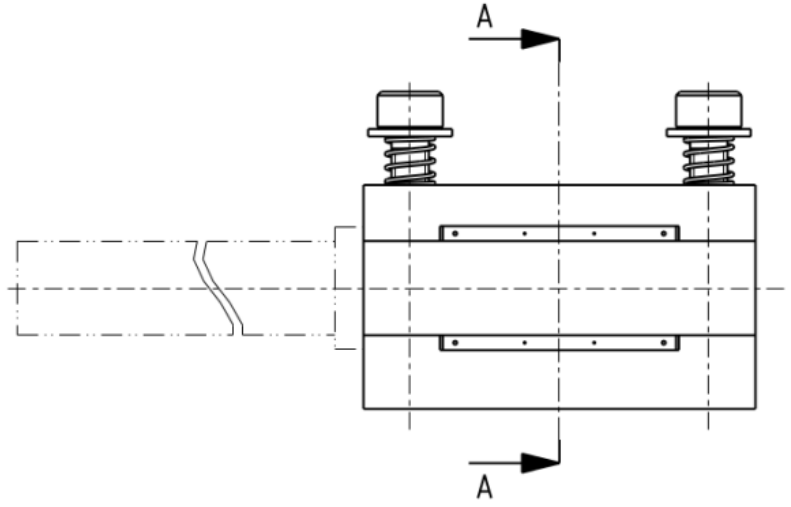

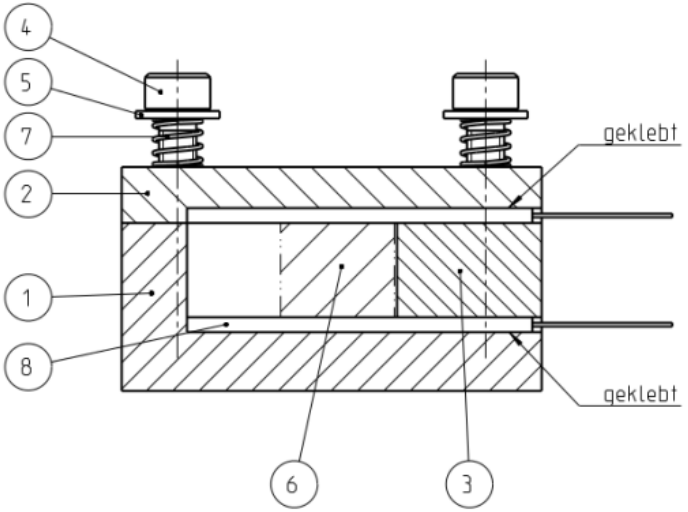

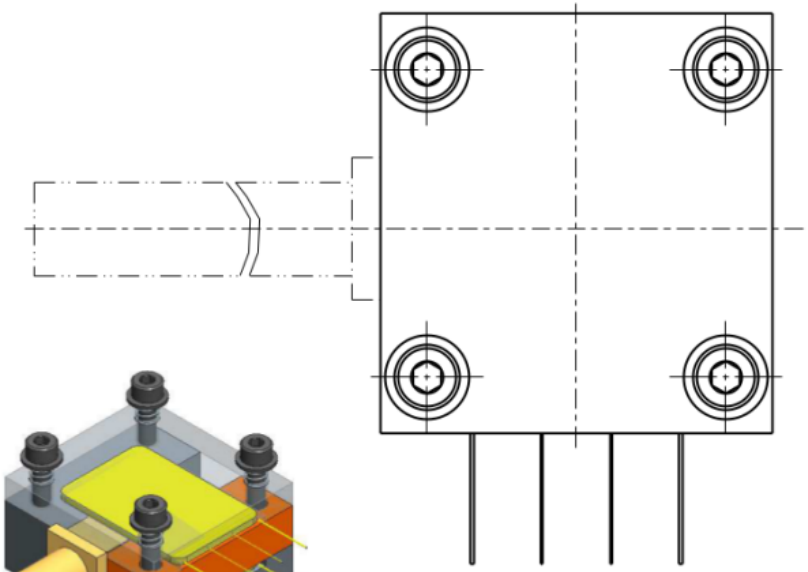

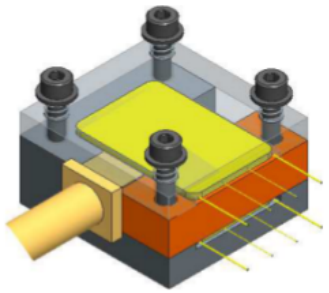

Pos.	ME	Benennung	Sachnummer/Kurzbezeichnung	Bemerkung
8	2	Flachheizer	35-2010A	Rausch
7	4	Druckfeder	D-043	Gutekunst
6	1	Probenhalter	vorhanden	
5	4	Scheibe	ISO 7089-4-A2	
4	4	Zylinderschraube	ISO 4762-M4x25-A2	
3	1	Klotz	12.221-08:03(4)	
2	1	Oberteil	12.221-08:02(4)	
1	1	Unterteil	12.221-08:01(4)	
1	2	3	4	5

Verwendungsbereich: ELBE

Zul. Abweichung: ISO 2768-mK

Oberflaeche:

Maßstab: 2:1

Gewicht: 0.184kg

Werkstoff:

	Datum	Name
Bearb.	28.05.2015	A. Nitzsche
Gepr.	28.05.2015	A. Winter
Bezugselement		W IA06853
EDV-Nr.		W IA06853

Benennung: Gehaeuse

HELMHOLTZ ZENTRUM DRESDEN ROSSENDORF
Abteilung FWFM

Zeichnungsnummer: 12.221-08(3)

Blatt 1 von 1 Bl

Ers. f.:

Letzte Aenderung: 28.05.2015

Zust. | Aenderung | Datum | Name

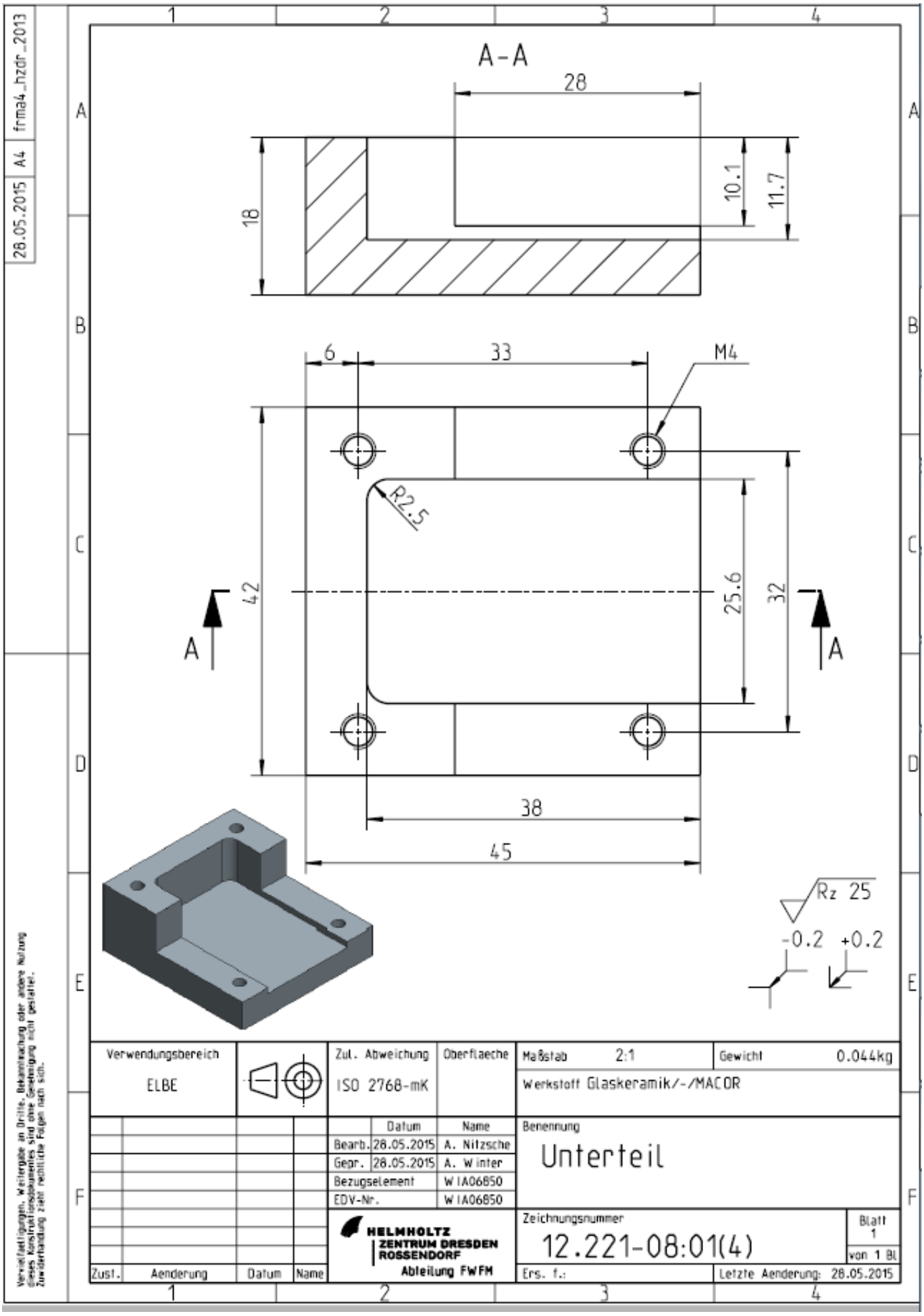
A-A
28
18
10.1
11.7
6
33
M4
R2.5
42
25.6
32
A
A
38
45
Rz 25
-0.2
+0.2
frma4_hzdr_2013
A4
28.05.2015
Verwendungsbereich
ELBE
Zul. Abweichung
ISO 2768-mK
Oberflaeche
Maßstab 2:1
Gewicht 0.044kg
Werkstoff Glaskeramik/-/MACOR
Datum
Name
Bearb. 28.05.2015 A. Nitzsche
Gepr. 28.05.2015 A. Winter
Bezugselement W1A06850
EDV-Nr. W1A06850
Benennung
Unterteil
HELMHOLTZ ZENTRUM DRESDEN ROSSENDORF
Abteilung FWFM
Zeichnungsnummer
12.221-08:01(4)
Blatt 1
von 1 Bl
Ers. f.:
Letzte Aenderung: 28.05.2015
Zust.
Aenderung
Datum
Name
Vervielfältigungen, Weitergabe an Dritte, Bekanntmachung oder andere Nutzung dieses Konstruktionsdokuments sind ohne Genehmigung nicht gestattet. Zuwiderhandlung zieht rechtliche Folgen nach sich.

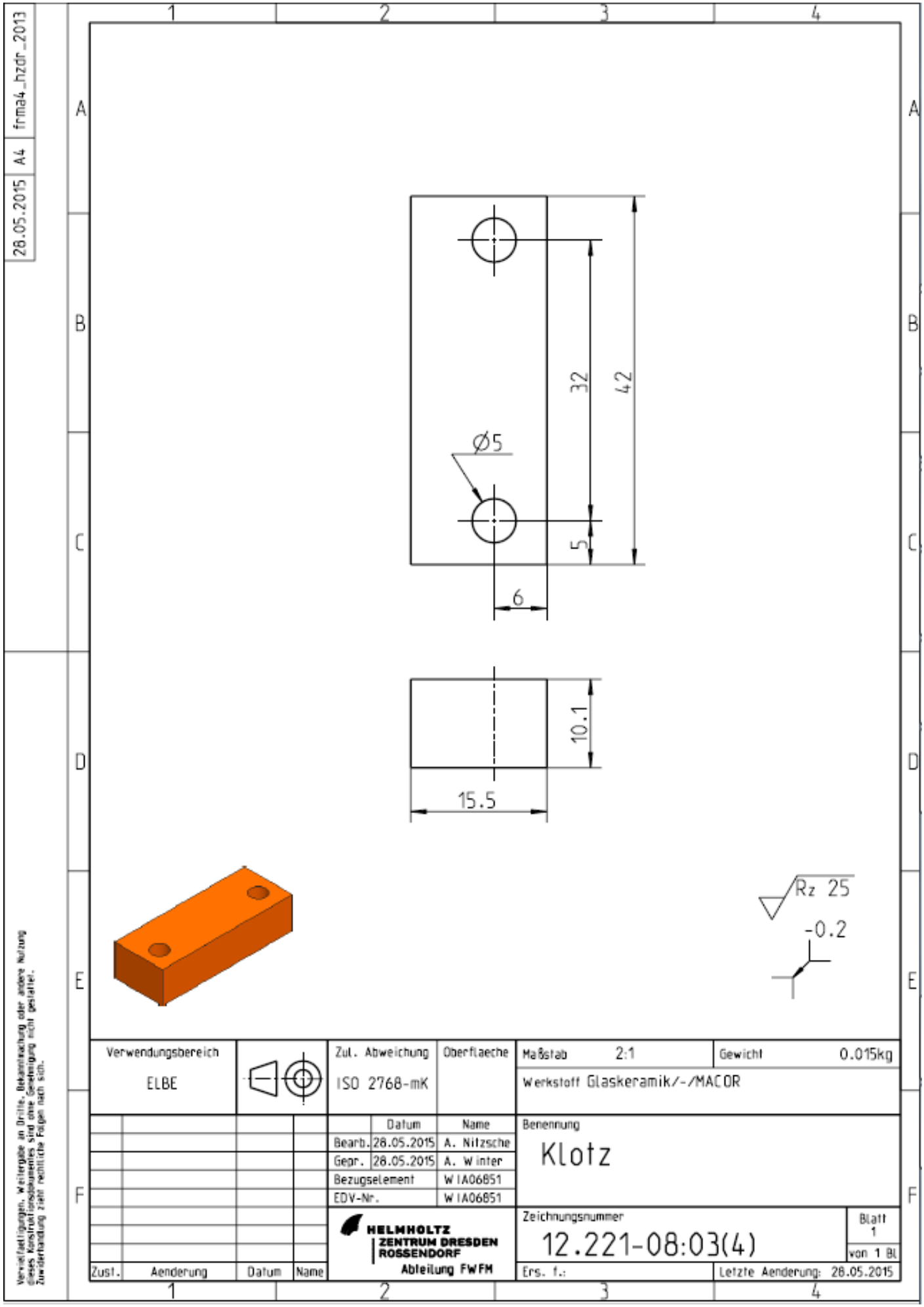
28.05.2015
A4
frma4_hzdr_2013
32
42
Ø5
5
6
10.1
15.5
Rz 25
-0.2
Verwendungsbereich
ELBE
Zul. Abweichung
ISO 2768-mK
Oberflaeche
Maßstab 2:1
Gewicht 0.015kg
Werkstoff Glaskeramik/-/MACOR
Datum
Name
Bearb. 28.05.2015 A. Nitzsche
Gepr. 28.05.2015 A. Winter
Bezugselement W IA06851
EDV-Nr. W IA06851
Benennung
Klotz
HELMHOLTZ ZENTRUM DRESDEN ROSSENDORF
Abteilung FWFM
Zeichnungsnummer
12.221-08:03(4)
Blatt 1
von 1 Bl
Zust. Aenderung Datum Name
Ers. f.:
Letzte Aenderung: 28.05.2015
Vervielfältigungen, Weitergabe an Dritte, Bekanntmachung oder andere Nutzung dieses Konstruktionsdokumentes sind ohne Genehmigung nicht gestattet. Zuwiderhandlung zieht rechtliche Folgen nach sich.

28.05.2015 | A4 | frma4_hzdr_2013

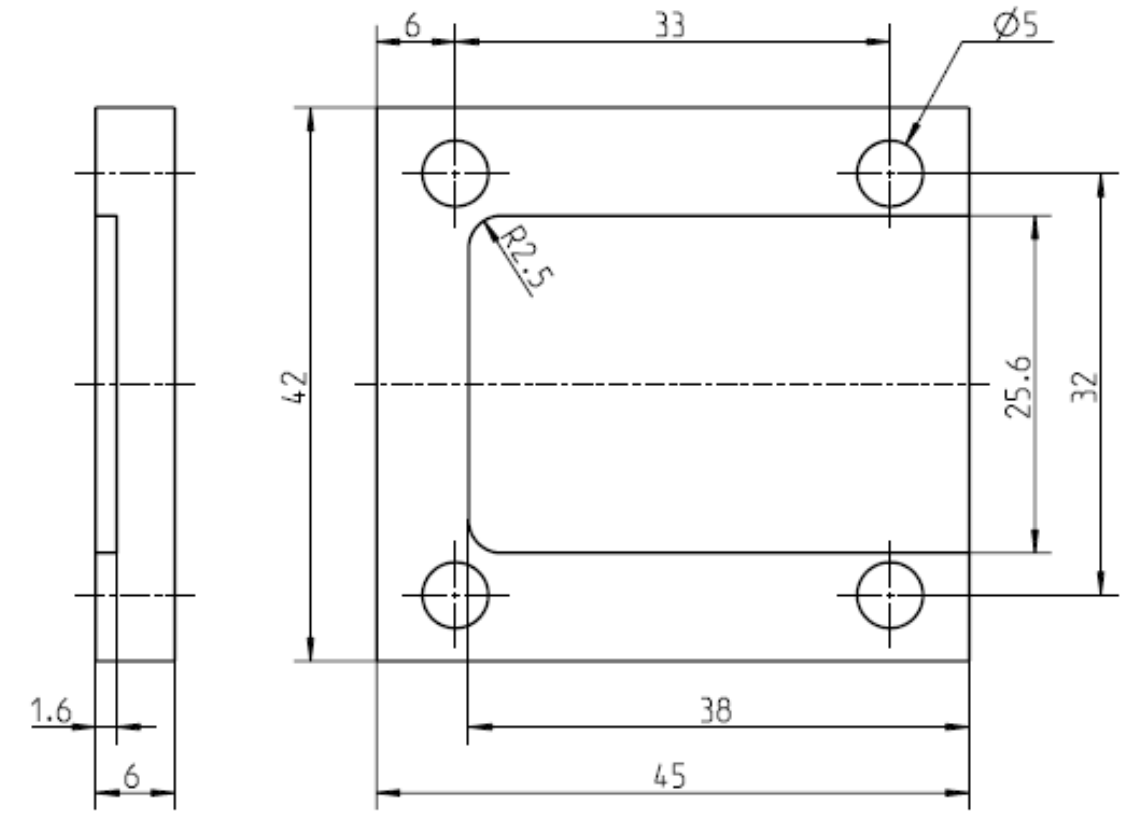

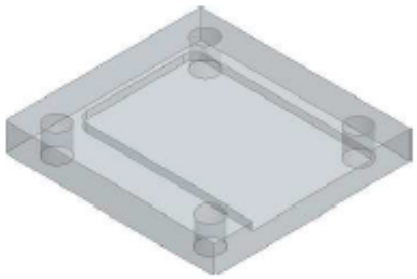

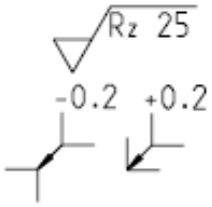

Verwendungsbereich: ELBE		Zul. Abweichung: ISO 2768-mK	Oberflaeche	Maßstab: 2:1	Gewicht: 0.023kg
				Werkstoff: Glaskeramik/-/MACOR	
		Datum	Name	Benennung: Oberteil	
		Bearb. 28.05.2015	A. Nitzsche		
		Gepr. 28.05.2015	A. Winter		
		Bezugselement	W IA06857		
		EDV-Nr.	W IA06857		
Zust.	Aenderung / Datum / Name	HELMHOLTZ ZENTRUM DRESDEN ROSSENDORF, Abteilung FWFM		Zeichnungsnummer: 12.221-08:02(4)	Blatt 1 von 1 Bl.
				Ers. f.:	Letzte Aenderung: 28.05.2015

APPENDIX D: TECHNICAL DETAILS FOR MEASUREMENTS UP TO 500 °C IN FAST NEUTRON SPECTRUM

The terminal of a stainless-steel tube was mounted with a female coaxial lemo connector. The outer shielding of the connector was constricted and glued in the steel tube, the inner contact was glued inside a small drilled hole at the terminal of the steel stick inside the tube. To glue and fix the aluminum capsule, the steel tube and the mentioned connector, the 597-A type conductive adhesive for high temperature from AREMCO Products Inc. was applied. The female lemo connector could be easily connected to standard coaxial connectors; thereby the signal of the diode was lead to a 50 cm long flexible coaxial cable. This cable was connected to a CAEN A1422 charge sensitive preamplifier. The measurements were controlled and the diode bias was adjusted by a Caen DT5780 multi-channel analyzer with its' DPP-PHA (Digital Pulse Processing for the Pulse Height Analysis) control software. To regulate the ceramic heating plates two Elektro-Automatik EA-PS 2084-05B laboratory power supplies were used.

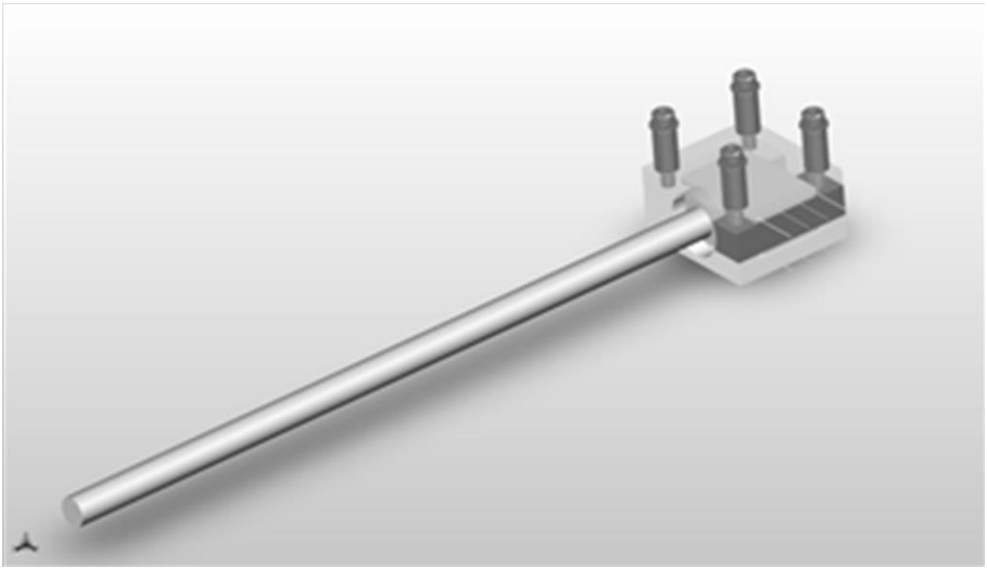

Small volume heating system with a macor ceramic house and two ceramic heating plates, surrounding the aluminum sample container box. The box was attached to a steel tube and to a steel stick inside the tube. The stick and the tube together are equivalent to a 50 Ohm coaxial signal transfer element and they have isolated the room temperature equipment from the heated measurement room

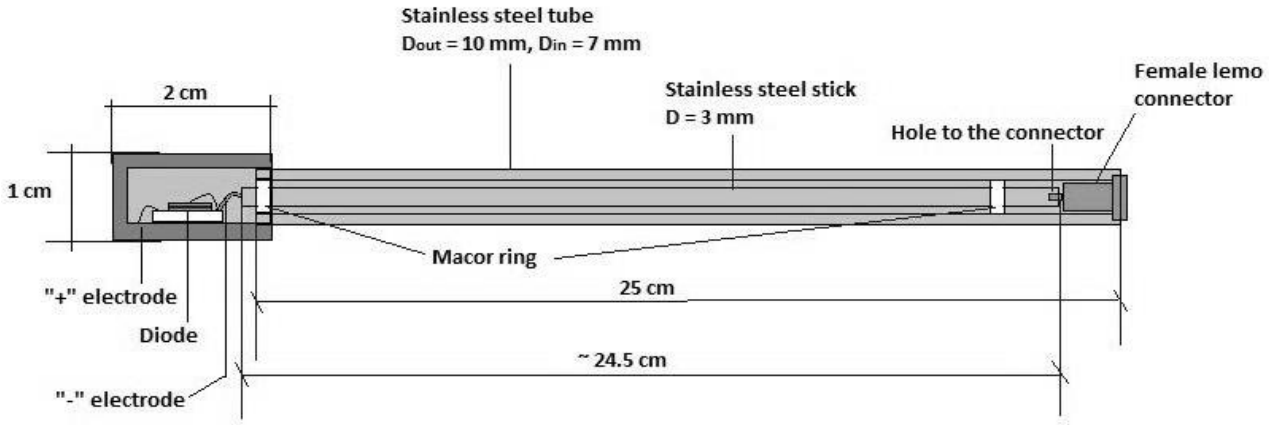

Cross-section of the developed sample container and signal transferring system for high temperature tests up to 500-600 °C

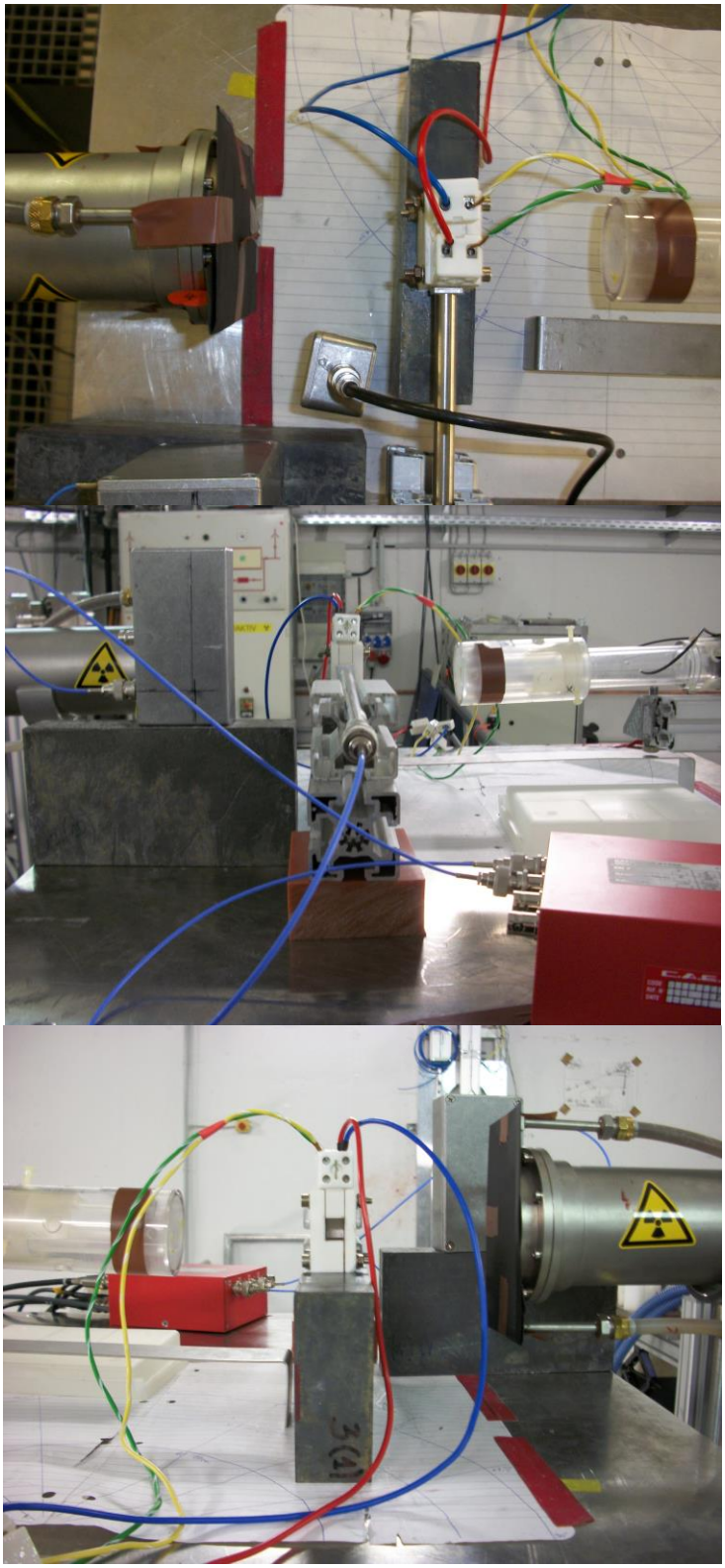

Set-up arrangement for fast neutron measurements at high temperatures up to 500 °C, a- Tritium target and macor housing from above, b- CEAN preamplifier attached to the 50 Ohm stainless steel coaxial cable through a coaxial connector, c- Tritium target, macor housing and CAEN preamplifier from the side

APPENDIX E: TECHNICAL DRAWINGS OF THE PARTS OF THE MAGNET CONTAINER CAPSULE

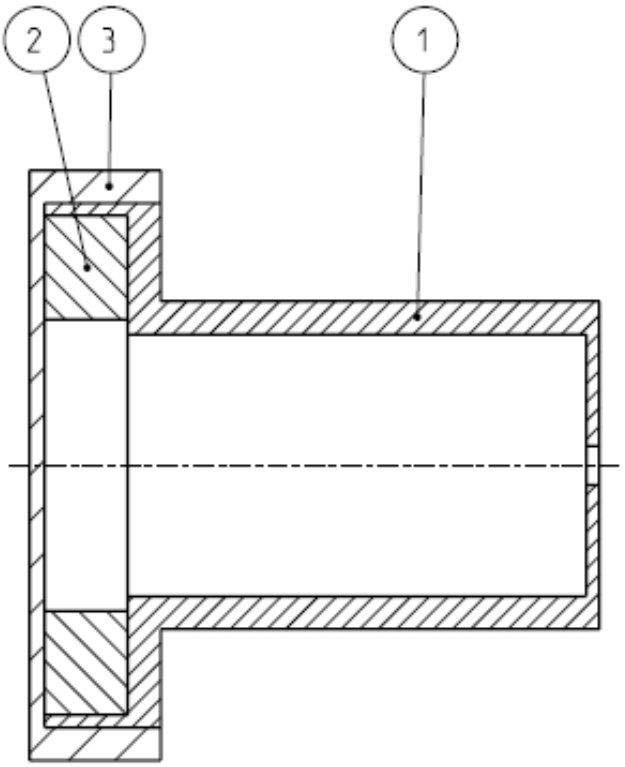

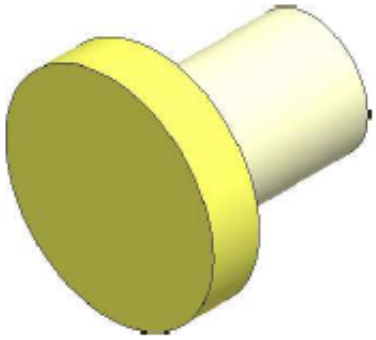

Pos.	ME	Benennung	Sachnummer/Kurzbezeichnung	Bemerkung
3	1	Deckel	12.221-07:03(4)	
2	1	Zwischenring	12.221-07:02(4)	
1	1	Aufnahme	12.221-07:01(4)	
1	2	3	4	5

Verwendungsbereich: ELBE

Zul. Abweichung: ISO 2768-mK

Oberflaeche:

Maßstab: 1:1

Gewicht: 0.407kg

Werkstoff:

	Datum	Name
Bearb.	27.05.2015	A. Nitzsche
Gepr.	27.05.2015	T. Süßmilch
Bezugselement		NIA16887
EDV-Nr.		NIA16887

Benennung: Magnettraeger

HELMHOLTZ ZENTRUM DRESDEN ROSSENDORF
Abteilung FWFM

Zeichnungsnummer: 12.221-07(4)

Blatt 1 von 1 Bl

Ers. f.:

Letzte Aenderung: 27.05.2015

Zust. | Aenderung | Datum | Name

27.05.2015 | A4 | frma4_hzdr_2013

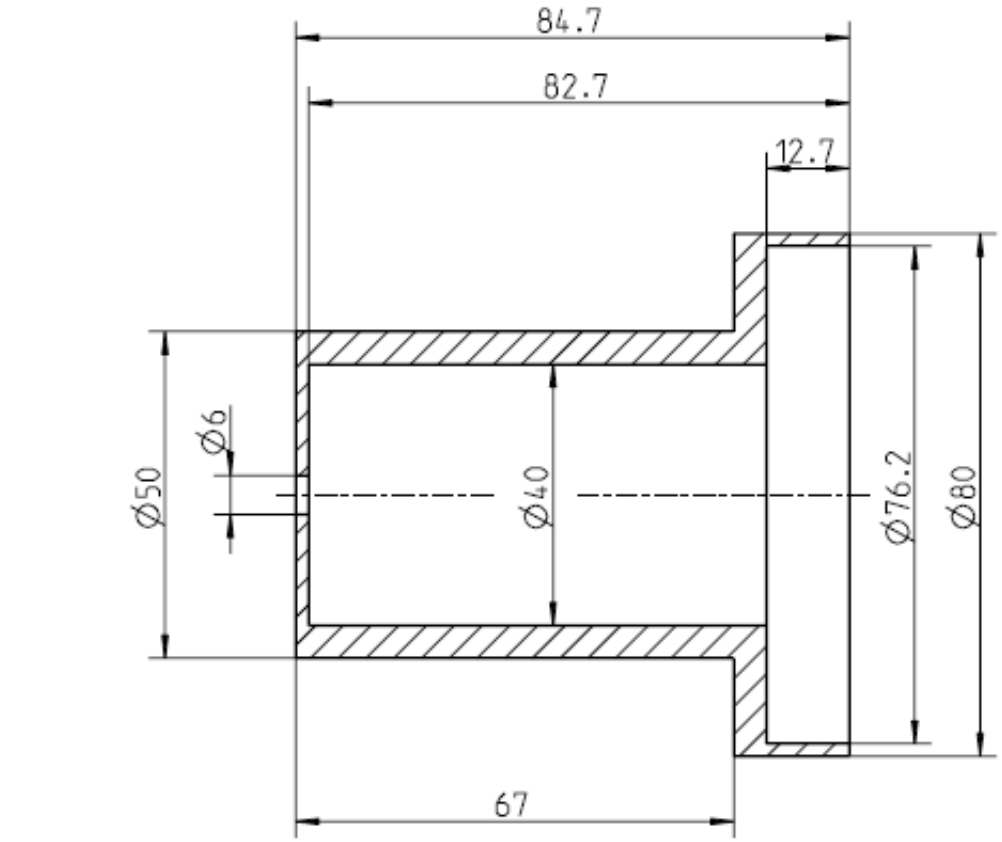

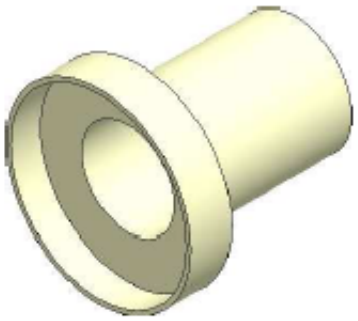

Rz 25
-0.2 +0.2

Verwendungsbereich: ELBE		Zul. Abweichung: ISO 2768-mK	Oberflaeche
Maßstab 1:1	Gewicht 0.201kg		
Werkstoff AlMgSi1/3.2315/EN AW-6082/-			

	Datum	Name
Bearb.	27.05.2015	A. Nitzsche
Gepr.	27.05.2015	T. Süßmilch
Bezugselement		NIA16888
EDV-Nr.		NIA16888

Benennung: Aufnahme

HELMHOLTZ ZENTRUM DRESDEN ROSSENDORF
Abteilung FWFM

Zeichnungsnummer: 12.221-07:01(4)

Blatt 1 von 1 Bl

Ers. f.:

Letzte Aenderung: 27.05.2015

Zust.	Aenderung	Datum	Name

27.05.2015 | A4 | frma4_hzdr_2013

27.05.2015 | A4 | frma4_hzdr_2013

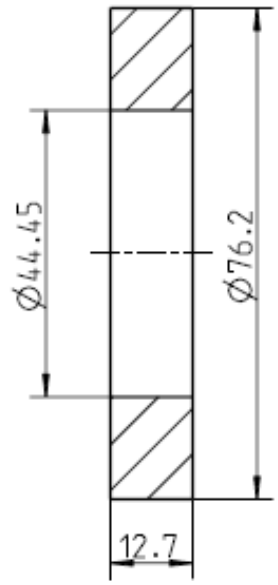

Rz 25

-0.2

Verwendungsbereich: ELBE		Zul. Abweichung: ISO 2768-mK	Oberflaeche	Maßstab 1:1	Gewicht 0.103kg
				Werkstoff AlMgSi1/3.2315/EN AW-6082/-	
			Datum	Name	Benennung: Zwischenring
		Bearb.	27.05.2015	A. Nitzsche	
		Gegr.	27.05.2015	T. Süßmilch	
		Bezugselement		NIA16889	
		EDV-Nr.		NIA16889	
Zust.	Aenderung / Datum / Name	HELMHOLTZ ZENTRUM DRESDEN ROSSENDORF, Abteilung FWFM		Zeichnungsnummer: 12.221-07:02(4)	Blatt 1 von 1 Bl
				Ers. f.:	Letzte Aenderung: 27.05.2015

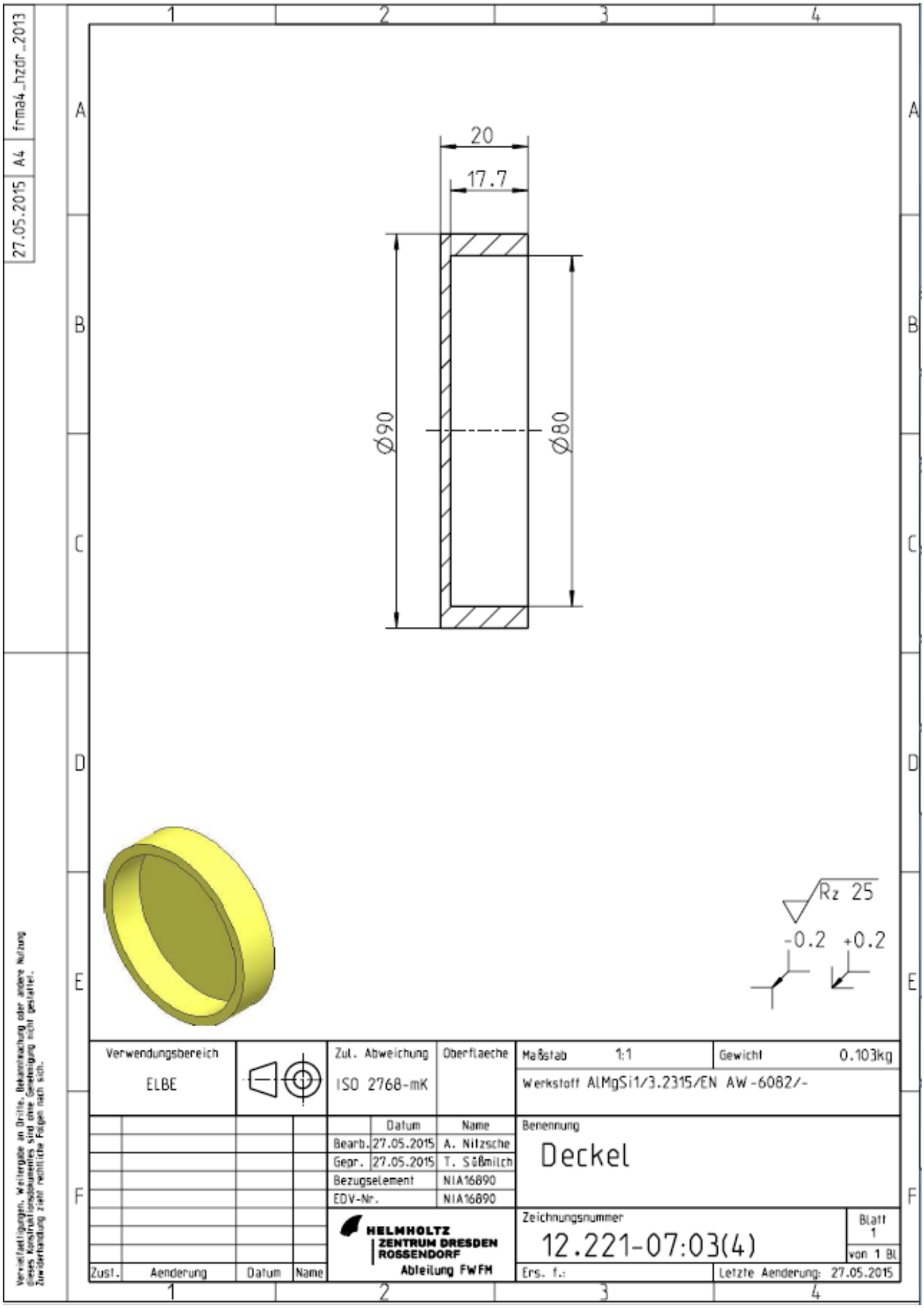
20
17.7
Ø90
Ø80
Rz 25
-0.2
+0.2
Verwendungsbereich
ELBE
Zul. Abweichung
ISO 2768-mK
Oberflaeche
Maßstab 1:1
Gewicht 0.103kg
Werkstoff AlMgSi1/3.2315/EN AW-6082/-
Datum
Name
Bearb. 27.05.2015 A. Nitzsche
Gepr. 27.05.2015 T. Süßmilch
Bezugselement NIA16890
EDV-Nr. NIA16890
Benennung
Deckel
HELMHOLTZ ZENTRUM DRESDEN ROSSENDORF
Abteilung FWFM
Zeichnungsnummer
12.221-07:03(4)
Blatt 1
von 1 Bl
Ers. f.:
Letzte Aenderung: 27.05.2015
Zust. Aenderung Datum Name
27.05.2015 A4 frma4_hzdr_2013
Vervielfältigungen, Weitergabe an Dritte, Bekanntmachung oder andere Nutzung dieses Konstruktionsdokumentes sind ohne Genehmigung nicht gestattet. Zuwiderhandlung zieht rechtliche Folgen nach sich.

APPENDIX F: CHARGE CARRIER VELOCITY IN MAGNETIC FIELD

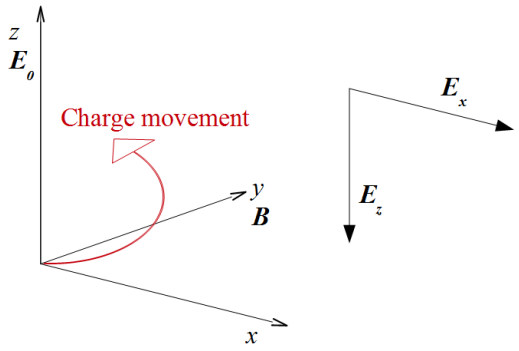

Charge carrier movement in orthogonal electric and magnetic fields

The direction and the velocity of the charge carriers (mostly electrons and holes) can change with the magnetic field compared to the case only assuming an electric field. To assess the velocity of a charged particle in an electric and magnetic field the electrical field due to the deflected particle has to be considered. The external electric field in z-direction ($\boldsymbol{E_0}$) drives the charge carriers in the z-direction. Due to the interaction with the applied magnetic field in y-direction ($\boldsymbol{B}$) the same charges experience a deflection in x-direction as indicated in the figure. The velocity vector of the charges has an x-component, which is characterized with an E_x electric field. Furthermore, the x-direction velocity component with the y-direction magnetic field generates an electric field in z-direction. This is characterized by E_z. The E_z component decelerates the charges. This reads to:

$$v_z = \mu(\boldsymbol{E_0} - E_z) \text{ and } v_x = \mu E_x ,$$

$$E_x = \boldsymbol{B} v_z \text{ and } E_z = \boldsymbol{B} v_x ,$$

where μ signs the Hall mobility of the charge carriers [99-101]. From above two equations, v_x and v_z can be expressed as:

$$v_x = \frac{\mu^2 \boldsymbol{B} \boldsymbol{E_0}}{1+(\mu \boldsymbol{B})^2} \text{ and } v_z = \frac{\mu \boldsymbol{E_0}}{1+(\mu \boldsymbol{B})^2}.$$

The sum of the square of both components provides the charge carrier velocity:

$$v^2 = {v_x}^2 + {v_z}^2 = \frac{(\mu \boldsymbol{E_0})^2}{1+(\mu \boldsymbol{B})^2} .$$

The last equation shows that increasing magnetic field yields a declining charge carrier velocity.

In case of biasing several kV/cm electric field through the space charge region of a diode appears. Therefore, only extreme high magnetic field could deflect moving charge carriers.

LIST OF ACRONYMS

BR1 - Belgian Reactor 1

D1-D6 – Diode 1 – Diode 6

DCLL - Dual Coolant Lithium Lead

DPP-PHA - Digital Pulse Processing for the Pulse Height Analysis

DT - Deuterium-Tritium

ELBE - Electron Linac for beams with high Brilliance and low Emittance

Geant4 - GEometry ANd Tracking

HCCB - Helium Cooled Ceramic Breeder

HCLL - Helium Cooled Lithium Lead

HCPB - Helium Cooled Pebble bed

HFR - High Flux Reactor

HV – High Voltage

ILL – Institut Laue-Langevin

ITER - International Thermonuclear Experimental Reactor

KIT – Karlsruhe Institute of Technology

INR – Institute of Neutron Physics and Reactor Technology

LLCB - Lithium Lead Ceramic Breeder

macor – machineable glass ceramic developed by Corning Inc.

MCA - Multi Channel Analyzer

SiC – Silicon-Carbide

SRIM – Stopping and Ranges of Ions in Matter

TBM – Test Blanket Module

TRIM - TRansport of Ions in Matter

TU Dresden – Technical University of Dresden

WCCB - Water Cooled Ceramic Breeder